Asymptotic Solutions and Numerical Methods for some Free-boundary Problems in Fluid Mechanics

Yiyun Fan

Supervisors: Prof John Billingham, Prof Kris van der Zee
School of Mathematical Sciences
University of Nottingham

Thesis submitted to the University of Nottingham
for the degree of Doctor of Philosophy

2023

Abstract

Free-boundary problems are encountered in a wide range of applications in fluid mechanics, such as the interaction of a ship with the surface of the ocean, and the failure of a dam. Since the free boundary is unknown and part of the solution, such problems are nonlinear and rarely have analytical solutions. In this thesis, we formulate and solve some free-boundary problems in inviscid fluid mechanics using asymptotic and numerical methods. We construct new asymptotic solutions for the two-fluid dam-break problem and a solid/two-fluid interaction problem with an inclined accelerating plate, and develop the numerical methods based on the finite element method for generic free-boundary problems.

The main outcomes of this research are as follows. The small-time outer asymptotic solutions have a singularity at the intersection point between the interface and the solid boundary for both problems, which can be resolved by rescaling into an inner region. A numerical approach based on the finite element method and Newton's method is developed to resolve the inner problem of the solid/single fluid inner region problem, which agrees with the results obtained by the boundary integral method in earlier work. Furthermore, we derive a Shape-Newton method as a fast nonlinear numerical solver to solve the generic free-boundary problem with Bernoulli-type boundary conditions on the free surface, which is tested on the problem of flow over a triangular obstacle. The application of this method can be extended to a range of more complicated free-boundary problems in fluid mechanics.

Acknowledgements

I would like to extend my heartfelt gratitude to my supervisors, Professor John Billingham and Professor Kris Van der Zee, for their invaluable guidance and unwavering support, particularly during the challenging times of the COVID-19 pandemic while I pursued remote studies. Throughout this journey, their supervision has been truly priceless, and I am deeply appreciative of their exceptional guidance.

My sincere thanks also go to the staff of the School of Mathematical Sciences, whose assistance proved indispensable during my studies.

To my family and friends, I am immensely grateful for their support and constant encouragement throughout this transformative journey.

Lastly, I would like to express my profound gratitude to both of my beloved late grandmothers, whose love, guidance, and unwavering dedication have left an indelible impact on my life. Although they are no longer with us, their presence and enduring influence will forever inspire and motivate me.

Contents

Abstract **i**

Acknowledgements **ii**

1 Introduction **1**

1.1 Related work 4

1.1.1 Fluid/Solid interaction problem with an accelerating plate . . 4

1.1.2 Dam-break problem 6

1.1.3 Numerical methods for free-boundary problems 10

1.2 Thesis Overview 12

2 Preliminaries **15**

2.1 Conformal Mapping and Schwarz-Christoffel Transformation 16

2.2 Plemelj Formula 18

2.3 Shape Calculus 20

3 The Initial Stage of The Two-Fluid Dam-Break Problem **25**

3.1 Introduction 25

3.2 Two fluid dam-break problem for $0 < \alpha < \frac{\pi}{2}$ 27

3.3 Asymptotic solution in the outer region for $t \ll 1$ 30

3.3.1 The eigenvalue problem 31

3.3.2 Asymptotic solution for $\bar{\rho} \ll 1$ and $r \ll 1$ 32

3.4 Solution using the Plemlj formula in the outer region for $t \to 0$ 38

3.4.1 The solution for $\bar{\rho} > 0$ 41

3.4.2 Solution for $\bar{\rho} = 0$ 43

3.5 Numerical approximation for outer region 43

3.5.1 Numerical results for $\bar{\rho} = 0$ 43

3.5.2 Numerical results for $\bar{\rho} > 0$ 45

3.6 Inner-region Solution for $t \to 0^+$ 48

3.7 Conclusion 55

4 The Initial Stage of Solid/Two Fluid Interaction Problem with an Inclined Accelerating Plate 56

4.1 Introduction 56

4.2 Governing equations 58

4.3 Asymptotic solution as $t \to 0^+$ in the outer region 61

4.3.1 Asymptotic solution in the outer region for $(\bar{x}, \bar{y}) \to 0^+$ 62

4.3.2 Solution using Plemelj Formula 65

4.4 Numerical results for the outer region problem 68

4.5 Inner region as $t \to 0^+$ for $\frac{\pi}{2} < \alpha < \pi$ 70

4.6 Conclusion 77

5 Fluid/solid Problem with an Inclined Accelerating Plate in the Inner Region 79

5.1 Introduction 79

5.2 Local solution of the linearised inner-region problem for $\alpha \to \frac{\pi}{2}$ 82

5.3 Coupled problem for the linearised problem 86

5.3.1 The weak form 87

5.3.2 Finite element method and the numerical iteration 89

5.3.3 Numerical results 92

5.4 The review and the reformulation of the inner-region problem 94

5.4.1 Weak forms 96

5.4.2 Linearisation 98

5.5 Newton's Method 100

5.5.1 Implementation 101

5.5.2 Numerical Results 105

5.6 Conclusion 108

6 Shape-Newton Method for Free-boundary Problems 111

6.1 Introduction 111

6.2 Steady Free-boundary Problem 114

6.2.1 Free-boundary Problem with Bernoulli Condition 114

6.2.2 Free-boundary Problem with Dirichlet Boundary Condition . . 116

6.3 The Weak Form 116

6.4 Shape Derivatives 118

6.5 Linearisation 119

6.5.1 Linearisation of $\mathcal{R}_1$ 119

6.5.2 Linearisation of $\mathcal{R}_2$ with Dirichlet condition 120

6.5.3 Linearisation of $\mathcal{R}_2$ with Bernoulli condition 121

6.6 Newton-like Schemes 123

6.6.1 Coupled scheme 124

6.6.2 Implementation 126

6.7 Numerical experiments 129

6.7.1 Dirichlet boundary condition 129

6.7.2 The submerged triangle problem 131

6.8 Conclusion 136

7 Conclusion 138

Bibliography 145

Appendices 153

A Two-fluid Dam-Break Problem Around The Upper Contact Point 153

B Single Fluid Problem with an Inclined Accelerating Plate in the Inner Region 158

C Simplified Free boundary problem with Dirichlet Condition or Tangential Condition 162

C.1 Simplified problem for Dirichlet boundary condition 162

C.1.1 Picard iteration 163

C.1.2 Newton's method 165
C.1.3 Numerical experiment 170
C.2 Simplified problem for tangential boundary condition 172
C.2.1 Picard iteration 172
C.2.2 Newton's method 174
C.2.3 Numerical experiment 175
D Submerged Triangle Problem **178**

List of Tables

5.1 The numerical scheme for the linearised single-fluid problem in the inner region. 90

5.2 The finite difference Newton's method solving for $(\delta\Phi, \delta\eta)$. 99

5.3 The algorithm for finite difference Newton's method solving for the single fluid/solid interaction problem in the inner region. 104

6.1 The coupled shape-Newton scheme solving for $(\delta\boldsymbol{\theta}, \delta\phi)$. 125

6.2 The coupled shape-Newton scheme for $(\delta\eta, \delta\phi)$. 126

6.3 The convergence in space, where $\alpha = \frac{\pi}{16}$, $w_0 = 0.1$, and $F = 3$. 133

C.1 The Picard iteration scheme. 165

C.2 The Newton scheme. 168

List of Figures

1.1 The sketch of a fluid with an accelerating plate. The acceleration is a and the initial depth of the fluid is L 4

1.2 The comparison between Ritter's solution (Simple wave theory) and the experimental observations, where d_o is the initial depth upstream. This graph is the Fig. 17.18 in [11]. 7

1.3 The sketch of a free-boundary problem in domain Ω with free boundary Γ_F. 10

2.1 An example sketch of Schwarz-Christoffel Transformation. 17

2.2 The sketch of $(+)$ and $(-)$ region on either side of Γ and the definition of Γ_ϵ. 19

3.1 The sketch of two fluids with different densities in a channel with an interface $y = -\tan \alpha x$ at $t = 0$, where $0 < \alpha \leq \pi/2$. 27

3.2 33

3.3 Period extension of the interface. 39

3.4 The comparison between numerical solution and asymptotic solution for $\bar{\rho} = 0$. The y-axis is $\frac{\hat{\phi}_1 - \hat{\phi}_1(0)}{r}$, where $\hat{\phi}_1(0)$ is the constant term in $\hat{\phi}_1$. Figure (a) and (b) show the results near the bottom contact point at $y = 0$ and the upper endpoint at $y = 1$ with $\alpha = \frac{\pi}{3}$, while Figure (c) and (d) show the results with $\alpha = \frac{\pi}{4}$. 44

3.5 The log-log plots of $\tilde{\phi}_1$ after subtracting constant and linear terms with respect to the radius r for various values of $\bar{\rho}$ with a different angle close to two intersection points. Figure 3.5a and 3.5b show the results near the bottom contact point and the upper contact point for $\bar{\rho} = 0.01$ with $\alpha = \frac{\pi}{3}$, while Figure 3.5c and 3.5d show the solutions near the bottom contact point and the upper contact point for $\bar{\rho} = 0.001$ with $\alpha = \frac{\pi}{4}$. The red lines represent the asymptotic solution, and the blue lines represent the numerical results. 46

3.6 The comparison between numerical results of leading order term in r (except the linear term) and β_0 against $\bar{\rho}$ for $\alpha = \frac{\pi}{3}$ and $\frac{\pi}{4}$. The upper subplot is for the upper contact point, and the lower subplot is for the lower contact point. The red lines are numerical power (the power of the numerical results of the leading order as $r \to 0$), and the blue lines are values of β_0. 47

3.7 The numerical results of the displacement of the interface $\bar{Y}(x)$ with respect to x for different $\bar{\rho}$ and different angles α. 49

3.8 The asymptotic form given by (3.6.40) for $\eta_0 = 0.5$, $\beta = 0.8$, $\bar{\rho} = 10$ and $B = 6$. The bold black line represents the plate, and the blue curve is the free surface. 54

4.1 The sketch of two fluids with different densities with an inclined plated at $y = -\tan\alpha x$. 58

4.2 The domain of solution of the boundary-value problem (4.3.27)-(4.3.31). 65

4.3 The sketch of the interface in w-plane. The solid curves are the interfaces after conformal mapping, and the dash curves are the arcs as part of the circle $u^2 + v^2 = R^2$. 67

4.4 The numerical power compared with asymptotic power for $d = 0.5$, $\rho = 5$ and $d = 0.7$, $\rho = 2$ against $\frac{\pi}{2} < \alpha < \pi$. The blue lines are the numerical coefficients, and the red curves are the asymptotic coefficients. 69

4.5 Two examples of the shape of the interface $\bar{\eta}$ scaled with respect to σ, plotted against $\tilde{x}$ for the situation $\alpha = 2.2$, $d = 0.5$ and $\rho = 2$, and the situation for $\alpha = 2.5$, $d = 0.7$ and $\rho = 5$. 70

4.6 The loglog plot of A_1 against with $\frac{1}{1-d}$ for $\alpha = 2.5$, $\bar{\rho} = 5$ and $\alpha = 2.2$, $\bar{\rho} = 1$. The blue lines represent the numerical results, and the red lines represent the asymptotic results $\beta_0 - \frac{\pi}{2\alpha}$ 71

4.7 The loglog plot of A_1 against with $\frac{1}{d}$ for $\alpha = 2.5$, $\bar{\rho} = 5$ and $\alpha = 2.2$, $\bar{\rho} = 1$. The blue lines represent the numerical results, and the red lines represent the fitting curve. 72

5.1 An example of the asymptotic form given by (5.2.33) for $B = 3$. The bold black line represents the plate, and the blue curve is the free surface. 86

5.2 The domain and the finite element mesh. 91

5.3 (a) and (b) show the numerical results ϕ_h, η_h and far-field conditions $\hat{\phi}_\infty$, $\hat{\eta}_\infty$. 93

5.4 The error convergence of $\boldsymbol{\eta}$ in L_2 norm. 94

5.5 Conforming finite element mesh. The left is the mesh with an initial guess of the free boundary Γ_0, while the right is the mesh with the updated free boundary Γ_F. 105

5.6 η for various α. The axis system has been rotated to be the same as the one used to construct the model. The black lines are the location of the inclined plates. 107

5.7 The numerical result of $\hat{\eta}$ where $x \to 0$ for $\alpha_c = 1.8886$. 107

5.8 108

5.9 The free surface close to the intersection when $\alpha = 1.75$ from [64]. In this figure $\hat{\eta} = \tilde{\eta} - \tilde{\eta}_0$ and $\hat{x}$ is the same as $\hat{X}$ in this chapter. 109

6.1 The sketch of the parametrization of the free boundary Γ_F by the displacement $\boldsymbol{\theta}(\boldsymbol{x}_0)$ with respect to the reference boundary Γ_0. 114

6.2 The initial domain and the change of the domain in three following Newton-like iterations. The free surface is updated vertically. 130

6.3 The Dirichlet error $||\phi - h||_{L_\infty}$ and surface error $||\eta - \hat{\eta}||_{L_\infty}$ on Γ_F measured in L_∞-form against the number of iterations. The upper plot shows the Dirichlet error, and the lower shows the surface error. The values of $N + 1$ are the number of the nodes along the x-axis. . . 131

6.4 The sketch of the domain we used for the second test case. α is denoted as the angle and w_0 as the half width of the triangle. 132

6.5 An example of the domain and the triangulation with $\alpha = \frac{\pi}{4}$, $F = 2$ and the half width of the triangle $w_0 = 0.5$. 133

6.6 The final domains for various α, w_0 and F, where their free boundarys are the numerical solutions. 134

6.7 The maximum value y_0 on the free boundary at $x = 0$ against F for different values of α and w_0. 135

6.8 The error $||\delta\phi||_{L_2}$ and surface error $||\delta\eta||_{L_2}$ on Γ_F measured in L_∞-form against the number of iterations with $\alpha = \frac{\pi}{8}$, $w_0 = 0.3$ and $F = 3$. The upper plot shows the Dirichlet error, and the lower shows the surface error. The values of $N + 1$ are the number of the nodes along the x-axis. 136

B.1 The sketch of a fluid with an inclined plate at $y = -\tan\alpha x$. 158

C.1 Comparison between Picard iteration and Newton's method for the second simplified problem. (a) and (c) are the results solved by Picard iteration, while (b) and (d) are for Newton's method. (e) and (f) compares the rate of convergence of Picard iteration and Newton's method. 171

C.2 Comparison between Picard iteration and Newton's method for the third simplified problem. (a) and (c) are the results solved by Picard iteration, while (b) and (d) are for Newton's method. (e) and (f) compares the rate of convergence of Picard iteration and Newton's method. 176

D.1 This shows two different types of solutions and the sketch of the flow. D.1a is a sketch of the flow for $U = \tilde{U}$ $L = \tilde{L}$ and $F \geq 1$. D.1b is an example of subcritical flow upstream and supercritical flow downstream. 178

D.2 τ is the maximum value of the deviation of the free surface. t_3 defines the geometry of the triangle by using conformal mapping and then mapping to a half-unit circle called $t-$plane. The dashed line shows the analytical values of the maximum of τ with respect to F. The curve noted 0 is the solitary wave when $t_4 = 0$. This graph is from [22]. 180

Chapter 1

Introduction

Studies of the wide variety of different free-boundary problems, using both asymptotic and numerical methods, have a long history. Such problems are encountered in a range of applications in fluid mechanics, such as the interaction of a ship with the surface of the ocean, whose idealised setting is the interaction of a moving flat surface with a free boundary (see e.g. [18, 84]). The second example relevant to this thesis is the dam-break problem, which models the sudden release of water due to the failure of a dam (see e.g. [19, 85]). In each case, one of the main features of the flow is the formation of a localised jet in the neighbourhood of a three-phase contact line [52, 53]. Understanding and quantifying the initial flow with a jet when a solid body or a body of fluid is set in motion is a crucial element in the design of ships and dams due to the possibility of damage to the solid body. Another type of free-boundary problem in fluid mechanics is flow over a submerged obstacle, such as a reef or submarine (see e.g.[33, 81]). Analysing how the shape of the free surface changes in this case is also relevant to ship hydrodynamics [65] and to the detection of submerged bodies by their effect on the free surface (see e.g.[23, 30, 73]).

We focus on inviscid, irrotational flows, which means that for our purposes, a free-boundary problem consists of a second-order elliptic partial differential equation and the necessary boundary data. The boundary conditions on the free surface that

determine its shape include the kinematic and Bernoulli conditions in inviscid fluid mechanics. Since the free boundary is unknown and part of the solution, free-boundary problems are nonlinear and rarely have analytical solutions. Asymptotic methods and numerical techniques are the two primary approaches to solving these problems. Although asymptotic methods can simplify the problem in limiting cases, for some free-boundary problems, the singularity at the free surface makes this extremely challenging [66]. Furthermore, the singular behaviour near the interaction of the free boundary with solid boundary and the nonlinearity of the free-boundary problems make it highly demanding to derive a suitable numerical method [100]. The finite element method simulates the free-surface flow throughout the entire region, providing comprehensive solutions to the problems. Approaches based on the finite element method solve problems with simple free-boundary conditions and can be very computationally intensive (see e.g. [71]).

In this thesis, we formulate and solve some free-boundary problems in inviscid fluid mechanics using asymptotic and numerical methods. New asymptotic solutions are constructed for free-boundary problems involving two different fluids. The first of these is the two-fluid dam-break problem, where a plate separating two fluids in an infinitely long channel is suddenly removed. The second is a solid/two-fluid interaction problem, namely an inclined accelerating plate moving towards two layers of different fluids. The numerical methods developed in this thesis are based on the finite element method and can be used to solve generic free-boundary problems with complicated, nonlinear free-boundary conditions, which can be further extended to solve the inner-region problems of the solid/fluid interaction problems, where the singularities have been resolved.

The main contributions of this research are as follows. Firstly, small-time asymptotic solutions for the two-fluid dam-break problem and a solid/two-fluid interaction problem are obtained close to the contact point where the interface meets the solid boundary. Both problems have the same formulation of the local problem

near the contact point. Most previous research in this area is on flows of a single fluid. For certain free-boundary problems, the singular behaviour on the free boundary needs to be resolved, which can be achieved by rescaling it into an inner region around the singularity point. We find the local eigensolutions at the contact point, which may be singular and determine the scaling for the inner problem, and solve the outer problem numerically using the Plemelj formula.

Secondly, the finite element method is applied to solve the small-time inner problem for the solid/single fluid interaction problem. This problem has previously been solved using the boundary integral method [64], which reformulates the problem onto the free boundary. We use the finite element method to discretize the entire domain into finite elements and approximate the solutions within these elements. The nonlinearity of this problem is addressed using Newton's method, which requires linearisation of the weak forms using a finite difference method to obtain a linear system, and the results show good agreement with the shape of the free surface.

Finally, the Shape-Newton method is developed as a fast numerical solver for generic steady free-boundary problems. The boundary conditions are in a more general form where we use Robin boundary conditions on the fixed boundaries, but one of the free boundary conditions is the nonlinear Bernoulli equation. Given approximations to the variables of the flow and the free boundary, the Newton-type solver iterates by finding the correction to the unknowns and updating the approximation until convergence. A linearised problem must be solved at each iteration, and we determine the appropriate formulation of this using shape calculus. The shape derivative is applied to linearise the generic free-boundary problem with respect to the current approximated shape of the free boundary. The benefit of this approach is that the problem is linearised in the current configuration instead of mapping back to a referenced domain such that the nonlocal effect of domain-perturbations can be avoided [88–90]. Furthermore, the Newton-type method converges superlinearly, which results in fewer iterations than methods with linear convergence rate. This

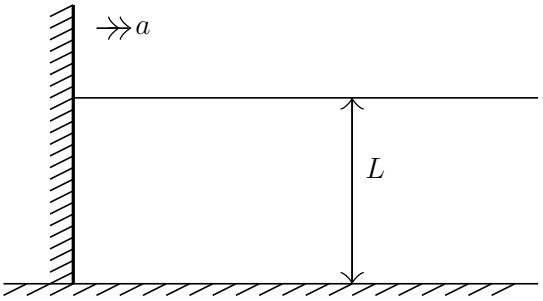

Figure 1.1: *The sketch of a fluid with an accelerating plate. The acceleration is a and the initial depth of the fluid is L*

method is applied to a test problem - steady flow over a submerged triangle - and we obtain results consistent with those given in [22].

1.1 Related work

1.1.1 Fluid/Solid interaction problem with an accelerating plate

The problem of fluid/solid interaction with a moving plate has been a topic of interest and importance in fluid mechanics for several decades. Figure 1.1 shows an example of the sketch of a fluid with an accelerating plate. This problem investigates the irrotational flow generated by a plate moving horizontally towards an inviscid and incompressible fluid. The pressure on a vertical plate which impulsively accelerates towards the fluid was first investigated by Chwang [15]. The analytical solution to pressure on the plate and the free surface of the fluid are obtained by the method of small-time expansions. Considering an example of constant acceleration, a singularity in the free surface at the intersection point of the free surface and the moving plate is observed. The singularity is also captured in the solutions derived in unpublished theoretical research by Peregrine [66]. To avoid the singularity, Joo et al. [48] investigate this problem using expansion in small Froude number and use a Fourier-integral method. A similar problem is also investigated by Roberts

[70]. The main features observed in results obtained by Joo et al. and Roberts is an infinite number of small-scale wiggles close to the intersection point, and the slope of the free surface at the contact line shows a jump to a finite value. This indicates that the asymptotic expansions in Froude number are not uniform at small time such that the initial condition of the displacement of the free surface is not satisfied. A similar situation appears in small-time asymptotic solutions for infinitely small acceleration as well, which is discussed by King and Needham [51]. In addition, to resolve the singularity, they rescale this problem into an inner region by equating the magnitude of terms retained at the leading-order and the neglected terms.

Needham et al. [64] further generalise this problem to the problem of a flow generated by an inclined accelerating plate, which has a constant angle α with the horizontal bottom, and solve the problem by asymptotic and numerical methods. Using small-time expansions, the asymptotic solution in the outer region is obtained by eigenfunction expansions and Schwarz-Christoffel conformal mappings, where the former method is convenient to find the solution away from the plate and the latter method helps to determine the coefficients in the expansions. The solution to the inner region problem is obtained using the boundary integral method, which shows that the free surface is always perpendicular to the plate and there are small oscillations near the contact point of the free surface and the plate when $\alpha \in \left(\frac{\pi}{2}, \pi\right)$. This is also consistent with the local solution of the inner problem. However, there are no solutions when α is larger than the critical value $\alpha_c \approx 1.791$. This can be reconciled when surface tension is included in this problem in [5], and the asymptotic solutions agree well with experimental results. The shape of the free surface now shows capillary waves ahead of the wavecrest. However, the solutions cannot be obtained after some time t_τ since the capillary waves self-intersect at time $t = t_\tau$. The mathematical model considered in [64] can also be applied to solve the bore–soliton–splash problem in [6], where Bokhove et al. investigate the flow generated by a wavemaker in a channel with a V-shaped channel and with vertical walls. The problem is de-

scribed using Benney-Luke equations, constructed based on variational principles with small amplitude and parameter and small dispersion parameter.

Uddin and Needham [84] also include the effect of weak surface tension when investigating the fluid/solid interaction problem with a vertical accelerating plate. The asymptotic solutions are obtained by introducing expansions in a dimensionless inverse Weber number $\mathcal{W}$. Compared with the experimental results in [54], the theoretical results show great agreement especially when time t is small.

Furthermore, Yang and Chwang [98] investigate this problem including the effect of viscosity and surface tension. This problem is discretized in finite-difference form using the finite-analytic method based on Chen et al. (see e.g.[13]), where the local analytical solutions are found for the linearised problems. They compare the experimental results in [99] by measuring the free surface and the pressure on the plate with the numerical results and Chwang's theoretical solutions [15]. The analytical solution is only consistent with the experimental results far away from the intersection point at small times, while the numerical results agree well with the experimental results. All the comparisons mentioned above indicate that the surface tension should be taken into account to balance the discontinuity in pressure distribution when the free surface meets with the plate in this problem.

In this thesis, we extend the work in [64] for an inviscid, irrotational fluid to two layers of immiscible, inviscid fluids with different densities without the effect of surface tension, where the bottom layer always has a higher density.

1.1.2 Dam-break problem

The dam-break problem is an important practical problem considered by many engineers and mathematicians because it can cause huge destruction to the surroundings. Initiated by the South Fork dam's (Johnstown) catastrophe, this problem was first idealized by Ritter [69] such that a solid barrier is suddenly removed from a body of water in a rectangular horizontal channel, which is assumed to be dry and

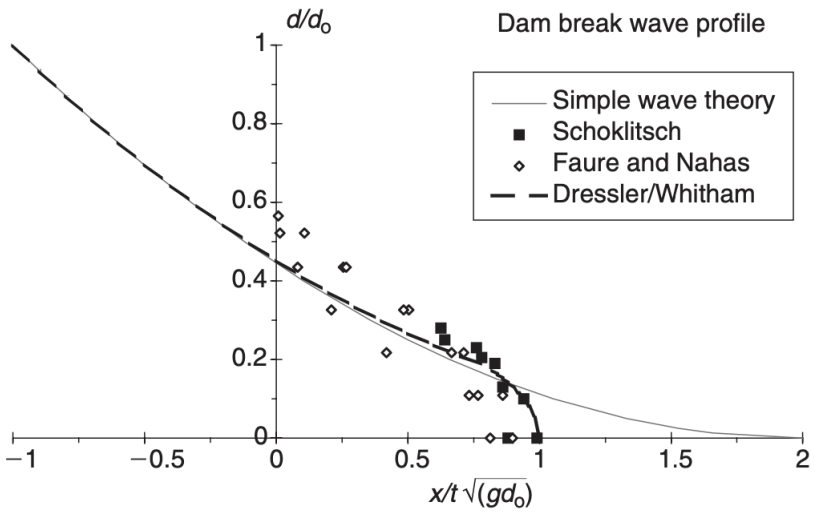

Figure 1.2: *The comparison between Ritter's solution (Simple wave theory) and the experimental observations, where d_o is the initial depth upstream. This graph is the Fig. 17.18 in [11].*

frictionless. Ignoring the vertical acceleration and assuming a hydrostatic pressure distribution, the solution is obtained by using simple waves and the method of characteristics for the Saint-Venant equations. The water depth and the flow velocity are always constant at the initial location of the dam. In addition, the free surface is in the form of a parabola tangent to the bottom bed at the intersection point. However, experimental results (see e.g.[12, 29, 57]) show that the assumption of hydrostatic pressure distribution is not reasonable for the initial instants, and the effect of friction cannot be ignored.

Figure 1.2 (as Fig. 17.18 in [11]) shows the comparison between Ritter's solution (Simple wave theory) and the experimental observations, where d_o is the initial depth upstream. The difference between the observed wave front and Ritter's solution shows that bottom friction should be considered in the problem. Dressler [26] and Whitham [97] solve the same problem including the effects of the bottom friction by using Chezy resistance. Their results are shown in Fig. 17.18 in [11], which agree well with the experimental results. Stoker [80] further extends this problem to a dam-break problem with a layer of water at the downstream side of the dam. The problem is solved by dividing the flow into four regions: the quiet downstream, the flow in

constant state, the simple wave, and the undisturbed upstream, where there is a shock wave between the quiet downstream and the flow in constant state. In the limit of zero depth of the downstream fluid, the flow is the same as in Ritter's idealised dam-break problem. With the benefit of solving the problem in a fixed region, Stoker [80] and Pohle [67] find the analytical solutions in Lagrangian coordinates. The solutions are obtained in the form of expansions in time by conformal mapping. Considering the Fourier series of the initial pressure, there is a singularity in the displacement of the flow in the second-order term at the intersection point of the dam and the bottom when the dam is suddenly removed due to the discontinuity in the pressure. However, since the free surface is part of the solution, it is hard to divide the boundary into free boundary and rigid boundary in advance, which indicates that the advantage of using Lagrangian coordinates may not be as expected.

In order to investigate the flow close to the intersection point and its singularity behaviour, Korobkin and Yilmaz [52] use the same methodology as in [51] in Eulerian coordinates. They apply asymptotic analysis to find leading-order solutions in the outer region and inner region for the initial stage of the flow by introducing a small non-dimensional parameter $\epsilon \to 0$. The flow studied in that paper is similar to the local flow studied in [51]. The solution at the leading order contains a singularity close to the intersection point such that this solution is considered as an outer solution, and thus, an inner solution needs to be found to resolve the singularity in free surface. The problem is solved by Fourier transform with outer solutions as the matching conditions. The main features of the flow close to the intersection point are self-similarity, and the decreasing angle between the free surface and the bottom with time. The free surface approaching the bottom has small oscillations, where amplitude decays in the far field. Yilmaz et al. [101] further extend this problem to dam-break flows of two immiscible fluids with different depths and densities at small times, where the leading-order problem is solved by Fourier series and a boundary element method. There is a logarithmic singularity in the shape of the free surface

at the intersection point of the free surface of the fluid with lower depth and the bottom except when the two fluids have the same density. The jet can be observed at the top of the interface (the triple point) in [52, 101] such that there is a power singularity in the shape of the free surface at the triple point. The singularity is affected by the ratio of the fluid densities such that when the density of the fluid with lower depth is much larger than the density of the other fluid, the singular behaviour is more obvious.

The initial stage of the dam-break problem of two fluids with equal depth has recently been studied by Korobin and Yilmaz [53]. The free surface of the fluid and its interface near the intersection points are analysed in Lagrangian coordinates by asymptotic and Fourier transform methods. The discontinuity in the outer solutions near the upper and bottom intersection points is resolved in the inner region, where the solution for the interface close to the bottom intersection point is self-similar. In addition, the displacement of the interface is independent of any parameter (e.g. ratio of the densities) in the inner region.

This work can be extended to a dam-break problem of two immiscible, inviscid fluids with different densities driven by a moving source, which can be further considered as a simplified model of a powder snow avalanche in the inner region by Billingham [4]. A Moore singularity (a curvature singularity developed in finite time) [4] is observed in the leading-order solution to the interface close to the bottom intersection point at small times. The motion is regularised by including a thin layer of denser fluid ahead of the original fluid layer. The problem is numerically solved by the vortex blob method based on the derivatives of the Plemelj formula. The interface rolls up and overturns away from the head of the flow for small density differences or Richardson number, while the overturning appears at the head of the layer when both the Bernoulli effect and gravity have a significant impact.

In this thesis, we study a dam-break problem with two inviscid, immiscible fluids with different densities initially at rest in an infinitely long channel. The fluids are

initially separated by a solid plate, which has a constant angle with the horizontal and is suddenly removed from the channel.

1.1.3 Numerical methods for free-boundary problems

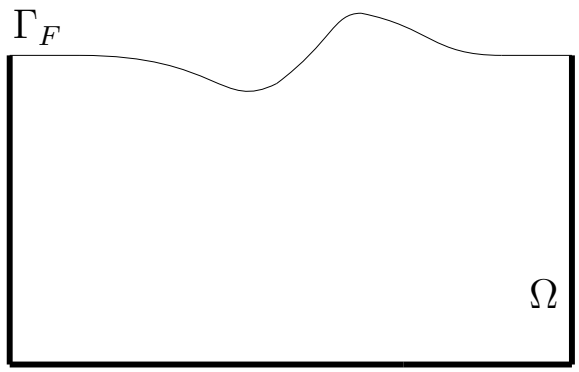

Figure 1.3: *The sketch of a free-boundary problem in domain Ω with free boundary Γ_F.*

Free-boundary problems are usually difficult to solve analytically since the problems are non-linear and the shape of the boundary needs to be determined as part of the solution. Thus the numerical methods are the main technique to solve such problems. The simplest two-dimensional model of free-boundary problem is to consider a time-independent problem of the potential of a flow satisfying Laplace's equation in a domain Ω where part of its boundary is a free surface denoted as Γ_F, as shown in Figure 1.3. The potential of the flow satisfies the Dirichlet boundary conditions on $\partial\Omega$ and Neumann boundary condition on Γ_F, which indicates that the flow has coupled free-boundary conditions. This kind of problem is called Bernoulli's free-boundary problem since one of the free-boundary conditions are simplified from the Bernoulli equation [71]. The most straightforward techniques are called trial free-boundary methods [18, 71]. Such iteration methods start with an initial estimate of the free boundary and the initial approximation of the potential is obtained from the boundary-value problem with one free-boundary condition. The approximation of the free boundary is then updated from the remaining free-boundary condition based on the approximation of the potential, and the process can be repeated until

the convergence. Related works are also made by Bouchon et al. [7] and Kuster et al. [55], where they define the free boundary as the level set $\phi = 0$ of the function ϕ. However, the iterations in this method exhibit slow linear convergence.

The shape optimization method is then considered to improve the rate of convergence. The main idea of this method is to construct a boundary-value problem as the state problem including only one condition on the free boundary and formulate a cost function with the remaining free-boundary condition. The most convenient way to formulate the cost function is to use the Dirichlet boundary condition in the free surface, which can be seen in [3, 37, 82]. Haslinger et al. [38] further combine a shape optimization method with a fictitious domain method by constructing a simpler domain $\hat{\Omega}$ from the domain Ω with complicated geometry. The fictitious domain solver allows the state problem can be solved on a fixed domain and a uniform grid, which means that the problem is efficiently solved and is easy to implement. Another way to improve the shape optimization method is to use a pseudo-solid approach [83] as a Newton-type linearization method such that the boundary nodes can move freely and the numerical method converges faster. The shape optimization method is further applied to more complicated free-boundary problems by including the Bernoulli equation or a compressible fluid (see e.g.[27, 49, 61, 86]). However, for different problems, the cost functions can be chosen differently, for example by using the Bernoulli equation or considering an energy formulation.

To construct a fast numerical solver for generic steady free-boundary problems, the third approach is to linearise the whole system and then apply a Newton-type method. There are two different linearization methods: domain-map linearization, and the application of shape calculus. The first method is to linearize the problem by mapping back to a reference domain [60, 87]. The second way is to apply shape calculus to the current geometry such that the whole problem can be linearized in the current domain [21, 77]. The combination of the second linearization approach and a Newton-type method is called the Shape-Newton method. Kärkkäinen and

Tiihonen use this technique for a stationary free boundary problem [49] and extend it to a simple example of a Bernoulli free-boundary problem with constant boundary conditions [50]. Van der Zee et al. [90] consider a different derivation of this method to a more general Bernoulli's problem by constructing one weak form for the whole problem and reformulating with a curvature-dependant boundary condition to analyse with C^1 continuous free boundary.

In this thesis, we extend the application of the Shape-Newton method to more generic free-boundary problems by considering Bernoulli's equation instead of a Dirichlet boundary condition on the free surface Γ_F and use a Robin boundary condition on the fixed boundary for a steady problem.

1.2 Thesis Overview

The research presented in this thesis is arranged in three topics: the preliminaries are in chapter 2, the asymptotic and numerical solutions of the two-fluid dam-break problem and solid/two-fluid interaction problem with an inclined accelerating plate in the outer region are given in Chapter 3-4, the finite element method for the solid/single fluid interaction problem with an inclined accelerating plate in the inner region is presented in Chapter 5, and the Shape-Newton method for some general free-boundary problems is studied in Chapter 6. At the beginning of this chapter, some past research about the dam-break problem, the solid/fluid interaction problem and numerical methods for free-boundary problems have been summarized. These are relevant to the contents in the following chapters. Some background about the techniques used in this thesis is also introduced in Chapter 2.

In Chapter 3, a two-dimensional problem is modelled by considering two inviscid, incompressible fluids with different densities initially at rest in a horizontal channel separated by a solid plate which has some angle $\alpha \in \left(0, \frac{\pi}{2}\right)$ with the horizontal solid boundaries. The plate is suddenly removed and the fluids start to

move under gravity. The behaviour of the flow at the initial stage is investigated, especially that close to the contact points: the upper contact point of the interface and the upper solid wall, and the lower contact point where the interface meets the bottom solid wall. We find the asymptotic solution near the two interaction points in the outer region for $t \ll 1$ by eigenfunction expansion and the Plemelj formula. A singularity in the shape of free surface has been captured close to the upper intersection point, which is resolved by rescaling the problem into an inner region. The local solution of the inner problem shows that the interface is always perpendicular to the solid boundary and there are small rapid oscillations.

In Chapter 4, we investigate the solid/two-fluid interaction problem with an inclined accelerating plate problem, where a plate having a constant angle $\alpha \in (\frac{\pi}{2}, \pi)$ with the horizontal accelerates uniformly towards two layers of immiscible, inviscid and incompressible fluids with different densities. The fluids are initially at rest. The formulation of the local problem close to the intersection point at the initial stage is the same as the two-fluid dam-break problem in Chapter 3. Thus, we can use the same asymptotic expansion as in Chapter 3 and find the singularity at the intersection point of the interface and the moving plate. Furthermore, we obtain the same formulation and local solution to the inner problem.

In Chapter 5, we use a numerical method based on the finite element method to solve the solid/single fluid interaction problem with an inclined accelerating plate in the inner region [64]. We start by using a simple trial method to solve the case where it is linearised by considering small perturbation to the angle of the vertical plate. This case is referred to as a linearised problem in terms of the angle of the plate. However, this simple iteration scheme fails to find the solution. Hence, we use Newton's method with the finite difference method to solve the entire inner problem and compare the numerical results with those obtained using the boundary integral method in [64].

Chapter 6 focuses on the Shape-Newton method for some generic steady free-

boundary problems, where the problem has the Bernoulli equation or the Dirichlet condition as one of the free boundary conditions. The condition on the fixed boundary is a Robin condition to generalise the problem and the second free-boundary condition is a Neumann condition. At each Newton iteration, the linearisation of the weak forms with respect to the current geometry is achieved by applying shape derivatives. A numerical test for the free-boundary problem with Dirichlet boundary condition is manufactured, while the test for the free-boundary problem with Bernoulli condition on the free boundary is the problem of a fluid flowing over a submerged triangle solved in [22].

The final chapter, Chapter 7, summarises the conclusion of the studies and investigations in this thesis and discusses potential future research.

Chapter 2

Preliminaries

We introduce some mathematical background related to this thesis in this chapter. In this thesis, the fluid flow is assumed to be inviscid, incompressible, and irrotational. By introducing the Cartesian coordinates (x, y) the time variable, t, the velocity potential $\phi(x, y, t)$ of the flow satisfies Laplace's equation,

$$\nabla^2 \phi = 0$$

in a region $\Omega(t)$. The boundary conditions on the inflow, bottom boundary Γ_B and free boundary Γ_f are based on the kinematic condition

$$\frac{\partial \phi}{\partial \boldsymbol{n}} = \boldsymbol{n} \cdot \frac{d\boldsymbol{x}}{dt},$$

where $\boldsymbol{n}$ is the outward unit normal to the boundaries and $\boldsymbol{x}$ represents the point (x, y).The outflow is assumed to have the Dirichlet boundary condition

$$\phi = 0.$$

The second free-boundary condition can be derived from the Navier-Stokes

equation:

$$\frac{\partial \boldsymbol{u}}{\partial t} + (\boldsymbol{u} \cdot \nabla)\boldsymbol{u} = -\frac{1}{\rho}\nabla p + \frac{\tau}{\rho}\nabla^2 \boldsymbol{u} + \boldsymbol{g},$$

where $\boldsymbol{u}$ is the velocity vector of the flow, ρ is the density of the fluid, p is the pressure, τ is the dynamic viscosity, and $\boldsymbol{g}$ represents the gravity. Since the fluid is inviscid, the viscosity τ is zero. Furthermore, using the incompressibility of the fluid (the density ρ is constant) and integrating the equation, we can derive the Bernoulli equation

$$\frac{\partial \phi}{\partial t} + \frac{1}{2}|\nabla \phi|^2 + y = 0, \quad \text{on } \Gamma_f,$$

as the second free-boundary condition.

Section 2.1 introduces the conformal mapping and Schwarz-Christoffel transformation, which is used in Chapter 4 to transform the domain into a region where we can numerically solve the outer problem. The numerical solutions in Chapter 3 and 4 are obtained by using Plemelj formula, the background of which is covered in Section 2.2. In Section 2.3, we introduce shape derivatives, which are applied to linearise the weak forms of the free-boundary problems with respect to the geometry of the domain. This linearisation allows us to employ a Newton-like scheme to numerically solve the problem.

2.1 Conformal Mapping and Schwarz-Christoffel Transformation

The conformal mapping technique has been commonly applied to solve problems in fluid mechanics, e.g. in [14, 24, 32, 42, 59, 64]. It can transform the region into another complex plane, where the solutions can be found more conveniently, and preserve the angles at the same time. Here, the introduction of the conformal mapping technique is based on [1], and is used in Chapter 4 to numerically solve the outer problem.

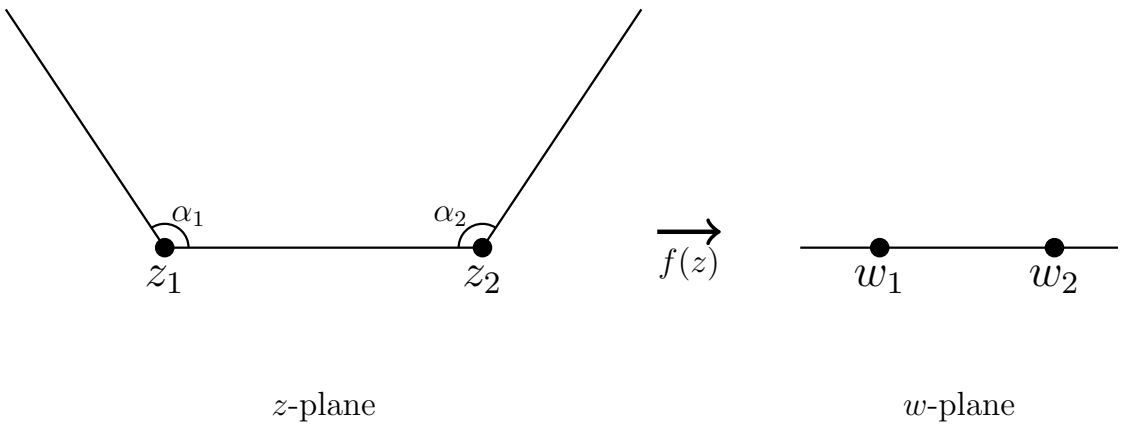

Figure 2.1: *An example sketch of Schwarz-Christoffel Transformation.*

Let A be a curve in the complex z-plane and A^* be some curve in another complex w-plane. The analytical function $w = f(z)$ where $f : A \to A^*$ is a function mapping the point $z = x + \mathrm{i}y$ in the z-plane into the point $w = u + \mathrm{i}v$ in the w-plane.

Definition 2.1. *The function $f(z)$ is **analytic** in $A \subseteq \mathcal{C}$ if for every point $z_0 \in A$, $f(z)$ is analytic, that is $f(z)$ is differentiable in a neighborhood of any point $z_0 \in A$.*

It is convenient to introduce a real parameter s such that $x = x(s)$, $y = y(s)$. Then, the derivative $\frac{dz(s)}{ds}$ is defined as

$$\frac{dz(s)}{ds} = \frac{dx(s)}{ds} + \mathrm{i}\frac{dy(s)}{ds}.$$

Let the point z_0 satisfy $z_0 \equiv z(s_0)$, the differentiation $\frac{dw(s)}{ds}$ for $s = s_0$ is obtained by the chain rule

$$\frac{dw(s)}{ds}\Big|_{s=s_0} = f'(z_0)\frac{dz(s)}{ds}\Big|_{s=s_0}.$$

Given $f'(z_0) \neq 0$ and $z'(s_0) \neq 0$, then $w'(s_0) \neq 0$ and $\arg(w'(s_0)) = \arg(z'(s_0)) + \arg(f'(z_0))$. Hence, under the mapping $f(z)$, the tangent to any curve at z_0 is rotated by an angle $\arg(f'(z_0))$ in w-plane and the angle between two curves is preserved.

Theorem 2.1. *Given a non-constant analytic function $f(z)$ in a domain A in the complex z-plane, for any point $z \in A$ such that $f'(z) \neq 0$, this mapping is **conformal**. The angle between two differentiable arcs is preserved.*

Definition 2.2. *The analytic function $f(z)$ is* ***univalent*** *in the domain A if $f(z)$ is a one-to-one map, and its inverse function $f^{-1}(z)$ is also univalent.*

The existence of the conformal mapping $f(z)$ is stated in the following theorem:

Theorem 2.2. ***(Riemann mapping theorem)*** *Let A be a simply connected domain in the z-plane, which is not the entire z-plane or the extended z-plane. There is a univalent function $f(z)$ such that $w = f(z)$ maps the domain A onto the disk $|w| < 1$.*

In this thesis, the Schwarz-Christoffel transformation is applied to transform the domain from the z-plane to the w-plane. An example sketch of the transformation is shown as Figure 2.1.

Theorem 2.3. ***(Schwarz-Christoffel)*** *Let Γ be the piecewise linear boundary of a polygonal domain in the w-plane, and let the interior angles at the vertices of the polygon be $\alpha_1, \ldots, \alpha_n$. Then the mapping is defined by the equation*

$$\frac{dw}{dz} = k\,(z - a_1)^{\frac{\alpha_1}{\pi}-1}\,(z - a_2)^{\frac{\alpha_2}{\pi}-1} \cdots (z - a_n)^{\frac{\alpha_n}{\pi}-1},$$

where k is some complex constant and $a_1 < a_2 < \cdots < a_n$ are the values along the real axis of the z-plane corresponding to the vertices of the polygon.

Thus, the Schwarz-Christoffel map $f(z)$ is given as the following integration

$$w \equiv f(z) = \int_0^z k\,(z' - a_1)^{\frac{\alpha_1}{\pi}-1}\,(z' - a_2)^{\frac{\alpha_2}{\pi}-1} \cdots (z' - a_n)^{\frac{\alpha_n}{\pi}-1}\,dz'. \tag{2.1.1}$$

2.2 Plemelj Formula

In Chapter 4, we use the Plemelj formula to numerically solve the initial stage of the solid/two fluid interaction problem with an accelerating inclined plate in the outer

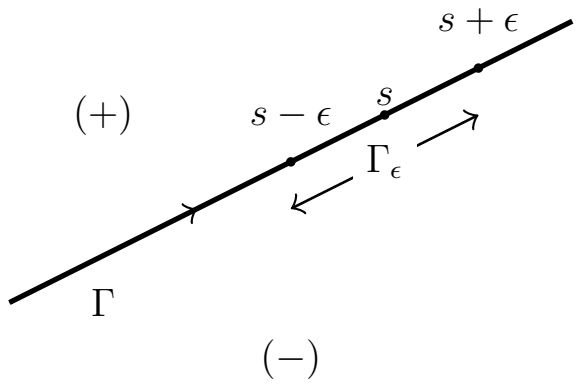

Figure 2.2: *The sketch of* $(+)$ *and* $(-)$ *region on either side of* Γ *and the definition of* Γ_ϵ.

region. The background and introduction of the Plemelj formula in this subsection are also based on [1]. Let $\phi(s)$ be a function satisfying the Hölder condition such that for any two points s_1 and s_2 on a smooth contour Γ,

$$|\phi(s_1) - \phi(s_2)| \leq k|s_1 - s_2|^\gamma, \quad k > 0, \quad 0 < \gamma \leq 1.$$

Consider the Cauchy type integral

$$\Phi(s') = \frac{1}{2\pi \mathrm{i}} \int_\Gamma \frac{\phi(s)}{s - s'} ds. \tag{2.2.1}$$

This integral is well defined when s' is not on Γ and it can be approximated as $|s| \to \infty$ off Γ by series expansion. However, to evaluate the value of this integral when s' is on Γ, it is important to understand how s' approaches Γ: the region on the left of the positive direction of Γ is denoted as $+$ region and the region on the right is denoted as $-$ region as shown in Figure 2.2. Thus, the value of $\Phi(s')$ has a limit $\Phi^+(s')$ when approaching Γ entirely on the curve in the left $(+)$ region, and correspondingly another limit $\Phi^-(s')$ when approaching Γ entirely along the contour in the right $(-)$ region. These two limits can be evaluated by the Plemelj formula defined as the following:

Theorem 2.4. ***(Plemelj formula)*** *Let* Γ *be a smooth contour and let* $\phi(s)$ *be a*

function satisfying the Hölder condition on Γ*. The Cauchy type integral*

$$\Phi(s') = \frac{1}{2\pi \mathrm{i}} \int_{\Gamma} \frac{\phi(s)}{s - s'} ds$$

has the limiting values $\Phi^{+}(s')$ *as* s *approaches the contour* Γ *from the left and* $\Phi^{-}(s')$ *from the right at point* s'*, where* s' *is not any of the end points of* Γ*. The limits are defined as*

$$\Phi^{+}(s') = \frac{1}{2}\phi(s') + \frac{1}{2\pi \mathrm{i}} ⨍ \frac{\phi(s)}{s - s'} ds, \tag{2.2.2}$$

$$\Phi^{-}(s') = -\frac{1}{2}\phi(s') + \frac{1}{2\pi \mathrm{i}} ⨍ \frac{\phi(s)}{s - s'} ds. \tag{2.2.3}$$

The integration symbol $⨍$ *denotes the principal value integral*

$$⨍ \frac{\phi(s)}{s - s'} ds = \lim_{\epsilon \to 0} \int_{\Gamma - \Gamma_{\epsilon}} \frac{\phi(s)}{s - s'} ds$$

where Γ_{ϵ} *is the part of* Γ *which is centered around the point* s' *with length* 2ϵ *as shown in Figure 2.2.*

2.3 Shape Calculus

The shape calculus is widely applied to problems where the shape or geometry of a domain is an object of investigation, for example in free-boundary problems and shape optimization. Here, we recall some basic background for shape derivatives mainly from the books [21, 77]. The shape derivatives are used in Chapter 6 to linearise the weak forms of the free-boundary problems with respect to the shape of the domain before applying a Newton-like scheme.

We define a functional J as $J : \mathcal{A} \to \mathbb{R}$, where $\mathcal{A}$ is a family of subsets of $\mathbb{R}^N$. This is a shape function if it satisfies $J(T(\mathcal{A})) = J(\mathcal{A})$ for any transformation $T(\mathcal{A}) = \mathcal{A}$.

Let D be a domain in $\mathbb{R}^N$ with boundary ∂D piecewise C^k for $k \geq 1$. Then the vector field v is defined as

$$v \in C\left([0,\epsilon); V(D)\right)$$

for time $t \in [0,\epsilon)$ where

$$\begin{aligned} V(D) &= \{v \in C^{0,1}(\bar{D};\mathbb{R}^N) | v \text{ is tangent to} \\ &\quad \text{the boundary } \partial D \text{ except for the singular points } x \text{ on } \partial D, v(x) = 0\}. \end{aligned}$$

Let $x(t,X)$ represent the solution of the following initial value problem

$$\begin{aligned} \frac{d}{dt}x(t,X) &= v\left(x(t,X)\right), \\ x(0,X) &= X. \end{aligned}$$

The transformation defined with respect to v is then defined as

$$T_t(X) = x(t,X)$$

for $x \in \bar{D}$ and $t \in [0,\epsilon)$.

Definition 2.3. ***(Eulerian derivative)****For any vector field $v \in C\left([0,\epsilon); V(D)\right)$, the Eulerian derivative of $J(\Omega)$ in the direction of the vector field v is defined as*

$$dJ(\Omega;v) = \lim_{t\to 0^+} \frac{J(\Omega_t) - J(\Omega)}{t},$$

where

$$\Omega_t = T_t(v)(\Omega).$$

Definition 2.4. ***(Shape differentiable)*** *If the mapping $v \to dJ(\Omega,v)$ is linear and continuous from $C\left([0,\epsilon); C^k(D,\mathbb{R}^N)\right)$ into $\mathbb{R}$ and the Eulerian derivative $dJ(\Omega,v)$ exists for all vector field v, then the functional $J(\Omega)$ is shape differentiable at Ω.*

Let Ω be an open and bounded set in $\mathbb{R}^2$ with a boundary Γ as a contour. The two examples of shape functional considered in this thesis are a domain integral of Ω,

$$J(\Omega) = \int_\Omega \phi \, d\Omega, \tag{2.3.1}$$

and a boundary integral on Γ

$$J(\Gamma) = \int_\Gamma \phi \, d\Gamma, \tag{2.3.2}$$

where $\phi \in W^{1,1}(\mathbb{R}^2)$.

Proposition 2.1. ***(Shape derivative of domain integral)*** *Let $\phi \in W^{1,1}(\mathbb{R}^N)$ and $v \in C_0^1(\mathcal{R}^N; \mathcal{R}^N)$, the domain integral $J(\Omega)$ is shape differentiable with the Eulerian derivative*

$$dJ(\Omega; v) = \int \operatorname{div}(Jv) \, d\Omega. \tag{2.3.3}$$

If the boundary $\Gamma = \partial\Omega$ of class C^1, then the shape derivative of $J(\Omega)$ is

$$dJ(\Omega; v) = \int_\Gamma \phi v \cdot \boldsymbol{n} \, d\Gamma, \tag{2.3.4}$$

where $\boldsymbol{n}$ is the exterior unit normal.

The proof can be found in [21, 77].

Definition 2.5. ***(Tangential divergence)*** *(i) Let Ω be a domain with the boundary Γ of class C^2, and the vector field $v \in C_0^1(\mathcal{R}^N; \mathcal{R}^N)$, the tangential divergence is defined as*

$$\operatorname{div}_\Gamma v = (\operatorname{div}(v) - (Dv \cdot \boldsymbol{n}) \cdot \boldsymbol{n})|_\Gamma, \tag{2.3.5}$$

where Dv is the Jacobian matrix of v.

(ii) Let Ω be a domain with the boundary Γ of class C^2, and the vector field $v \in C_0^1(\Gamma; \mathcal{R}^N)$, the tangential divergence of v on Γ is defined as

$$\operatorname{div}_\Gamma v = (\operatorname{div}\bar{v} - (D\bar{v} \cdot \boldsymbol{n}) \cdot \boldsymbol{n})|_\Gamma, \tag{2.3.6}$$

where $\bar{v}$ is the extension of v of class C^1 to an open neighbourhood of Γ.

Definition 2.6. ***(Tangential gradient)*** *Let $f \in C^2(\Gamma)$ and $\bar{f}$ be the smooth extension of f with $\bar{f}|_\Gamma = f$, the tangential gradient is defined as*

$$\nabla_\Gamma f = \nabla \bar{f}|_\Gamma - \frac{\partial \bar{f}}{\partial \boldsymbol{n}} \boldsymbol{n}. \tag{2.3.7}$$

Now using tangential divergence and tangential gradient, the shape derivative of boundary integral can be introduced as the following.

Proposition 2.2. ***(Shape derivative of boundary integral)*** *Let $\phi \in W^{2,1}(\mathbb{R}^N)$ and $v \in C_0^1(\mathbb{R}^N; \mathbb{R}^N)$, the Eulerian derivative of the boundary integral $J(\Gamma)$ is*

$$dJ(\Gamma; v) = \int_\Gamma (\nabla \phi \cdot v + \phi \mathrm{div}_\Gamma v)\, d\Gamma. \tag{2.3.8}$$

Proposition 2.3. ***(Tangential Green's formula)*** *Let the function $f \in C^1(\Gamma)$ and $v \in C_0^1(\mathbb{R}^N; \mathbb{R}^N)$ with $v \cdot \boldsymbol{n} = 0$ for every point on Γ, the tangential Green's formula is*

$$\int_\Gamma \nabla_\Gamma f \cdot v \, d\Gamma = -\int_\Gamma f \mathrm{div}_\Gamma v \, d\Gamma. \tag{2.3.9}$$

The proof of proposition 2.2 and 2.3 can be found in [21, 77].

Following the same calculation as in [39], let $v_\tau = v - (v \cdot \boldsymbol{n})\boldsymbol{n}$ represent the tangential part of the vector field v with respect to the contour Γ, then

$$\begin{aligned}
\mathrm{div}_\Gamma v &= \mathrm{div}_\Gamma v_\tau + \mathrm{div}_\Gamma \left((v \cdot \boldsymbol{n})\boldsymbol{n}\right), \\
&= \mathrm{div}_\Gamma v_\tau + \left[\mathrm{div}\left((v \cdot \boldsymbol{n})\boldsymbol{n}\right) - \left(D\left((v \cdot \boldsymbol{n})\boldsymbol{n}\right) \cdot \boldsymbol{n}\right) \boldsymbol{n}|_\Gamma\right], \\
&= \mathrm{div}_\Gamma v_\tau + (v \cdot \boldsymbol{n}) \left[\mathrm{div}\boldsymbol{n} - (D\boldsymbol{n} \cdot \boldsymbol{n})\boldsymbol{n}|_\Gamma\right], \\
&= \mathrm{div}_\Gamma v_\tau + (v \cdot \boldsymbol{n}) \mathrm{div}_\Gamma \boldsymbol{n}, \\
&= \mathrm{div}_\Gamma v_\tau + \kappa v \cdot \boldsymbol{n},
\end{aligned}$$

where $\boldsymbol{n}$ is the unit normal on Γ and $\kappa = \mathrm{div}_\Gamma \boldsymbol{n}$ is the curvature of Γ.

Hence, the shape derivative of the boundary integral $J(\Gamma)$ can be evaluated as follows in [39]

$$\begin{aligned}
dJ(\Gamma; v) &= \int_\Gamma \left(\nabla\phi \cdot v + \phi \mathrm{div}_\Gamma v\right) d\Gamma, \\
&= \int_\Gamma \left[\left(\nabla_\Gamma \phi + \frac{\partial \phi}{\partial \boldsymbol{n}} \boldsymbol{n}\right) \cdot v + \phi \left(\mathrm{div}_\Gamma v_\tau + \kappa v \cdot \boldsymbol{n}\right)\right] d\Gamma, \\
&= \int_\Gamma \left[\nabla_\Gamma \phi \cdot v + \phi \mathrm{div}_\Gamma v_\tau + \left(\phi\kappa + \frac{\partial \phi}{\partial \boldsymbol{n}} \boldsymbol{n}\right)(v \cdot \boldsymbol{n})\right] d\Gamma, \\
&= \int_\Gamma \left[\nabla_\Gamma \phi \cdot v_\tau + \phi \mathrm{div}_\Gamma v_\tau + \left(\phi\kappa + \frac{\partial \phi}{\partial \boldsymbol{n}} \boldsymbol{n}\right)(v \cdot \boldsymbol{n})\right] d\Gamma,
\end{aligned}$$

Lemma 2.1. *Under the same assumption as in Proposition 2.2, the shape derivative of boundary integral is*

$$dJ(\Gamma; v) = \int_\Gamma \left[\nabla_\Gamma \phi \cdot v_\tau + \phi \mathrm{div}_\Gamma v_\tau + \left(\phi\kappa + \frac{\partial \phi}{\partial \boldsymbol{n}} \boldsymbol{n}\right)(v \cdot \boldsymbol{n})\right] d\Gamma. \tag{2.3.10}$$

Chapter 3

The Initial Stage of The Two-Fluid Dam-Break Problem

3.1 Introduction

The flow generated from removing a plate, which separates two immiscible fluids with equal depth in a channel, can be treated as a two-fluid dam-break problem. The interface between the two fluids begins to move under gravity when the dam is removed at the initial instant $t = 0$, initiating the two-dimensional irrotational flow in the channel. Neglecting the effects of the lighter fluid, this problem can be simplified to the dam-break problem with a dry bed (see e.g. [31, 69, 72]).

Stoker [80] and Pohle [68] solve the dam-break problem in the dry-bed case using Lagrangian coordinates, which allows the problem to be solved in a fixed region. However, Korobkin and Yilmaz [52] realised that partitioning the boundary into the free and rigid boundaries can be challenging in the Lagrangian formulation of the dam-break problem since the free surface is unknown and part of the solution. In contrast, they investigate this problem at the initial stage using an asymptotic method by introducing a small dimensionless parameter $\epsilon \to 0$ without any physical meaning. The flow singularity can be observed in the solutions, which can be resolved

by rescaling into an inner region close to the intersection point. The inner solution found by Korobkin and Yilmaz is self-similar and describes the propagation of a jet along the dry bed. Yilmaz et al. [101] extend this problem from a dry bed to a wet bed, where a vertical plate separates two immiscible fluids with different depths. A jet formation at the triple point is found in a small-time asymptotic solution, using the Fourier series method the velocity potential and the boundary element method. They found that the singularity of the flow depends on the densities of the two fluids. Stansby et al. [79] present experimental results of the dam-break problem in both dry-bed and wet-bed cases, where a jet is observed for the dry-bed case at small times while a vertical, mushroom-like jet occurs for the wet-bed case. Similar problems in a sloping channel in both dry-bed and wet-bed cases have been investigated by Hunt [43, 44] using a kinematic-wave approximation.

Korobkin and Yimaz [53] recently investigated a two-fluid dam-break problem, where the flow of two immiscible fluids with different densities of equal depth is generated by the sudden removal of a vertical plate at the initial stage. The singular behaviour appears at the top contact point, where the interface meets both free surfaces of the two fluids, and the bottom intersection point, where the interface meets the solid bottom bed. The inner solution close to the bottom contact point shows the self-similarity in the interface, where the displacement of the interface is not affected by any parameters such as the densities of the two fluids; however, the inner-region problem near the top intersection point is not solved in that paper either by analytical or numerical methods.

Billingham [4] formulated a simple mathematical model for a powder snow avalanche as a two-fluid dam-break problem with a moving source. Using small-time expansion, an outer-region problem is solved by the Plemelj formula, and its local solution is obtained around the moving source containing a logarithmic singularity.

In this chapter, we solve a two-fluid dam-break problem in the outer region by asymptotic and numerical methods following similar methods to [4]. The interface

between the two fluids initially has a constant angle $\alpha \in \left(0, \frac{\pi}{2}\right)$ with the horizontal, and the regions occupied by the fluids are bounded both at the top and the bottom by solid horizontal walls. In section 3.2, we present the formulation of the mathematical model. The asymptotic solution using the small-time expansion near the top and bottom interaction points for non-dimensional time $t \ll 1$ is developed in section 3.3. In section 3.3.1, the analytical solutions of the velocity potential are obtained for the eigenvalue problem. We investigate the asymptotic solution of the limiting case where the densities of the two fluids are almost equal in section 3.3.2. The derivation of the Plemelj formula for the outer problem is found in section 3.4, and its numerical results are compared with the eigensolutions in section 3.5, where a singularity appears in both solutions at the upper contact point in the interface. The formulation and the local solution of the inner region close to the upper contact point following the similar method in [64] is presented in section 3.6.

3.2 Two fluid dam-break problem for $0 < \alpha < \frac{\pi}{2}$

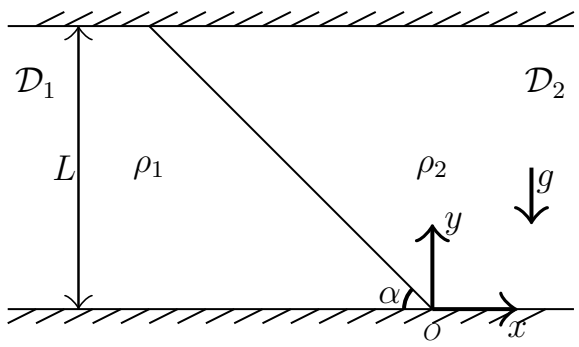

Figure 3.1: *The sketch of two fluids with different densities in a channel with an interface* $y = -\tan\alpha x$ *at* $t = 0$*, where* $0 < \alpha \leq \pi/2$*.*

As shown in Figure 3.1, in a channel with depth L, there are two inviscid, incompressible fluids initially lying at rest, and the interface between two fluids is initially a straight line $y = -x\tan\alpha$, where α is the angle between the interface and the negative x-axis. These two fluids will start to move due to the effect of gravity. Since the fluids are inviscid and stationary when $t = 0$, the flow is irrotational when

$t > 0$. We denote the fluid with the larger density ρ_1 as fluid 1, while the fluid with the smaller density ρ_2 is denoted as fluid 2. The region occupied by fluid i with density ρ_i is $\mathcal{D}_i$ for respectively $i = 1, 2$, where time $t \geq 0$. Correspondingly, we use the notation $\phi_i(x, y, t)$ for $i = 1, 2$ as the velocity potential for the flow in $\mathcal{D}_i$. For the condition shown in Figure 3.1, the region $\mathcal{D}_1$ is on the left side of the interface, and the angle α should always be smaller than $\frac{\pi}{2}$. Otherwise, the fluid with larger density ρ_1 will be affected by gravity to move downwards, and the problem will be ill-posed, which is known as Rayleigh–Taylor instability [74]. Similarly, when the region $\mathcal{D}_1$ is on the right side of the interface, the angle α should always be greater than $\frac{\pi}{2}$.

The location of the interface $\partial\mathcal{D}(t)$ between $\mathcal{D}_1$ and $\mathcal{D}_2$ is denoted as $\mathbf{x} = \mathbf{X}(t) \equiv (x, y) = (x, Y(x, t))$, with $(x_b(t), y_b(t))$ being the lower contact point between the interface $\partial\mathcal{D}(t)$ and $(x_p(t), y_p(t))$ being the upper contact point between the interface $\partial\mathcal{D}(t)$. The bottom boundary is at $y = 0$, and the upper boundary is at $y = L$. Initially, the lower contact point is at the origin with $(x_b(0), y_b(0)) = (0, 0)$, and the upper contact point is at $(x_p(0), y_p(0)) = (-L \cot \alpha, L)$.

We introduce dimensionless variables and a dimensionless density difference

$$x' = \frac{x}{L}, \quad y' = \frac{y}{L}, \quad \phi_i' = \frac{\phi_i}{L\sqrt{gL}}, \quad t' = t\sqrt{g/L}, \quad \bar{\rho} = \frac{\rho_1 - \rho_2}{\rho_2} \geq 0,$$

with g the acceleration due to gravity. Primes can now be dropped for convenience of notation, and the dimensionless depth of the channel becomes 1.

It is now convenient to define the domains as

$$\begin{aligned}
\mathcal{D}_1(t) &= \left\{ (x,y) \in \mathbb{R}^2 : \begin{cases} x < x_p(t), 0 \le y \le 1, \\ x_p(t) \le x \le x_b(t), 0 \le y \le Y(x,t), \end{cases} \right\}, \\
\mathcal{D}_2(t) &= \left\{ (x,y) \in \mathbb{R}^2 : \begin{cases} x_p(t) \le x \le x_b(t), Y(x,t) \le y \le 1, \\ x_b(t) < x, 0 \le y \le 1 \end{cases} \right\}.
\end{aligned} \tag{3.2.1}$$

The Laplace equation governs the irrotational fluid motion [78]

$$\nabla^2 \phi_i = 0 \quad (x,y) \in \mathcal{D}_i, \quad t > 0, \quad \text{for } i = 1, 2, \tag{3.2.2}$$

with Bernoulli equation [78]

$$(1+\bar{\rho})(\frac{\partial \phi_1}{\partial t} + \frac{1}{2}|\nabla \phi_1|^2) - (\frac{\partial \phi_2}{\partial t} + \frac{1}{2}|\nabla \phi_2|^2) = -\bar{\rho} y, \quad \text{at } y = Y(x,t), \tag{3.2.3}$$

and kinematic boundary condition on the interface

$$\mathbf{n} \cdot \frac{\partial \mathbf{X}}{\partial t} = \mathbf{n} \cdot \nabla \phi_1 = \mathbf{n} \cdot \nabla \phi_2, \quad \text{at } \mathbf{x} = \mathbf{X}(x,t), \tag{3.2.4}$$

where $\nabla = (\partial_x, \partial_y)$, $Y(x,t)$ is the y-component of the interface, and $\mathbf{n}$ is the unit normal vector pointing outward to $\mathcal{D}_1$.

At the solid boundaries, we have the no-penetration condition,

$$\frac{\partial \phi_1}{\partial y} = \frac{\partial \phi_2}{\partial y} = 0, \quad \text{at } y = 0 \text{ and } y = 1. \tag{3.2.5}$$

In addition, we have the initial condition

$$\phi_i(x, y, 0) = 0, \quad (x, y) \in \mathcal{D}_i, \quad \text{for } i = 1, 2, \tag{3.2.6}$$

$$Y(x, 0) = Y_0(x) = -x \tan\alpha, \quad -\cot\alpha < x < 0, \quad 0 < \alpha < \frac{\pi}{2}. \tag{3.2.7}$$

We are interested in solving this initial/boundary-value problem (IBVP) (3.2.2)-(3.2.7) as $t \to 0^+$ by using asymptotic as well as numerical methods.

3.3 Asymptotic solution in the outer region for $t \ll 1$

We start by finding the asymptotic solution in an outer region in which $(x, y) = O(1)$ as $t \to 0^+$, and we will analyse the outer problem around the lower contact point in detail. The analysis for the situation around the upper contact point is similar, and the detail is in Appendix A. After that, we investigate the inner region to understand better the behaviour of the interface behaviour near the contact points (x_p, y_p).

According to (3.2.3) and (3.2.4), we introduce the scaled variables

$$\phi_i(x, y, t) = t\bar{\phi}_i(x, y), \quad Y(x, t) = Y_0(x) + t^2\bar{Y}(x). \tag{3.3.1}$$

As $t \to 0^+$, we have $\bar{\phi}_i = O(1)$ for $i = 1, 2$ and $\bar{Y} = O(1)$. Now, the leading order problem from (3.2.2)-(3.2.5) is

$$\nabla^2\bar{\phi}_i = 0 \quad \text{in } \mathcal{D}_i(0), \quad i = 1, 2, \tag{3.3.2}$$

$$\frac{\partial\bar{\phi}_i}{\partial y} = 0 \quad \text{at } y = 0 \text{ and } y = 1\ , \tag{3.3.3}$$

$$(1 + \bar{\rho})\bar{\phi}_1 - \bar{\phi}_2 = -\bar{\rho}y \quad \text{at } y = Y_0(x), \tag{3.3.4}$$

$$2\bar{Y} = \frac{\partial\bar{\phi}_i}{\partial x}\tan\alpha + \frac{\partial\bar{\phi}_i}{\partial y} \quad \text{at } y = Y_0(x), \tag{3.3.5}$$

for $0 < \alpha < \frac{\pi}{2}$.

We will now further investigate the asymptotic solution around the contact points at $(x_b(0), y_b(0))$ and $(x_p(0), y_p(0))$. Note that the local problem around the upper intersection point $(x_p(0), y_p(0))$ is similar to the local problem around the lower contact point $(x_b(0), y_b(0))$ by shifting the origin to the upper intersection point.

3.3.1 The eigenvalue problem

We now consider the leading order solution for $\bar{\phi}_i$ close to the lower contact point at the origin. Considering the Laplace equation (3.3.2) and the boundary condition (3.3.3), we seek a solution of the eigenfunction form

$$\bar{\phi}_1 \sim A_1 r^{\beta_0} \cos \beta_0 (\pi - \theta), \quad \bar{\phi}_2 \sim A_2 r^{\beta_0} \cos \beta_0 \theta, \tag{3.3.6}$$

as $r \to 0$, where $(x, y) = (r\cos\theta, r\sin\theta)$, and A_1, A_2, β_0 are real constants. We assume $\beta_0 \neq 1$ such that the solutions of the form (3.3.6) are not linear solutions. The condition (3.3.4) at $O(r^{\beta_0})$ is then

$$(1 + \bar{\rho})\, \bar{\phi}_1 - \bar{\phi}_2 = 0. \tag{3.3.7}$$

The right-hand side term is neglected under the assumption that $\beta_0 \neq 0$. On substitution from (3.3.6) into (3.3.5) and (3.3.7) with $\theta = \pi - \alpha$ on the interface $\partial_{\mathcal{D}}(0)$, we find that

$$(1 + \bar{\rho})\, A_1 \cos(\beta_0 \alpha) = A_2 \cos(\beta_0(\pi - \alpha)),$$
$$A_1 \sin(\beta_0 \alpha) = -A_2 \sin(\beta_0(\pi - \alpha)).$$

Thus, the eigenvalue problem for β_0 is simply

$$\frac{\tan \beta_0 \alpha}{1+\bar{\rho}} = -\tan \beta_0 (\pi - \alpha) . \tag{3.3.8}$$

Similarly, for the upper contact point at $(x_p(0), y_p(0))$, we can find

$$\frac{\tan \beta_0 (\pi - \alpha)}{1+\bar{\rho}} = -\tan \beta_0 \alpha, \tag{3.3.9}$$

for β_0 by shifting the origin to $(x_p(0), y_p(0))$ for $r \to 0$.

Figure 3.2 shows an example of the relation between β_0 and $\bar{\rho}$ for both upper and lower intersection points with $\alpha = 0.1$, 0.4, 0.7, 1, 1.3 and 1.5. The value of β_0 is always larger than 1 for the lower contact point but lower than 1 for the upper contact point. In addition, the values of β_0 will converge to some value as $\bar{\rho} \to \infty$. This indicates a singularity exists at the upper contact point in the interface due to the leading order term in $\bar{Y}(x)$ is of order $\beta_0 - 1 < 0$, which requires us to look into an inner region around the intersection points $(x_p(0), y_p(0))$, and will be illustrated in Section 3.6.

3.3.2 Asymptotic solution for $\bar{\rho} \ll 1$ and $r \ll 1$

Now, we consider the case $\bar{\rho} \to 0$ to understand the dynamics and test the numerical results.

The velocity potential $\bar{\phi}_i(x, y)$ can be scaled as

$$\bar{\phi}_i(x, y) = \bar{\rho}\hat{\phi}_i(x, y), \quad \hat{\phi}_i(x, y) = O(1), \tag{3.3.10}$$

and we introduce the asymptotic expansion

$$\hat{\phi}_i(x, y) = \hat{\phi}_{i0}(x, y) + \bar{\rho}\hat{\phi}_{i1}(x, y) + O(\bar{\rho}^2). \tag{3.3.11}$$

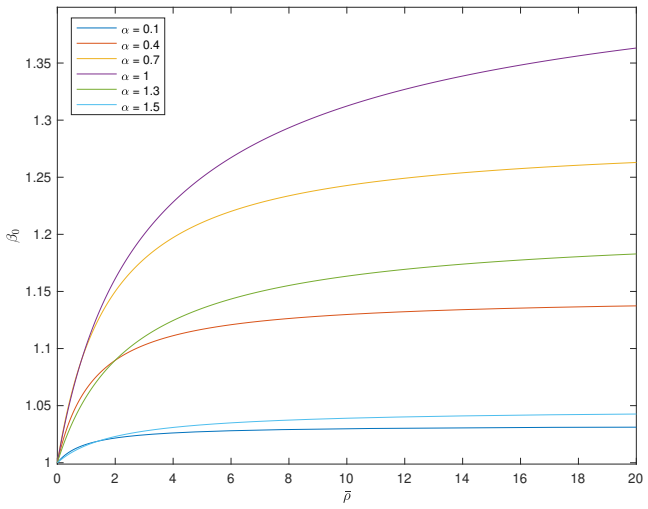

(a) *The relation between β_0 and $\bar{\rho}$ for the lower contact point with $\alpha = 0.1$, 0.4, 0.7, 1, 1.3, and 1.5.*

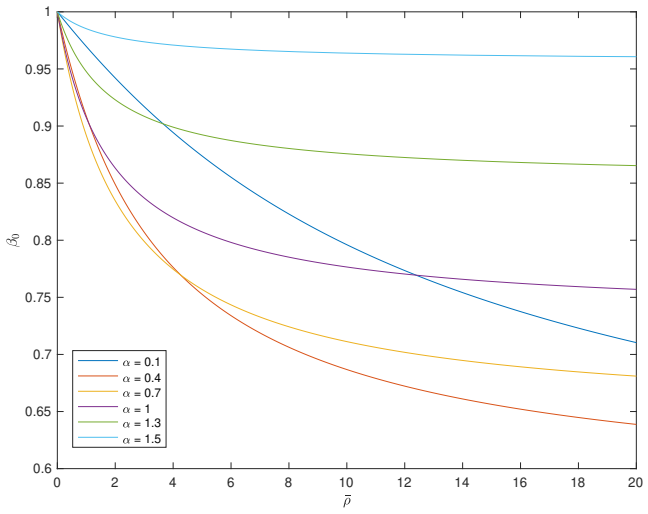

(b) *The relation between β_0 and $\bar{\rho}$ for the upper contact point with $\alpha = 0.1$, 0.4, 0.7, 1, 1.3, and 1.5.*

Figure 3.2

For convenience, we use polar coordinates, and the boundary value problem (3.3.2)-(3.3.5) at the leading order becomes

$$\nabla^2 \hat{\phi}_{i0} = 0 \quad \text{in } \mathcal{D}_i(0), \quad i = 1, 2, \tag{3.3.12}$$

$$\frac{\partial \hat{\phi}_{10}}{\partial \theta} = 0 \quad \text{at } \theta = \pi, \tag{3.3.13}$$

$$\frac{\partial \hat{\phi}_{20}}{\partial \theta} = 0 \quad \text{at } \theta = 0, \tag{3.3.14}$$

$$\hat{\phi}_{10} - \hat{\phi}_{20} = -r \sin\theta \quad \text{at } \theta = \pi - \alpha, \tag{3.3.15}$$

$$\frac{\partial \hat{\phi}_{10}}{\partial \theta} = \frac{\partial \hat{\phi}_{20}}{\partial \theta} \quad \text{at } \theta = \pi - \alpha. \tag{3.3.16}$$

There is a logarithmic singularity as $r \to 0$ due to the incompatibility in the boundary conditions (3.3.14) and (3.3.15). Similar to [4], we look for a local solution of the form

$$\hat{\phi}_{10}(r, \theta) \sim A(r \log r \cos\theta + r(\pi - \theta)\sin\theta) + B_1 r \cos\theta, \tag{3.3.17}$$

$$\hat{\phi}_{20}(r, \theta) \sim A(r \log r \cos\theta - r\theta \sin\theta) + B_2 r \cos\theta, \tag{3.3.18}$$

as $r \to 0$. On substitution from (3.3.17) and (3.3.18) into the boundary condition (3.3.15) and (3.3.16), we obtain

$$A = -\frac{\sin^2\alpha}{\pi}, B_2 - B_1 = -\sin\alpha\cos\alpha. \tag{3.3.19}$$

As $r \to 0$, we have $\phi_{i0} = O(r \log r)$, so the Bernoulli condition at order $O(\bar{\rho})$ for $\hat{\phi}_{i1}$ satisfies

$$\hat{\phi}_{11} - \hat{\phi}_{21} = -\hat{\phi}_{10} = O(r \log r) \quad \text{at } \theta = \pi - \alpha \text{ as } r \to 0. \tag{3.3.20}$$

Note that when $\bar{\rho} \log r = O(1)$ as $r \to 0$, $\bar{\rho}\hat{\phi}_{i1} = O(r)$ and this will cause a non-

uniformity in $\hat{\phi}_i$. Thus, the new variable $\tilde{s}$ is introduced as

$$\tilde{s} = \bar{\rho} \log r, \quad \tilde{s} = O(1), \quad \tilde{s} < 0 \quad \text{as } r \to 0 \text{ , } \bar{\rho} \to 0. \tag{3.3.21}$$

Consequently,

$$r = e^{\frac{\tilde{s}}{\bar{\rho}}}, \quad \hat{\phi}_i = O(\bar{\rho}^{-1} e^{\frac{\tilde{s}}{\bar{\rho}}}) \quad \text{when } \tilde{s} = O(1). \tag{3.3.22}$$

Laplace's equation can now be written in terms of $(\tilde{s}, \theta)$ as

$$\bar{\rho}^2 \frac{\partial^2 \hat{\phi}_i}{\partial \tilde{s}^2} + \frac{\partial^2 \hat{\phi}_i}{\partial \theta^2} = 0. \tag{3.3.23}$$

Let

$$\hat{\phi}_i = r\tilde{\phi}_i = \bar{\rho}^{-1} e^{\frac{\tilde{s}}{\bar{\rho}}} \tilde{\phi}_i, \quad \tilde{\phi}_i = O(1), \quad \text{as } r \to 0, \quad \bar{\rho} \to 0, \tag{3.3.24}$$

then the new form of Laplace's equation is given by substituting (3.3.24) into (3.3.23) as

$$\frac{\partial^2 \tilde{\phi}_i}{\partial \theta^2} + \tilde{\phi}_i + 2\bar{\rho} \frac{\partial \tilde{\phi}_i}{\partial \tilde{s}} + \bar{\rho}^2 \frac{\partial^2 \tilde{\phi}_i}{\partial \tilde{s}^2} = 0, \tag{3.3.25}$$

with the boundary conditions

$$\frac{\partial \tilde{\phi}_1}{\partial \theta} = 0 \quad \text{at } \theta = \pi, \tag{3.3.26}$$

$$\frac{\partial \tilde{\phi}_2}{\partial \theta} = 0 \quad \text{at } \theta = 0, \tag{3.3.27}$$

$$(1 + \bar{\rho})\tilde{\phi}_1 - \tilde{\phi}_2 = -\bar{\rho} \sin \alpha \quad \text{at } \theta = \pi - \alpha, \tag{3.3.28}$$

$$\frac{\partial \tilde{\phi}_1}{\partial \theta} = \frac{\partial \tilde{\phi}_2}{\partial \theta} \quad \text{at } \theta = \pi - \alpha. \tag{3.3.29}$$

Based on (3.3.24) and the matching condition

$$\hat{\phi}_i \sim -\frac{\sin^2 \alpha}{\pi} r \log r \cos \theta, \quad \text{as } r \to 0, \tag{3.3.30}$$

$\tilde{\phi}_i$ must satisfy

$$\tilde{\phi}_i \sim -\frac{\sin^2\alpha}{\pi}\tilde{s}\cos\theta \quad \text{as } \tilde{s} \to 0. \tag{3.3.31}$$

Now we introduce the asymptotic expansion

$$\tilde{\phi}_i(\tilde{s}) = \tilde{\phi}_{i0}(\tilde{s}) + \bar{\rho}\tilde{\phi}_{i1}(\tilde{s}) + O(\bar{\rho}^2),$$

and find the leading order term

$$\tilde{\phi}_{i0} = c(\tilde{s})\cos\theta, \quad c(\tilde{s}) \sim -\frac{\sin^2\alpha}{\pi}\tilde{s} \quad \text{as } \tilde{s} \to 0. \tag{3.3.32}$$

The Laplace's equation (3.3.25) at $O(\bar{\rho})$ is given by

$$\frac{\partial^2\tilde{\phi}_{i1}}{\partial\theta^2} + \tilde{\phi}_{i1} = -2\frac{\partial\tilde{\phi}_{i0}}{\partial s} = -2c'(\tilde{s})\cos\theta. \tag{3.3.33}$$

Thus, considering the boundary conditions (3.3.26) and (3.3.27), the local solution is

$$\tilde{\phi}_{11}(\tilde{s},\theta) = c'(\tilde{s})(\pi-\theta)\sin\theta + b_1\cos\theta, \tag{3.3.34}$$

$$\tilde{\phi}_{21}(\tilde{s},\theta) = -c'(\tilde{s})\theta\sin\theta + b_2\cos\theta. \tag{3.3.35}$$

The boundary conditions (3.3.26)−(3.3.29) are applied to these local solutions and give

$$c(\tilde{s}) = \tan\alpha + ke^{\frac{\cos\alpha\sin\alpha}{\pi}\tilde{s}}$$

where k is a constant. According to the matching condition (3.3.32), we find that

$$c(\tilde{s}) = \tan\alpha(1 - e^{\frac{\cos\alpha\sin\alpha}{\pi}\tilde{s}}), \tag{3.3.36}$$

which gives

$$\tilde{\phi}_{i0} = \tan\alpha(1 - e^{\frac{\cos\alpha\sin\alpha}{\pi}\tilde{s}})\cos\theta. \tag{3.3.37}$$

By using this result, we find that

$$\bar{\phi}_i = \bar{\rho}\hat{\phi}_i = r\tilde{\phi}_i \sim \tan\alpha(r\cos\theta - r^{1+\frac{\sin\alpha\cos\alpha}{\pi}\bar{\rho}}\cos\theta), \quad \text{as } r \to 0,\ \bar{\rho} \to 0. \tag{3.3.38}$$

This also indicates that the solution (3.3.8) to the eigenvalue problem in Section 3.3.1 is

$$\beta_0 \sim 1 + \frac{\sin\alpha\cos\alpha}{\pi}\bar{\rho} \quad \text{as } \bar{\rho} \to 0. \tag{3.3.39}$$

To obtain the solution in the function form (3.3.6), we include higher order term of $\bar{\rho}$ to obtain $\cos[(1 + \frac{\sin\alpha\cos\alpha}{\pi}\bar{\rho})\theta]$ since

$$\cos\theta \approx \cos[(1 + \frac{\sin\alpha\cos\alpha}{\pi}\bar{\rho})\theta],$$

as $\bar{\rho} \to 0$.

Consequently, the local solution must have the form

$$\bar{\phi}_i \sim \tan\alpha(r\cos\theta - r^{1+\frac{\sin\alpha\cos\alpha}{\pi}\bar{\rho}}\cos[(1+\frac{\sin\alpha\cos\alpha}{\pi}\bar{\rho})\theta]) \quad \text{as } r \to 0,\ \bar{\rho} \to 0. \tag{3.3.40}$$

However, this does not satisfy the boundary condition (3.3.26) for $\bar{\phi}_1$ at $\theta = \pi$. Thus, in order to satisfy all the boundary conditions (3.3.26)-(3.3.29), the local solution is

$$\bar{\phi}_1(r,\theta) \sim \tan\alpha\{r\cos\theta + r^{1+\frac{\sin\alpha\cos\alpha}{\pi}\bar{\rho}}\cos[(1+\frac{\sin\alpha\cos\alpha}{\pi}\bar{\rho})(\pi-\theta)]\}, \tag{3.3.41}$$

$$\bar{\phi}_2(r,\theta) \sim \tan\alpha\{r\cos\theta - r^{1+\frac{\sin\alpha\cos\alpha}{\pi}\bar{\rho}}\cos[(1+\frac{\sin\alpha\cos\alpha}{\pi}\bar{\rho})\theta]\}, \tag{3.3.42}$$

as $r \to 0$.

On substitution of (3.3.40) into (3.3.1), we have

$$\phi_i \sim tr\cos\theta\tan\alpha \quad \text{as } t \to 0, r \to 0.$$

Given $x = r\cos\theta$, we derive that the velocity of the flow in the channel as

$$\phi_{i,x} \sim t\tan\alpha \quad \text{as } t \to 0 \text{ at contact point.} \tag{3.3.43}$$

This indicates that

$$\frac{d(\phi_x)}{dt} \sim \tan\alpha = -\frac{dY}{dx}, \tag{3.3.44}$$

which is consistent with the equation (3.87) in [64].

Similarly, for the contact point (x_p, y_p) at $y = 1$, we shift the coordinate system by introducing $x' = x + \cot(\alpha)$ and $y' = y - 1$ as our new coordinates, and we drop the prime for convenience. With the same rescaling method, the local solution can be found as

$$\bar{\phi}_1(r,\theta) \sim \tan\alpha\{-r\cos\theta + r^{1-\frac{\cos\alpha\sin\alpha}{\pi}\bar{\rho}}\cos[(1-\frac{\cos\alpha\sin\alpha}{\pi}\bar{\rho})(\pi+\theta)]\}, \tag{3.3.45}$$

$$\bar{\phi}_2(r,\theta) \sim \tan\alpha\{-r\cos\theta + r^{1-\frac{\cos\alpha\sin\alpha}{\pi}\bar{\rho}}\cos[(1-\frac{\cos\alpha\sin\alpha}{\pi}\bar{\rho})\theta]\}. \tag{3.3.46}$$

More details of obtaining (3.3.45) and (3.3.46) can be found in Appendix A.

Since $0 < \alpha < \frac{\pi}{2}$ and $\bar{\rho} > 0$, the leading order local solution $\bar{\phi}_i$ is of order r for the problem around the lower contact point and of order $r^{1-\frac{\cos\alpha\sin\alpha}{\pi}\bar{\rho}}$ for the problem around the upper contact point. Hence, we can also conclude that there is a singularity around the upper contact point but not around the lower contact point, which is consistent with the analysis for the eigenvalue problem.

3.4 Solution using the Plemlj formula in the outer region for $t \to 0$

In this section, since the displacement of the interface is $Y(x,t) \sim -x\tan\alpha$ as $t \to 0$, we will use the Plemelj formula on the interface to solve the boundary-value problem

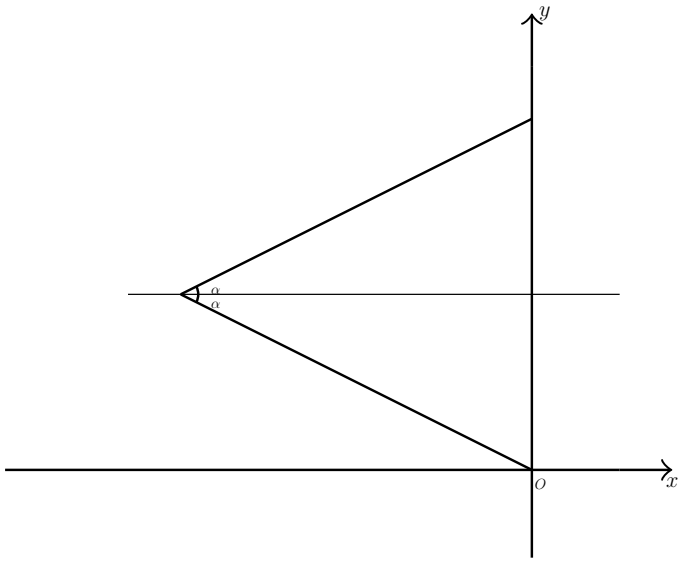

Figure 3.3: *Period extension of the interface.*

numerically by introducing the complex potential $\Phi_i = \bar{\phi}_i + \mathrm{i}\bar{\psi}_i$ in $\mathcal{D}_i$ with complex variable $z = x + \mathrm{i}y$ for $i = 1, 2$, where $\bar{\psi}_i$ is the stream function of the flow. As explained in Section 2.2, the Plemelj formula evaluates the limiting values of the integral (2.2.1) at some point on the contour, where the singularity appears in the integration. The periodic extension of the surface is necessary to apply the Plemelj formula, which ensures all the singularities along the contour are included in the integration and simplifies the calculation. We reflect the interface with the straight line $y = 1$ as shown in Figure 3.3 as a one-period interval and extend it periodically. The Plemelj formula (see [1]) for Φ_1 and Φ_2 is

$$\bar{\Phi}_1(z) = \frac{1}{2}\mu(s) + \frac{1}{2\pi\mathrm{i}} \fint_{-\infty}^{\infty} \frac{\mu(s')}{z(s') - z(s)} \frac{dz}{ds}(s')ds', \tag{3.4.1}$$

$$\bar{\Phi}_2(z) = -\frac{1}{2}\mu(s) + \frac{1}{2\pi\mathrm{i}} \fint_{-\infty}^{\infty} \frac{\mu(s')}{z(s') - z(s)} \frac{dz}{ds}(s')ds', \tag{3.4.2}$$

where $\mu(s) = \bar{\phi}_1(s) - \bar{\phi}_2(s)$, and s is the arclength of the point at z. The integral $\fint$ represents the principal value integral

$$\fint_L \frac{\mu(s')}{z(s') - z(s)} \frac{dz}{ds}(s')ds' = \lim_{\epsilon \to 0} \int_{L - L_\epsilon} \frac{\mu(s')}{z(s') - z(s)} \frac{dz}{ds}(s')ds', \tag{3.4.3}$$

where L is a smooth contour (closed or open) and L_ϵ is the part of L with length 2ϵ centered around $z(s)$.

Then the velocity potential is

$$\bar{\phi}_1(z) = \frac{1}{2}\mu(s) + \mathrm{Re}\left[\frac{1}{2\pi \mathrm{i}} \fint_{-\infty}^{\infty} \frac{\mu(s')}{z(s') - z(s)} \frac{dz}{ds}(s') ds'\right], \tag{3.4.4}$$

$$\bar{\phi}_2(z) = -\frac{1}{2}\mu(s) + \mathrm{Re}\left[\frac{1}{2\pi \mathrm{i}} \fint_{-\infty}^{\infty} \frac{\mu(s')}{z(s') - z(s)} \frac{dz}{ds}(s') ds'\right], \tag{3.4.5}$$

as the real part of Φ_i. For simplicity, we will mainly focus on the Plemelj formula for $\bar{\phi}_1$.

To avoid the singularity, the formula (3.4.4) can be rewritten as

$$\bar{\phi}_1(s) = \frac{1}{2}\mu(s) + \mathrm{Re}\left[\frac{1}{2\pi \mathrm{i}} \fint_{-\infty}^{\infty} \frac{\mu(s') - \mu(s)}{z(s) - z(s')} \frac{dz}{ds}(s') ds'\right], \tag{3.4.6}$$

for a periodic, open interval, or

$$\bar{\phi}_1(s) = \mu(s) + \mathrm{Re}\left[\frac{1}{2\pi \mathrm{i}} \fint_{-\infty}^{\infty} \frac{\mu(s') - \mu(s)}{z(s) - z(s')} \frac{dz}{ds}(s') ds'\right], \tag{3.4.7}$$

for a closed interval (see [2]). In this chapter, we will use (3.4.6) only since we construct a periodic interface extension.

After rotation counter-clockwise through an angle $\pi/2$, we obtain the new coordinate system $(x^*, y^*) = (1-y, \cot\alpha - x)$. Let $z^* = x^* + iy^*$, and we drop the asterisk for convenience. The location of the interface $z(s)$ with respect to the arclength s in the new coordinate system is now given as

$$z(s) = \begin{cases} (\csc(\alpha) - s)e^{i(\pi/2-\alpha)}, & s \in [0, \csc(\alpha)], \quad x \in [-1, 0] \\ -se^{i(\pi/2+\alpha)}, & s \in [-\csc(\alpha), 0], \quad x \in [0, 1] \end{cases} \tag{3.4.8}$$

in the period $-\csc(\alpha) < s < \csc(\alpha)$, which is equivalent to the period $-1 < x < 1$.

Based on [2], the periodic form of the Plemelj formula (3.4.4) can be derived as

$$\begin{aligned}\bar{\phi}_1(s) &= \frac{1}{2}\mu(s) + \mathrm{Re}\left[\frac{1}{2\pi \mathrm{i}}\sum_{n=-\infty}^{\infty}\int_{-n\csc(\alpha)}^{(n+1)\csc(\alpha)} \frac{\mu(s')}{z(s')-z(s)}\frac{dz}{ds}(s')ds'\right], \\ &= \frac{1}{2}\mu(s) + \mathrm{Re}\left[\frac{1}{2\pi \mathrm{i}}\int_{-\csc(\alpha)}^{\csc(\alpha)} (\mu(s'))\sum_{n=-\infty}^{\infty}\frac{1}{z(s')-z(s)-2n}\frac{dz}{ds}(s')ds'\right].\end{aligned} \tag{3.4.9}$$

The summation can be simplified as

$$\begin{aligned}\sum_{n=-\infty}^{\infty}\frac{1}{z(s')-z(s)-2n} &= \frac{1}{z(s')-z(s)} + \sum_{n=1}^{\infty}\left(\frac{1}{z(s')-z(s)-2n} + \frac{1}{z(s')-z(s)+2n}\right) \\ &= \frac{1}{z(s')-z(s)} + 2\sum_{n=1}^{\infty}\frac{z(s')-z(s)}{(z(s')-z(s))^2-(2n)^2} \quad .\end{aligned} \tag{3.4.10}$$

Substituting (3.4.10) into (3.4.9) and using the identity in [9]

$$\frac{1}{z} + 2z\sum_{n=1}^{\infty} -\frac{1}{z^2-n^2\pi^2} = \cot(z), \tag{3.4.11}$$

we obtain the periodic Plemelj formula

$$\bar{\phi}_1(s) = \frac{1}{2}\mu(s) + \mathrm{Re}\left[\frac{1}{4\mathrm{i}}\int_{-\csc(\alpha)}^{\csc(\alpha)} (\mu(s'))\cot[\frac{\pi}{2}(z(s')-z(s))]\frac{dz}{ds}(s')ds'\right]. \tag{3.4.12}$$

3.4.1 The solution for $\bar{\rho} > 0$

For $\bar{\rho} > 0$, we can use the Plemelj formula to solve the problem (3.3.2)-(3.3.5). The boundary condition (3.3.4) is now

$$\bar{\phi}_1 - \bar{\phi}_2 = -\bar{\rho}(|z(s)|\cos(\pi/2-\alpha) + \bar{\phi}_1(s)),$$

for $-\csc(\alpha) < s < \csc(\alpha)$. Thus, we have

$$\mu(s) = -\bar{\rho}\left(|z(s)|\sin\alpha + \bar{\phi}_1(s)\right), \tag{3.4.13}$$

for $-\csc(\alpha) < s < \csc(\alpha)$ in the new coordinate system.

We can obtain the formula for $\bar{\phi}_1$ by using (3.4.13),

$$\bar{\phi}_1(s) \;=\; -\frac{\bar{\rho}}{2}\left(|z(s)|\sin\alpha + \bar{\phi}_1(s)\right) + \mathrm{Re(I)}, \tag{3.4.14}$$

where

$$\mathrm{I} = \frac{1}{4\mathrm{i}}\int_{-\csc(\alpha)}^{\csc(\alpha)} \bar{\rho}\left(-|z(s')|\sin\alpha - \bar{\phi}_1(s') + |z(s)|\sin\alpha + \bar{\phi}_1(s)\right)\cot[\frac{\pi}{2}(z(s')-z(s))]\frac{dz}{ds}(s')ds. \tag{3.4.15}$$

A Fredholm integral equation of the second kind for $\bar{\phi}_1$ can be found by rearranging this formula as

$$\bar{\phi}_1(s) \;=\; \frac{\bar{\rho}}{1+\frac{1}{2}\bar{\rho}}\left\{-\frac{1}{2}|z(s)|\sin\alpha + \mathrm{Re(I)}\right\}. \tag{3.4.16}$$

Thus,

$$\bar{\phi}_2(s) \;=\; \frac{1}{1+\frac{1}{2}\bar{\rho}}\left\{\frac{\bar{\rho}}{2}|z(s)|\sin\alpha + \left(\frac{\bar{\rho}^2}{2} + 1 + \frac{\bar{\rho}}{2}\right)\mathrm{Re(I)}\right\}. \tag{3.4.17}$$

This formula can be solved as a linear system using the Trapezium rule to evaluate the integral. To further determine the solution for the displacement of the interface $\bar{Y}$, we consider the stream function

$$\bar{\psi}(s) = \mathrm{Im}\left[-\frac{1}{4\mathrm{i}}\int_{-\csc\alpha}^{\csc(\alpha)}(\mu(s')-\mu(s))\cot[\frac{\pi}{2}(z(s')-z(s))]\frac{dz}{ds}(s')ds'\right], \tag{3.4.18}$$

such that $\frac{d\bar{\psi}}{ds} = \mathbf{n}\cdot\nabla\bar{\phi}_i$. Thus, we can find the displacement of the interface $\bar{Y}$ using the boundary condition (3.3.5).

3.4.2 Solution for $\bar{\rho} = 0$

When $\bar{\rho} = 0$, we consider the scaled variables (3.3.10) and use Plemelj formula to solve (3.3.12)-(3.3.16) for $\hat{\phi}_1$ instead. Now we have

$$\mu(s) = |z(s)| \sin\alpha, \tag{3.4.19}$$

for $-\csc(\alpha) < s < \csc(\alpha)$ in the new coordinate system, and thus the Plemelj formula for $\hat{\phi}_1(s)$ is similar to $\bar{\phi}_1(s)$, which is

$$\begin{aligned}\hat{\phi}_1(s) &= -\frac{1}{2}|z(s)|\sin\alpha \\ &\quad + Re\left[\frac{1}{4\mathrm{i}}\int_{-\csc(\alpha)}^{\csc(\alpha)} (-|z(s')|\sin\alpha + |z(s)|\sin\alpha)\cot[\frac{\pi}{2}(z(s') - z(s))]\frac{dz}{ds}(s')ds\right].\end{aligned} \tag{3.4.20}$$

This can be solved straightforwardly for $\hat{\phi}_1(s)$.

3.5 Numerical approximation for outer region

In this section, we will compare the numerical results from the Plemelj formula and the asymptotic solutions in the outer region for $\bar{\rho} = 0$, $\bar{\rho} \ll 1$ and $\bar{\rho} \gg 1$ as $t \to 0$.

3.5.1 Numerical results for $\bar{\rho} = 0$

We first consider the numerical solution for $\hat{\phi}_1$ with $\bar{\rho} = 0$ by directly evaluating the integration (3.4.20) numerically. The asymptotic solution (3.3.17) suggests that

$$\frac{\hat{\phi}_1}{r} \sim A\cos\theta\log r, \quad r \to 0.$$

Figure 3.4 show the graphs of numerical solutions in blue and asymptotic solutions in red in terms of $\log(r)$ at both endpoints, where Figure 3.4a, 3.4b show the results

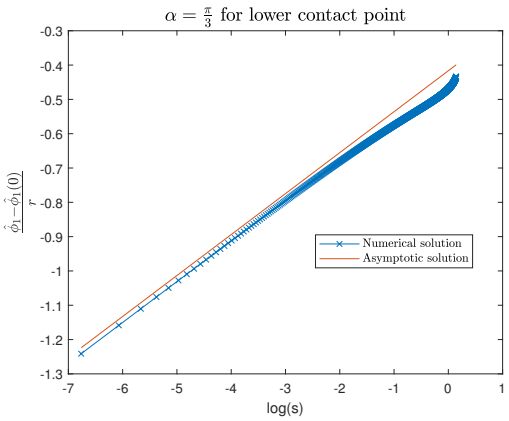

(a) $\alpha = \frac{\pi}{3}$, *numerical results compared with the asymptotic solution near the bottom contact point at* $y = 0$.

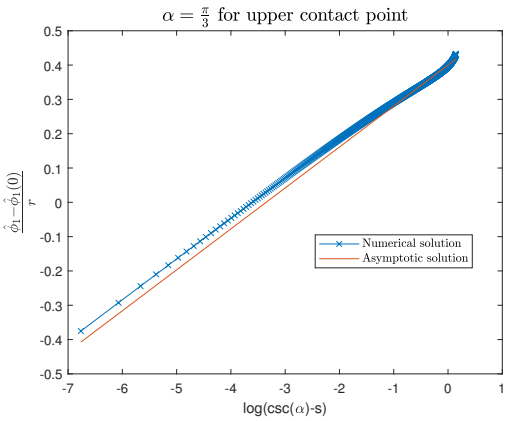

(b) $\alpha = \frac{\pi}{3}$, *numerical results compared with the asymptotic solution near the upper contact point at* $y = 1$.

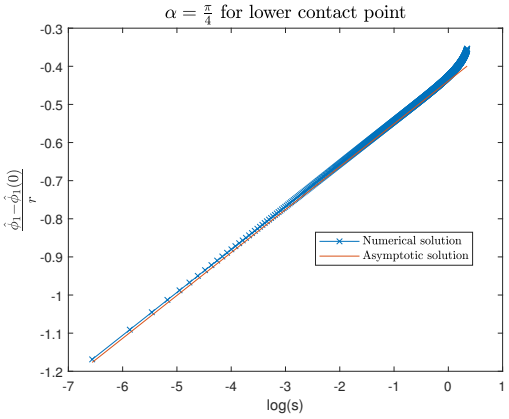

(c) $\alpha = \frac{\pi}{4}$, *numerical results compared with the asymptotic solution near the bottom contact point at* $y = 0$.

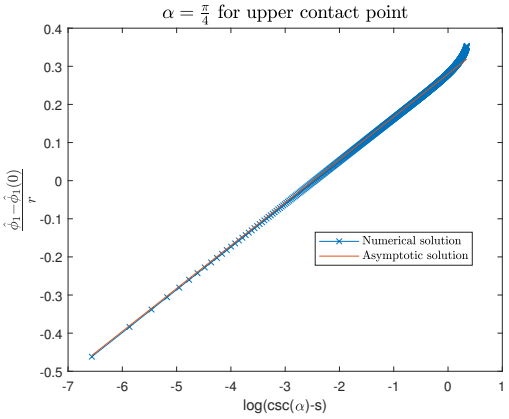

(d) $\alpha = \frac{\pi}{4}$, *numerical results compared with the asymptotic solution near the upper contact point at* $y = 1$.

Figure 3.4: *The comparison between numerical solution and asymptotic solution for* $\bar{\rho} = 0$. *The y-axis is* $\frac{\hat{\phi}_1 - \hat{\phi}_1(0)}{r}$, *where* $\hat{\phi}_1(0)$ *is the constant term in* $\hat{\phi}_1$. *Figure (a) and (b) show the results near the bottom contact point at* $y = 0$ *and the upper endpoint at* $y = 1$ *with* $\alpha = \frac{\pi}{3}$, *while Figure (c) and (d) show the results with* $\alpha = \frac{\pi}{4}$.

for $\alpha = \pi/3$, and Figure 3.4c, 3.4d show the results for $\alpha = \pi/4$. In addition, Figure 3.4a, 3.4c compares the results close the the bottom contact point at $y = 0$, while Figure 3.4b, 3.4d compares the results near the upper contact point at $y = 1$. The y-axis in the graph is $\frac{\hat{\phi}_1 - \hat{\phi}_1(0)}{r}$ such that the impact of the constant term in $\hat{\phi}_1$ can be avoided by subtracting the value $\hat{\phi}_1(0)$ at $r = 0$. The numerical results show the excellent agreement between the numerical solution and the asymptotic solution close to the intersection points at $y = 0$ and $y = 1$ by showing the straight lines when $r \to 0$ in Figure 3.4. The asymptotic solutions are only valid as $r \to 0$. Therefore, there are inconsistencies in Figure 3.4 as $r \to 1$.

3.5.2 Numerical results for $\bar{\rho} > 0$

We compare the asymptotic solution (3.3.41), (3.3.45) with the numerical results of (3.4.16) solved by Trapezium rule for $\bar{\rho} \ll 1$, which is shown in Figure 3.5. Figure 3.5 shows the log-log plots of $\bar{\phi}_1$ after subtracting constant and linear terms with respect to the radius r for various values of $\bar{\rho}$ with a different angle close to two intersection points. Figure 3.5a and 3.5b show the results near the bottom contact point and the upper contact point for $\bar{\rho} = 0.01$ with $\alpha = \frac{\pi}{3}$, while Figure 3.5c and 3.5d show the solutions near the bottom contact point and the upper contact point for $\bar{\rho} = 0.001$ with $\alpha = \frac{\pi}{4}$. The red lines represent the asymptotic solution, and the blue lines represent the numerical results. The numerical results close to the bottom and upper contact points are perfectly consistent with the asymptotic solution.

Now we look into the numerical simulation (3.3.41) and (3.3.45) for $\bar{\rho} \gg 0$. It is straightforward to solve the condition (3.3.8) numerically, where β_0 has a limit as $\bar{\rho} \to \infty$ for $r \to 0$. In Figure 3.6, we compare the numerical results of the leading order term (except the linear term) with β_0 against $\bar{\rho}$ for $\alpha = \frac{\pi}{3}$ and $\frac{\pi}{4}$ around both the lower and upper contact points. The red lines represent the numerical power (the order of magnitude of the numerical results of the leading order as $r \to 0$), and the blue lines are values of β_0. As shown in Figure 3.6, for the upper contact

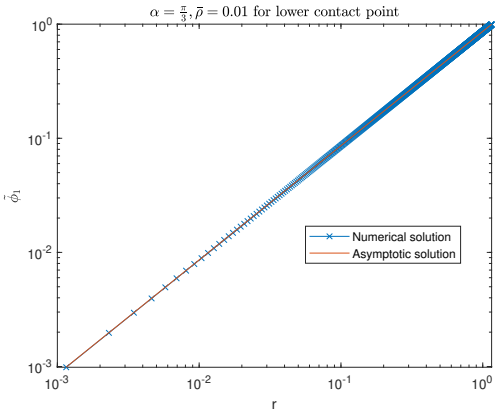

(a) $\alpha = \frac{\pi}{3}$ *and* $\bar{\rho} = 0.01$*, numerical results compared with the asymptotic solution near the bottom contact point.*

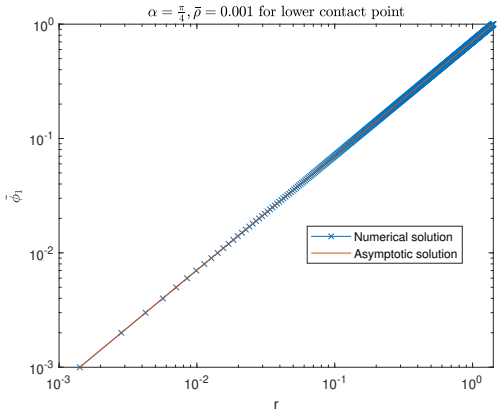

(b) $\alpha = \frac{\pi}{4}$ *and* $\bar{\rho} = 0.001$*, numerical results compared with the asymptotic solution near the bottom contact point.*

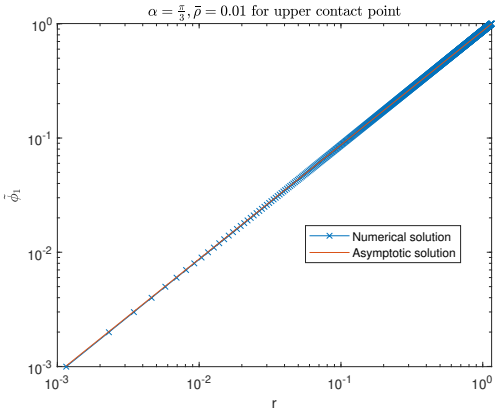

(c) $\alpha = \frac{\pi}{3}$ *and* $\bar{\rho} = 0.01$*, numerical results compared with the asymptotic solution close to the upper contact point.*

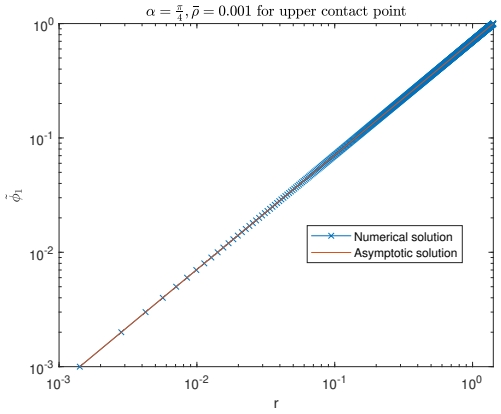

(d) $\alpha = \frac{\pi}{4}$ *and* $\bar{\rho} = 0.001$*, numerical results compared with the asymptotic solution close to the upper contact point.*

Figure 3.5: *The log-log plots of* $\tilde{\phi}_1$ *after subtracting constant and linear terms with respect to the radius* r *for various values of* $\bar{\rho}$ *with a different angle close to two intersection points. Figure 3.5a and 3.5b show the results near the bottom contact point and the upper contact point for* $\bar{\rho} = 0.01$ *with* $\alpha = \frac{\pi}{3}$*, while Figure 3.5c and 3.5d show the solutions near the bottom contact point and the upper contact point for* $\bar{\rho} = 0.001$ *with* $\alpha = \frac{\pi}{4}$*. The red lines represent the asymptotic solution, and the blue lines represent the numerical results.*

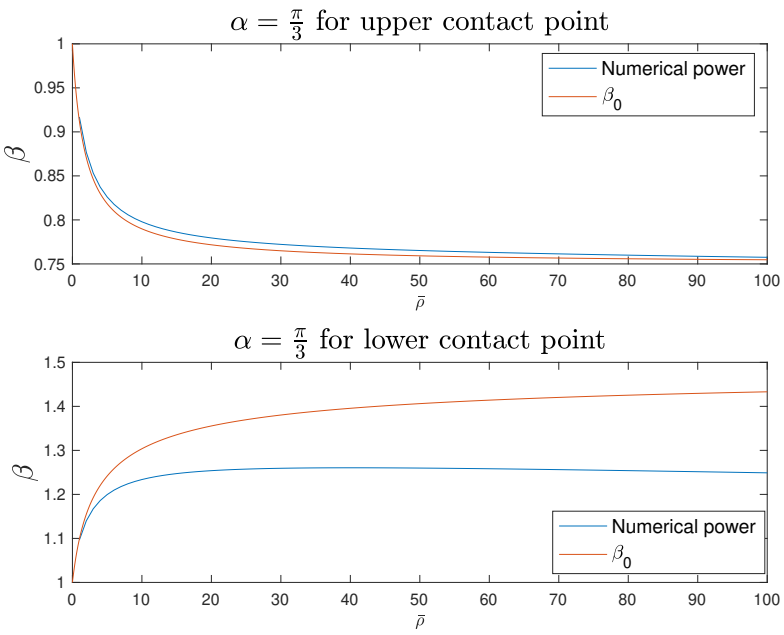

(a) $\alpha = \frac{\pi}{3}$, *numerical results of the leading order in* r *compared with* β_0 .

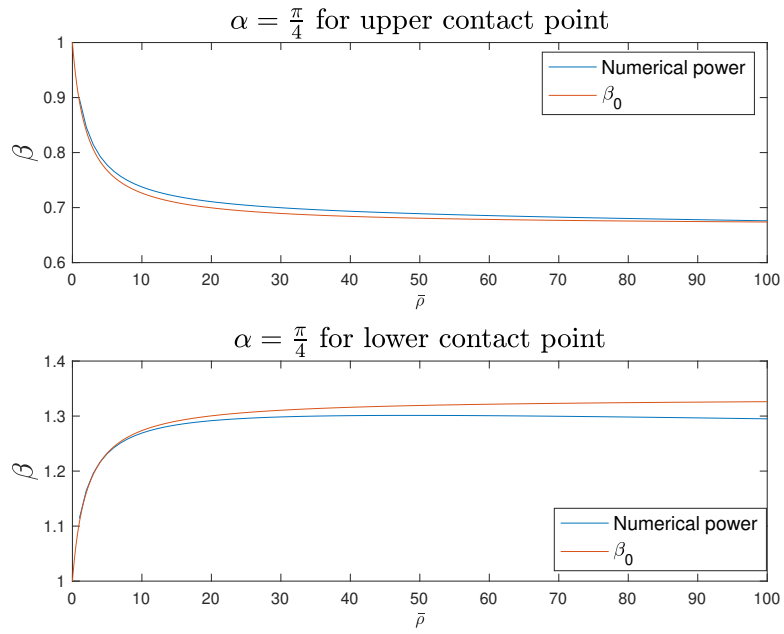

(b) $\alpha = \frac{\pi}{4}$, *numerical results of the leading order in* r *compared with* β_0.

Figure 3.6: *The comparison between numerical results of leading order term in* r *(except the linear term) and* β_0 *against* $\bar{\rho}$ *for* $\alpha = \frac{\pi}{3}$ *and* $\frac{\pi}{4}$. *The upper subplot is for the upper contact point, and the lower subplot is for the lower contact point. The red lines are numerical power (the power of the numerical results of the leading order as* $r \to 0$*), and the blue lines are values of* β_0.

points, the leading order is very close to the lower bound of β_0 as $\bar{\rho} \to \infty$ for $r \to 0$. In addition, the blue lines are also consistent with the red lines when $\bar{\rho}$ is close to 0 around both contact points. However, for lower contact points, the differences between the numerical results of the leading order term (except linear term) and analytical values β_0 are slightly more significant. The possible reason is that the leading order term is linear for the lower point, and the terms of order r^β are the correction to the linear term, which can be affected by other higher-order terms. We also find that the order of magnitude of the leading order term around the upper contact point is always lower than 1, indicating singularities on the interface near that intersection point. Figure 3.7 shows the numerical approximation to the interface $\bar{Y}(x)$ for $\bar{\rho} = 5, \alpha = \frac{\pi}{3}$ and $\bar{\rho} = 10, \alpha = \frac{\pi}{4}$ by solving (3.3.5). The singular behaviour indicates that we must consider the inner region solution around the upper contact point.

3.6 Inner-region Solution for $t \to 0^+$

Now we look into the inner region around the upper contact point. We set $(x, y) = O(\mathcal{X}(t))$, with $\mathcal{X}(t) = o(1)$ as $t \to 0^+$, in the inner region. According to (3.3.1), the interface is now required to satisfy $Y(x, t) = O(\mathcal{X}(t))$ as $t \to 0^+$ in the inner region. It then follows from (3.3.5) and (3.3.6) that

$$\mathcal{X}(t) \sim O(t^2 \mathcal{X}(t)^{\beta_0 - 1}) \quad \text{as } t \to 0^+,$$

which indicates that

$$\mathcal{X}(t) = O(t^\beta) \quad \text{as } t \to 0^+, \tag{3.6.1}$$

where $\beta = \frac{1}{1 - \frac{\beta_0}{2}}$.

We can now choose $\mathcal{X}(t) = t^\beta$ without loss of generality. Hence, from (3.3.1)

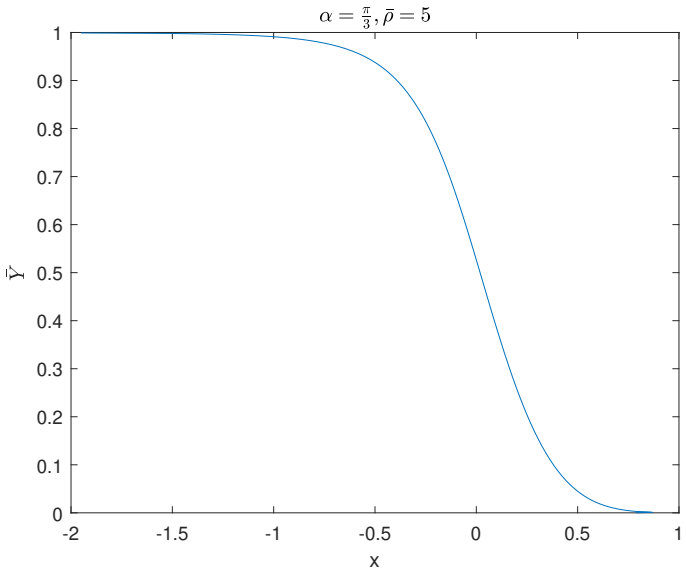

(a) $\bar{Y}(x)$ *with respect to* x *for* $\bar{\rho} = 5$ *with* $\alpha = \frac{\pi}{3}$.

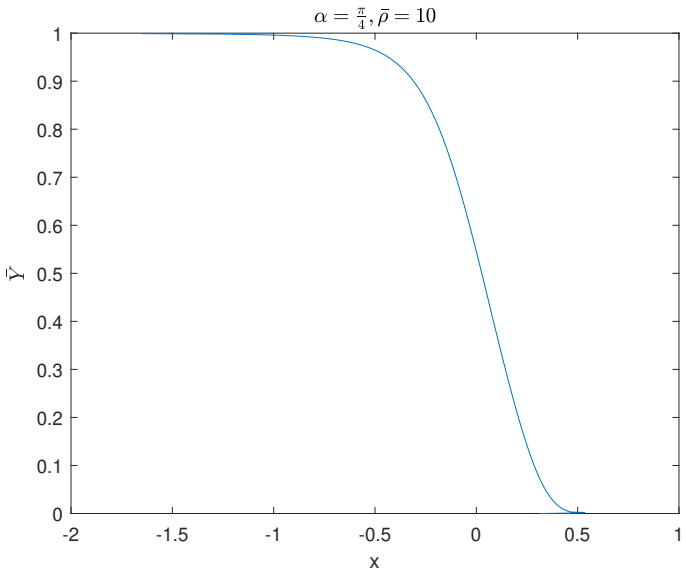

(b) $\bar{Y}(x)$ *with respect to* x *for* $\bar{\rho} = 10$ *with* $\alpha = \frac{\pi}{4}$.

Figure 3.7: *The numerical results of the displacement of the interface* $\bar{Y}(x)$ *with respect to* x *for different* $\bar{\rho}$ *and different angles* α.

and (3.3.6), we have

$$\phi_i = O(t^{2\beta-1}) \quad \text{as } t \to 0^+ \tag{3.6.2}$$

in the inner region for $i = 1, 2$. We introduce scaled inner coordinates $(\tilde{X}, \tilde{Y})$ by the transformation

$$x = t^\beta \tilde{X}, y = t^\beta \tilde{Y} \tag{3.6.3}$$

with $(\tilde{X}, \tilde{Y}) = O(1)$ as $t \to 0^+$ in the inner region. The asymptotic solutions in the inner region have the form

$$\phi_i(\tilde{X}, \tilde{Y}, t) = t^{2\beta-1}\tilde{\phi}_i(\tilde{X}, \tilde{Y}) + o(t^{2\beta-1}) \quad \text{for } i = 1, 2, \quad Y(\tilde{X}, t) = t^\beta \tilde{Y}_0(\tilde{X}) + o(t^\beta), \tag{3.6.4}$$

as $t \to 0^+$ in the inner region. After substitution into (3.2.2)-(3.2.4), the full BVP in terms of inner coordinates in the leading order is

$$\tilde{\nabla}^2 \tilde{\phi}_i = 0 \quad \text{in } \mathcal{D}_i, \tag{3.6.5}$$

$$\tilde{\nabla}\phi_i \cdot \tilde{\mathbf{n}} = 0, \quad \tilde{Y} = 0, \tag{3.6.6}$$

$$(2\beta - 1)\left[(1+\bar{\rho})\,\tilde{\phi}_1 - \tilde{\phi}_2\right] - \beta\left[(1+\bar{\rho})\left(\tilde{X}\tilde{\phi}_{1\tilde{X}} + \tilde{Y}\tilde{\phi}_{1\tilde{Y}}\right) - \left(\tilde{X}\tilde{\phi}_{2\tilde{X}} + \tilde{Y}\tilde{\phi}_{2\tilde{Y}}\right)\right] + \frac{1}{2}\left[(1+\bar{\rho})\left|\tilde{\nabla}\tilde{\phi}_1\right|^2 - \left|\tilde{\nabla}\tilde{\phi}_2\right|^2\right] = 0, \quad \tilde{Y} = \tilde{Y}_0(\tilde{X}), \tag{3.6.7}$$

$$\beta\tilde{Y}_0 + (\tilde{\phi}_{i\tilde{X}} - \beta\tilde{X})\tilde{Y}_{0\tilde{X}} - \tilde{\phi}_{i\tilde{Y}} = 0, \quad \tilde{Y} = \tilde{Y}_0(\tilde{X}), \tag{3.6.8}$$

$$\tilde{\phi}_1 \sim A_1 \tilde{R}^{\beta_0}\cos(\beta_0\tilde{\theta}) \quad \text{as } \tilde{R} \to \infty, \tag{3.6.9}$$

$$\tilde{\phi}_2 \sim A_2 \tilde{R}^{\beta_0}\cos(\beta_0(\pi - \tilde{\theta})) \quad \text{as } \tilde{R} \to \infty, \tag{3.6.10}$$

where $\tilde{\nabla} = (\frac{\partial}{\partial\tilde{X}}, \frac{\partial}{\partial\tilde{Y}})$. The final two conditions are the matching conditions between the asymptotic expansion (3.6.4) in the inner region and the asymptotic solution (3.3.6) in the outer region, where we use the polar coordinates $\tilde{R}^2 = \tilde{X}^2 + \tilde{Y}^2$ and $\tan\tilde{\theta} = \frac{\tilde{Y}}{\tilde{X}}$. The real constants A_1 and A_2 can be determined numerically by the Plemelj formula.

We can scale A_1 out of the problem by introducing

$$\tilde{X} = l\tilde{X}^*, \quad \tilde{Y} = l\tilde{Y}^*, \quad \tilde{Y}_0 = l\tilde{Y}_0^*, \quad \tilde{R} = l\tilde{R}^*, \quad \tilde{\phi}_i = l^2\tilde{\phi}_i^*, \quad \text{for } i = 1, 2, \tag{3.6.11}$$

where $l = (-A_1)^{\frac{1}{2}\beta}$ as $A_1 < 0$, and we drop the asterisk for convenience.

On substitution from (3.6.11) into (3.6.5)-(3.6.10), the BVP is then

$$\tilde{\nabla}^2\tilde{\phi}_i = 0, \quad \text{in } \mathcal{D}_i, \tag{3.6.12}$$

$$\tilde{\nabla}\tilde{\phi}_i \cdot \tilde{\mathbf{n}} = 0, \quad \tilde{Y} = 0, \tag{3.6.13}$$

$$\begin{aligned}(1+\bar{\rho})\left[(2\beta-1)\tilde{\phi}_1 - \beta\left(\tilde{X}\tilde{\phi}_{1,\tilde{X}} + \tilde{Y}\tilde{\phi}_{1,\tilde{Y}}\right) + \tfrac{1}{2}\left|\tilde{\nabla}\tilde{\phi}_1\right|^2\right] \\ -\left[(2\beta-1)\tilde{\phi}_2 - \beta\left(\tilde{X}\tilde{\phi}_{2,\tilde{X}} + \tilde{Y}\tilde{\phi}_{2,\tilde{Y}}\right) + \tfrac{1}{2}\left|\tilde{\nabla}\tilde{\phi}_2\right|^2\right] = 0, \quad \tilde{Y} = \tilde{Y}_0(\tilde{X}),\end{aligned} \tag{3.6.14}$$

$$\beta\tilde{Y}_0 + (\tilde{\phi}_{i,\tilde{X}} - \beta\tilde{X})\tilde{Y}_{0\tilde{X}} - \tilde{\phi}_{i,\tilde{Y}} = 0, \quad \tilde{Y} = \tilde{Y}_0(\tilde{X}), \tag{3.6.15}$$

$$\tilde{\phi}_1 \sim \tilde{R}^{\beta_0}\cos\beta_0\tilde{\theta} \quad \text{as } \tilde{R} \to \infty, \tag{3.6.16}$$

$$\tilde{\phi}_2 \sim \tfrac{A_2}{A_1}\tilde{R}^{\beta_0}\cos\left(\beta_0\left(\pi - \tilde{\theta}\right)\right) \quad \text{as } \tilde{R} \to \infty. \tag{3.6.17}$$

Now we rotate the coordinates counter-clockwise through an angle $\pi/2$ such that the plate lies on the new vertical axis $\hat{y}$ and the new horizontal axis $\hat{x}$ is in a direction normal to the plate. We denote the interface by $\hat{y} = \eta(\hat{x})$ for $\hat{x} \geq 0$. The local problem (3.6.12)-(3.6.15) has the exact solution in the form

$$\eta(\hat{x}) = \eta_0, \quad \hat{x} \geq 0, \tag{3.6.18}$$

$$\tilde{\phi}_1 = \beta\eta_0\hat{y} + \tilde{\phi}_{10}, \quad \hat{x} \geq 0, \hat{y} \leq \eta_0, \tag{3.6.19}$$

$$\tilde{\phi}_2 = \beta\eta_0\hat{y} + \tilde{\phi}_{20}, \quad \hat{x} \geq 0, \hat{y} \leq \eta_0, \tag{3.6.20}$$

where η_0, $\tilde{\phi}_{10}$, $\tilde{\phi}_{20}$ are constants satisfying $(1+\bar{\rho})\tilde{\phi}_{10} - \tilde{\phi}_{20} = \frac{\bar{\rho}\beta\eta_0^2(1-\frac{3}{2}\beta)}{2\beta-1}$ from the Bernoulli condition (3.6.14) in the inner region. The solutions (3.6.18)-(3.6.20) do not satisfy the far-field condition (3.6.15) and (3.6.17), but it shows the leading order form of the solution to the problem (3.6.12)-(3.6.15) in the inner region as $\hat{x} \to 0$.

We now consider the corrections to (3.6.18)-(3.6.20) as $\hat{x} \to 0$ by introducing $\hat{\eta}$, $\tilde{\phi}_{11}$, and $\tilde{\phi}_{21}$ such that

$$\eta(\hat{x}) = \eta_0 + \hat{\eta}(\hat{x}), \quad \hat{x} \geq 0, \quad \hat{y} \leq \eta_0, \tag{3.6.21}$$

$$\tilde{\phi}_1(\hat{x}, \hat{y}) = \left[\beta\eta_0\hat{y} + \tilde{\phi}_{10}\right] + \tilde{\phi}_{11}(\hat{x}, \hat{y}), \quad \hat{x} \geq 0, \quad \hat{y} \leq \eta_0 \tag{3.6.22}$$

$$\tilde{\phi}_2(\hat{x}, \hat{y}) = \left[\beta\eta_0\hat{y} + \tilde{\phi}_{20}\right] + \tilde{\phi}_{21}(\hat{x}, \hat{y}), \quad \hat{x} \geq 0, \quad \hat{y} \leq \eta_0, \tag{3.6.23}$$

where $\hat{\eta}(\hat{x}) = o(1)$ as $\hat{x} \to 0$, and $\tilde{\phi}_{i1}(\hat{x}, \hat{y}) = o(1)$ as $(\hat{x}, \hat{y}) \to (0, \eta_0)$. For convenience, we introduce the shifted coordinate

$$\bar{y} = \hat{y} - \eta_0.$$

On substitution from (3.6.21)-(3.6.23) into (3.6.12)-(3.6.15), the BVP is

$$\hat{\nabla}\tilde{\phi}_{i1} = 0 \quad \text{in } \mathcal{D}_i, \tag{3.6.24}$$

$$\tilde{\phi}_{i1,\hat{x}} = 0, \quad \hat{x} = 0, \bar{y} < 0, \tag{3.6.25}$$

$$(2\beta - 1)\left[(1 + \bar{\rho})\,\tilde{\phi}_{11} - \tilde{\phi}_{21}\right] - \beta\hat{x}\left[(1 + \bar{\rho})\,\tilde{\phi}_{11,\hat{x}} - \tilde{\phi}_{21,\hat{x}}\right] + (\beta - 1)\,\beta\eta_0\bar{\rho}\hat{\eta} = 0, \quad \bar{y} = 0 \tag{3.6.26}$$

$$\beta\tilde{\eta} + \left(\tilde{\phi}_{i1,\hat{x}} - \beta\hat{x}\right)\hat{\eta}_{\hat{x}} - \tilde{\phi}_{i1,\bar{y}} = 0, \quad \bar{y} = 0, \tag{3.6.27}$$

where $\hat{\nabla} = \left(\frac{\partial}{\partial\hat{x}}, \frac{\partial}{\partial\hat{y}}\right)$. By defining $\Phi(\hat{x}, \bar{y}) = (1 + \bar{\rho})\,\tilde{\phi}_{11} - \tilde{\phi}_{21}$, and eliminating $\hat{\eta}$ from (3.6.24)-(3.6.27), condition (3.6.26) and (3.6.27) now become

$$(2\beta - 1)\left(\hat{x}\Phi_{\hat{x}} - \Phi\right) - \beta\hat{x}^2\Phi_{\hat{x}\hat{x}} - (\beta - 1)\,\eta_0\Phi_{\bar{y}} = 0, \quad \hat{x} \geq 0, \bar{y} = 0, \tag{3.6.28}$$

$$\hat{\eta}(\hat{x}) = \frac{1}{(\beta - 1)\,\beta\eta_0\bar{\rho}}\left[\beta\hat{x}\Phi_{\hat{x}}(\hat{x}, 0) - (2\beta - 1)\,\Phi(\hat{x}, 0)\right], \quad \hat{x} \geq 0. \tag{3.6.29}$$

We introduce the complex variable $\hat{z} = \hat{x} + \mathrm{i}\bar{y}$, after which we write

$$\Phi(\hat{x}, \bar{y}) = \mathrm{Re}(f(z)), \quad \hat{z} \in \hat{\mathcal{D}}, \tag{3.6.30}$$

with $\hat{\mathcal{D}} := \{(\hat{x}, \bar{y}) : 0 < \hat{x}, \bar{y} < 0\}$. The conditions (3.6.25) and (3.6.29) then require

$$\beta \hat{x}^2 f''(\hat{x}) + [(\beta - 1)\, \eta_0 \mathrm{i} - (2\beta - 1)\, \hat{x}]\, f'(\hat{x}) + (2\beta - 1)\, f(\hat{x}) = 0, \quad \hat{x} \geq 0, \tag{3.6.31}$$

$$\mathrm{Re}(f'(\mathrm{i}\bar{y})) = 0, \quad \bar{y} < 0. \tag{3.6.32}$$

This is the same formation as that in [64] for the single fluid problem with an inclined accelerating plate in the inner region as $\hat{x} \to 0$, and the numerical results in that paper show that $\eta_0 > 0$.

Following the similar analysis in [64], the structure (3.6.31) leads to

$$f(\hat{x}) = \exp g(\hat{x}), \quad \hat{x} > 0, \tag{3.6.33}$$

with

$$g(\hat{x}) = \frac{k_0}{\hat{x}} + k_1 \log(\hat{x}) + o(1), \quad \hat{x} \to 0, \tag{3.6.34}$$

where $k_0, k_1 \in \mathbb{C}$ will be determined next. On substitution from (3.6.33) and (3.6.34) into (3.6.31), we find that

$$k_0 = \mathrm{i}\left(1 - \frac{1}{\beta}\right)\eta_0, \quad k_1 = 4 - \frac{1}{\beta}, \tag{3.6.35}$$

by looking at the leading order terms $O(\hat{x}^{-2})$ and $O(\hat{x}^{-1})$. Thus we take

$$f(\hat{z}) = A \exp\left\{\frac{\mathrm{i}(1 - \frac{1}{\beta})\eta_0}{\hat{z}} + (4 - \frac{1}{\beta}) \log(\hat{z}) + o(1)\right\}, \quad \text{as } |\hat{z}| \to 0, \tag{3.6.36}$$

with $A \in \mathbb{C}$ an arbitrary constant. Condition (3.6.32) requires

$$\arg(A) = (4 - \frac{1}{\beta})\frac{\pi}{2} + r\pi, \quad r = 0 \text{ or } 1. \tag{3.6.37}$$

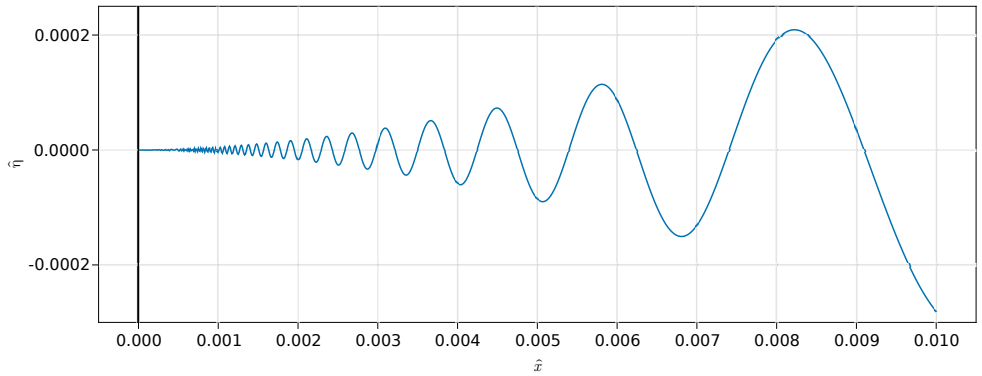

Figure 3.8: *The asymptotic form given by* (3.6.40) *for* $\eta_0 = 0.5$, $\beta = 0.8$, $\bar{\rho} = 10$ *and* $B = 6$. *The bold black line represents the plate, and the blue curve is the free surface.*

Hence, we have

$$f(\hat{z}) = B \exp\left\{ \frac{\mathrm{i}(1-\frac{1}{\beta})}{\hat{z}} \eta_0 + (4 - \frac{1}{\beta}) \log(\hat{z}) + (4 - \frac{1}{\beta}) \frac{\pi}{2} \mathrm{i} + \pi + o(1) \right\}, \tag{3.6.38}$$

as $|\hat{z}| \to 0$ with $B \in \mathbb{R}$ a globally determined constant. Therefore, we have the solution

$$\Phi(\hat{R}, \hat{\Theta}) \sim -B \hat{R}^{4-\frac{1}{\beta}} \exp\left\{ (1 - \frac{1}{\beta}) \eta_0 \hat{R}^{-1} \sin \hat{\Theta} \right\} \cos\left[(1 - \frac{1}{\beta}) \eta_0 \hat{R}^{-1} \cos \hat{\Theta} + (4 - \frac{1}{\beta})(\hat{\Theta} + \frac{\pi}{2}) \right], \tag{3.6.39}$$

as $\hat{R} \to 0$ uniformly for $\hat{\Theta} \in [0, \frac{\pi}{2}]$ where $\hat{R} = |\hat{z}|$ and $\hat{\Theta} = \arg(\hat{z})$. Finally, we have the correction of the interface

$$\hat{\eta}(\hat{x}) = \frac{B}{\beta^2 \bar{\rho}} \hat{x}^{3-\frac{1}{\beta}} \sin\left[(1 - \frac{1}{\beta}) \eta_0 \hat{x}^{-1} + (4 - \frac{1}{\beta}) \frac{\pi}{2} \right], \quad \text{as } \hat{x} \to 0. \tag{3.6.40}$$

An example of the shape of the interface $\hat{\eta}(\hat{x})$ is shown in Figure 3.8 for $\eta_0 = 0.5$, $\beta = 0.8$, $\bar{\rho} = 10$, where the bold black line represents the plate, and the blue curve is the free surface. Similar to the inner solutions of the problem in [64], the small oscillations can be observed near the intersection point in the interface and there is a singularity at the intersection point when $\hat{x} = 0$. In addition, the interface is always perpendicular to the plate.

However, since the solution (3.6.39) is a local solution in the inner region as

$\hat{R} \to 0$ instead of the asymptotic inner solution, the value of B and the composite asymptotic solutions for the whole problem (3.2.2)-(3.2.7) cannot be obtained by combining (3.6.39) and the outer solutions.

Since $0 < \beta_0 < 1$, we have $1 - \frac{1}{\beta} > 0$. Thus, from (3.6.39), it shows that $\Phi(\hat{R}, \hat{\Theta}) = o(1)$ as $\hat{R} \to 0$ uniformly for $\hat{\Theta} \in \left(-\frac{\pi}{2}, 0\right)$ requires $\eta_0 > 0$. The value of η_0 can be determined by numerical solutions, and it can be investigated in the future.

3.7 Conclusion

In this chapter, we have investigated the two-fluid dam-break problem by analysing the behaviour of the interface between two immiscible, ideal fluids. The new asymptotic solutions in the outer region are found when time t is small. Initially, the fluids stay at rest in a channel, and the interface has an angle α with the horizontal. We first solve this problem for the fluid with larger density in the outer region as $t \to 0^+$ using eigenfunction expansions and the Plemelj formula with the periodic extension of the interface. The local solutions for the limiting case when the density difference $\bar{\rho}$ is very small have also been found. The numerical results compared with the asymptotic and local solutions indicate a singularity in the interface around the intersection point between the interface and the solid upper boundary.

The inner-region problem is then introduced, where the local solution of the inner-region problem has the same formulation as that of the single fluid/solid interaction problem with an accelerating problem in the inner region [64]. The local form indicates that the interface is perpendicular to the solid boundary, and there are small oscillations around the intersection point. The inner problem is very hard to solve numerically by finite element method, but it may be possible to apply the shape-Newton method in the future.

Chapter 4

The Initial Stage of Solid/Two Fluid Interaction Problem with an Inclined Accelerating Plate

4.1 Introduction

Solid/fluid interaction problems arise in many real-world applications where a fluid flow interacts with a solid moving object. Examples of such problems include a ship moving through the ocean, where the bow creates splashing. Investigating the effects of these phenomena is crucial to the design of ships, as they can significantly impact the performance and stability of the vessel (see e.g. [95]).

Over the past few decades, there have been many investigations into the two-dimensional irrotational flow generated by a constant acceleration of a vertical plate towards an inviscid, incompressible fluid. A review of relevant studies can be found in Section 1.1.1.

The fluid/solid interaction problem is further studied using an impulsively moving plate. The situation considered is when a plate suddenly starts moving with a small constant velocity towards an inviscid, incompressible fluid initially at rest.

Greenhow and Lin [36] perform experiments on such a problem and take a series of pictures of how the shape of the flow behaviour. The water rises up to the wavemaker, and a jet is observed from the intersection point of the free surface and the wavemaker. Compared with the theoretical leading-order solutions obtained by Peregrine [66], great agreement is shown except around the intersection point, where Peregrine's solution shows the logarithmic singularity. Needham et al. [63] use a similar method in [64] by expansions in small time. An inner-inner region is introduced to resolve the singularity in the inner solution at the point where the free surface meets the plate. The boundary value problem in the inner-inner region is also solved numerically by the boundary integral method. However, Roberts [70] considers expansion in the amplitude of the motion instead of expansion in time to avoid the singularity at the intersection point, and the shape of the free surface close to the intersection point is perpendicular to the plate with small rapid oscillations.

It is worth noting that wedge-entry problems, which are used as the models of ship slamming, are also related to the solid/fluid interaction problem. Such problems are constructed as a two-dimensional solid plate with an angle α entering a fluid that is initially stationary, and their solutions are self-similar in the jet region close to the plate edges (see, e.g. [41, 45, 46, 76, 93, 94, 102]).

In this chapter, we extend the solid/fluid interaction problem with an inclined accelerating plate in [64] to the solid/two-fluid interaction problem where an inclined accelerating plate moves towards two layers of immiscible, inviscid, and incompressible fluids which are initially at rest. We notice that its local problem has the same formulation as the two-fluid dam-break problem in Chapter 3, implying that the approach to solving this problem is similar. To investigate the behaviour of the interface between the fluids, we find the solutions at the initial stage in the outer region using eigenfunction expansion and the Plemelj formula.

The outline of this chapter is as follows. First, the problem is formulated in section 4.2. Then, the solutions in the outer region using small-time expansion will

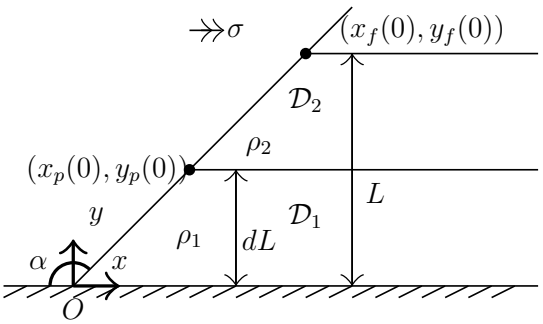

Figure 4.1: *The sketch of two fluids with different densities with an inclined plated at* $y = -\tan\alpha x$.

be solved in 4.3. The asymptotic solutions using eigenfunction expansions near the intersection point where the interface meets the accelerating plate are derived in section 4.3.1. The outer-region solutions based on the Plemelj formula are shown in section 4.3.2. The solutions using the Plemelj formula are evaluated by Gaussian quadrature in a truncated domain and are compared with the eigensolutions in 4.4, where a singularity appears at the contact point. Finally, in section 4.5, to resolve the singularity, an inner-region problem is formulated and its local solution is derived following the same method as in section 3.6.

4.2 Governing equations

We consider two layers of immiscible, inviscid and incompressible fluid with different densities initially lying at rest above a horizontal bed. There is an inclined plate moving towards the fluids with a constant acceleration $\sigma > 0$, which has an angle $\alpha > \frac{\pi}{2}$ with the horizontal bed. As the sketch shown in Figure 4.1, the intersection point between the moving plate and the bed is fixed as the origin, and the Cartesian coordinate system is defined by x axis pointing horizontally into the fluid layer and y axis pointing vertically up. The region $\mathcal{D}_2$ occupied by fluid 2 of lower density ρ_2 with velocity potential $\phi_2(x, y, t)$ lies above the region $\mathcal{D}_1$, which is occupied by fluid 1 of density ρ_1 with velocity potential $\phi_1(x, y, t)$. The initial free surface of this flow is located at $y = L$, and the location of the interface between two fluids is denoted

by $y = \eta(x,t)$ whose initial displacement is at $y = dL$ where the constant $d < 1$. We now introduce dimensionless variables and dimensionless density difference

$$x' = \tfrac{x}{L}, \quad y' = \tfrac{y}{L}, \quad \eta' = \tfrac{\eta}{L}, \quad \phi_i = \tfrac{\phi_i'}{L}\sqrt{gL}, \quad t' = t\sqrt{\tfrac{g}{L}}, \quad \sigma' = \tfrac{\sigma}{g}, \tag{4.2.1}$$

$$\bar{\rho} = \tfrac{\rho_1 - \rho_2}{\rho_2}, \tag{4.2.2}$$

with g the acceleration due to gravity. We drop primes for convenience of notation. To make the plate stationary, we introduce the coordinate $\bar{x}$ defined by $\bar{x} = x - s(t)$, where $s = \frac{1}{2}\sigma t^2$ measures the distance of the movement of the plate in the (x,y)-plane. The interface is now at $y = \eta(\bar{x},t)$ such that the interface meets the plate at the intersection point $(x_p(t), y_p(t))$. The location of the free surface is denoted as $y = \eta_f(\bar{x},t)$, with $(x_f(t), y_f(t))$ being the contact point between the free surface and the plate. Now the domain can be defined as

$$\begin{aligned}
\mathcal{D}_1(t) &= \left\{ (\bar{x},y) \in \mathbb{R}^2 : \begin{cases} 0 < x \leq x_p(t), \quad -\bar{x}\tan\alpha < y < \eta(\bar{x},t), \\ x > x_p(t), \quad 0 < y < d; \end{cases} \right\}, \\
\mathcal{D}_2(t) &= \left\{ (\bar{x},y) \in \mathbb{R}^2 : \begin{cases} x_p(t) < x \leq x_f(t), \quad -x_p(t)\tan\alpha < y < y_p(t), \\ x > x_f(t), d < y < \eta_f(t). \end{cases} \right\}
\end{aligned}$$

The governing equations and boundary conditions are

$$\nabla^2 \phi_i = 0, \quad (\bar{x}, y) \in \mathcal{D}_i(t), \quad t > 0; \tag{4.2.3}$$

$$\frac{\partial \phi_1}{\partial y} = 0, \quad \text{at } y = 0; \tag{4.2.4}$$

$$\mathbf{n} \cdot \nabla \phi_i = \sigma t \sin \alpha, \quad \text{at } y = -\bar{x} \tan \alpha; \tag{4.2.5}$$

$$\phi_2 = 0, \quad \text{at } y = \eta_f(\bar{x}, t); \tag{4.2.6}$$

$$\eta_t + (\phi_{i\bar{x}} - \sigma t)\eta_{\bar{x}} - \phi_{iy} = 0, \quad \text{at } y = \eta(\bar{x}, t); \tag{4.2.7}$$

$$\begin{gathered}(1+\bar{\rho})(\tfrac{\partial \phi_1}{\partial t} - \sigma t \phi_{1\bar{x}} + \tfrac{1}{2} \mid \nabla \phi_1 \mid^2) - (\tfrac{\partial \phi_2}{\partial t} - \sigma t \phi_{2\bar{x}} + \tfrac{1}{2} \mid \nabla \phi_2 \mid^2) = -\bar{\rho} y, \\ \text{at } y = \eta(\bar{x}, t),\end{gathered} \tag{4.2.8}$$

for $i = 1, 2$ where $\nabla = (\frac{\partial}{\partial \bar{x}}, \frac{\partial}{\partial y})$ and $\mathbf{n} = (\sin \alpha, \cos \alpha)$ is the unit normal to the plate pointing into the flow. In addition, we have the initial condition

$$\phi_i(\bar{x}, y, 0) = 0, \quad (\bar{x}, y) \in \mathcal{D}_i; \tag{4.2.9}$$

$$\eta(\bar{x}, 0) = d, \quad \bar{x} \geq -d \cot \alpha. \tag{4.2.10}$$

In the following, we will find the asymptotic and numerical solutions for this problem as $t \to 0^+$. When $d \to 1$ or $\bar{\rho} \to \infty$, the fluid in $\mathcal{D}_2(t)$ is just a thin layer or with a very small density such that the upper layer of the fluid can be neglected in this problem, and thus the problem can be treated as the single fluid problem with an accelerating plate in [64]. Since we focus more on the interface between two layers of flow, we can ignore the free-boundary condition (4.2.6).

4.3 Asymptotic solution as $t \to 0^+$ in the outer region

We start with finding the solutions in an outer region in which $(\bar{x}, y) = O(1)$ as $t \to 0^+$. According to conditions (4.2.5), (4.2.7), and (4.2.8), the asymptotic solution in the outer region has the form that $\phi_i = O(t)$ and $\eta = O(t^2)$ as $t \to 0^+$. Hence, we introduce the asymptotic expansions

$$\phi_i(\bar{x}, y, t) = \sigma t \sin\alpha \bar{\phi}_i(\bar{x}, y) + O(t^2), i = 1, 2, \quad \eta(\bar{x}, t) = d + t^2 \bar{\eta}(\bar{x}) + O(t^3) \quad (4.3.1)$$

as $t \to 0^+$ in the outer region. At leading order, we obtain the boundary-value problem

$$\nabla^2 \bar{\phi}_i = 0, \quad (\bar{x}, y) \in \mathcal{D}_i; \quad (4.3.2)$$

$$\frac{\partial \bar{\phi}_1}{\partial y} = 0, \quad \text{at } y = 0; \quad (4.3.3)$$

$$\mathbf{n} \cdot \nabla \bar{\phi}_i = 1, \quad \text{at } y = -\bar{x} \tan\alpha; \quad (4.3.4)$$

$$\bar{\eta} = \tfrac{1}{2} \sigma \sin\alpha \bar{\phi}_{iy}, \quad \text{at } y = d; \quad (4.3.5)$$

$$\sigma \sin\alpha [(1 + \bar{\rho}) \bar{\phi}_1 - \bar{\phi}_2] = -\bar{\rho} d, \quad \text{at } y = d \quad (4.3.6)$$

for $i = 1, 2$.

To get rid of the constant term in the condition (4.3.6), we further define $\bar{\phi}_i(\bar{x}, y) = \hat{\phi}_i - \frac{d}{\sigma \sin\alpha}$ for $i = 1, 2$ such that the boundary-value problem for $\hat{\phi}_i$

is

$$\nabla^2 \hat{\phi}_i = 0, \quad (\bar{x}, y) \in \mathcal{D}_i; \tag{4.3.7}$$

$$\frac{\partial \hat{\phi}_1}{\partial y} = 0, \quad \text{at } y = 0; \tag{4.3.8}$$

$$\mathbf{n} \cdot \nabla \hat{\phi}_i = 1, \quad \text{at } y = -\bar{x} \tan \alpha; \tag{4.3.9}$$

$$\bar{\eta}(\bar{x}) = \tfrac{1}{2}\sigma \sin \alpha \hat{\phi}_{iy}, \quad \text{at } y = d; \tag{4.3.10}$$

$$(1 + \bar{\rho})\hat{\phi}_1 - \hat{\phi}_2 = 0, \quad \text{at } y = d. \tag{4.3.11}$$

4.3.1 Asymptotic solution in the outer region for $(\bar{x}, \bar{y}) \to 0^+$

The local problem near the intersection point between the moving plate and the interface in the outer region is the same as the two-fluid dam-break problem in the outer region in Chapter 3. To see this, the coordinates $(\bar{x}, y)$ need to be shifted by introducing the new coordinates $(\tilde{x}, \tilde{y}) = (\bar{x} + d \cot \alpha, y - d)$ such that the origin is then at the intersection point of the interface and the accelerating plate. We further introduce $\hat{\phi}_i = \tilde{\phi}_i + \Phi$, where Φ is the solution for the single fluid problem with an inclined plate in [64]. The boundary value problem (4.3.7)-(4.3.11) become

$$\tilde{\nabla}^2 \tilde{\phi}_i = 0, \quad (\tilde{x}, \tilde{y}) \in \mathcal{D}_i; \tag{4.3.12}$$

$$\frac{\partial \tilde{\phi}_1}{\partial \tilde{y}} = 0, \quad \text{at } \tilde{y} = -d; \tag{4.3.13}$$

$$\tilde{\mathbf{n}} \cdot \nabla \tilde{\phi}_i = 0, \quad \text{at } \tilde{y} = -\tilde{x} \tan \alpha; \tag{4.3.14}$$

$$\bar{\eta}(\tilde{x}) = \tfrac{1}{2}\sigma \sin \alpha \left(\tilde{\phi}_{i\tilde{y}} + \Phi_{\tilde{y}} \right), \quad \text{at } \tilde{y} = 0; \tag{4.3.15}$$

$$(1 + \bar{\rho})\tilde{\phi}_1 - \tilde{\phi}_2 = -\bar{\rho}\Phi, \quad \text{at } \tilde{y} = 0, \tag{4.3.16}$$

for $i = 1, 2$, where $\tilde{\nabla} = \left(\frac{\partial}{\partial \tilde{x}}, \frac{\partial}{\partial \tilde{y}} \right)$ and $\tilde{\boldsymbol{n}}$ is the unit normal vector to the plate pointing outward the flow.

According to [64], the asymptotic expansion for Φ with real constants $\tilde{A}_n$ is

$$\Phi(\tilde{r},\tilde{\theta}) = \frac{\tilde{r}\sin\tilde{\theta}}{\cos\alpha} + \sum_{n=0}^{\infty} \tilde{A}_n \tilde{r}^{\left(n+\frac{1}{2}\right)\frac{\pi}{\alpha}} \sin\left[\left(n+\frac{1}{2}\right)\frac{\pi\tilde{\theta}}{\alpha}\right], \quad \text{as } \tilde{r} \to 0, \tag{4.3.17}$$

where $\tilde{x} = \tilde{r}\cos\tilde{\theta}$ and $\tilde{y} = \tilde{r}\sin\tilde{\theta}$. The interface is now at $\tilde{\theta} = 0$ in the outer region problem as $\tilde{r} \to 0$. Hence, following

$$\Phi(\tilde{r}, 0) = 0,$$

we obtain the Bernoulli condition (4.3.16) and the kinematic condition (4.3.15) on the interface as

$$\bar{\eta}(\tilde{x}) = \frac{1}{2}\sin\alpha\left(\tilde{\phi}_{i\tilde{y}} + \Phi_{\tilde{y}}\right), \quad \text{at } \tilde{y} = 0; \tag{4.3.18}$$

$$(1+\bar{\rho})\,\tilde{\phi}_1 - \tilde{\phi}_2 = 0, \quad \text{at } \tilde{y} = 0, \quad \text{as } \tilde{r} \to 0. \tag{4.3.19}$$

By rotating the coordinate system counterclockwise with an angle α such that the moving plate is now horizontal, we introduce the coordinates (X, Y) and the boundary value problem in the outer region is the same as the two fluid dam-break problem in the outer region of the upper contact point. Hence, we have the same asymptotic form as (3.3.6)

$$\tilde{\phi}_1(R,\Theta) \sim A_1 R^{\beta_0}\cos\beta_0\Theta, \quad \tilde{\phi}_2(R,\Theta) \sim A_2 R^{\beta_0}\cos\beta_0\left(\pi - \Theta\right), \tag{4.3.20}$$

where $X = R\cos\Theta$ and $Y = R\sin\Theta$. The power β_0 satisfies the condition (3.3.9)

$$\frac{\tan\beta_0\alpha}{1+\bar{\rho}} = -\tan\beta_0(\pi - \alpha), \tag{4.3.21}$$

such that $\beta_0 < 1$ for $\alpha \in \left(\frac{\pi}{2}, \pi\right)$. Hence,

$$\hat{\phi}_i(R,\Theta) \sim \tilde{\phi}_i(R,\Theta), \quad \text{as } R \to 0^+. \tag{4.3.22}$$

To analyse how depth d of the bottom fluid affects the solutions, we consider the limit $d \to 1$ such that the fluid in $\mathcal{D}_2$ is just a thin layer at the top. In this case, the outer region problem for $\hat{\phi}_1$ can be solved as the solid/single fluid problem with an inclined accelerating plate in [64]. Considering the domain shown in Figure 4.1 with the coordinate system $(\tilde{x}, \tilde{y})$ as introduced at the beginning of this subsection, we have $\hat{\phi}_1(\tilde{r}, \tilde{\theta}) = O\left(\Phi(\tilde{r}, \tilde{\theta})\right)$ where

$$\Phi(\tilde{r}, \tilde{\theta}) \sim \tilde{r}^{\frac{\pi}{2\alpha}} \cos\left(\frac{\pi}{2\alpha}\tilde{\theta}\right), \quad \text{as } \tilde{r} \to 0^+.$$

We introduce the scaled polar coordinates $\hat{r} = \frac{\tilde{r}}{1-d}$ as $d \to 1$. Then, the scaled asymptotic expansion for $\hat{\phi}_1$ and $\hat{\phi}_2$ in this inner region problem are

$$\hat{\phi}_1 \sim (1-d)^{\frac{\pi}{2\alpha}} \hat{\phi}_{10}, \quad \hat{\phi}_2 \sim (1-d)^{\frac{\pi}{2\alpha}} \hat{\phi}_{20}. \tag{4.3.23}$$

with the matching conditions

$$\hat{\phi}_{10} \sim A\hat{r}^{\frac{\pi}{2\alpha}} \cos\left(\frac{\pi}{2\alpha}\tilde{\theta}\right), \quad \hat{\phi}_{20} \sim A'\hat{r}^{\frac{\pi}{2\alpha}} \cos\left[\frac{\pi}{2\alpha}(\pi - \tilde{\theta})\right] \quad \text{as } \hat{r} \to \infty, \tag{4.3.24}$$

where A and A' are some constants.

Combining the scaled inner-region solution (4.3.23) with (4.3.20) and (4.3.24), we could have

$$A_1 \sim (1-d)^{\frac{\pi}{2\alpha} - \beta_0} A. \tag{4.3.25}$$

The other situation is considering the bottom layer fluid with depth $d \to 0$ such that there is a very thin layer of fluid at the bottom. This is different from the single fluid problem since the fluid in $\mathcal{D}_1$ cannot be treated as the solid horizontal bed, but we still have

$$A_1 \sim A_0 d^c, \tag{4.3.26}$$

where the constants A_0 and c can be determined numerically. However, as $d \to 0$,

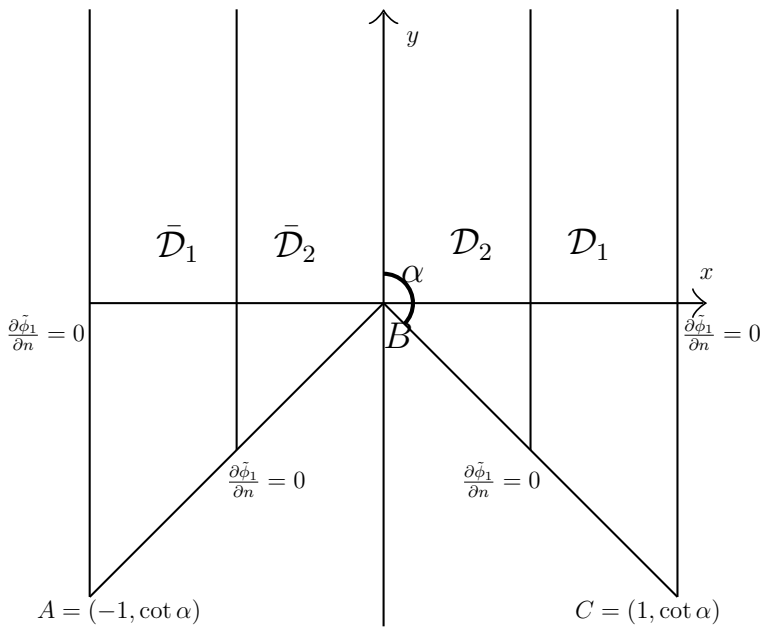

Figure 4.2: *The domain of solution of the boundary-value problem* (4.3.27)-(4.3.31).

the region $\mathcal{D}_1$ would be too small to find the numerical solution for $\hat{\phi}_1$. Hence, it would be difficult to find c.

It follows from the asymptotic solution (4.3.18) and (4.3.20) that as $R \to 0^+$, there is a singularity in $\bar{\eta}$ for $\alpha \in (\frac{\pi}{2}, \pi)$. This can also be proven by the numerical results found using the Plemelj formula. The behaviour of the singularity in $\bar{\eta}$ requires us to introduce an inner region such that $(\bar{x}, y) = o(t)$ as $t \to 0^+$, which will explain the details in the next section.

4.3.2 Solution using Plemelj Formula

We move back to the original domain as shown in Figure 4.1, and first anti-reflect the whole region with respect to the free surface and rotate through $\frac{\pi}{2}$ as shown in Figure 4.2. The reflection of domain $\mathcal{D}_1$ and $\mathcal{D}_2$ on the right handside of $y-$axis is denoted as $\bar{\mathcal{D}}_1$ and $\bar{\mathcal{D}}_2$ respectively. According to Schwarz reflection principle [16], since $\tilde{\phi}_i$ for $i = 1, 2$ is analytical and continuous, the corresponding results $\tilde{\phi}_i$ for $i = 1, 2$ in $\bar{\mathcal{D}}_1$ and $\bar{\mathcal{D}}_2$ are analytical and continuous as well. Thus, $\tilde{\phi}_2$ is analytic

and continuous in $\mathcal{D}_2 \bigcup \bar{\mathcal{D}}_2$. The boundary-value problem for $\tilde{\phi}_i$ is now given by

$$\nabla^2 \tilde{\phi}_i = 0, \quad (\bar{x}, y) \in \mathcal{D}_i; \tag{4.3.27}$$

$$\frac{\partial \tilde{\phi}_1}{\partial y} = 0, \quad \text{at } \bar{x} = \pm 1; \tag{4.3.28}$$

$$\mathbf{n} \cdot \nabla \tilde{\phi}_i = 0, \quad \text{at } y = \bar{x} \cot \alpha, \quad 0 < \bar{x} \leq 1; \tag{4.3.29}$$

$$\mathbf{n} \cdot \nabla \tilde{\phi}_i = 0, \quad \text{at } y = -\bar{x} \cot \alpha, \quad -1 \leq \bar{x} < 0; \tag{4.3.30}$$

$$(1 + \bar{\rho}) \tilde{\phi}_1 - \tilde{\phi}_2 = -\bar{\rho} \Phi, \quad \text{at } \bar{x} = \pm d. \tag{4.3.31}$$

The kinematic boundary conditions (4.3.29) and (4.3.30) are both zero such that we could apply the Plemelj formula to solve this problem. Before we solve the complex integral in the Plemelj formula, we must first find a suitable contour for this problem.

We can use Schwarz-Christoffel transformation [1] to map the domain of the solution of (4.3.27)-(4.3.31) from the $z(\equiv x + \mathrm{i}y)$-plane to the $w(\equiv u + \mathrm{i}v)$-plane:

$$z = \frac{2e^{\mathrm{i}(\frac{\pi}{2} - \alpha)}}{\pi} \int_0^w s^{\frac{2\alpha}{\pi} - 1} (1 - s^2)^{-\frac{\alpha}{\pi}} ds. \tag{4.3.32}$$

Note that the coefficient in [64] is incorrect, but we correct it in this chapter. We map the origin in z-plane to the origin in w-plane, and the corner points A to $v = -1$ and C to $v = 1$, respectively.

To apply the Plemelj formula, we further reflect the domain with u-axis as shown in Figure 4.3. The solid curves represent the interface after conformal mapping such that they are bounded by $|v| = 1$ as $|u| \to +\infty$, while the dash curves with the radius $R \to +\infty$ are used to truncate the domain for the calculation. We define the complex potential $\Phi_i(z) = \tilde{\phi}_i + \mathrm{i}\psi_i$ in $\mathcal{D}_i$, where ψ_i represents the stream function. The Plemelj formula presented in Theorem 2.4 can now be applied to solve this

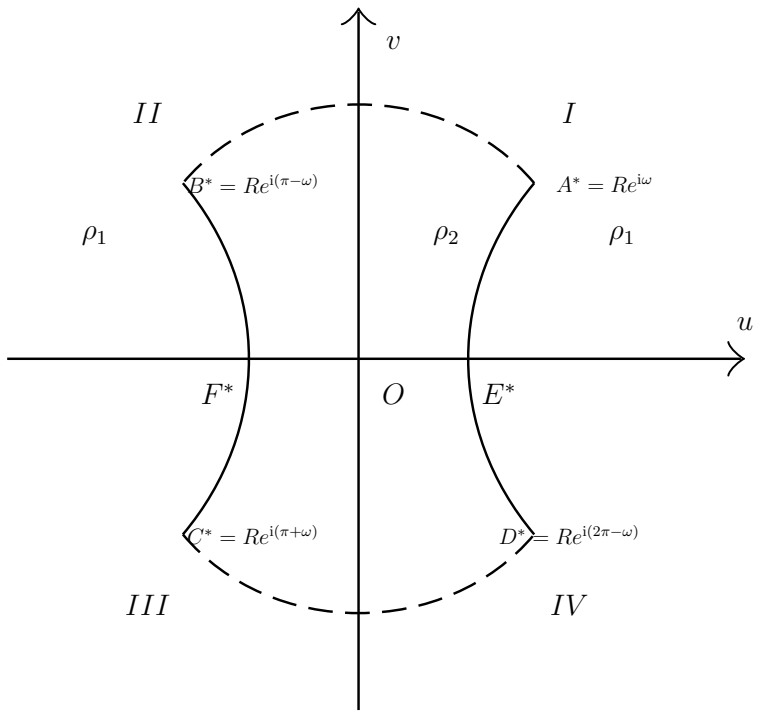

Figure 4.3: *The sketch of the interface in w-plane. The solid curves are the interfaces after conformal mapping, and the dash curves are the arcs as part of the circle $u^2+v^2 = R^2$.*

problem for Φ_1 and Φ_2 as

$$\Phi_1(s) = \frac{1}{2}\mu(s) + \frac{1}{2\pi\mathrm{i}}\fint_{-\infty}^{\infty} \frac{\mu(s')}{w(s')-w(s)}\frac{dw}{ds}(s')ds', \tag{4.3.33}$$

$$\Phi_2(s) = -\frac{1}{2}\mu(s) + \frac{1}{2\pi\mathrm{i}}\fint_{-\infty}^{\infty} \frac{\mu(s')}{w(s')-w(s)}\frac{dw}{ds}(s')ds', \tag{4.3.34}$$

where $\mu(s) = \tilde{\phi}_1(s) - \tilde{\phi}_2(s)$, and s is the arclength of the point at $w(s)$.

Thus, we can obtain the Plemelj formula for $\tilde{\phi}_1$ and $\tilde{\phi}_2$ as

$$\tilde{\phi}_1(s) = \frac{1}{2}\left(\tilde{\phi}_1(s) - \tilde{\phi}_2(s)\right) + Re\left(\frac{1}{2\pi\mathrm{i}}\fint \frac{\tilde{\phi}_1(s') - \tilde{\phi}_2(s')}{w(s')-w(s)}\frac{dw}{ds'}ds'\right), \tag{4.3.35}$$

$$\tilde{\phi}_2(s) = -\frac{1}{2}\left(\tilde{\phi}_1(s) - \tilde{\phi}_2(s)\right) + Re\left(\frac{1}{2\pi\mathrm{i}}\fint \frac{\tilde{\phi}_1(s') - \tilde{\phi}_2(s')}{w(s')-w(s)}\frac{dw}{ds'}ds'\right). \tag{4.3.36}$$

According to (4.3.31), we have

$$\mu(s) \equiv \tilde{\phi}_1(s) - \tilde{\phi}_2(s) = -\bar{\rho}\left(\tilde{\phi}_1(s) + \Phi(s)\right). \tag{4.3.37}$$

In [64], by using the Fourier transform, the solution for the single fluid problem is

$$\Phi(u,v) = \frac{1}{\pi}\int_0^1 s^{\frac{2\alpha}{\pi}-1}(1-s^2)^{-\frac{\alpha}{\pi}} \log\left|\frac{(u-s)^2+v^2}{(u+s)^2+v^2}\right| ds, \tag{4.3.38}$$

where s represents the arc-length from the origin to the point at (u,v). On substitution from (4.3.37) into (4.3.35) to eliminate $\tilde{\phi}_2$, we obtain

$$\tilde{\phi}_1(s) = -\frac{\bar{\rho}}{2}\left(\Phi(s)+\tilde{\phi}_1(s)\right) + Re\left(\frac{1}{2\pi \mathrm{i}}\fint \frac{-\bar{\rho}\left(\Phi(s')+\tilde{\phi}_1(s')\right)}{(w(s')-w(s))}\frac{dw}{ds'}ds'\right). \tag{4.3.39}$$

Since $\hat{\phi}_1(s) = \tilde{\phi}_1 + \Phi(s)$, (4.3.39) can be rewritten as

$$\begin{aligned}\hat{\phi}_1(s) &= \Phi(s) - \frac{\bar{\rho}}{2}\hat{\phi}_1(s) + Re\left(\frac{1}{2\pi \mathrm{i}}\fint \frac{-\bar{\rho}\hat{\phi}_1(s')}{(w(s')-w(s))}\frac{dw}{dx'}ds'\right),\\ &= \frac{1}{1+\frac{\bar{\rho}}{2}}\left[\Phi(s) + Re\left(\frac{1}{2\pi \mathrm{i}}\fint \frac{-\bar{\rho}\hat{\phi}_1(s')}{(w(s')-w(s))}\frac{dw}{dx'}ds'\right)\right].\end{aligned} \tag{4.3.40}$$

4.4 Numerical results for the outer region problem

To evaluate the Plemelj formula, we consider the contour integral along the closed contour in the counter-clockwise direction as shown in Figure 4.3 with the points $A^* = Re^{\mathrm{i}\omega}, B^* = Re^{\mathrm{i}(\pi-\omega)}, C^* = Re^{\mathrm{i}(\pi+\omega)}$, and $D^* = Re^{\mathrm{i}(2\pi-\omega)}$ as $R \to 0$. The argument ω can be found numerically using (4.3.32). The dash lines in Figure 4.3 are the arc as part of the circle $u^2+v^2=R^2$. The formula for $\hat{\phi}_1(s)$

$$\hat{\phi}_1(s) = \frac{1}{1+\frac{\bar{\rho}}{2}}\left[\Phi(s) + Re\left(\frac{1}{2\pi \mathrm{i}}\fint \frac{-\bar{\rho}\hat{\phi}_1(s')}{(w(s')-w(s))}\frac{dw}{dx'}ds'\right)\right], \tag{4.4.1}$$

is evaluated along the closed contour with the counter-clockwise direction from point A^* to point D^*.

Solving (4.4.1) by Gaussian quadrature as a linear system, we can compare the

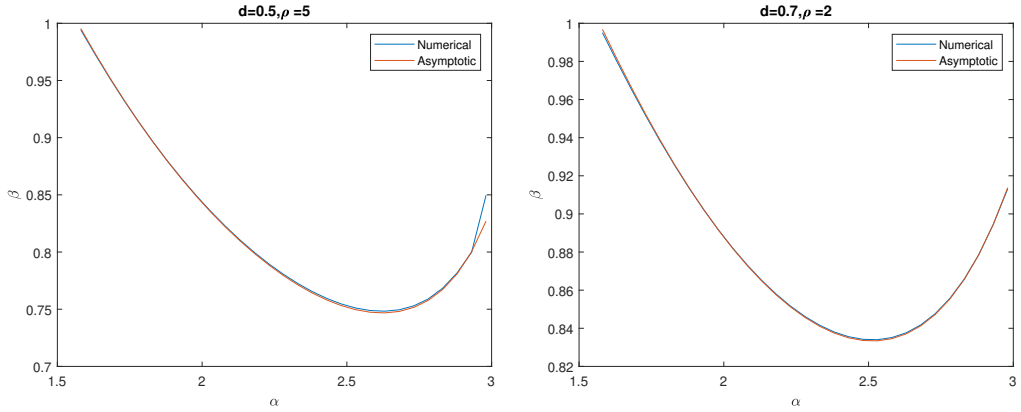

(a) *Numerical power compared with the asymptotic power for $d = 0.5$ and $\rho = 5$ with $\frac{\pi}{2} < \alpha < \pi$.*

(b) *Numerical power compared with the asymptotic power for $d = 0.7$ and $\rho = 2$ with $\frac{\pi}{2} < \alpha < \pi$.*

Figure 4.4: *The numerical power compared with asymptotic power for $d = 0.5$, $\rho = 5$ and $d = 0.7$, $\rho = 2$ against $\frac{\pi}{2} < \alpha < \pi$. The blue lines are the numerical coefficients, and the red curves are the asymptotic coefficients.*

leading order of the numerical results of $\hat{\phi}_1$ with β_0 satisfying (4.3.21). The power β of the leading order of the numerical results is found by fitting lines of $\log(\hat{\phi}_1)$ against $\log(r)$. Figure 4.4 shows the graphs of β obtained from numerical results compared with β_0 from the eigenvalue problem for the angle $\frac{\pi}{2} < \alpha < \pi$, in which the blue lines represent the numerical results while the red lines are for the asymptotic solutions. Figure 4.4a shows the results for $d = 0.5$, $\rho = 5$, and Figure 4.4b shows the results for $d = 0.7$, $\rho = 2$. The numerical solutions agree perfectly with the asymptotic solution, except for $\alpha \to \pi$ in Figure 4.4a due to the strong singularity as $r \to 0$ in β_0. The values of β are always lower than 1 as shown in Figure 4.4. Figure 4.5 shows the shape of the interface $\bar{\eta}$ scaled with respect to σ, where Figure 4.5a shows the results for $\alpha = 2.2$, $d = 0.5$ and $\rho = 2$, and Figure 4.5b shows the results for $\alpha = 2.5$, $d = 0.7$ and $\rho = 5$. Thus, the inner region problem is required to be resolved for $r \to 0$.

Figure 4.6 shows the log-log plots of the coefficient A_1 in terms of $\frac{1}{1-d}$ compared with the curve $O\left((1-d)^{\frac{\pi}{2\alpha}-\beta_0}\right)$ for different angles α to test condition (4.3.25), in which the blue lines represent the numerical results while the red lines show the asymptotic results. Figure 4.6a shows the results for $\alpha = 2.5$ and $\bar{\rho} = 5$, while

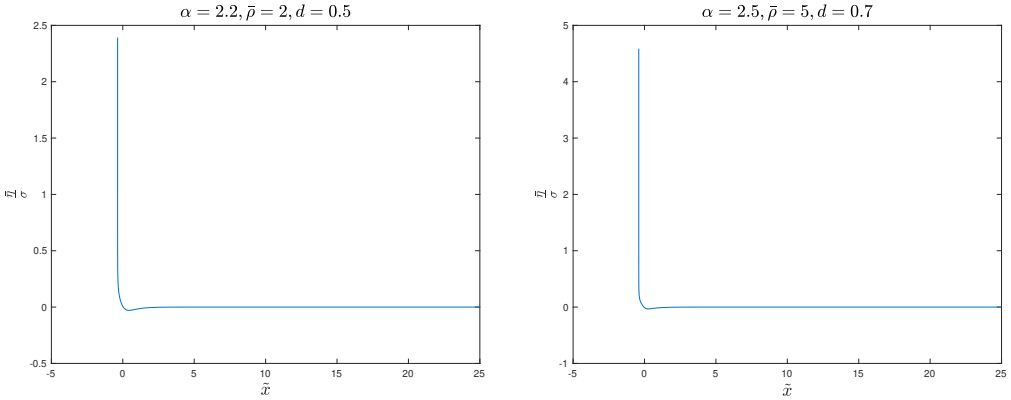

(a) *The elevation of the interface $\bar{\eta}$, scaled with respect to the acceleration σ, plotted against $\tilde{x}$ for $\alpha = 2.2$, $d = 0.5$ and $\rho = 2$.*

(b) *The elevation of the interface $\bar{\eta}$, scaled with respect to the acceleration σ, plotted against $\tilde{x}$ for $\alpha = 2.5$, $d = 0.7$ and $\rho = 5$.*

Figure 4.5: *Two examples of the shape of the interface $\bar{\eta}$ scaled with respect to σ, plotted against $\tilde{x}$ for the situation $\alpha = 2.2$, $d = 0.5$ and $\rho = 2$, and the situation for $\alpha = 2.5$, $d = 0.7$ and $\rho = 5$.*

Figure 4.6b shows the results for $\alpha = 2.2$ and $\bar{\rho} = 1$. In both figures, we can observe that even though the two curves are not consistent for small values of d, as $d \to 1$, the numerical results agree well with the condition (4.3.25).

Similarly, the log-log plots of the coefficient A_1 with respect to $\frac{1}{d}$ compared with the fitting curve are shown in Figure 4.7, where the blue lines represent the numerical results and the red lines show the fitting curves. Figure 4.7a shows the results for $\alpha = 2.5$ and $\bar{\rho} = 5$, while Figure 4.7b shows the results for $\alpha = 2.2$ and $\bar{\rho} = 1$. As $d \to 0$, the numerical results of $\hat{\phi}_1$ can be unstable due to the small region $\mathcal{D}_1$, where the disagreement appears especially in Figure 4.7a with larger angle α.

4.5 Inner region as $t \to 0^+$ for $\frac{\pi}{2} < \alpha < \pi$

Now we look into the inner region around the intersection point of the interface and the moving plate. We set $(x, y) = O(\mathcal{X}(t))$, with $\mathcal{X}(t) = o(1)$ as $t \to 0^+$, in the inner region. According to (3.3.1), the interface is now required to satisfy

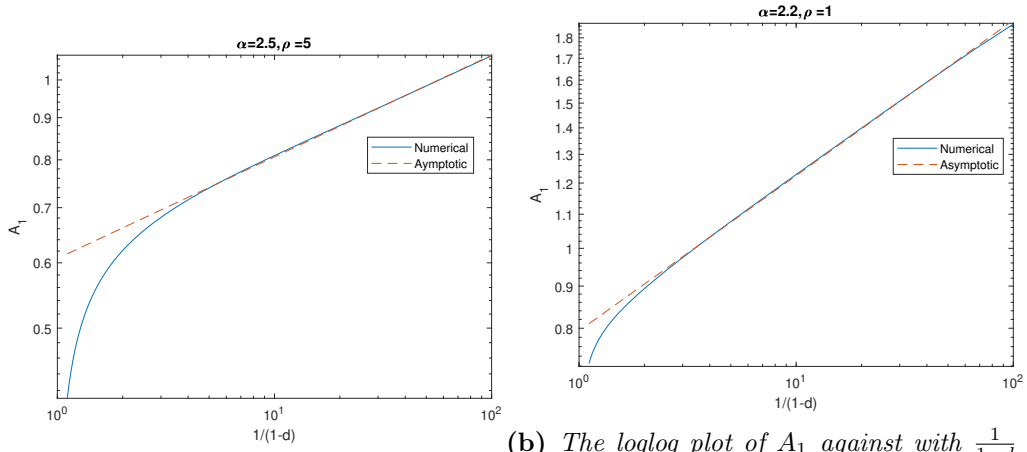

(a) *The loglog plot of A_1 against with $\frac{1}{1-d}$ for $\alpha = 2.5$ and $\bar{\rho} = 5$. The blue line is the numerical result, and the red line is the asymptotic result $\beta_0 - \frac{\pi}{2\alpha}$.*

(b) *The loglog plot of A_1 against with $\frac{1}{1-d}$ for $\alpha = 2.2$ and $\bar{\rho} = 1$. The blue line is is the numerical result, and the red line is the asymptotic result $\beta_0 - \frac{\pi}{2\alpha}$ in condition (4.3.25).*

Figure 4.6: *The loglog plot of A_1 against with $\frac{1}{1-d}$ for $\alpha = 2.5$, $\bar{\rho} = 5$ and $\alpha = 2.2$, $\bar{\rho} = 1$. The blue lines represent the numerical results, and the red lines represent the asymptotic results $\beta_0 - \frac{\pi}{2\alpha}$*

$y(x,t) = O\left(\mathcal{X}(t)\right)$ as $t \to 0^+$ in the inner region. It then follows from (4.3.5) that

$$\bar{\phi}_{iy} = O\left(r^{\beta_0 - 1}\right) \sim \mathcal{X}(t)^{\beta_0 - 1}, \quad \bar{\eta} \sim O(t^2 \mathcal{X}(t)^{\beta_0 - 1}) \quad \text{as } t \to 0^+.$$

Using (4.3.1), we have

$$\mathcal{X}(t) \sim O(t^2 \mathcal{X}(t)^{\beta_0 - 1})$$

which indicates that

$$\mathcal{X}(t) = O(t^{\gamma}) \quad \text{as } t \to 0^+, \tag{4.5.1}$$

where $\gamma = \frac{1}{1 - \frac{\beta_0}{2}}$.

We can now choose $\mathcal{X}(t) = t^{\gamma}$ without loss of generality. Hence, from (4.3.1) and (4.3.20), we have

$$\phi_i = O(t^{2\gamma - 1}) \quad \text{as } t \to 0^+ \tag{4.5.2}$$

in the inner region for $i = 1, 2$. We introduce the scaled inner coordinates $(\bar{X}, \bar{Y})$ by the transformation

$$\bar{x} = t^{\gamma} \bar{X}, y = t^{\gamma} \bar{Y} \tag{4.5.3}$$

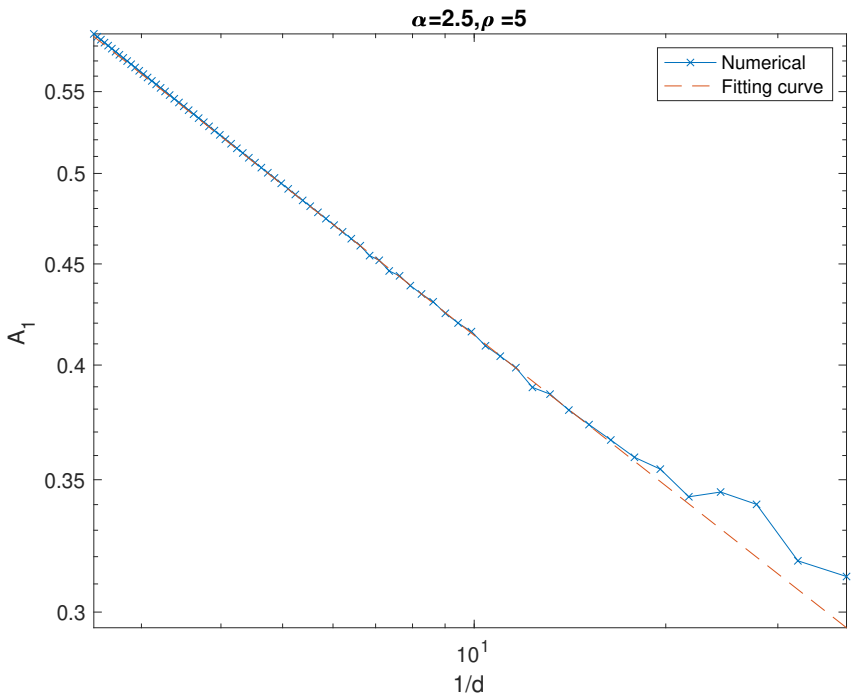

(a) *The loglog plot of A_1 against with $\frac{1}{d}$ for $\alpha = 2.5$ and $\bar{\rho} = 5$. The blue line is the numerical result, and the red line is the fitting curve.*

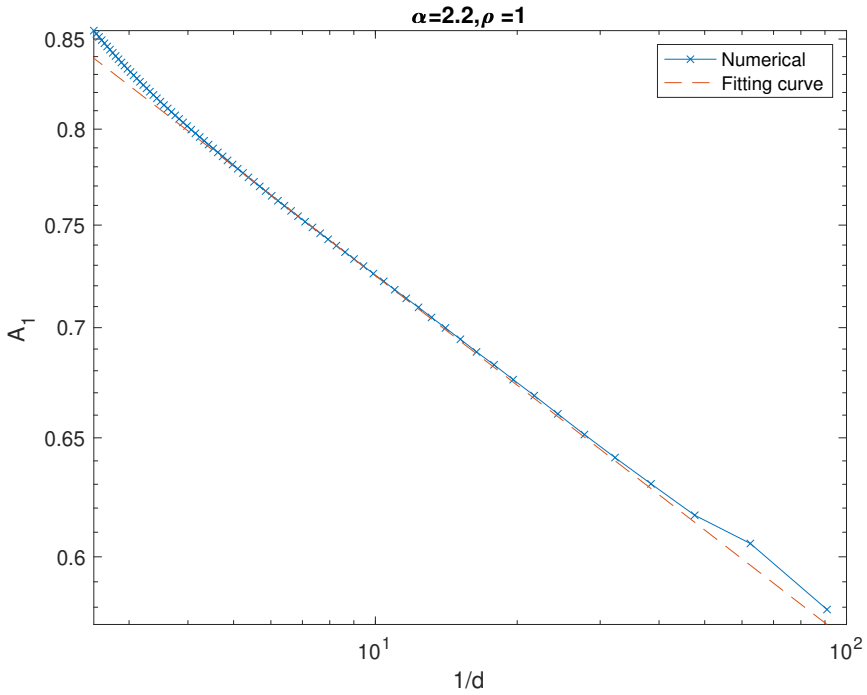

(b) *The loglog plot of A_1 against with $\frac{1}{d}$ for $\alpha = 2.2$ and $\bar{\rho} = 1$. The blue line is the numerical result, and the red line is the fitting curve.*

Figure 4.7: *The loglog plot of A_1 against with $\frac{1}{d}$ for $\alpha = 2.5$, $\bar{\rho} = 5$ and $\alpha = 2.2$, $\bar{\rho} = 1$. The blue lines represent the numerical results, and the red lines represent the fitting curve.*

with $(\bar{X}, \bar{Y}) = O(1)$ as $t \to 0^+$ in the inner region. The asymptotic solutions in the inner region have the form

$$\phi_i(\bar{X}, \bar{Y}, t) = t^{2\gamma-1}\tilde{\phi}_{i0}(\bar{X}, \bar{Y}) + o(t^{2\gamma-1}) \quad \text{for } i = 1, 2, \quad \eta(\bar{X}, t) = t^{\gamma}\eta_0(\bar{X}) + o(t^{\gamma}), \tag{4.5.4}$$

as $t \to 0^+$ in the inner region. After substitution into (4.2.3)-(4.2.8), the full BVP in terms of inner coordinates in the leading order is

$$\bar{\nabla}^2\tilde{\phi}_{i0} = 0 \quad \text{in } \mathcal{D}_i, \tag{4.5.5}$$

$$\bar{\nabla}\tilde{\phi}_{i0} \cdot \bar{\mathbf{n}} = 0, \quad \bar{Y} = 0, \tag{4.5.6}$$

$$\begin{gathered}(2\gamma - 1)\left[(1+\bar{\rho})\,\tilde{\phi}_{10} - \tilde{\phi}_{20}\right] - \gamma\,(1+\bar{\rho})\left(\bar{X}\tilde{\phi}_{10,\bar{X}} + \eta_0\tilde{\phi}_{10,\bar{Y}}\right) \\ -\gamma\left(\bar{X}\tilde{\phi}_{20,\bar{X}} + \eta_0\tilde{\phi}_{20,\bar{Y}}\right) + \tfrac{1}{2}\left[(1+\bar{\rho})\left|\bar{\nabla}\tilde{\phi}_{10}\right|^2 - \left|\bar{\nabla}\tilde{\phi}_{20}\right|^2\right] = 0, \quad \bar{Y} = \eta_0(\bar{X}),\end{gathered} \tag{4.5.7}$$

$$\gamma\eta_0 + (\tilde{\phi}_{i0,\bar{X}} - \gamma\bar{X})\eta_{0\bar{X}} - \tilde{\phi}_{i0,\bar{Y}} = 0, \quad \bar{Y} = \eta_0(\bar{X}), \tag{4.5.8}$$

$$\tilde{\phi}_{10} \sim A_1\sigma\sin\alpha\bar{R}^{\beta_0}\cos(\beta_0\bar{\theta}) \quad \text{as } \bar{R} \to \infty, \tag{4.5.9}$$

$$\tilde{\phi}_{20} \sim A_2\sigma\sin\alpha\bar{R}^{\beta_0}\cos(\beta_0(\pi - \bar{\theta})) \quad \text{as } \bar{R} \to \infty, \tag{4.5.10}$$

where $\bar{\nabla} = (\frac{\partial}{\partial\bar{X}}, \frac{\partial}{\partial\bar{Y}})$, $(\bar{X}, \bar{Y}) = (\bar{R}\cos\bar{\theta}, \bar{R}\sin\bar{\theta})$, and $\bar{\boldsymbol{n}}$ is the unit normal vector to the moving plate pointing outwards the flow in the inner coordinates. The far-field conditions (4.5.9) and (4.5.10) are obtained from Van Dyke's matching principle [91] by matching between the asymptotic expansion (4.5.4) in the inner region and the asymptotic solution (4.3.20) in the outer region.

We can scale A_1 and $\sigma\sin\alpha$ out of the problem by introducing

$$\bar{X} = l\bar{X}^*, \quad \bar{Y} = l\bar{Y}^*, \quad \eta_0 = l\eta_0^*, \quad \bar{R} = l\bar{R}^*, \quad \tilde{\phi}_{i0} = l^2\tilde{\phi}_{i0}^*, \quad \text{for } i = 1, 2, \tag{4.5.11}$$

where $l = (-A_1)^{\frac{1}{2}\gamma}$ as $A_1 < 0$, and we drop the asterisk for convenience.

On substitution from (4.5.11) into (4.5.5)-(4.5.10), the BVP in the inner region

is then

$$\bar{\nabla}^2 \tilde{\phi}_{i0} = 0, \quad \text{in } \mathcal{D}_i, \tag{4.5.12}$$

$$\bar{\nabla}\tilde{\phi}_{i0} \cdot \tilde{\mathbf{n}} = 0, \quad \bar{Y} = 0, \tag{4.5.13}$$

$$\begin{aligned}(1+\bar{\rho})\left[(2\gamma-1)\tilde{\phi}_{10} - \gamma\left(\bar{X}\tilde{\phi}_{10,\bar{X}} + \eta_0\tilde{\phi}_{10,\bar{Y}}\right) + \tfrac{1}{2}\left|\bar{\nabla}\tilde{\phi}_{10}\right|^2\right] \\ -\left[(2\gamma-1)\tilde{\phi}_{20} - \gamma\left(\bar{X}\tilde{\phi}_{20,\bar{X}} + \eta_0\tilde{\phi}_{20,\bar{Y}}\right) + \tfrac{1}{2}\left|\bar{\nabla}\tilde{\phi}_{20}\right|^2\right] = 0, \quad \bar{Y} = \eta_0(\bar{X}),\end{aligned} \tag{4.5.14}$$

$$\gamma\eta_0 + (\tilde{\phi}_{i0,\bar{X}} - \gamma\bar{X})\eta_{0\bar{X}} - \tilde{\phi}_{i0,\bar{Y}} = 0, \quad \bar{Y} = \eta_0(\bar{X}), \tag{4.5.15}$$

$$\tilde{\phi}_{10} \sim \bar{R}^{\beta_0}\cos\beta_0\bar{\theta} \quad \text{as } \bar{R} \to \infty, \tag{4.5.16}$$

$$\tilde{\phi}_{20} \sim \tfrac{A_2}{A_1}\bar{R}^{\beta_0}\cos\left(\beta_0\left(\pi - \bar{\theta}\right)\right) \quad \text{as } \bar{R} \to \infty. \tag{4.5.17}$$

This BVP in the inner region is the same as the two-fluid dam break problem in the inner region in Chapter 3, and we can use the same method to find the local form of the solution. Now we rotate the coordinates counter-clockwise through an angle $\alpha - \pi/2$ such that the plate lies on the new vertical axis $\hat{y}$ and the new horizontal axis $\hat{x}$ is in a direction normal to the plate. We denote the interface by $\hat{y} = \hat{\eta}(\hat{x})$ for $\hat{x} \geq 0$. The local problem (4.5.12)-(4.5.15) has the exact solution in the form

$$\hat{\eta}(\hat{x}) = \hat{\eta}_0, \quad \hat{x} \geq 0, \tag{4.5.18}$$

$$\tilde{\phi}_{10} = \gamma\hat{\eta}_0\hat{y} + \hat{\phi}_{10}, \quad \hat{x} \geq 0, \hat{y} \leq \eta_0, \tag{4.5.19}$$

$$\tilde{\phi}_{20} = \gamma\hat{\eta}_0\hat{y} + \hat{\phi}_{20}, \quad \hat{x} \geq 0, \hat{y} \leq \eta_0, \tag{4.5.20}$$

where $\hat{\eta}_0$, $\hat{\phi}_{10}$, $\hat{\phi}_{20}$ are constants satisfying $(1+\bar{\rho})\hat{\phi}_{10} - \hat{\phi}_{20} = \frac{\bar{\rho}\gamma\eta_0^2(1-\frac{3}{2}\gamma)}{2\gamma-1}$ from the Bernoulli condition (4.5.14) in the inner region. However, this solution does not satisfy the far-field condition (4.5.16) and (4.5.17), but it shows the leading order form of the solution to the problem (4.5.12)-(4.5.15) in the inner region as $\hat{x} \to 0$.

Now the corrections to (4.5.18)-(4.5.20) as $\hat{x} \to 0$ is considered by introducing

$\tilde{\eta}$, $\hat{\phi}_{11}$, and $\hat{\phi}_{21}$ such that

$$\hat{\eta}(\hat{x}) = \hat{\eta}_0 + \tilde{\eta}(\hat{x}), \quad \hat{x} \geq 0, \hat{y} \leq \hat{\eta}_0, \tag{4.5.21}$$

$$\tilde{\phi}_{10}(\hat{x}, \hat{y}) = \left[\gamma \hat{\eta}_0 \hat{y} + \hat{\phi}_{10}\right] + \hat{\phi}_{11}(\hat{x}, \hat{y}), \quad \hat{x} \geq 0, \hat{y} \leq \hat{\eta}_0 \tag{4.5.22}$$

$$\tilde{\phi}_{20}(\hat{x}, \hat{y}) = \left[\gamma \hat{\eta}_0 \hat{y} + \hat{\phi}_{20}\right] + \hat{\phi}_{21}(\hat{x}, \hat{y}), \quad \hat{x} \geq 0, \hat{y} \leq \hat{\eta}_0 \tag{4.5.23}$$

where $\tilde{\eta}(\hat{x}) = o(1)$ as $\hat{x} \to 0$, and $\hat{\phi}_{i1}(\hat{x}, \hat{y}) = o(1)$ as $(\hat{x}, \hat{y}) \to (0, \hat{\eta}_0)$. For convenience, we introduce the shifted coordinate

$$\bar{y} = \hat{y} - \hat{\eta}_0.$$

On substitution from (4.5.21)-(4.5.23) into (4.5.12)-(4.5.15), the BVP is

$$\hat{\nabla} \hat{\phi}_{i1} = 0 \quad \text{in } \mathcal{D}_i, \tag{4.5.24}$$

$$\hat{\phi}_{i1,\hat{x}} = 0, \quad \hat{x} = 0, \quad \bar{y} < 0, \tag{4.5.25}$$

$$\begin{aligned}(2\gamma - 1)\left[(1 + \bar{\rho})\,\hat{\phi}_{11} - \hat{\phi}_{21}\right] - \gamma \hat{x}\left[(1 + \bar{\rho})\,\hat{\phi}_{11,\hat{x}} - \hat{\phi}_{21,\hat{x}}\right] \\ + (\gamma - 1)\,\gamma \hat{\eta}_0 \bar{\rho} \tilde{\eta} = 0, \quad \bar{y} = 0\end{aligned} \tag{4.5.26}$$

$$\gamma \tilde{\eta} + \left(\hat{\phi}_{i1,\hat{x}} - \gamma \hat{x}\right) \tilde{\eta}_{\hat{x}} - \hat{\phi}_{i1,\bar{y}} = 0, \quad \bar{y} = 0, \tag{4.5.27}$$

where $\hat{\nabla} = \left(\frac{\partial}{\partial \hat{x}}, \frac{\partial}{\partial \bar{y}}\right)$. By defining $\Phi(\hat{x}, \hat{y}) = (1 + \bar{\rho})\,\hat{\phi}_{11} - \hat{\phi}_{21}$, and eliminating $\tilde{\eta}$ from (4.5.24)-(4.5.27), condition (4.5.26) and (4.5.27) now become

$$(2\gamma - 1)\,(\hat{x}\Phi_{\hat{x}} - \Phi) - \gamma \hat{x}^2 \Phi_{\hat{x}\hat{x}} - (\gamma - 1)\,\hat{\eta}_0 \Phi_{\bar{y}} = 0, \quad \hat{x} \geq 0, \bar{y} = 0, \tag{4.5.28}$$

$$\tilde{\eta}(\hat{x}) = \frac{1}{(\gamma - 1)\,\beta \hat{\eta}_0 \bar{\rho}}\left[\gamma \hat{x} \Phi_{\hat{x}}(\hat{x}, 0) - (2\gamma - 1)\,\Phi(\hat{x}, 0)\right], \quad \hat{x} \geq 0. \tag{4.5.29}$$

We introduce the complex variable $\hat{z} = \hat{x} + \mathrm{i}\bar{y}$, after which we write

$$\Phi(\hat{x}, \hat{y}) = \mathrm{Re}(f(z)), \quad \hat{z} \in \hat{\mathcal{D}}, \tag{4.5.30}$$

with $\hat{\mathcal{D}} := \{(\hat{x}, \hat{y}) : 0 < \hat{x}, \hat{y} < 0\}$. The condition (4.5.25) and (4.5.29) then require

$$\gamma \hat{x}^2 f''(\hat{x}) + [(\gamma - 1)\,\hat{\eta}_0 \mathrm{i} - (2\gamma - 1)\,\hat{x}]\, f'(\hat{x}) + (2\gamma - 1)\, f(\hat{x}) = 0, \quad \hat{x} \geq 0, \tag{4.5.31}$$

$$\mathrm{Re}(f'(\mathrm{i}\hat{y})) = 0, \quad \bar{y} < 0. \tag{4.5.32}$$

As mentioned in Chapter 3, this is the same formation as that in [64] for the single fluid problem with an inclined accelerating plate in the inner region as $\hat{x} \to 0$. Following the same technique, the structure (4.5.31) leads to

$$f(\hat{x}) = \exp g(\hat{x}), \quad \hat{x} > 0, \tag{4.5.33}$$

with

$$g(\hat{x}) = \frac{k_0}{\hat{x}} + k_1 \log(\hat{x}) + o(1), \quad \hat{x} \to 0, \tag{4.5.34}$$

where $k_0, k_1 \in \mathbb{C}$ will be determined next. On substitution from (4.5.33) and (4.5.34) into (4.5.31), we find that

$$k_0 = \left(1 - \frac{1}{\gamma}\right) \hat{\eta}_0 \mathrm{i}, \quad k_1 = 4 - \frac{1}{\gamma}, \tag{4.5.35}$$

by looking at the leading order terms $O(x^{-2})$ and $O(x^{-1})$. Thus we take

$$f(\hat{z}) = A \exp\left\{ \frac{\mathrm{i}(1 - \frac{1}{\gamma})\hat{\eta}_0}{\hat{z}} + (4 - \frac{1}{\gamma}) \log(\hat{z}) + o(1) \right\}, \quad \text{as } |\hat{z}| \to 0, \tag{4.5.36}$$

with $A \in \mathbb{C}$ an arbitrary constant. Condition (4.5.32) requires

$$\arg(A) = (4 - \frac{1}{\gamma})\frac{\pi}{2} + r\pi, \quad r = 0 \text{ or } 1. \tag{4.5.37}$$

Hence, we have

$$f(\hat{z}) = B\exp\left\{\frac{\mathrm{i}(1-\frac{1}{\gamma})}{\hat{z}}\hat{\eta}_0 + (4-\frac{1}{\gamma})\log(\hat{z}) + (4-\frac{1}{\gamma})\frac{\pi}{2}\mathrm{i} + \pi + o(1)\right\}, \tag{4.5.38}$$

as $|\hat{z}| \to 0$ with $B \in \mathbb{R}$ a globally determined constant. Therefore, we have the solution

$$\Phi(\hat{R},\hat{\Theta}) \sim -k\hat{R}^{4-\frac{1}{\gamma}}\exp\left\{(1-\frac{1}{\gamma})\hat{\eta}_0\hat{R}^{-1}\sin\hat{\Theta}\right\}\cos\left\{(1-\frac{1}{\gamma})\hat{\eta}_0\hat{R}^{-1}\cos\hat{\Theta} + (4-\frac{1}{\gamma})(\hat{\Theta}+\frac{\pi}{2})\right\}, \tag{4.5.39}$$

as $\hat{R} \to 0$ uniformly for $\hat{\Theta} \in [0, \frac{\pi}{2}]$ where $\hat{R} = |\hat{z}|$ and $\hat{\Theta} = \arg(\hat{z})$. Finally, we have the correction of the interface

$$\tilde{\eta}(\hat{x}) = \frac{k}{\gamma^2\bar{\rho}}\hat{x}^{3-\frac{1}{\gamma}}\sin\left[(1-\frac{1}{\gamma})\hat{\eta}_0\hat{x}^{-1} + (4-\frac{1}{\gamma})\frac{\pi}{2}\right], \quad \text{as } \hat{x} \to 0. \tag{4.5.40}$$

An example of the graph of $\tilde{\eta}(\hat{x})$ is the same as Figure 3.8. Since $0 < \beta_0 < 1$, we have $1 - \frac{1}{\gamma} > 0$. Thus, from (4.5.39), it is obvious that $\Phi(\hat{R},\hat{\Theta}) = o(1)$ as $\hat{R} \to 0$ uniformly for $\hat{\Theta} \in \left(-\frac{\pi}{2}, 0\right)$ requires $\hat{\eta}_0 > 0$.

Similar to the dam-break problem in Chapter 3, the local solution (4.5.39) is a local solution in the inner region as $\hat{R} \to 0$, hence we cannot obtain the exact value of B and the composite asymptotic solutions for the whole problem.

4.6 Conclusion

In this chapter, we find the asymptotic and numerical solutions to the problem of an inclined plate moving towards two layers of ideal fluids with constant acceleration in small-time approximation. This problem is locally equivalent to the two-fluid dam-break problem in chapter 3, so we can follow the same approach to solve this problem.

In the outer region for $t \to 0^+$ and $\alpha > \frac{\pi}{2}$, we find that there is a singularity in

the shape of the interface close to the intersection point between the plate and the interface of two fluids. We derive the Plemelj formula for the velocity potential of the bottom fluid in the outer region when $t \to 0^+$ using conformal mapping, which can be numerically evaluated by Gaussian quadrature. The asymptotic analysis and the numerical results show that the velocity potential is of order r^{β_0}, as $r \to 0$ and β_0 can be found precisely from the eigenvalue problem, whose values are always lower than 1. Since the location of the interface is of order $r^{\beta_0 - 1}$, there is a singularity close to the intersection point.

We are also interested in the effect of the depth d of the bottom fluid in the solutions. When $d \to 1$, the upper fluid is just a thin layer, and the outer region problem can be treated as a single fluid problem as in [64] for the bottom fluid. Considering the solution of inner region problem for the limit $d \to 1$, the coefficient in the asymptotic form of $\tilde{\phi}_1$ is of order $(1-d)^{\frac{\pi}{2\alpha - \beta_0}}$. Another situation is when $d \to 0$ such that the bottom fluid can be neglected in the outer region. In this case, we found that the coefficient is of order d^{γ}, where γ can be determined numerically. The numerical results also show great agreement with the asymptotic results.

To resolve the singularity at the intersection point of the interface and the moving plate, the problem is rescaled into an inner region. Similar to the inner-region problem of the two-fluid dam-break problem in chapter 3, we can find its local solutions such that the interface is always vertical to the plate and contains small oscillations close to the contact point. Although the inner-region problem has not been numerically solved so far, it can be solved by the Shape-Newton method in the future.

Chapter 5

Fluid/solid Problem with an Inclined Accelerating Plate in the Inner Region

5.1 Introduction

One of the main features that appear in the initial stage of both the two-fluid dam-break problem and solid/two-fluid interaction problem in chapters 3 and chapter 4 is the singular behaviour around the contact point of the interface and the solid boundary, which can be resolved by rescaling into an inner region. However, the difficulty of solving the inner problem analytically emphasises the importance of developing an appropriate numerical method. When the influence of the fluid with lighter density can be ignored, the problem can be regarded as the solid/fluid interaction problem in [64], which has been solved numerically by the boundary integral method.

Numerous studies have been conducted on using numerical techniques to solve dam-break problems and solid/fluid interaction problems. Similar to [64], Stansby et al. [79] also conducted numerical simulations of a dam-break problem by boundary

integral method based on [17, 25], where the singularity is artificially removed by using a thin layer of water downstream and smoothing the right angle on the boundary. Some other numerical methods to simulate the dam-break problem are developed by solving the nonlinear shallow-water equations using different methods, including the finite volume and finite difference methods (see e.g.[8, 31, 34, 47, 104, 105]). The numerical schemes to solve the solid/fluid interaction problem are mainly designed for time-dependent flow fields, such as the marker-and-cell method using an Eulerian mesh of calculation cells with finite difference approximation and complex variable method employing Cauchy's theorem (see e.g. [10, 35, 92, 96, 99]).

In this chapter, we apply the finite element method and nonlinear solvers to solve the solid/single fluid interaction problem with an inclined accelerating plate in the inner region in [64], especially for $\frac{\pi}{2} < \alpha < \alpha_c$, such that this numerical method can be possibly applied to the inner-region problem of two fluid dam-break problems in Chapter 3 and the solid/two fluid interaction problem as discussed in Chapter 4.

The inner-region problems involve two variables: the velocity potential of the fluid and the location of the free surface, with two different boundary conditions on the free boundary. They are two-way boundary-coupled problems, where the whole region and the free surface can be separated as different domains. The coupled problem is solved for different dependent variables in multiple domains, where the domains should be solved dependently, and the variables cannot be explicitly eliminated [103].

Picard iteration and Newton's method are two standard methods to solve nonlinear algebraic equations that arise in the numerical solution of the nonlinear partial differential equations [56]. The former technique is easy to implement, but its convergence rate is linear and slow. Newton's method is more challenging to implement since it requires the Jacobian matrix, which can be approximated by the finite difference method, but it shows better performance in the convergence rate. The comparison of these two methods will be shown in Appendix C, where we con-

struct a nonlinear free boundary problem with a Neumann boundary condition and a Dirichlet boundary condition on the free boundary. The Neumann free-boundary condition and the boundary conditions on the fixed boundary are the same as the original inner problem. This problem can be solved as a linear system because the Neumann boundary condition has a linearised weak form. Another simplified problem has the same boundary conditions except that it has a tangential boundary condition on the free boundary instead of a Dirichlet boundary condition. As mentioned before, Picard's iteration converges much slower. Moreover, it cannot converge to a solution for the single fluid problem on a fine mesh, which motivates us to use Newton's method.

To start with a simple test problem, we consider the linearised solid/fluid interaction problem in the inner region as $\alpha - \frac{\pi}{2} \ll 1$ to avoid the nonlinearity of the free-boundary condition in this chapter, which is illustrated in section 5.2. A simple iteration has been developed, which involves solving for the velocity potential using a given approximation of the free surface and subsequently updating the free surface with the approximated velocity potential iteratively until convergence is achieved. This numerical scheme will be demonstrated in section 5.3, where the numerical results will be presented along with a comparison to the far-field condition. In section 5.4, we will review the inner-region problem and reformulate it into a coupled problem in vector form, whose weak forms are shown in section 5.4.1 and the linearisation is derived in 5.4.2. The implementation of Newton's method and comparing its numerical results with those obtained by the boundary integral method in [64] are presented in section 5.5.

5.2 Local solution of the linearised inner-region problem for $\alpha \to \frac{\pi}{2}$

Now we consider the solid/single fluid interaction problem with an inclined accelerating plate in the inner region in [64], which is a simplified version of the problem in Chapter 4 by choosing $\rho_2 = 0$. The angle of the plate with the horizontal is denoted as α. The inner-region problem in [64] is

$$\tilde{\nabla}^2\phi_0 = 0, \quad -\infty < \tilde{X} < \infty, \tilde{Y} < \begin{cases} -\tilde{X}\tan\alpha, \tilde{X} < \tilde{X}_0 \\ \eta_0\left(\tilde{X}\right), \tilde{X} \geq \tilde{X}_0 \end{cases}; \quad (5.2.1)$$

$$\tilde{\nabla}\phi_0 \cdot \tilde{\boldsymbol{n}} = 0, \quad \tilde{X} < \tilde{X}_0, \tilde{Y} = -\tilde{X}\tan\alpha; \quad (5.2.2)$$

$$\gamma\tilde{\eta}_0 + \left(\phi_{0\tilde{X}} - \gamma\tilde{X}\right)\eta_{0\tilde{X}} - \phi_{0,\tilde{Y}} = 0, \quad \tilde{X} > \tilde{X}_0, \tilde{Y} = \eta_0\left(\tilde{X}\right); \quad (5.2.3)$$

$$(2\gamma - 1)\phi_0 - \gamma\eta_0\phi_{0\tilde{Y}} - \gamma\tilde{X}\phi_{0\tilde{X}} + \frac{1}{2}\left|\tilde{\nabla}\phi_0\right|^2 = 0, \quad \tilde{X} > \tilde{X}_0, \tilde{Y} = \eta_0\left(\tilde{X}\right), \quad (5.2.4)$$

with the far-field conditions

$$\phi_0\left(\tilde{R}, \theta\right) \sim \tilde{R}^{\frac{\pi}{2\alpha}}\sin\frac{\pi\theta}{2\alpha} + \frac{\pi^2}{12\alpha^2\cos 2\alpha}\tilde{R}^{\frac{\pi}{\alpha}-2}\cos\left[\left(\frac{\pi}{\alpha} - 2\right)(\theta + \alpha)\right]$$
$$\text{as } \tilde{R} \to +\infty, -\alpha < \theta < 0; \quad (5.2.5)$$

$$\eta_0\left(\tilde{X}\right) \sim -\frac{\pi}{4\alpha}\tilde{X}^{\frac{\pi}{2\alpha}-1}, \quad \text{as } \tilde{X} \to +\infty, \quad (5.2.6)$$

where $\tilde{\nabla} = (\partial_{\tilde{X}}, \partial_{\tilde{Y}})$, $\gamma = \frac{1}{1-\frac{\pi}{4\alpha}}$, $\left(\tilde{R}, \theta\right)$ is the polar coordinates in the inner region, and $\tilde{X}_0$ is the $\tilde{X}$-coordinate of the contact point between free surface and the moving plate. The detail about this problem is shown in Appendix B.

Before using finite element method and Newton's method to this nonlinear free-boundary problem, we start by linearising this problem as $\alpha \to \frac{\pi}{2}$ such that the linearised problem can be solved in a fixed domain. The linearised problem is derived by considering the effect of small perturbation on the vertical angle of the moving plate. The analytical solution for this linearised problem can be found by

following the same method as in [64] for $\alpha > \frac{\pi}{2}$. For $\alpha = \frac{\pi}{2}$, the exact solution of (5.2.1)-(5.2.6) is $\tilde{\eta}\left(\tilde{X}\right) = \frac{1}{2}$ and $\tilde{\phi}\left(\tilde{X}, \tilde{Y}\right) = \tilde{Y} - \frac{1}{3}$. Now, we introduce a small perturbation to α,$\tilde{\eta}\left(\tilde{X}\right)$ and $\tilde{\phi}\left(\tilde{X}, \tilde{Y}\right)$, such that

$$\alpha = \frac{\pi}{2} + \delta \tag{5.2.7}$$

$$\tilde{\eta}\left(\tilde{X}\right) = \frac{1}{2} + \delta\hat{\eta}(\tilde{X}) \tag{5.2.8}$$

$$\tilde{\phi}\left(\tilde{X}, \tilde{Y}\right) = \tilde{Y} - \frac{1}{3} + \delta\hat{\phi}\left(\tilde{X}, \tilde{Y}\right), \tag{5.2.9}$$

where δ is a small constant.

The coefficient γ, which is used to scale the inner coordinates, now becomes

$$\gamma = \frac{1}{1 - \frac{\pi}{4\left(\frac{\pi}{2}+\delta\right)}} = 2 - \frac{4\delta}{\pi + 4\delta}. \tag{5.2.10}$$

We can further introduce $\hat{\gamma} = -\frac{4}{\pi}$ such that $\gamma = 2 + \delta\hat{\gamma} + o\left(\delta\right)$.

On substitution from (5.2.7)-(5.2.10) into (5.2.1)-(5.2.6), we obtain the linearised boundary-value problem

$$\tilde{\nabla}^2\hat{\phi} = 0, \quad 0 < \tilde{X} < \infty, \quad \tilde{Y} < \frac{1}{2} \tag{5.2.11}$$

$$\tilde{\nabla}\hat{\phi} \cdot \tilde{\boldsymbol{n}} = 1, \quad \tilde{Y} < \frac{1}{2}, \quad \tilde{X} = 0; \tag{5.2.12}$$

$$-6\hat{\phi} + 6\tilde{X}\hat{\phi}_{\tilde{X}} - 4\tilde{X}^2\hat{\phi}_{\tilde{X}\tilde{X}} - \hat{\phi}_{\tilde{Y}} - \frac{10}{3\pi} = 0, \quad \tilde{Y} = \frac{1}{2}; \tag{5.2.13}$$

$$\hat{\phi}(\tilde{R}, \theta) \sim -\frac{2}{\pi}\tilde{R}\theta\cos\theta - \frac{2}{\pi}\log(\tilde{R})\tilde{R}\sin\theta + \frac{4}{3\pi}\log(\tilde{R}) + \frac{4}{3\pi} \quad \text{as } \tilde{R} \to \infty; \tag{5.2.14}$$

$$\hat{\eta}\left(\tilde{X}\right) \sim -\frac{1}{\pi}(\log(\tilde{X}) + 1) \quad \text{as } \tilde{X} \to \infty, \tag{5.2.15}$$

where the free-boundary boundary condition (5.2.13) is the combination of conditions (5.2.3) and (5.2.4) to eliminate $\hat{\eta}$, which are

$$2\hat{\eta} + \frac{1}{2}\hat{\gamma} - 2\tilde{X}\hat{\eta}_{\tilde{X}} - \hat{\phi}_{\tilde{Y}} = 0, \quad \tilde{Y} = \frac{1}{2}; \tag{5.2.16}$$

$$\hat{\eta} + 3\hat{\phi} - \frac{1}{6}\hat{\gamma} - 2\tilde{X}\hat{\phi}_{\tilde{X}} = 0, \quad \tilde{Y} = \frac{1}{2}. \tag{5.2.17}$$

For convenience, we introduce a shifted coordinate $\hat{Y}$ and the velocity potential $\hat{\phi}_1$

$$\hat{Y} = \tilde{Y} - \frac{1}{2}, \quad \hat{\phi}_1 = \hat{\phi} - \tilde{X}. \tag{5.2.18}$$

The contact point between the free boundary and the plate is always the origin, and the boundary condition (5.2.12) becomes a natural boundary condition for $\hat{\phi}_1$. The boundary-value problem for $\hat{\phi}_1$ is now given by

$$\hat{\nabla}^2 \hat{\phi}_1 = 0, \quad 0 < \tilde{X} < \infty, \quad \hat{Y} < 0; \tag{5.2.19}$$

$$\hat{\nabla} \hat{\phi}_1 \cdot \hat{\boldsymbol{n}} = 0, \quad \hat{Y} < 0, \quad \tilde{X} = 0; \tag{5.2.20}$$

$$-6\hat{\phi}_1 + 6\tilde{X}\hat{\phi}_{1,\tilde{X}} - 4\tilde{X}^2\hat{\phi}_{1,\tilde{X}\tilde{X}} - \hat{\phi}_{1,\hat{Y}} - \frac{10}{3\pi} = 0, \quad \hat{Y} = 0, \tag{5.2.21}$$

where $\hat{\nabla} = (\partial_{\tilde{X}}, \partial_{\hat{Y}})$ and $\hat{\boldsymbol{n}}$ is the unit normal vector to the plate pointing out of the fluid.

In order to find the local solutions as $\tilde{X}^2 + \hat{Y}^2 \to 0$, we introduce the complex variable $\hat{z} = \tilde{X} + \mathrm{i}\hat{Y}$, and

$$\hat{\phi}_1 = Re(f(\hat{z})), \quad \hat{z} \in \hat{D} \tag{5.2.22}$$

with the domain $\hat{D} = \left\{ \left(\tilde{X}, \hat{Y} \right) : \tilde{X} > 0, \hat{Y} < 0 \right\}$, and the mapping $f : \hat{D} \to \mathcal{C}$. The condition (5.2.20) and (5.2.21) then can be reformulated in terms of f as

$$-6f + 6\tilde{X}f' - 4\tilde{X}^2 f'' - \mathrm{i}f' - \frac{10}{3\pi} = 0, \quad \hat{Y} = 0, \tag{5.2.23}$$

$$Re\left(f'\left(\mathrm{i}y\right)\right) = 0, \quad \tilde{X} = 0. \tag{5.2.24}$$

The condition (5.2.23) now has a solution which can be written as

$$f(\tilde{X}) = \exp(g(\tilde{X})) - \frac{5}{9\pi}, \quad \tilde{X} > 0, \tag{5.2.25}$$

with

$$g(\tilde{X}) = \frac{k_1}{\tilde{X}} + k_2 \log(\tilde{X}) + o(1), \tag{5.2.26}$$

as $\tilde{X} \to 0$ with k_1, k_2 some complex-valued constants. On substitution from (5.2.25) and (5.2.26) into condition (5.2.23), the equation is now

$$\left(-4k_1^2 + \mathrm{i}k_1\right) \tilde{X}^{-2} + \left(-14k_1 + 8k_1k_2 - \mathrm{i}k_2\right) \tilde{X}^{-1} + o\left(x^{-1}\right) = 0, \tag{5.2.27}$$

and then we find that

$$k_1 = \frac{\mathrm{i}}{4}, \quad k_2 = \frac{7}{2}. \tag{5.2.28}$$

Thus, we take

$$f(\hat{z}) = A \exp\left(\frac{\mathrm{i}}{4\hat{z}} + \frac{7}{2}\log(\hat{z}) + o(1)\right) - \frac{5}{9\pi}, \tag{5.2.29}$$

as $|\hat{z}| \to 0$. The condition (5.2.24) requires that

$$\arg(A) = \frac{7\pi}{4} + \pi r \tag{5.2.30}$$

for $r = 0$ or $r = 1$.

Hence, we have

$$f(\hat{z}) = B \exp\left(\frac{\mathrm{i}}{4\hat{z}} + \frac{7}{2}\log(\hat{z}) + \frac{7\pi}{4}\mathrm{i} + o(1)\right) - \frac{5}{9\pi} \tag{5.2.31}$$

as $|\hat{z}| \to 0$, with B as a globally determined real-valued constant. Thus we obtain

$$\hat{\phi}(\hat{R}, \hat{\theta}) \sim B\hat{R}^{\frac{7}{2}} \exp\left\{\frac{1}{4}\hat{R}^{-1}\sin\hat{\theta}\right\} \cos\left(\frac{1}{4}\hat{R}^{-1}\cos\hat{\theta} + \frac{7}{2}(\hat{\theta} + \frac{\pi}{2})\right) - \frac{5}{9\pi}, \tag{5.2.32}$$

as $\hat{R} \to 0$ and $\hat{\theta} \in [-\frac{\pi}{2}, 0]$ where $\left(\hat{R}, \hat{\theta}\right)$ is the polar coordinates. This solution is consistent with local solution in [64] when $\alpha = \frac{\pi}{2}$. Furthermore, $\hat{\phi}(\hat{R}, \hat{\theta}) = o(1)$ as $\hat{R} \to 0$ since $\sin\hat{\theta} < 0$. On substitution from (5.2.32) into (5.2.21), the local solution

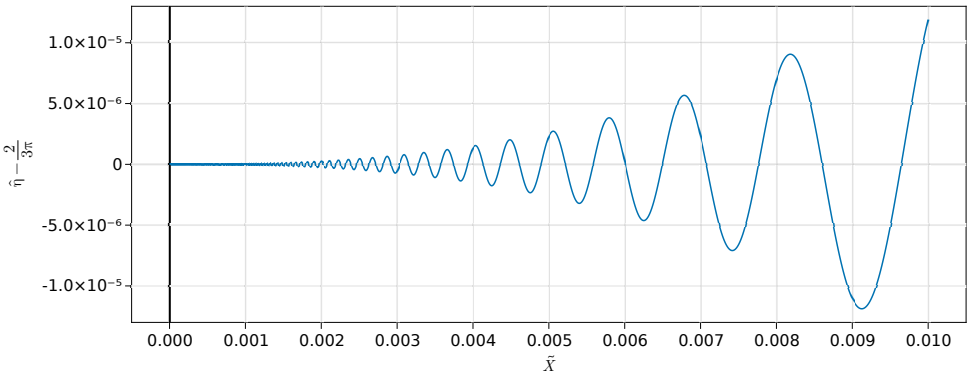

Figure 5.1: *An example of the asymptotic form given by* (5.2.33) *for* $B = 3$. *The bold black line represents the plate, and the blue curve is the free surface.*

of $\hat{\eta}$ can be found as

$$\hat{\eta}\left(\tilde{X}\right) \sim -\frac{B}{2}\tilde{X}^{\frac{5}{2}} \sin\left(\frac{1}{4}\tilde{X}^{-1} + \frac{7\pi}{4}\right) + \frac{2}{3\pi}, \quad \tilde{X} \to 0. \tag{5.2.33}$$

Small oscillations can be observed on the free surface close to the intersection point as the blue curve shown in Figure 5.1, and the free surface is always perpendicular to the plate, which is the bold black line. We also note that a singularity appears in $\hat{\eta}\left(\tilde{X}\right)$ as $\tilde{X} \to 0$.

5.3 Coupled problem for the linearised problem

Now, we are going to develop a numerical scheme to solve the linearised single fluid problem (5.2.11)-(5.2.15) for $\hat{\phi}$ and $\hat{\eta}$. We introduce the domain denoted by $\Omega = \left\{\left(\tilde{X}, \hat{Y}\right) : 0 < \tilde{X} < L, -L + \frac{1}{2} < \hat{Y} < \frac{1}{2}\right\}$ with the fixed boundary Γ_L at $\tilde{X} = 0$ as $L \to \infty$, and the free boundary Γ_F. We also denote Γ_D as the boundary at $\tilde{X} = L$ and $\hat{Y} = -L + \frac{1}{2}$ such that the domain is truncated and the far-field conditions (5.2.14), (5.2.15) are now the boundary conditions on Γ_D. In this problem, the free surface Γ_F is fixed at $\hat{Y} = \frac{1}{2}$ such that the free boundary does not need to be updated by iteration. Now using (5.2.16) and (5.2.17) instead of (5.2.13), the

system (5.2.11)-(5.2.15) becomes

$$-\hat{\nabla}^2\hat{\phi} = 0, \quad \text{in } \Omega; \tag{5.3.1}$$

$$\hat{\nabla}\hat{\phi}\cdot\hat{\boldsymbol{n}} = 1, \quad \text{on } \Gamma_L; \tag{5.3.2}$$

$$2\hat{\eta} + \frac{1}{2}\hat{\gamma} - 2\tilde{X}\hat{\eta}_{\tilde{X}} - \hat{\phi}_{\hat{Y}} = 0, \quad \hat{Y} = \frac{1}{2}; \tag{5.3.3}$$

$$\hat{\eta} + 3\hat{\phi} - \frac{1}{6}\hat{\gamma} - 2\tilde{X}\hat{\phi}_{\tilde{X}} = 0, \quad \hat{Y} = \frac{1}{2}; \tag{5.3.4}$$

$$\hat{\phi}\left(\hat{R},\hat{\theta}\right) = \hat{\phi}_\infty\left(\hat{R},\hat{\theta}\right) \sim -\frac{2}{\pi}\hat{R}\hat{\theta}\cos\theta - \frac{2}{\pi}\log\left(\hat{R}\right)\hat{R}\sin\hat{\theta} + \frac{4}{3\pi}\log\left(\hat{R}\right) + \frac{4}{3\pi} \quad \text{on } \Gamma_D; \tag{5.3.5}$$

$$\hat{\eta}\left(\tilde{X}\right) = \hat{\eta}_\infty\left(\tilde{X}\right) \sim -\frac{1}{\pi}\left(\log\left(\tilde{X}\right) + 1\right) \quad \text{on } \Gamma_D, \tag{5.3.6}$$

where $\hat{\gamma} = -\frac{4}{\pi}$.

Since the boundary Γ_F is fixed at $\hat{Y} = \frac{1}{2}$, the unit normal vector to this boundary is $\hat{\boldsymbol{n}} = (0,1)$. Then (5.3.3) could be rewritten as a Neumann boundary condition

$$\hat{\nabla}\hat{\phi}\cdot\hat{\boldsymbol{n}} = 2\hat{\eta} - \frac{2}{\pi} - 2\tilde{X}\hat{\eta}_{\tilde{X}}, \quad \hat{Y} = \frac{1}{2}. \tag{5.3.7}$$

5.3.1 The weak form

Now we need to find the weak form for this linearised problem. We introduce the test functions $v \in V := \{v \in \mathcal{C}^1(\Omega)\,|v = 0 \text{ on } \Gamma_F\}$, $\hat{v} \in \hat{V} := \{\hat{v} \in \mathcal{C}^1(\Gamma_F)\,|\hat{v} = 0 \text{ at } \tilde{X} = L\}$ and $w \in W := \{w \in \mathcal{C}^0(\Gamma_F)\}$. Multiplying (5.3.1) with the test function v, integrating over Ω, and using the penalty method by introducing a large constant μ for implementing the Dirichlet boundary condition (5.3.5), we have

$$\begin{aligned} 0 &= -\int_\Omega \hat{\nabla}^2\hat{\phi}v d\Omega \\ &= \int_\Omega \hat{\nabla}\hat{\phi}\cdot\hat{\nabla}v d\Omega - \int_{\partial\Omega}\boldsymbol{n}\cdot\hat{\nabla}\hat{\phi}v ds \\ &= \int_\Omega \hat{\nabla}\hat{\phi}\cdot\hat{\nabla}v d\Omega + \int_{\Gamma_D}\mu(\hat{\phi}-\hat{\phi}_\infty)v ds - \int_{\Gamma_L} v ds. \end{aligned} \tag{5.3.8}$$

The second step is derived by integration by parts and the divergence theorem

$$\int_{\Omega} \hat{\nabla} \cdot f d\Omega = \int_{\partial\Omega} \hat{\boldsymbol{n}} \cdot f ds.$$

Considering a test function $\tilde{v}$ as the natural lifting of $\hat{v}$ into $\mathcal{C}^1(\Omega)$ such that $\tilde{v}$ is the extension of $\hat{v}$ defined on Γ_F into Ω, the weak form on the boundary Γ_F can be obtained by multiplying the test function $\hat{v}$ with (5.3.7) and integration by parts, which is

$$\begin{aligned} \int_{\Gamma_F} \hat{\nabla}\hat{\phi} \cdot \hat{\boldsymbol{n}} \hat{v} d\tilde{X} &= \int_{\Omega} \hat{\nabla}\hat{\phi} \cdot \hat{\nabla}\tilde{v} d\Omega \\ &= \int_{\Gamma_F} \left(2\hat{\eta} - \frac{2}{\pi}\right) \hat{v} d\tilde{X} + \int_{\Gamma_F} 2(\tilde{X}\hat{v})_{\tilde{X}} \hat{\eta} d\tilde{X} - 2L\hat{\eta}_{\infty}(L)\hat{v}(L). \end{aligned} \tag{5.3.9}$$

Note that $\hat{v} = 0$ at $\tilde{X} = L$ on the free boundary can avoid the impact of the penalty method (the large value of μ) used for the Dirichlet boundary condition there. Instead, the strong form is considered such that

$$\lambda\hat{\phi}\big|_{\tilde{X}=L,\Gamma_F} = \lambda\hat{\phi}_{\infty}(R_{\infty}, \theta_{\infty}), \tag{5.3.10}$$

where λ is some constant introduced for implementation purpose, $R_{\infty}^2 = L^2 + (\hat{\eta}(L))^2$, and $\tan\theta_{\infty} = 1/(2L)$.

Rearranging the equation (5.3.9), the weak form on the boundary Γ_F is

$$\int_{\Omega} \hat{\nabla}\hat{\phi} \cdot \hat{\nabla}\tilde{v} d\Omega - \int_{\Gamma_F} 2\hat{\eta}\hat{v} d\tilde{X} - \int_{\Gamma_F} 2\hat{\eta}(\tilde{X}\hat{v})_{\tilde{X}} d\tilde{X} = -2L\hat{\eta}_{\infty}(L)\hat{v}(L) - \int_{\Gamma_F} \frac{2}{\pi}\hat{v} d\tilde{X}. \tag{5.3.11}$$

The second weak form on the free boundary can be obtained by multiplying the

test function w with (5.3.4), which is

$$\int_{\Gamma_F} \left(\hat{\eta} + 3\hat{\phi} - 2\tilde{X}\hat{\phi}_{\tilde{X}}\right) w d\tilde{X} = \int_{\Gamma_F} -\frac{2}{3\pi} w d\tilde{X}. \tag{5.3.12}$$

Thus, we have the coupled weak formulation as the following. Find $\left(\hat{\phi}, \hat{\eta}\right) \in \mathcal{C}^1(\Omega) \times \mathcal{C}^0(\Gamma_F)$:

$$\begin{aligned}
\int_\Omega \hat{\nabla}\hat{\phi} \cdot \hat{\nabla} v d\Omega + \int_{\Gamma_D} \mu(\hat{\phi} - \hat{\phi}_\infty) v ds - \int_{\Gamma_L} v ds &= 0, \quad \forall v \in V, \\
\int_\Omega \hat{\nabla}\hat{\phi} \cdot \hat{\nabla}\tilde{v} d\Omega - \int_{\Gamma_F} 2\hat{\eta}\hat{v} d\tilde{X} - \int_{\Gamma_F} 2\hat{\eta}(\tilde{X}\hat{v})_{\tilde{X}} d\tilde{X} &= -2L\hat{\eta}_\infty(L)\hat{v}(L) - \int_{\Gamma_F} \frac{2}{\pi}\hat{v} d\tilde{X}, \quad \forall \hat{v} \in \hat{V}, \\
\int_{\Gamma_F} \left(\hat{\eta} + 3\hat{\phi} - 2\tilde{X}\hat{\phi}_{\tilde{X}}\right) w d\tilde{X} &= \int_{\Gamma_F} -\frac{2}{3\pi} w d\tilde{X}, \quad \forall w \in W, \\
\lambda\hat{\phi}\big|_{\tilde{X}=L,\Gamma_F} &= \lambda\hat{\phi}_\infty(R_\infty, \theta_\infty).
\end{aligned} \tag{5.3.13}$$

5.3.2 Finite element method and the numerical iteration

Let span$\{\zeta_i\}$, span$\{\hat{\zeta}_i\}$, span$\{\tilde{\zeta}_i\}$ and span$\{\xi_i\}$ be the basis for V, $\hat{V}$, $\tilde{V}$ and W correspondingly. The finite element approximation (η_h, ϕ_h) for $(\hat{\eta}, \hat{\phi})$ is defined as

$$\eta_h\left(\tilde{X}\right) = \sum_i \eta_{h,i}\xi_i\left(\tilde{X}\right); \tag{5.3.14}$$

$$\phi_h\left(\tilde{X}, \hat{Y}\right) = \begin{cases} \sum_i \phi_{h,i}\zeta_i\left(\tilde{X}, \hat{Y}\right) & \text{in } \Omega \setminus \Gamma_F, \\ \sum_i \phi_{h,i}\tilde{\zeta}_i\left(\tilde{X}, \hat{Y}\right) & \text{on } \Gamma_F. \end{cases} \tag{5.3.15}$$

The weak formulations (5.3.13) are now equivalent to

$$\int_\Omega \hat{\nabla}\phi_h \cdot \hat{\nabla}\zeta_i d\Omega + \int_{\Gamma_D} \mu(\phi_h - \hat{\phi}_\infty)\zeta_i ds - \int_{\Gamma_L} \zeta_i ds = 0, \tag{5.3.16}$$

$$\int_{\Gamma_F} \left(\eta_h + 3\phi_h - 2\tilde{X}\phi_{h,\tilde{X}}\right) \xi_i d\tilde{X} = \int_{\Gamma_F} -\tfrac{2}{3\pi}\xi_i d\tilde{X}, \tag{5.3.17}$$

$$\lambda\phi_h\big|_{\tilde{X}=L,\Gamma_F} = \lambda\hat{\phi}_\infty(R_\infty, \theta_\infty), \tag{5.3.18}$$

$$\int_\Omega \hat{\nabla}\phi_h \cdot \hat{\nabla}\tilde{\zeta}_i d\Omega - \int_{\Gamma_F} 2\eta_h\hat{\zeta}_i d\tilde{X} - \int_{\Gamma_F} 2\eta_h(\tilde{X}\hat{\zeta}_i)_{\tilde{X}} d\tilde{X} = -2L\hat{\eta}_\infty(L)\hat{\zeta}_i(L) - \int_{\Gamma_F} \tfrac{2}{\pi}\hat{\zeta}_i d\tilde{X}, \tag{5.3.19}$$

0. Initialize with $\boldsymbol{\eta}^0$ and let $k = 0$.
1. Given $\boldsymbol{\eta}^k$, solve the system (5.3.16)-(5.3.18) for $\boldsymbol{\Phi}^k$.
2. Given $\boldsymbol{\Phi}^k$, solve the equation (5.3.19) for $\boldsymbol{\eta}^{k+1}$.
3. Set $k \leftarrow k+1$, and repeat steps 1-3 until convergence for $\boldsymbol{\eta}^k$.

Table 5.1: The numerical scheme for the linearised single-fluid problem in the inner region.

for $i = 1, 2, ..., N_i$, with N_i as the number of the interior nodes in the mesh.

We collect the independent variables into the vectors

$$\boldsymbol{\Phi} = \begin{pmatrix} \phi_{h,1} \\ \phi_{h,2} \\ \vdots \end{pmatrix} \qquad \boldsymbol{\eta} = \begin{pmatrix} \eta_{h,1} \\ \eta_{h,2} \\ \vdots \end{pmatrix}.$$

The numerical scheme to solve the problem (5.3.16)-(5.3.19) is shown in Table 5.1, which solves the system (5.3.16)-(5.3.18) for $\boldsymbol{\Phi}^k$ with given $\boldsymbol{\eta}^k$ at kth iteration and substitutes $\boldsymbol{\Phi}^k$ into the kinematic boundary condition (5.3.19) to find $\boldsymbol{\eta}^{k+1}$ until the error $|\boldsymbol{\eta}^{k+1} - \boldsymbol{\eta}^k|$ smaller than the tolerance for $\boldsymbol{\eta}$.

On substitution from (5.3.14) and (5.3.15) into (5.3.16)-(5.3.19), we can write the step 1. and 2. in Table 5.1 as a linear system using the notation

$$\boldsymbol{A}\boldsymbol{\Phi}^k = \boldsymbol{b}_1, \quad \boldsymbol{B}\boldsymbol{\eta}^{k+1} = \boldsymbol{b}_2, \tag{5.3.20}$$

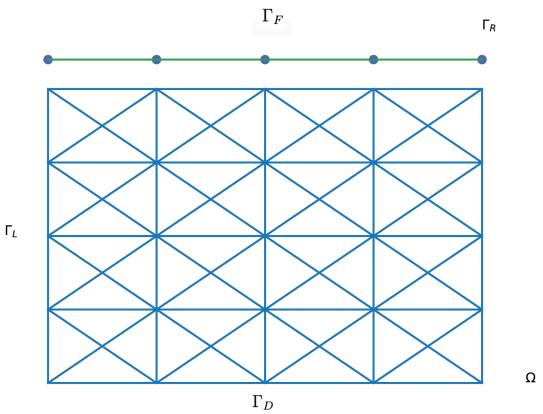

Figure 5.2: *The domain and the finite element mesh.*

where

$$\boldsymbol{A}_{ij} = \begin{cases} \int_\Omega \hat{\nabla}\zeta_i \cdot \hat{\nabla}\zeta_j d\Omega + \int_{\Gamma_D} \mu\zeta_i\zeta_j ds, & \text{for } \left(\tilde{X}_j, \hat{Y}_j\right) \in \Omega \setminus \Gamma_F, \\ \int_{\Gamma_F} \left(3\tilde{\zeta}_j - 2\tilde{X}\tilde{\zeta}_{j,\tilde{X}}\right) \xi_i d\tilde{X}, & \text{on } \Gamma_F \text{ and } \tilde{X} \neq L, \\ \lambda, \quad \text{at } \left(L, \frac{1}{2}\right), \end{cases} \tag{5.3.21}$$

$$\boldsymbol{b}_{1,i} = \begin{cases} \int_{\Gamma_D} \mu\hat{\phi}_\infty\zeta_i ds + \int_{\Gamma_L} \zeta_i ds, & \text{for } \left(\tilde{X}_j, \hat{Y}_j\right) \in \Omega \setminus \Gamma_F, \\ \int_{\Gamma_F} -\frac{2}{3\pi}\xi_i d\tilde{X} - \int_{\Gamma_F} \eta_h^k \xi_i d\tilde{X}, & \text{on } \Gamma_F \text{ and } \tilde{X} \neq L, \\ \lambda\hat{\phi}_\infty\left(R_\infty, \theta_\infty\right), & \text{otherwise}, \end{cases} \tag{5.3.22}$$

$$\boldsymbol{B}_{ij} = \int_{\Gamma_F} -2\xi_j\hat{\zeta}_i d\tilde{X} - \int_{\Gamma_F} 2\xi_j \left(\tilde{X}\hat{\zeta}_i\right)_{\tilde{X}} d\tilde{X}, \tag{5.3.23}$$

$$\boldsymbol{b}_{2,i} = -2L\hat{\eta}_\infty(L)\,\hat{\zeta}_i(L) - \int_{\Gamma_F} \frac{2}{\pi}\hat{\zeta}_i d\tilde{X} - \int_\Omega \hat{\nabla}\phi_h^k \cdot \hat{\nabla}\tilde{\zeta}_i d\Omega. \tag{5.3.24}$$

The triangulation of region Ω and linear finite elements of the boundary Γ_F at $\hat{Y} = \frac{1}{2}$ are shown in Figure 5.2. For simplicity, we denote the node at $(\tilde{X}, \hat{Y}) = (L, \frac{1}{2})$ as Γ_R. As in [56], consider a triangle K with nodes $\boldsymbol{N}_i = (\tilde{X}_i, \hat{Y}_i)$, $i = 1, 2, 3$. To each node $\boldsymbol{N}_i$ there is a hat function ζ_i, such that

$$\zeta_i\left(\tilde{X}, \hat{Y}\right) = a_i + b_i\tilde{X} + c_i\hat{Y}, \text{ and } \zeta_i(\boldsymbol{N}_j) = \begin{cases} 1, & i = j \\ 0, & i \neq j \end{cases} \tag{5.3.25}$$

where

$$a_i = \frac{\tilde{X}_j\hat{Y}_k - \tilde{X}_k\hat{Y}_j}{2 \mid K \mid}, \quad b_i = \frac{\hat{Y}_j - \hat{Y}_k}{2 \mid K \mid}, \quad c_i = \frac{\tilde{X}_k - \tilde{X}_j}{2 \mid K \mid},$$

for $i, j, k = 1, 2, 3$. Furthermore, we have a piecewise linear function $\hat{\zeta}_i$ and a piecewise constant function ξ_i on Γ_F such that

$$\xi_i\left(\tilde{X}_j\right) = \begin{cases} 1, & i = j, \\ 0, & \text{otherwse}, \end{cases} \qquad \hat{\zeta}_i\left(\tilde{X}\right) = \begin{cases} \frac{\tilde{X}-\tilde{X}_{i-1}}{\tilde{X}_i-\tilde{X}_{i-1}}, & \tilde{X}_{i-1} < \tilde{X} < \tilde{X}_i, \\ \frac{\tilde{X}_{i+1}-\tilde{X}}{\tilde{X}_{i+1}-\tilde{X}_i}, & \tilde{X}_i < \tilde{X} < \tilde{X}_{i+1}, \end{cases} \tag{5.3.26}$$

where $\tilde{X}_i$ is the $\tilde{X}$-coordinate of the node on Γ_F. Because $\tilde{\zeta}$ is the natural lifting of $\hat{\zeta}$, it is defined in the same way as $\hat{\zeta}$, that is,

$$\tilde{\zeta}_i\left(\tilde{X}, \hat{Y}\right) = a_i + b_i\tilde{X} + c_i\hat{Y}. \tag{5.3.27}$$

5.3.3 Numerical results

We compare the numerical results with far-field conditions in Figure 5.3. The numerical solutions for ϕ_h and η_h on Γ_F are consistent with the far-field conditions for large values of x on Γ_F, but the results are not consistent with the local solutions (5.2.22) and (5.2.33) when $\hat{R} \to 0$. Furthermore, the error convergence calculated as $\| \boldsymbol{\eta}_h^{i+1} - \boldsymbol{\eta}_h^i \|_{L_2}$ is also presented in Figure 5.4, in which the convergence rate is lower than 1 and is slow. Since the numerical solutions differ from the local solutions and fail to resolve the small oscillations in (5.2.33) near the intersection point, Newton's method is employed, as explained in the subsequent sections.

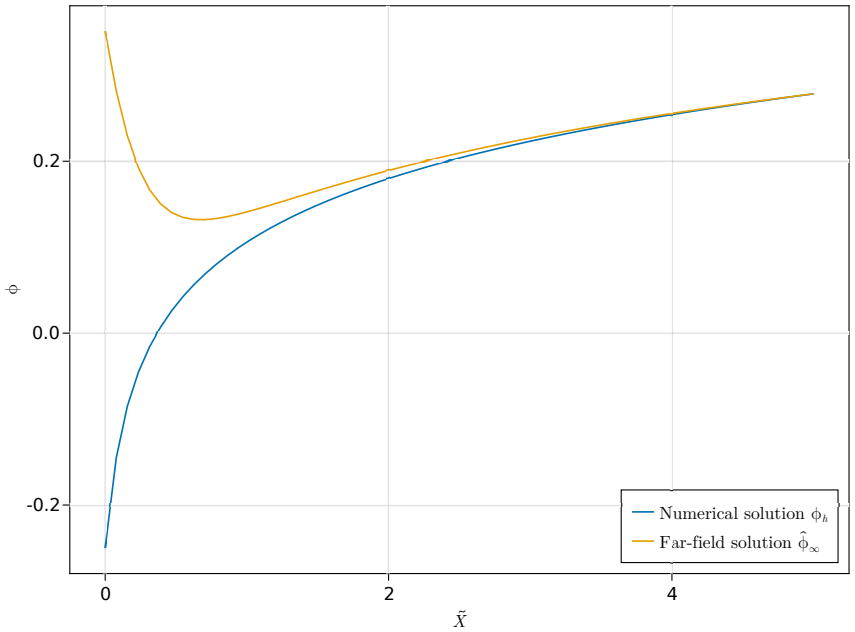

(a) *The numerical results ϕ_h and far-field condition for $\hat{\phi}_\infty$ on Γ_F.*

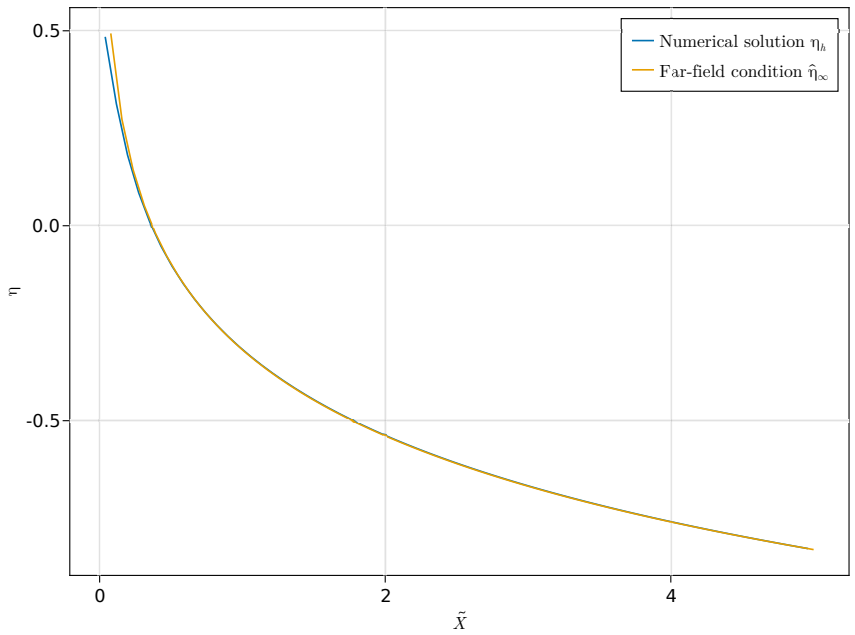

(b) *The numerical results η_h and far-field condition $\hat{\eta}_\infty$ on Γ_F.*

Figure 5.3: *(a) and (b) show the numerical results ϕ_h, η_h and far-field conditions $\hat{\phi}_\infty$, $\hat{\eta}_\infty$.*

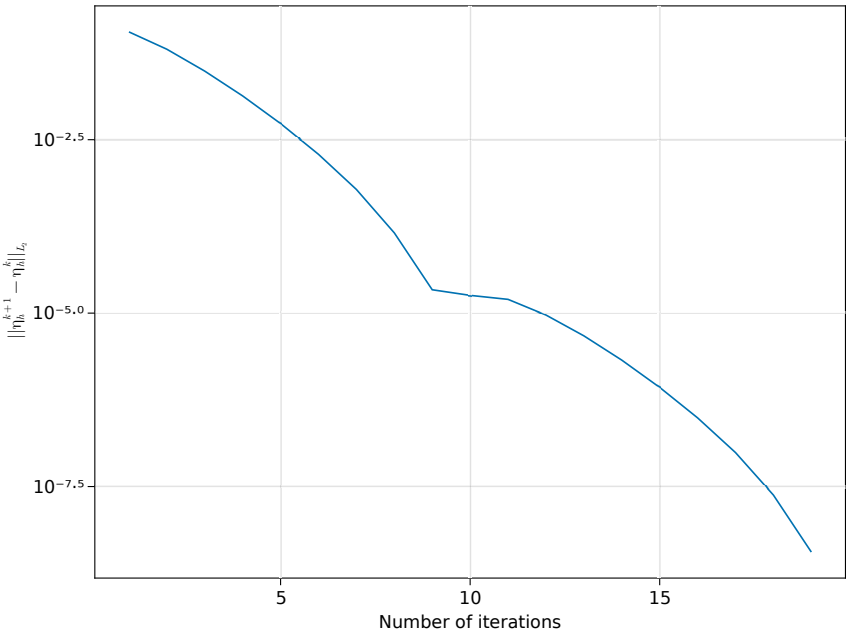

Figure 5.4: *The error convergence of $\boldsymbol{\eta}$ in L_2 norm.*

5.4 The review and the reformulation of the inner-region problem

To apply a numerical method to solve the problem (5.2.1)-(5.2.6), the free-boundary conditions (5.2.3) and (5.2.4) can be reformulated as

$$\nabla\phi \cdot \boldsymbol{n} = \gamma \boldsymbol{X} \cdot \boldsymbol{n}, \quad X > X_0, Y = \eta(X); \tag{5.4.1}$$

$$\frac{1}{2}|\nabla\phi|^2 - \gamma \boldsymbol{X} \cdot \nabla\phi + (2\gamma - 1)\phi = 0, \quad X > X_0, Y = \eta(X); \tag{5.4.2}$$

where $\boldsymbol{X} = (X, Y)$.

Now according to the Appendix B in [64], to reformulate this problem into a more convenient form, we rotate this coordinate system counterclockwise with $\alpha - \frac{\pi}{2}$ to give a new coordinate system $(\hat{X}, \hat{Y})$ (which is the different coordinate system from those in Appendix B), such that the plate is always vertical. The velocity potential is now denoted as $\hat{\Phi}(\hat{X}, \hat{Y})$ and the displacement of the free surface is denoted as $\left(\hat{X}, \hat{\eta}(\hat{X})\right)$. The contact point between the plate and the free surface

is denoted by $\left(\hat{X}_0, \hat{Y}_0\right)$, which is initially at the origin. We introduce the unit tangential vector $\hat{\boldsymbol{\tau}}$ of the free surface Γ_F as $\hat{\boldsymbol{\tau}} = \frac{1}{\sqrt{1+\left(\hat{\eta}_{\hat{X}}\right)^2}}\left(1, \hat{\eta}_{\hat{X}}\right)$ and the unit normal vector $\hat{\boldsymbol{n}}$ of Γ_F as $\hat{\boldsymbol{n}} = \frac{1}{\sqrt{1+\left(\hat{\eta}_{\hat{X}}\right)^2}}\left(-\hat{\eta}_{\hat{X}}, 1\right)$. Thus we have

$$\nabla\phi = \left(\hat{\nabla}\hat{\Phi}\cdot\hat{\boldsymbol{\tau}}\right)\hat{\boldsymbol{\tau}} + \left(\hat{\nabla}\hat{\Phi}\cdot\hat{\boldsymbol{n}}\right)\hat{\boldsymbol{n}}, \tag{5.4.3}$$

where $\nabla = (\partial_X, \partial_Y)$ is defined in the original coordinate system (X, Y) and $\hat{\nabla} = (\partial_{\hat{X}}, \partial_{\hat{Y}})$ is defined in the new coordinate system $(\hat{X}, \hat{Y})$. For simplicity, we introduce $\hat{\Phi}_{\hat{\boldsymbol{n}}} = \hat{\nabla}\hat{\Phi}\cdot\hat{\boldsymbol{n}}$ and $\hat{\Phi}_{\hat{\boldsymbol{\tau}}} = \hat{\nabla}\hat{\Phi}\cdot\hat{\boldsymbol{\tau}}$. On substitution from (5.4.3) and (5.4.1) into the Bernoulli condition (5.4.2), we obtain

$$\frac{1}{2}\left(\hat{\Phi}_{\hat{\boldsymbol{\tau}}}\right)^2 - \gamma\hat{\boldsymbol{X}}\cdot\hat{\boldsymbol{\tau}}\hat{\Phi}_{\hat{\boldsymbol{\tau}}} + (2\gamma-1)\hat{\Phi} - \frac{1}{2}\gamma^2\left(\hat{\boldsymbol{X}}\cdot\hat{\boldsymbol{n}}\right)^2 = 0, \quad \hat{X} > \hat{X}_0, \hat{Y} = \hat{\eta}(\hat{X}). \tag{5.4.4}$$

We denote the velocity potential on the free surface Γ_F as $\hat{\Phi}_F$. Now the coupled problem for the numerical method is reformulated as

$$\hat{\Phi}_{F,\hat{\boldsymbol{n}}} = \gamma\hat{\boldsymbol{X}}\cdot\hat{\boldsymbol{n}}, \quad \hat{X} > \hat{X}_0, \hat{Y} = \hat{\eta}(\hat{X}); \tag{5.4.5}$$

$$\frac{1}{2}\left(\hat{\Phi}_{F,\hat{\boldsymbol{\tau}}}\right)^2 - \gamma\hat{\boldsymbol{X}}\cdot\hat{\boldsymbol{\tau}}\hat{\Phi}_{F,\hat{\boldsymbol{\tau}}} + (2\gamma-1)\hat{\Phi}_F - \frac{1}{2}\gamma^2\left(\hat{\boldsymbol{X}}\cdot\hat{\boldsymbol{n}}\right)^2 = 0, \quad \hat{X} > \hat{X}_0, \hat{Y} = \hat{\eta}(\hat{X}); \tag{5.4.6}$$

$$\hat{\Phi}_F\left(\hat{R}, \hat{\theta}\right) \sim -\hat{R}^{\frac{\pi}{2\alpha}}\cos\left[\frac{\pi}{2\alpha}\left(\hat{\theta} + \frac{\pi}{2}\right)\right] + \frac{\pi^2}{12\alpha^2\cos 2\alpha}\hat{R}^{\frac{\pi}{\alpha}-2}\cos\left[\left(\frac{\pi}{\alpha} - 2\right)\left(\theta + \frac{\pi}{2}\right)\right]$$
$$\text{as } \hat{R} = \sqrt{\hat{L}^2 + \left(\hat{\eta}(\hat{L})\right)^2} \to +\infty, \hat{\theta} = \arctan\frac{\hat{\eta}(\hat{L})}{\hat{L}}; \tag{5.4.7}$$

$$\hat{\eta}\left(\hat{L}\right) = \hat{\eta}_\infty\left(\hat{L}\right) \quad \text{as } \hat{L} \to +\infty; \tag{5.4.8}$$

where

$$\hat{\nabla}^2\hat{\Phi} = 0, \quad -\infty < \hat{X} < \infty, \hat{Y} < \hat{\eta}; \tag{5.4.9}$$

$$\hat{\Phi}_{\hat{\boldsymbol{n}}} = 0, \quad \hat{X} = 0, \hat{Y} < \hat{Y}_0; \tag{5.4.10}$$

$$\hat{\Phi} = \hat{\Phi}_F, \quad \hat{X} > \hat{X}_0, \hat{Y} = \hat{\eta}(\hat{X}); \tag{5.4.11}$$

$$\hat{\Phi}\left(\hat{R}, \hat{\theta}\right) = \hat{\Phi}_\infty\left(\hat{R}, \hat{\theta}\right) \text{ as } \hat{R} \to +\infty, -\frac{\pi}{2} < \hat{\theta} < \alpha - \frac{\pi}{2}, \tag{5.4.12}$$

with

$$\begin{aligned}
\hat{\eta}_\infty\left(\hat{X}\right) &\sim -\cot\alpha\hat{X} + \frac{\pi}{4\alpha\sin\alpha}\left(\frac{\hat{X}}{\sin\alpha}\right)^{\frac{\pi}{2\alpha}-1} \\
\hat{\Phi}_\infty\left(\hat{R}, \hat{\theta}\right) &\sim -\hat{R}^{\frac{\pi}{2\alpha}}\cos\left[\frac{\pi}{2\alpha}\left(\hat{\theta} + \frac{\pi}{2}\right)\right] + \frac{\pi^2}{12\alpha^2\cos 2\alpha}\hat{R}^{\frac{\pi}{\alpha}-2}\cos\left[\left(\frac{\pi}{\alpha} - 2\right)\left(\hat{\theta} + \frac{\pi}{2}\right)\right].
\end{aligned}$$

This reformulation allows us to solve for $\hat{\Phi}$ in the fixed domain first and then find the solutions for $(\hat{\Phi}_F, \hat{\eta})$ on Γ_F which satisfies the free-boundary conditions simultaneously.

5.4.1 Weak forms

The domain occupied by the fluid is denoted as $\Omega := \{\left(\hat{X}, \hat{Y}\right) : 0 \leq \hat{X} \leq \hat{L}, -\hat{L} \leq \hat{Y} \leq \hat{\eta}\left(\hat{X}\right)\}$ for $\hat{L} \to +\infty$. The boundary $\partial\Omega$ can be separated into four parts: the free boundary Γ_F at $\hat{Y} = \hat{\eta}\left(\hat{X}\right)$, the boundary of the plate Γ_L at $\hat{X} = 0$, and the truncated boundary $\Gamma_D := \{\left(\hat{X}, \hat{Y}\right) : \hat{X} = \hat{L}, \text{ or } \hat{Y} = -\hat{L}\}$ where the far-field condition is applied.

The first weak form is obtained from the BVP (5.4.9)-(5.4.12) which solves the velocity potential $\hat{\phi}$ in the domain Ω. We introduce the test function $v \in V := \{v \in \mathcal{C}^1(\Omega) \,|v = 0 \text{ on } \Gamma_F\}$. Multiplying (5.4.9) with the test function v, integrating over

Ω, and using the boundary condition (5.4.10)-(5.4.12), we obtain:

$$\begin{aligned} -\int_{\Omega} \hat{\nabla}^2 \hat{\Phi} v d\Omega &= \int_{\Omega} \hat{\nabla}\hat{\Phi} \cdot \hat{\nabla} v d\Omega - \int_{\partial\Omega} \hat{\Phi}_{\boldsymbol{n}} v d\Gamma \\ &= \int_{\Omega} \hat{\nabla}\hat{\Phi} \cdot \hat{\nabla} v d\Omega + \int_{\Gamma_D} \mu \left(\hat{\Phi} - \hat{\Phi}_{\infty}\right) v d\Gamma + \int_{\Gamma_F} \mu \left(\hat{\Phi} - \hat{\Phi}_F\right) v d\Gamma, \\ &= 0. \end{aligned} \tag{5.4.13}$$

To find the velocity potential $\hat{\Phi}_F$ on the free boundary and the displacement of the free surface $\hat{\eta}$, we need to introduce the weak forms of (5.4.5) and (5.4.6). We multiply (5.4.5),(5.4.6) with a test function $w \in W := \{w \in \mathcal{C}^0(\Gamma_F) : w = 0 \text{ at } \hat{X} = 0\}$ and then integrate over Γ_F to obtain

$$\mathcal{R}_1((\hat{\Phi}_F, \hat{\eta}); w) = 0, \quad \forall w \in W, \tag{5.4.14}$$

$$\mathcal{R}_2((\hat{\Phi}_F, \hat{\eta}); w) = 0, \quad \forall w \in W, \tag{5.4.15}$$

where the semilinear forms $\mathcal{R}_1((\hat{\Phi}_F, \hat{\eta}); w)$ and $\mathcal{R}_2((\hat{\Phi}_F, \hat{\eta}); w)$ are defined as

$$\mathcal{R}_1((\hat{\Phi}_F, \hat{\eta}); w) = \int_{\Gamma_F} \hat{\Phi}_{F,\boldsymbol{n}} w d\Gamma - \int_{\Gamma_F} \gamma \hat{\boldsymbol{X}} \cdot \hat{\boldsymbol{n}} w d\Gamma, \tag{5.4.16}$$

$$\mathcal{R}_2((\hat{\Phi}_F, \hat{\eta}); w) = \int_{\Gamma_F} \left[\frac{1}{2}\left(\hat{\Phi}_{F,\hat{\boldsymbol{\tau}}}\right)^2 - \gamma \hat{\boldsymbol{X}} \cdot \hat{\boldsymbol{\tau}} \hat{\Phi}_{F,\hat{\boldsymbol{\tau}}} + (2\gamma - 1)\hat{\Phi}_F - \frac{1}{2}\gamma^2 \left(\hat{\boldsymbol{X}} \cdot \hat{\boldsymbol{n}}\right)^2\right] w d\Gamma. \tag{5.4.17}$$

The semilinear form $\mathcal{R}_2((\hat{\Phi}_F, \hat{\eta}); w)$ is derived by integration by parts and the divergence theorem.

Assuming a referenced boundary Γ_0 at $\hat{Y} = 0$ and the boundary Γ_η at $\hat{Y} = \hat{\eta}\left(\hat{X}\right)$, we define the map

$$T_\eta : \gamma_0 \to \Gamma_\eta, \quad T_\eta(\boldsymbol{x}_0) = \boldsymbol{x}_0 + \begin{pmatrix} 0 \\ \hat{\eta}(x_0) \end{pmatrix} \tag{5.4.18}$$

such that for any test function $\tilde{w} \in \tilde{W} := \{\tilde{w} \in \mathcal{C}^0(\Gamma_0) : \tilde{w} = 0 \text{ at } \hat{X} = 0\}$,

$$w = \tilde{w} \circ T_\eta^{-1},$$

where $\boldsymbol{x}_0 = (x_0, y_0)$ on Γ_0. Thus

$$\begin{aligned}\int_{\Gamma_F} (\cdot)\, w d\Gamma &= \int_{\Gamma_F} (\cdot) \left(\tilde{w} \circ T_\eta^{-1}\right) d\Gamma \\ &= \int_{\Gamma_0} (\cdot) \circ T_\eta \tilde{w} \sqrt{1 + \left(\hat{\eta}'\left(\hat{X}\right)\right)^2} d\hat{X}.\end{aligned}$$

Then, the semilinear form $\mathcal{R}_1((\hat{\Phi}_F, \hat{\eta}); w)$ can be reformulated as

$$\begin{aligned}\mathcal{R}_1((\hat{\Phi}_F, \hat{\eta}); w) &= \int_{\Gamma_F} \hat{\Phi}_{F,\hat{\boldsymbol{n}}} w d\Gamma - \int_{\Gamma_F} \gamma \hat{\boldsymbol{X}} \cdot \hat{\boldsymbol{n}} \left(\tilde{w} \circ T_\eta^{-1}\right) d\Gamma \\ &= \int_\Omega \hat{\nabla}\hat{\Phi} \cdot \hat{\nabla}\hat{w} d\Omega - \int_{\Gamma_0} \gamma \left(-\hat{X}\hat{\eta}'(\hat{X}) + \hat{\eta}(\hat{X})\right) \tilde{w} d\hat{X},\end{aligned} \tag{5.4.19}$$

where we change the variables from the arclength to $\hat{X}$ and $\hat{\boldsymbol{X}} \cdot \hat{\boldsymbol{n}} = \frac{-\hat{X}\hat{\eta}'(\hat{X}) + \hat{\eta}(\hat{X})}{\sqrt{1 + \left(\hat{\eta}'(\hat{X})\right)^2}}$. In the second step, we use integration by parts as well with $\hat{w} \in \hat{W}$ as the natural lifting of w into $\mathcal{C}^1(\Omega)$ and the natural lifting of $\hat{\Phi}_F$ is just $\hat{\Phi}$.

5.4.2 Linearisation

We linearise $\mathcal{R}_1((\hat{\Phi}_F, \hat{\eta}); w)$ and $\mathcal{R}_2((\hat{\Phi}_F, \hat{\eta}); w)$ at an arbitrary approximation pair $\left(\tilde{\Phi}_F, \tilde{\eta}\left(\hat{X}\right)\right)$ by evaluating the partial derivative of the weak forms (5.4.17) and (5.4.19) with respect to $\hat{\Phi}_F$ and $\hat{\eta}$. We assume that the approximation-pair is compatible on Γ_F and satisfies the boundary conditions at $\hat{X} = \hat{L}$ within the approximated domain $\tilde{\Omega}$. We also denote the corresponding approximate free boundary as $\tilde{\Gamma}_F : \tilde{\boldsymbol{X}} = \left(\hat{X}, \tilde{\eta}\left(\hat{X}\right)\right)$.

Recall the definition of the derivative of a function; we find the partial derivative

1. Initialize with $\left(\tilde{\Phi}_F^0, \tilde{\eta}^0\right)$; set $k = 0$.
2. Given $\left(\tilde{\Phi}_F^k, \tilde{\eta}^k\right)$, solve the boundary-value problem (5.4.9)-(5.4.12) for $\hat{\Phi}^k$.
3. Given $\left(\tilde{\Phi}_F^k, \tilde{\eta}^k\right)$ and $\hat{\Phi}^k$, find the partial derivatives $\partial_{\delta\Phi}\mathcal{R}_i\left(\left(\tilde{\Phi}_F, \tilde{\eta}\right); w\right)$ and $\partial_{\delta\eta}\mathcal{R}_1\left(\left(\tilde{\Phi}_F, \tilde{\eta}\right); w\right)$ for $i = 1, 2$.
4. Solve the free boundary problem (5.5.4) and (5.5.5) with the boundary condition (5.4.7) and (5.4.8) for $(\delta\Phi, \delta\eta)$.
5. Update the free boundary displacement $\tilde{\eta}^{k+1}$ as
$$\tilde{\eta}^{k+1} = \tilde{\eta}^k + \delta\eta.$$
and $\tilde{\Phi}_F^{k+1}$ as
$$\tilde{\Phi}_F^{k+1} = \tilde{\Phi}_F^k + \delta\Phi.$$
Then repeat from step 2. until convergence.

Table 5.2: The finite difference Newton's method solving for $(\delta\Phi, \delta\eta)$.

with respect to $\hat{\Phi}_F$ as

$$\partial_{\delta\Phi}\mathcal{R}_i\left(\left(\tilde{\Phi}_F, \tilde{\eta}\right); w\right) = \lim_{\epsilon\to 0}\frac{\mathcal{R}_i\left(\left(\tilde{\Phi}_F + \epsilon, \tilde{\eta}\right); w\right) - \mathcal{R}_i\left(\left(\tilde{\Phi}_F, \tilde{\eta}\right); w\right)}{\epsilon}, \tag{5.4.20}$$

and the partial derivatives with respect to $\hat{\eta}$ as

$$\partial_{\delta\eta}\mathcal{R}_i\left(\left(\tilde{\Phi}_F, \tilde{\eta}\right); w\right) = \lim_{\epsilon\to 0}\frac{\mathcal{R}_i\left(\left(\tilde{\Phi}_F, \tilde{\eta} + \epsilon\right); w\right) - \mathcal{R}_i\left(\left(\tilde{\Phi}_F, \tilde{\eta}\right); w\right)}{\epsilon}, \tag{5.4.21}$$

for $i = 1, 2$.

Note that when evaluating $\mathcal{R}_2\left(\left(\tilde{\Phi}_F, \tilde{\eta} + \epsilon\right); w\right)$, this semilinear form should be integrated along the approximated free boundary $\hat{\Gamma}_F : \hat{\eta} = \tilde{\eta}(\hat{X}) + \epsilon$.

5.5 Newton's Method

Now we introduce the approximations $\left(\tilde{\Phi}_F, \tilde{\eta}\right)$

$$\hat{\Phi}_F = \tilde{\Phi}_F + \delta\Phi, \quad \hat{\eta}(\hat{X}) = \tilde{\eta}(\hat{X}) + \delta\eta, \tag{5.5.1}$$

where $\delta\Phi$ and $\delta\eta$ are the corrections evaluated in the approximated domain $\tilde{\Omega}$. The Newton's method for $(\delta\Phi_F, \delta\eta)$ would be

$$\left\langle \partial_{(\delta\Phi,\delta\eta)}\mathcal{R}_1\left(\left(\tilde{\Phi}_F, \tilde{\eta}\right); w\right), (\delta\Phi, \delta\eta)\right\rangle = -\mathcal{R}_1\left(\left(\tilde{\Phi}, \tilde{\eta}\right); w\right) \quad \forall w \in W, \tag{5.5.2}$$

$$\left\langle \partial_{(\delta\Phi,\delta\eta)}\mathcal{R}_2\left(\left(\tilde{\Phi}_F, \tilde{\eta}\right); w\right), (\delta\Phi, \delta\eta)\right\rangle = -\mathcal{R}_2\left(\left(\tilde{\Phi}, \tilde{\eta}\right); w\right) \quad \forall w \in W. \tag{5.5.3}$$

Following from (5.4.20)-(5.4.21), we obtain the following scheme

$$\begin{aligned} -\mathcal{R}_1\left(\left(\tilde{\Phi}_F, \tilde{\eta}\right); w\right) &= \lim_{\delta\Phi\to 0} \frac{\mathcal{R}_1\left((\tilde{\Phi}_F + \delta\Phi, \tilde{\eta}); w\right) - \mathcal{R}_1\left((\tilde{\Phi}_F, \tilde{\eta}); w\right)}{\delta\Phi} \\ &+ \lim_{\delta\eta\to 0} \frac{\mathcal{R}_1\left((\tilde{\Phi}_F, \tilde{\eta} + \delta\eta); w\right) - \mathcal{R}_1\left((\tilde{\Phi}_F, \tilde{\eta}); w\right)}{\delta\eta}; \end{aligned} \tag{5.5.4}$$

$$\begin{aligned} -\mathcal{R}_2\left(\left(\tilde{\Phi}_F, \tilde{\eta}\right); w\right) &= \lim_{\delta\Phi\to 0} \frac{\mathcal{R}_2\left((\tilde{\Phi}_F + \delta\Phi, \tilde{\eta}); w\right) - \mathcal{R}_2\left((\tilde{\Phi}_F, \tilde{\eta}); w\right)}{\delta\Phi} \\ &+ \lim_{\delta\eta\to 0} \frac{\mathcal{R}_2\left((\tilde{\Phi}_F, \tilde{\eta} + \delta\eta); w\right) - \mathcal{R}_2\left((\tilde{\Phi}_F, \tilde{\eta}); w\right)}{\delta\eta}, \end{aligned} \tag{5.5.5}$$

for $\forall w \in W$.

Newton's scheme is shown in Table.5.2. Recall that in (5.4.19) it requires $\hat{\Phi}$, thus in each iteration, we need to solve the boundary value problem (5.4.9)-(5.4.12) for $\hat{\Phi}$ before solving for the correction pair $(\delta\Phi, \delta\eta)$.

As we mentioned at the end of section 5.4.1, to evaluate the semilinear forms $\mathcal{R}_2\left(\left(\tilde{\Phi}_F, \tilde{\eta} + \delta\eta\right); w\right)$ and $\mathcal{R}_2\left(\left(\tilde{\Phi}_F, \tilde{\eta} + \eta\right); w\right)$, we need to integrate in the domain $\hat{\Omega}$ with the free boundary $\hat{\Gamma} : \hat{\eta}(X) = \tilde{\eta}\left(\hat{X}\right) + \delta\eta$ and along the free boundary $\hat{\Gamma}$. It also requires us to find $\hat{\Phi}$ in $\hat{\Omega}$ by solving the boundary problem (5.4.9)-(5.4.12).

5.5.1 Implementation

We consider $\hat{\Phi} \in V$, $\hat{\Phi}_F \in \hat{V} := \{\hat{v} \in \mathcal{C}^1(\Gamma_F)\}$, and $\hat{\eta} \in \hat{V}$ such that

$$\delta\Phi \in \hat{V}, \quad \tilde{\Phi}_F \in \hat{V}, \quad \delta\eta \in \hat{V}, \quad \tilde{\eta} \in \hat{V}.$$

Let $\{\hat{\zeta}_i\}_{i=1}^n$, $\{\hat{\xi}_i\}_{i=1}^n$, $\{\tilde{\xi}_i\}_{i=1}^n$ and $\{\xi_i\}_{i=1}^n$ be the basis for $\hat{V}$, $\hat{W}$, $\tilde{W}$ and W correspondingly associated with n nodes on Γ_F. The finite element approximation pair $(\delta\Phi_h, \delta\eta_h)$ for $(\delta\Phi, \delta\eta)$ is defined as

$$\delta\Phi_h\left(\hat{X}, \hat{Y}\right) = \sum_i \delta\Phi_{h,i}\hat{\zeta}_i\left(\hat{X}, \hat{Y}\right); \tag{5.5.6}$$

$$\delta\eta_h\left(\hat{X}\right) = \sum_i \delta\eta_{h,i}\hat{\zeta}_i\left(\hat{X}, \tilde{\eta}(\hat{X})\right). \tag{5.5.7}$$

Similarly, we have the finite element approximation pair (Φ_h, η_h) for $(\tilde{\Phi}_F, \tilde{\eta})$ defined as

$$\Phi_h\left(\hat{X}, \hat{Y}\right) = \sum_i \Phi_{h,i}\hat{\zeta}_i\left(\hat{X}, \hat{Y}\right); \tag{5.5.8}$$

$$\eta_h\left(\hat{X}\right) = \sum_i \eta_{h,i}\hat{\zeta}_i\left(\hat{X}, \tilde{\eta}(\hat{X})\right). \tag{5.5.9}$$

Furthermore, let $\{\psi_i\}_{i=1}^N$ be the basis for V associated with N interior nodes in Ω, we have the finite element approximation ϕ_h for $\hat{\Phi}$

$$\phi_h\left(\hat{X}, \hat{Y}\right) = \sum_i \phi_{h,i}\psi_i\left(\hat{X}, \hat{Y}\right). \tag{5.5.10}$$

We collect the independent variables in the vectors

$$\delta\boldsymbol{\Phi} = \begin{pmatrix} \delta\Phi_{h,1} \\ \delta\Phi_{h,2} \\ \vdots \end{pmatrix}, \quad \delta\boldsymbol{\eta} = \begin{pmatrix} \delta\eta_{h,1} \\ \delta\eta_{h,2} \\ \vdots \end{pmatrix}, \quad \boldsymbol{\Phi}_h = \begin{pmatrix} \Phi_{h,1} \\ \Phi_{h,2} \\ \vdots \end{pmatrix}, \quad \boldsymbol{\eta}_h = \begin{pmatrix} \eta_{h,1} \\ \eta_{h,2} \\ \vdots \end{pmatrix}.$$

Now the Newton's scheme (5.5.4) and (5.5.5) can be written as a linear system

$$\boldsymbol{J} \cdot \begin{pmatrix} \delta \boldsymbol{\Phi} \\ \delta \boldsymbol{\eta} \end{pmatrix} = \boldsymbol{r}. \tag{5.5.11}$$

The Jacobian matrix $\boldsymbol{J}$ and the residual vector $\boldsymbol{r}$ are denoted as

$$\boldsymbol{J} = \begin{pmatrix} \boldsymbol{A} & \boldsymbol{B} \\ \boldsymbol{C} & \boldsymbol{D} \end{pmatrix}, \qquad \boldsymbol{r} = \begin{pmatrix} \boldsymbol{r}^1 \\ \boldsymbol{r}^2 \end{pmatrix}, \tag{5.5.12}$$

where

$$\begin{aligned}
\boldsymbol{A}_{ij} &= \partial_{\delta\Phi}\mathcal{R}_1\left(\left(\Phi_{h,j}\hat{\zeta}_j, \eta_h\right); \xi_i\right) = \lim_{\epsilon\to 0} \frac{\mathcal{R}_1\left(\left((\Phi_{h,j}+\epsilon)\hat{\zeta}_j, \eta_h\right); \xi_i\right) - \mathcal{R}_1\left(\left(\Phi_{h,j}\hat{\zeta}_j, \eta_h\right); \xi_i\right)}{\epsilon}, \\
\boldsymbol{B}_{ij} &= \partial_{\delta\eta}\mathcal{R}_1\left(\left(\Phi_h, \eta_{h,j}\hat{\zeta}_j\right); \xi_i\right) = \lim_{\epsilon\to 0} \frac{\mathcal{R}_1\left(\left(\Phi_h, (\eta_{h,j}+\epsilon)\hat{\zeta}_j\right); \xi_i\right) - \mathcal{R}_1\left(\left(\Phi_h, \eta_{h,j}\hat{\zeta}_j\right); \xi_i\right)}{\epsilon}, \\
\boldsymbol{C}_{ij} &= \partial_{\delta\Phi}\mathcal{R}_2\left(\left((\Phi_{h,j}\hat{\zeta}_j, \eta_h\right); \xi_i\right) = \lim_{\epsilon\to 0} \frac{\mathcal{R}_2\left(\left(\Phi_{h,j}+\epsilon)\hat{\zeta}_j, \eta_h\right); \xi_i\right) - \mathcal{R}_2\left(\left(\Phi_{h,j}\hat{\zeta}_j, \eta_h\right); \xi_i\right)}{\epsilon}, \\
\boldsymbol{D}_{ij} &= \partial_{\delta\eta}\mathcal{R}_2\left(\left(\Phi_h, \eta_{h,j}\hat{\zeta}_j\right); \xi_i\right) = \lim_{\epsilon\to 0} \frac{\mathcal{R}_2\left(\left(\Phi_h, (\eta_h+\epsilon)\hat{\zeta}_j\right); \xi_i\right) - \mathcal{R}_2\left(\left(\Phi_h, \eta_{h,j}\hat{\zeta}_j\right); \xi_i\right)}{\epsilon}, \\
\boldsymbol{r}_i^1 &= \mathcal{R}_1\left((\Phi_h, \eta_h); \xi_i\right) = \int_{\Gamma_F} \hat{\nabla}\phi_h \cdot \hat{\nabla}\hat{\xi}_i d\Gamma - \int_{\Gamma_0} \gamma\left(-\hat{X}\eta_h' + \eta_h\right)\tilde{\xi}_i dx, \\
\boldsymbol{r}_i^2 &= \mathcal{R}_2\left((\Phi_h, \eta_h); \xi_i\right) = \int_{\Gamma_F} \left[\frac{1}{2}\Phi_{h,\hat{\boldsymbol{\tau}}}^2 - \gamma\hat{\boldsymbol{X}} \cdot \hat{\boldsymbol{\tau}}\Phi_{h,\hat{\boldsymbol{\tau}}} + (2\gamma-1)\Phi_h - \frac{1}{2}\gamma^2\left(\hat{\boldsymbol{X}} \cdot \hat{\boldsymbol{n}}\right)^2\right]\xi_i d\Gamma.
\end{aligned} \tag{5.5.13}$$

The first order derivative η_h' and the tangential derivative $\Phi_{h,\hat{\boldsymbol{\tau}}}$ can be approximated by forward difference method as

$$\eta_{h,i}' = \frac{\eta_{h,i+1} - \eta_{h,i}}{\hat{X}_{i+1} - \hat{X}_i}, \qquad \Phi_{h,\hat{\boldsymbol{\tau}}} = \frac{d\Phi_h}{d\hat{s}} = \frac{\Phi_{h,i+1} - \Phi_{h,i}}{\hat{s}_{i+1} - \hat{s}_i}, \tag{5.5.14}$$

where $\hat{s}$ is the arc length measured from the contact point of the free surface and the inclined plate to the nodes $\left(\hat{X}_i, \hat{Y}_i\right)$.

The blocks $\boldsymbol{A}$ and $\boldsymbol{C}$ can be implemented straightforwardly. However, the implementation for block $\boldsymbol{B}$ and $\boldsymbol{D}$ requires an approximation along the free-boundary $\hat{\Gamma}_F : \left\{ \left(\hat{X}, \hat{Y} \right) : \hat{Y} = \sum_i (\eta_{h,i} + \epsilon) \hat{\zeta}_i \right\}$. Thus, we also need to find an approximation for ϕ_h in Ω with the free boundary $\hat{\Gamma}_F$ to estimate the block $\boldsymbol{B}$, which can be found by solving the boundary-value problem (5.4.9)-(5.4.12).

The finite element approximation of the weak form (5.4.13) for ϕ_h is obtained as:

$$\int_\Omega \hat{\nabla}^2 \phi_h v d\Omega = \int_\Omega \hat{\nabla} \phi_h \cdot \hat{\nabla} v d\Omega + \int_{\Gamma_D} \mu \left(\phi_h - \hat{\Phi}_\infty \right) v d\Gamma + \int_{\Gamma_F} \mu \left(\phi_h - \Phi_h \right) v d\Gamma. \tag{5.5.15}$$

We collect the degrees of freedom in the vector

$$\boldsymbol{\phi} = \begin{pmatrix} \phi_{h,1} \\ \phi_{h,2} \\ \vdots \end{pmatrix}.$$

Inserting (5.5.10) into (5.5.15), we have the linear system

$$\boldsymbol{M} \cdot \boldsymbol{\phi} = \boldsymbol{b} \tag{5.5.16}$$

where

$$\begin{aligned} \boldsymbol{M}_{ij} &= \int_\Omega \hat{\nabla} \psi_i \cdot \hat{\nabla} \psi_j d\Omega + \int_{\Gamma_D} \mu \psi_i \psi_j f \Gamma + \int_{\Gamma_F} \mu \psi_i \psi_j d\Gamma, \\ \boldsymbol{b}_i &= \int_{\Gamma_D} \mu \hat{\Phi}_\infty \psi_i d\Gamma + \int_{\Gamma_F} \mu \Phi_h \psi_i d\Gamma. \end{aligned}$$

The discrete Newton-Galerkin method is now formulated with the algorithm shown in Table 5.3. Figure 5.5 illustrates the triangulation of region Ω and linear finite elements of the boundary Γ_F with the reference boundary Γ_0. For simplicity, we denote the node at $(\hat{X}, \hat{Y}) = (\hat{L}, \hat{Y})$ as Γ_R. Similar to Section 6.6.2, we consider

1. Initialize with $\left(\boldsymbol{\Phi}_h^0, \boldsymbol{\eta}_h^0\right)$; set $k = 0$.

2. Given $\left(\boldsymbol{\Phi}_h^k, \boldsymbol{\eta}_h^k\right)$, solve the boundary-value problem (5.5.16) for $\boldsymbol{\phi}_h^k$.
3. Given $\left(\boldsymbol{\Phi}_h^k, \boldsymbol{\eta}_h^k\right)$ and $\boldsymbol{\phi}_h^k$, find the Jacobian matrix $\boldsymbol{J}$ and the residuals $\boldsymbol{r}$ with entries defined as (5.5.13).
4. Solve the linear system (5.5.11) for $(\delta\boldsymbol{\Phi}_h, \delta\boldsymbol{\eta}_h)$.

5. Update the free boundary displacement $\boldsymbol{\eta}_h^{k+1}$ as

$$\boldsymbol{\eta}_h^{k+1} = \boldsymbol{\eta}_h^k + \delta\boldsymbol{\eta}.$$

and $\boldsymbol{\Phi}_h^{k+1}$ as

$$\boldsymbol{\Phi}_h^{k+1} = \boldsymbol{\Phi}_h^k + \delta\boldsymbol{\Phi}_h.$$

Then repeat from step 2. until convergence.

Table 5.3: The algorithm for finite difference Newton's method solving for the single fluid/solid interaction problem in the inner region.

a triangle K with nodes $\boldsymbol{N}_i = (\hat{X}_i, \hat{Y}_i)$, $i = 1, 2, 3$. To each node $\boldsymbol{N}_i$ there is a hat function ψ_i, such that

$$\psi_i\left(\hat{X}, \hat{Y}\right) = a_i + b_i\hat{X} + c_i\hat{Y}, \text{ and } \quad \psi_i(\boldsymbol{N}_j) = \begin{cases} 1, & i = j \\ 0, & i \neq j \end{cases}, \tag{5.5.17}$$

where

$$a_i = \frac{\hat{X}_j\hat{Y}_k - \hat{X}_k\hat{Y}_j}{2 \mid K \mid}, \quad b_i = \frac{\hat{Y}_j - \hat{Y}_k}{2 \mid K \mid}, \quad c_i = \frac{\hat{X}_k - \hat{X}_j}{2 \mid K \mid},$$

for $i, j, k = 1, 2, 3$ with $|K|$ representing the area of the triangle K.

Furthermore, we have a piecewise linear function $\hat{\zeta}_i$ and a piecewise constant function ξ_i on Γ_F such that

$$\xi_i\left(\hat{s}_j\right) = \begin{cases} 1, & i = j, \\ 0, & \text{otherwse}, \end{cases} \qquad \hat{\zeta}_i\left(\hat{s}\right) = \begin{cases} \frac{\hat{s}-\hat{s}_{i-1}}{\hat{s}_i-\hat{s}_{i-1}}, & \hat{s}_{i-1} < \hat{s} < \hat{s}_i, \\ \frac{\hat{s}_{i+1}-\hat{s}}{\hat{s}_{i+1}-\hat{s}_i}, & \hat{s}_i < \hat{s} < \hat{s}_{i+1}, \end{cases}. \tag{5.5.18}$$

Similarly, we have the piecewise constant function $\tilde{\zeta}_i$ on the reference configuration

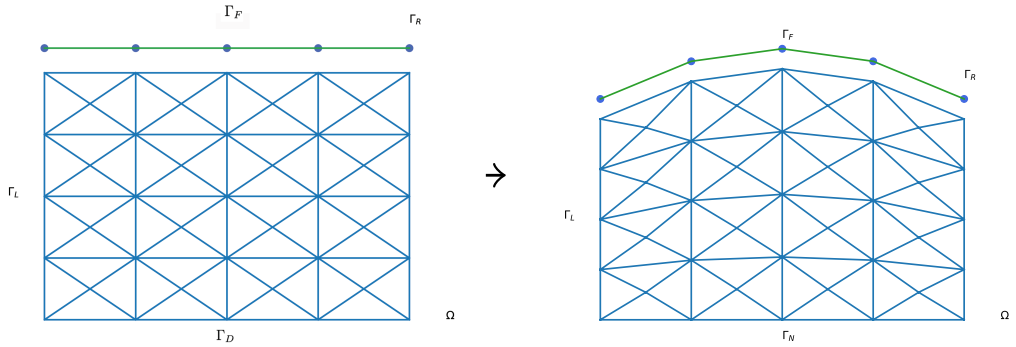

Figure 5.5: *Conforming finite element mesh. The left is the mesh with an initial guess of the free boundary* Γ_0*, while the right is the mesh with the updated free boundary* Γ_F*.*

Γ_0 as

$$\tilde{\xi}_i\left(\hat{X}_j\right) = \begin{cases} 1, & i = j, \\ 0, & \text{otherwse}, \end{cases}.$$

Because $\hat{\xi}_i$ is the natural lifting of ξ_i into $\mathcal{C}^1(\Omega)$, it is defined in the same way as ψ_i, that is,

$$\hat{\xi}_i\left(\hat{X}, \hat{Y}\right) = a_i + b_i\hat{X} + c_i\hat{Y}.$$

5.5.2 Numerical Results

Following the algorithm given in Table 5.3 with continuation in the angle α, we find that the displacement $\hat{\eta}$ of the free boundary is always perpendicular to the plate, and there is no solution for $\alpha \geq \alpha_c$, where

$$\alpha_c \approx 1.8886.$$

We start with $\alpha = \frac{\pi}{2}$, then slightly raise the value of α with the numerical results $\hat{\eta}$ from the problem with a lower value of α as the initial guess of the free surface. The critical value of α_c can be determined once the numerical solver cannot converge to a solution.

Figure 5.6 shows graphs of the free surface for $\hat{X} \geq \hat{X}_0$, where the straight black

lines represent the moving plates with various angles $\alpha \in \left[\frac{\pi}{2}, \alpha_c\right]$. The condition that the free surface is perpendicular to the plate is consistent with the analysis in [64] such that

$$\eta_{\hat{X}}(\hat{X}_0) = \cot \alpha.$$

However, the critical value of angle α in that paper is approximately 1.791, slightly lower than our results. The possible reasons are that our mesh is not fine enough, and the value of L is also not large enough. Here, we discretized the x-axis non-uniformly with 500 points such that the initial length of the elements is 2×10^{-3}. The Jacobian matrix is only updated when it is necessary to shorten the running time: after every five iterations and when it converges to a solution. We set the value of μ to 10^{10}, which is a reasonable value to impose a Dirichlet boundary condition; see e.g. [56].

For convenience, the following results are shown for $\hat{\eta}$, where the axis has been rotated such that the plate is always vertical. In Figure 5.7, we show the numerical solution of the free surface $\hat{\eta}$ with $\alpha \approx \alpha_c$, where there is no corner point observed and the shape of the free surface is quite smooth. An example solution for $\hat{\eta}$ for $\alpha = 1.75$ is shown in Figure 5.8a compared with the results solved by boundary integral method, where the blue curve is the numerical result solved by Newton's method, and the red curve is the numerical result obtained using boundary integral method. The nonuniform grid used in the boundary integral method has the initial spacing h_0 for arc length $s < 0.07$, gradually increasing to $10h_0$ for $0.07 < s < 1$ and $100h_0$ for $1 < s < s_\infty$, where h_0 is 2×10^{-3} and $s_\infty = 25.24$ in this case. The results agree well with each other, except when $\hat{X} \to 0^+$. Figure 5.8b shows the detailed behaviour of free surface $\hat{\eta}$ when $\hat{X} \to 0^+$. The small oscillation on the free surface can be observed for the results obtained by the boundary integral method, but the result solved by Newton's method does not capture the oscillation when close to the intersection point. We include an example graph (as Figure 5.9) of the free surface obtained by boundary integral method for $\alpha = 1.75$ from

[64] to show the oscillations captured. The possible reason that the finite element method cannot capture the small oscillation close to the plate is that it introduces additional numerical dissipation due to the discretization of the Laplace operator in the interior such that fewer oscillations are resolved on the grid than the results obtained by boundary integral method.

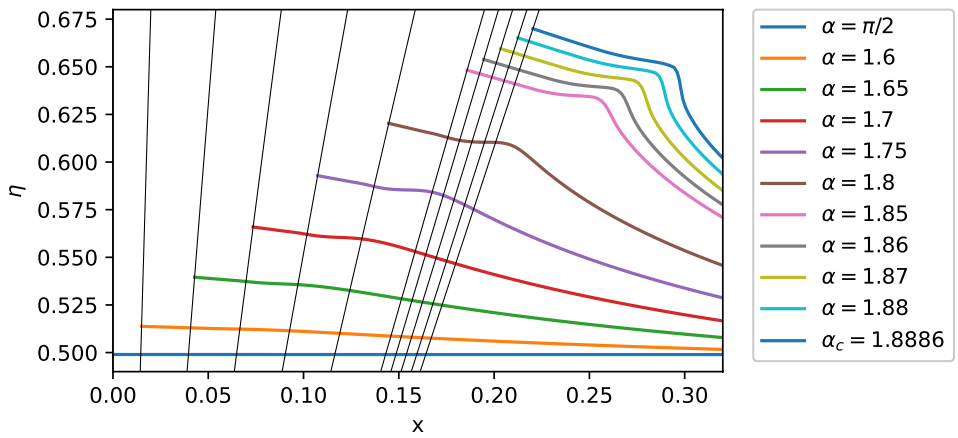

Figure 5.6: *η for various α. The axis system has been rotated to be the same as the one used to construct the model. The black lines are the location of the inclined plates.*

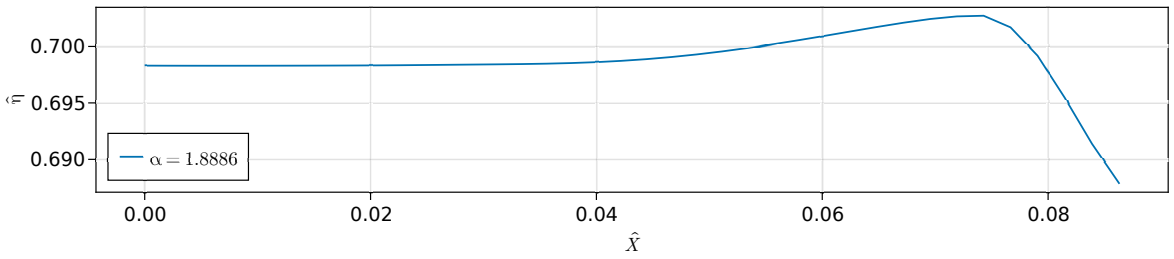

Figure 5.7: *The numerical result of $\hat{\eta}$ where $x \to 0$ for $\alpha_c = 1.8886$.*

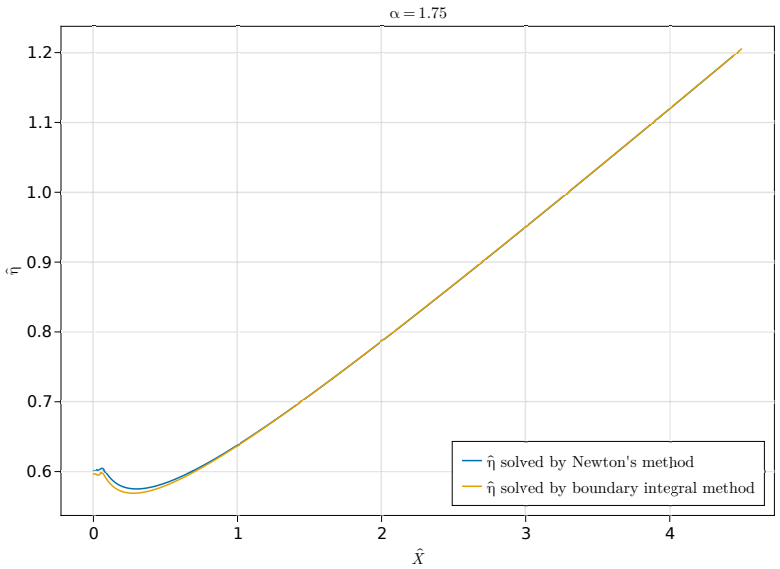

(a) *Numerical results of $\hat{\eta}$ solved by Newton's method compared with the results solved by boundary integral method for $\alpha = 1.75$.*

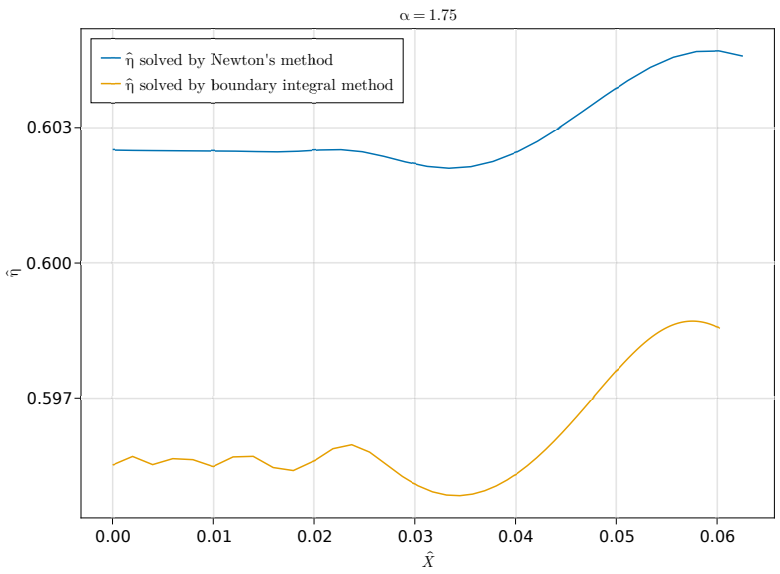

(b) *The numerical results of $\hat{\eta}$ solved by Newton's method compared with the results solved by the boundary integral method where $x \to 0$ for $\alpha = 1.75$.*

Figure 5.8

5.6 Conclusion

In this chapter, we have used a finite element method to solve the solid/single fluid interaction problem with an accelerating plate in the inner region as $\alpha > \frac{\pi}{2}$ derived

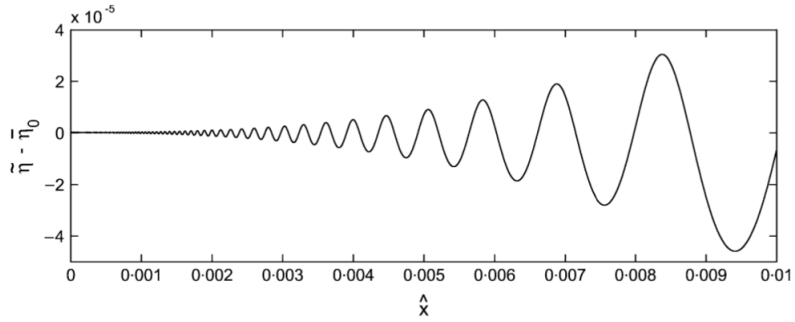

Figure 5.9: *The free surface close to the intersection when* $\alpha = 1.75$ *from [64]. In this figure* $\hat{\eta} = \tilde{\eta} - \tilde{\eta}_0$ *and* $\hat{x}$ *is the same as* $\hat{X}$ *in this chapter.*

from [64], which is a simplified version of two fluid/solid interaction problem in Chapter 4. We first solve the linearised problem by considering a small angle-perturbation to the vertical plate such that the free boundary is fixed and the nonlinear Bernoulli condition on the free boundary is linearised. Thus, we can easily find the local form of the solution. The main feature of the displacement of the free surface is that it is always perpendicular to the moving plate, and there are small oscillations around the intersection point between the free surface and the plate.

To find the numerical method for solving this linearised free-boundary problem, the most straightforward method is the trial method, which solves the boundary value problem with one free-boundary condition on a fixed domain and then updates the free surface with the remaining free-boundary condition. To ensure the stability of the numerical method, the finite element approximation of the location of the free surface η is the sum of piecewise constant functions, and the approximation of the velocity potential ϕ is the sum of piecewise linear functions. The numerical results converge to the far-field condition very quickly; however, they do not have the same qualitative behaviours as the local form of the solutions. Furthermore, the numerical results of the location of the free surface are not vertical to the plate and do not capture the small oscillations. Despite the disagreement between the numerical and local solutions, we believe the numerical solution can be treated as another solution to this linearised problem due to the consistency with the far-field condition. On

the other hand, the rate of convergence of this simple iteration method is very slow. Hence, we consider using Newton's method to solve the entire inner problem.

The entire problem is reformulated as a coupled problem in vector form: one problem is constructed only with the Bernoulli condition and kinematic condition on the free surface in the inner region to find the velocity potential $\hat{\Phi}_F$ and the displacement of the free surface $\hat{\eta}$; the results found by the former problem is then used to solve the boundary value problem for velocity potential in the whole region. The benefit is that $\hat{\Phi}_F$ and $\hat{\eta}$ can be found simultaneously. Newton's method is applied to the free-surface problem, where the Jacobian matrix is constructed using the finite difference method to the weak forms. The finite approximations of $\hat{\Phi}_F$ and $\hat{\eta}$ are estimated by piecewise linear functions.

The numerical results of the entire inner problem show that the free surface is always vertical to the plate, consistent with the conclusion in [64]. The angle α has a critical value $\alpha_c \approx 1.8886$ such that no solution can be found for the situation $\alpha > \alpha_c$. However, the value of α_c here is slightly larger than the value in [64], and the small oscillations cannot be captured. Besides, even though the Jacobian matrix is updated after every five iterations, the running time of this method is too long with 500 nodes on the x-axis, where it takes hours to find the critical value of angle α.

Chapter 6

Shape-Newton Method for Free-boundary Problems

6.1 Introduction

[1]

Free boundary problems have many applications in fluid mechanics, such as open-channel flow, fluid/solid interaction and hydrodynamics. Solving such problems is difficult because the geometry of the domain needs to be determined together with other variables in this problem. A simplified but important model problem is the Bernoulli free-boundary problem, which considers a (linear) Dirichlet boundary condition, as well as a Neumann boundary condition on the free boundary [18, 71]. This problem is not to be confused with the Bernoulli *equation*, which is the pressure boundary condition in irrotational fluid mechanics, and which we will study in this paper. The nonlinearity of the Bernoulli equation poses an additional challenge to numerical algorithms.

There are several computational approaches to solving free-boundary problems. The first is to solve the boundary value problem with a single free-boundary con-

[1] The paper available as `arXiv:2305.14254 [math.NA]` [28] forms the basis of chapter.

dition for the field variables on a fixed approximated domain, and then update the free surface derived from the remaining free boundary condition, which is not included in the boundary value problem. These fixed-point type methods are called *trial* methods, which converge linearly and cannot always find a solution. Details can be found, for example, in [7, 55, 71].

The second approach is to formulate a shape optimization problem to improve the convergence rate. This method aims to construct a boundary-value problem as the state problem with one free-boundary condition and formulate a cost function with the remaining free-boundary condition. This approach may require gradient information. The formulation and application of shape optimization to free boundary problems can be found in, e.g. [27, 37, 38, 82, 83, 86].

The third approach requires *linearising* the whole system and applying a Newton-type method. The use of shape calculus and a Newton-type method is called the shape-Newton method. One linearisation method, called *domain-map* linearisation, requires to transform the free-boundary problem to an equivalent boundary value problem on a fixed domain and then linearise the transformed problem with respect to the domain map [60, 87]. An alternative way to linearise the free-boundary problem is to apply *shape linearisation* [21, 77]. Kärkkäinen and Tiihonen used this technique to solve Bernoulli free-boundary problems [49, 50]. The application to a more general Bernoulli free-boundary problem has been investigated in Van der Zee et el [90] by considering the whole problem in one weak form and using C^1-continuous B-splines to represent discrete free boundaries, in order to allow the exact computation of the curvature in the shape derivatives. Montardini et al. [62] extend this method by incorporating a collocation approach to update the boundary, and compare both methods by imposing Dirichlet or periodic boundary conditions on the vertical fixed boundary of the domain. The results show that the collocation scheme has slightly worse accuracy but higher efficiency.

In the current work, we derive the shape-Newton method for a more general

free-boundary problem by considering the nonlinear Bernoulli boundary condition on the free boundary. We also recall the method for the Bernoulli free-boundary problem, which has a Dirichlet boundary condition on the free boundary. Similar to Kärkkäinen and Tiihonen, the problem will be set up in terms of two weak forms: one derived from the boundary value problem with the Neumann boundary condition over the current domain, and the other from the remaining free boundary condition (Dirichlet condition or nonlinear Bernoulli condition).

The linearisation for the Dirichlet free-boundary problem is known [90]. However, the linearisation for the Bernoulli equation has not been derived before: we obtain a surprisingly elegant expression for the shape derivative, which involves the normal derivative of the velocity squared ($|\nabla^2\phi|$). We show in detail how this can be equivalently computed using only the velocity and curvatures; see Section 6.5.3.

We present our shape-Newton scheme in both strong and weak form, and without reference to any particular underlying discretisation. We will show a numerical experiment involving open channel flow over a submerged triangle. The shape-Newton method converges superlinearly, and the results agree well with exact solutions and results from [22].

The contents of this chapter are arranged as follows. We will first introduce the model problem either with the Dirichlet boundary condition or the Bernoulli equation on the free boundary in Section 6.2. In Section 6.3, we will derive the weak form for both problems. Then, we will introduce some basic concepts about shape derivatives in Section 6.4 and the linearisation by applying Hadamard shape derivatives for the free-boundary problem follows in Section 6.5. In Section 6.6, we will illustrate the Newton-like and coupled schemes. The numerical experiments will be shown in Section 6.7, following the conclusions in Section 6.8.

6.2 Steady Free-boundary Problem

In this section, we will introduce the steady free boundary problem with either a Bernoulli condition or the Dirichlet condition on the free boundary. The Bernoulli condition is commonly used when considering steady, incompressible, and inviscid flow, but it is nonlinear, making the boundary value problem more challenging to solve. To be more general, the boundary conditions on the fixed boundaries are Robin boundary conditions.

6.2.1 Free-boundary Problem with Bernoulli Condition

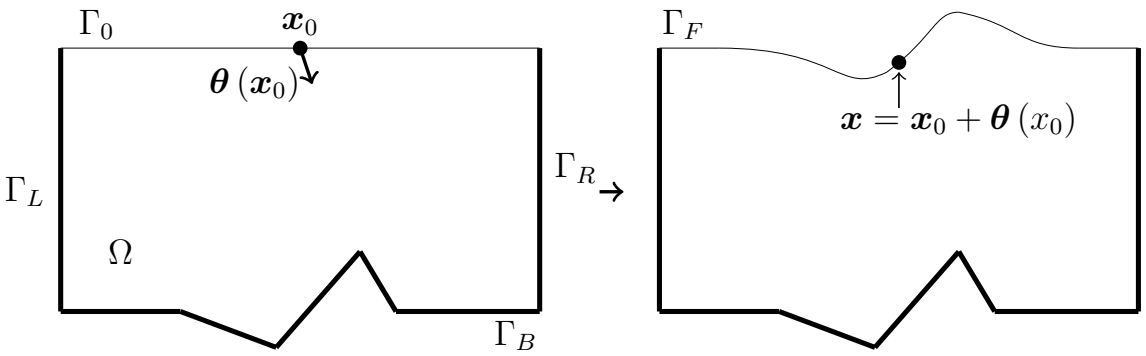

Figure 6.1: *The sketch of the parametrization of the free boundary* Γ_F *by the displacement* $\boldsymbol{\theta}(\boldsymbol{x}_0)$ *with respect to the reference boundary* Γ_0.

The free boundary problem with a Bernoulli condition can be abstracted as seeking an unknown domain $\Omega \subset \mathbb{R}^N$ and a corresponding scalar function $\phi : \Omega \to \mathbb{R}$. The boundary $\partial\Omega$ contains a free boundary Γ_F, a left boundary Γ_L for input flow, a right boundary Γ_R for output flow, and the bed Γ_B. Figure 6.1 is an example of the domain and the parametrization of the free boundary Γ_F. The bed boundary has any shape and does not have to be the same as shown in Figure 6.1. The vertical displacement of the free boundary is denoted as $\eta(x)$. The problem can be presented

as

$$
\begin{aligned}
-\Delta\phi &= f, \quad \text{in } \Omega, && (6.2.1)\\
\partial_{\boldsymbol{n}}\phi &= 0, \quad \text{on } \Gamma_F, && (6.2.2)\\
\partial_{\boldsymbol{n}}\phi + \omega\phi &= g + \omega h, \quad \text{on } \partial\Omega \setminus \Gamma_F, && (6.2.3)\\
a\left|\nabla\phi\right|^2 + b\eta + c &= 0, \quad \text{on } \Gamma_F, && (6.2.4)
\end{aligned}
$$

where $\partial_{\boldsymbol{n}}(\cdot) = \boldsymbol{n}\cdot\nabla(\cdot)$ is the normal derivative with $\boldsymbol{n}$ being the unit normal vector to the boundary pointing out of the domain. The condition (6.2.4) with real-valued constants a, b, and c represents the Bernoulli condition. We have Robin boundary conditions on $\partial\Omega \setminus \Gamma_F$ where ω, g and h are the boundary data. Thus we can approximate either a Neumann or Dirichlet-type condition depending on the values of ω. The Neumann boundary condition usually represents the kinematic condition, where the perpendicular fluid velocity is zero on the free or solid boundary. On the other hand, choosing ω to be extremely large yields the approximated Dirichlet boundary condition $\phi = h$. Furthermore, we can have mixed boundary conditions with various values of ω on different parts of the boundaries (i.e. Γ_L, Γ_R and Γ_B). Sufficiently $\mathcal{C}^1$-smooth data f, g and h allow us to find a nontrivial solution pair (Γ_F, ϕ).

By introducing a vector field $\boldsymbol{\theta} : \Gamma_0 \to \mathbb{R}^N$, the displacement of the free boundary with respect to the referenced boundary Γ_0 can be defined as

$$
\Gamma_F := \left\{\mathbf{x} \in \mathbb{R}^N | \mathbf{x} = \mathbf{x}_0 + \boldsymbol{\theta}(\mathbf{x}_0), \forall \mathbf{x}_0 \in \Gamma_0\right\}, \tag{6.2.5}
$$

to parametrize the domain Ω and the free boundary Γ_F, as shown in Figure 6.1. This allows us to write the problem (6.2.1)-(6.2.4) in terms of the pair $(\boldsymbol{\theta}, \phi)$. Considering $\eta(x)$ in (6.2.4) denoted as the y-component of θ, the problem (6.2.1)-(6.2.4) can alternatively be solved in terms of the pair (η, ϕ) for fixed values of x.

6.2.2 Free-boundary Problem with Dirichlet Boundary Condition

A more straightforward model problem is introduced by replacing the Bernoulli condition with the Dirichlet condition on the free boundary. The dependence on ϕ is now linear. The boundary value problem is now linear and easier to solve. The abstract problem is

$$-\Delta\phi = f, \quad \text{in } \Omega, \tag{6.2.6}$$

$$\partial_{\boldsymbol{n}}\phi = 0, \quad \text{on } \Gamma_F, \tag{6.2.7}$$

$$\partial_{\boldsymbol{n}}\phi + \omega\phi = g + \omega h, \quad \text{on } \partial\Omega \setminus \Gamma_F, \tag{6.2.8}$$

$$\phi - h = 0, \quad \text{on } \Gamma_F, \tag{6.2.9}$$

where $g \leq 0$ for input flow and h is assumed to be sufficiently smooth on $\mathbb{R}^N$.

By choosing $\omega \to \infty$ for Dirichlet boundary conditions on $\partial\Omega \setminus \Gamma_F$, this problem becomes the classical Bernoulli free-boundary problem for an ideal fluid, called Bernoulli free-boundary problem [71].

6.3 The Weak Form

We will first find the weak forms of both free-boundary problems to apply shape-calculus techniques to linearise this problem. Let Γ_D represent the boundary $\partial\Omega \setminus \Gamma_F$ with Dirichlet boundary conditions and x_L represent the x-component of the left node on the free boundary Γ_F, we introduce the test functions $v \in V := \{v \in \mathcal{C}^1(\Omega) | v = 0 \text{ on } \Gamma_D\}$ and $w \in W := \{w \in \mathcal{C}^1(\Gamma_F) | w = 0 \text{ on } x_L\}$. If no Dirichlet boundary conditions are given on any part of the boundary $\partial\Omega \setminus \Gamma_F$, then the test function v satisfies $v \in V := \mathcal{C}^1(\Omega)$.

Since the only difference between the two free-boundary problems in Section 6.2 is the Bernoulli condition and the Dirichlet condition on the free boundary, the first

weak form in the domain Ω is the same in both situations. It can be obtained by integrating the multiplication of the Laplacian equation ((6.2.1) or (6.2.6)) and the test function v over Ω, then applying the Green's formula with the Robin boundary conditions on $\partial\Omega \setminus \Gamma_F$ and Neumann boundary condition on Γ_F, yielding

$$\mathcal{R}_1\left((\boldsymbol{\theta}, \phi)\,; v\right) = 0, \quad \forall v \in V, \tag{6.3.1}$$

where the semilinear form $\mathcal{R}_1\left((\boldsymbol{\theta}, \phi)\,; v\right)$ is defined as

$$\begin{aligned} \mathcal{R}_1\left((\boldsymbol{\theta}, \phi)\,; v\right) &= -\int_\Omega \Delta\phi \cdot v d\Omega - \int_\Omega f v d\Omega, \\ &= \int_\Omega \nabla\phi \cdot \nabla v d\Omega - \int_{\partial\Omega\setminus\Gamma_F} (gv + \omega h - \omega\phi)\,\mathrm{ds} - \int_\Omega f v d\Omega. \end{aligned} \tag{6.3.2}$$

However, when $\omega \to \infty$ yields the Dirichlet boundary condition on the fixed boundary, we will replace the weak form on the fixed boundary with the strong form $\phi = h$ instead to enforce ϕ to satisfy the boundary condition.

The second weak form is different on the free boundary, which can be derived by multiplying with test function w and integrating over Γ_F,

$$\mathcal{R}_2\left((\boldsymbol{\theta}, \phi)\,; w\right) = 0, \quad \forall w \in W, \tag{6.3.3}$$

with the definition of the semilinear form $\mathcal{R}_2\left((\boldsymbol{\theta}, \phi)\,; w\right)$ as

$$\mathcal{R}_2\left((\boldsymbol{\theta}, \phi)\,; w\right) = \int_{\Gamma_F} (\mathrm{B.C})\, w d\Gamma, \tag{6.3.4}$$

where (B.C) can either be the left hand side of Bernoulli condition (6.2.4) or Dirichlet condition (6.2.9).

6.4 Shape Derivatives

The linearisation of $\mathcal{R}_1\left(\left(\boldsymbol{\theta},\phi\right);v\right)$ and $\mathcal{R}_2\left(\left(\boldsymbol{\theta},\phi\right);w\right)$ needs the differentiation of the weak forms with respect to the geometry. In this case, the geometry itself is treated as a variable. Thus the shape derivatives are applied to find the differentiation defined in a fixed domain, which requires some appropriate smoothness assumptions. Some essential background for shape derivatives, mainly from the books [21, 77] is explained in section 2.3.

The weak forms (6.3.2) and (6.3.4) contain domain integrals $\int_\Omega (\cdot)\, d\Omega$ and boundary integrals $\int_{\Gamma_F} (\cdot)\, d\Gamma$. The shape derivatives for a domain integral and a boundary integral can be obtained by applying the Hadamard formula [21, 77] and we recall the Proposition 2.1 and Lemma 2.1 as follows:

Theorem 6.4.1. *(Shape derivative of domain integral) Suppose $\phi \in W^{1,1}\left(\mathbb{R}^N\right)$ and Ω is an open and bounded domain; we have the domain integral*

$$J\left(\Omega\right) = \int_\Omega \phi d\Omega.$$

If Γ is the boundary of Ω of class C^1, then its shape derivative with respect to the perturbation $\delta\boldsymbol{\theta} \in C^{0,1}\left(\mathbb{R}^N;\mathbb{R}^N\right)$ is given by

$$\left\langle dJ\left(\Omega\right), \delta\boldsymbol{\theta}\right\rangle = \int_\Gamma \phi\delta\boldsymbol{\theta}\cdot\boldsymbol{n}d\Gamma,$$

where $\boldsymbol{n}$ denotes the outward normal derivative to Ω.

Theorem 6.4.2. *(Shape derivative of boundary integral) Suppose $\phi \in W^{2,1}\left(\mathbb{R}^N\right)$ and Ω is an open and bounded domain with the boundary Γ of class $C^{1,1}$, we have the boundary integral*

$$J\left(\Gamma\right) = \int_\Gamma \phi d\Gamma.$$

Then its shape derivative with respect to the perturbation $\delta\boldsymbol{\theta} \in C^{0,1}\left(\mathbb{R}^N;\mathbb{R}^N\right)$ is

given by

$$\langle dJ(\Gamma), \delta\boldsymbol{\theta}\rangle = \int_{\Gamma} (\partial_{\boldsymbol{n}}\phi + \kappa\phi)\, \delta\boldsymbol{\theta}\cdot\boldsymbol{n} d\Gamma,$$

where $\boldsymbol{n}$ *denotes the normal vector to* Γ *and* κ *is the curvature of* Γ.

6.5 Linearisation

We wish to linearise $\mathcal{R}_1((\boldsymbol{\theta}, u); v)$ and $\mathcal{R}_2((\boldsymbol{\theta}, \phi); w)$ at an approximation pair $\left(\hat{\boldsymbol{\theta}}, \hat{\phi}\right)$ close to the exact solutions by finding the partial derivative of the weak forms with respect to ϕ and $\boldsymbol{\theta}$. We assume that $\hat{\phi}$, close to ϕ is any approximation satisfying the boundary conditions on $\partial\Omega \setminus \Gamma_F$ that lives in the approximate domain $\hat{\Omega}$ with the free boundary $\hat{\Gamma}$ induced by the approximation $\hat{\boldsymbol{\theta}}$. The y-component of $\hat{\boldsymbol{\theta}}$ is denoted as $\hat{\eta}$.

The Gâteaux derivative at $\hat{\phi}$ in the direction $\delta\phi$ and the linearisation for the Dirichlet boundary condition is relatively standard, similar to [90], while the approximation of the linearisation for Bernoulli condition is surprisingly elegant and straightforward.

6.5.1 Linearisation of $\mathcal{R}_1$

The Gâteaux derivative at $\hat{\phi}$ in the direction $\delta\phi$ can be evaluated as

$$\begin{aligned}\left\langle \partial_{\phi}\mathcal{R}_1\left(\left(\hat{\boldsymbol{\theta}}, \hat{\phi}\right); v\right), \delta\phi\right\rangle &= \lim_{\epsilon\to 0} \frac{\mathcal{R}_1\left(\left(\boldsymbol{\theta}, \hat{\phi} + t\delta\phi\right); v\right) - \mathcal{R}_1\left(\left(\boldsymbol{\theta}, \hat{\phi}\right); v\right)}{\epsilon} \\ &= \int_{\hat{\Omega}} \nabla\delta\phi\cdot\nabla v d\Omega. \end{aligned} \tag{6.5.1}$$

Then the linearisation with respect to $\boldsymbol{\theta}$ can be obtained by applying Hadamard formulas from Theorem 6.4.1 to (6.3.2) which yields

$$\left\langle \partial_{\boldsymbol{\theta}}\mathcal{R}_1\left(\left(\hat{\boldsymbol{\theta}}, \hat{\phi}\right); v\right), \delta\boldsymbol{\theta}\right\rangle = \int_{\hat{\Gamma}} \nabla\hat{\phi}\cdot\nabla v\delta\boldsymbol{\theta}\cdot\boldsymbol{n} d\Gamma - \int_{\hat{\Gamma}} f v\delta\boldsymbol{\theta}\cdot\boldsymbol{n} d\Gamma. \tag{6.5.2}$$

The tangential gradient ∇_Γ and tangential divergence div_Γ are defined as

$$\nabla_\Gamma(\cdot) = \nabla(\cdot) - \partial_{\boldsymbol{n}}(\cdot)\boldsymbol{n}, \qquad \mathrm{div}_\Gamma = \mathrm{div}(\cdot) - \partial_n(\cdot)\mathbf{n}. \tag{6.5.3}$$

By substituting (6.5.3) into (6.5.2) and applying the tangential Green's identity (explained in section 2.3, and also see [21], [77]), (6.5.2) can be approximated as

$$\begin{aligned}
\left\langle \partial_{\boldsymbol{\theta}}\mathcal{R}_1\left(\left(\hat{\boldsymbol{\theta}}, \hat{\phi}\right); v\right), \delta\boldsymbol{\theta}\right\rangle &= \int_{\hat{\Gamma}} \left(\nabla_\Gamma\hat{\phi}\cdot\nabla_\Gamma v + \partial_n\hat{\phi}\partial_n v\right)\delta\boldsymbol{\theta}\cdot\mathbf{n}d\Gamma - \int_{\hat{\Gamma}} fv\delta\boldsymbol{\theta}\cdot\boldsymbol{n}d\Gamma \\
&\approx -\int_{\hat{\Gamma}} \mathrm{div}_\Gamma\left(\delta\boldsymbol{\theta}\cdot\mathbf{n}\nabla_\Gamma\hat{\phi}\right) vd\Gamma - \int_{\hat{\Gamma}} fv\delta\boldsymbol{\theta}\cdot\boldsymbol{n}d\Gamma \\
&\approx -\int_{\hat{\Gamma}} \mathrm{div}_\Gamma\left(\delta\boldsymbol{\theta}\cdot\mathbf{n}\nabla\hat{\phi}\right) vd\Gamma - \int_{\hat{\Gamma}} fv\delta\boldsymbol{\theta}\cdot\boldsymbol{n}d\Gamma.
\end{aligned} \tag{6.5.4}$$

Due to the Neumann boundary condition (6.2.2) (or (6.2.7)), $\partial_n\hat{\phi}$ is very small, and the related term is neglected in the second and third steps.

6.5.2 Linearisation of $\mathcal{R}_2$ with Dirichlet condition

Using the Dirichlet boundary condition (6.2.9), we have

$$\mathcal{R}_2\left((\boldsymbol{\theta}, \phi); w\right) = \int_{\Gamma_F} (\phi - h)\, wd\Gamma. \tag{6.5.5}$$

Similar to the linearisation of $\mathcal{R}_1$ with respect to ϕ, it is very straightforward to evaluate the Gâteaux derivative at ϕ in the direction $\delta\phi$,

$$\left\langle \partial_{\boldsymbol{\theta}}\mathcal{R}_2\left(\left(\hat{\boldsymbol{\theta}}, \hat{\phi}\right); w\right), \delta\phi\right\rangle = \int_{\hat{\Gamma}} \delta\phi w d\Gamma. \tag{6.5.6}$$

Then by using the Hadamard formula on the boundary integral (6.5.5), we have

the shape linearisation

$$\begin{aligned}\left\langle \partial_{\boldsymbol{\theta}}\mathcal{R}_2\left(\left(\hat{\boldsymbol{\theta}},\hat{\phi}\right);v\right),\delta\boldsymbol{\theta}\right\rangle &= \int_{\hat{\Gamma}}\left(\partial_{\boldsymbol{n}}+\kappa\right)\left[\left(\hat{\phi}-h\right)w\right]\delta\boldsymbol{\theta}\cdot\boldsymbol{n}d\Gamma,\\ &= \int_{\hat{\Gamma}}\left[\partial_{\boldsymbol{n}}\left(\hat{\phi}-h\right)w+\left(\hat{\phi}-h\right)\partial_{\boldsymbol{n}}w+\kappa\left(\hat{\phi}-h\right)w\right]\delta\boldsymbol{\theta}\cdot\boldsymbol{n}d\Gamma.\end{aligned} \tag{6.5.7}$$

Using the Dirichlet condition (6.2.9) and Neumann condition (6.2.7) on the free boundary, we can neglect the $(\phi-h)-$term and $(\partial_{\boldsymbol{n}}\phi)-$term in (6.5.7). We then have the approximation

$$\left\langle \partial_{\boldsymbol{\theta}}\mathcal{R}_2\left(\left(\hat{\boldsymbol{\theta}},\hat{\phi}\right);v\right),\delta\boldsymbol{\theta}\right\rangle \approx -\int_{\hat{\Gamma}}(\partial_{\boldsymbol{n}}h)w\delta\boldsymbol{\theta}\cdot\boldsymbol{n}d\Gamma. \tag{6.5.8}$$

6.5.3 Linearisation of $\mathcal{R}_2$ with Bernoulli condition

Substituting the Bernoulli condition (6.2.4) into the weak form (6.3.4), we have

$$\mathcal{R}_2\left(\left(\boldsymbol{\theta},\phi\right);w\right)=\int_{\Gamma_F}\left(a\left|\nabla\phi\right|^2+b\eta+c\right)wd\Gamma. \tag{6.5.9}$$

The linearisation in terms of ϕ at approximation $\hat{\phi}$ is

$$\left\langle \partial_{\boldsymbol{\theta}}\mathcal{R}_2\left(\left(\hat{\boldsymbol{\theta}},\hat{\phi}\right);w\right),\delta\phi\right\rangle=\int_{\hat{\Gamma}}2a\nabla\hat{\phi}\cdot\nabla\delta\phi wd\Gamma. \tag{6.5.10}$$

To find the Gâteaux derivative with respect to $\boldsymbol{\theta}$ at $\hat{\theta}$, applying Hadamard

formula yields

$$\begin{aligned}
\left\langle \partial_{\boldsymbol{\theta}} \mathcal{R}_2 \left(\left(\hat{\boldsymbol{\theta}}, \hat{\phi} \right); v \right), \delta \boldsymbol{\theta} \right\rangle &= \int_{\hat{\Gamma}} (\partial_{\boldsymbol{n}} + \kappa) \left[\left(a \left| \nabla \hat{\phi} \right|^2 + b\hat{\eta} + c \right) w \right] \delta \boldsymbol{\theta} \cdot \boldsymbol{n} d\Gamma, \\
&= \int_{\hat{\Gamma}} \left(a \partial_{\boldsymbol{n}} \left(\left| \nabla \hat{\phi} \right|^2 \right) + b n_y \right) w \delta \boldsymbol{\theta} \cdot \boldsymbol{n} d\Gamma \\
&\quad + \int_{\hat{\Gamma}} \left(a \left| \nabla \hat{\phi} \right|^2 + b\hat{\eta} + c \right) \partial_{\boldsymbol{n}} w \delta \boldsymbol{\theta} \cdot \boldsymbol{n} d\Gamma \\
&\quad + \int_{\hat{\Gamma}} \kappa \left(a \left| \nabla \hat{\phi} \right|^2 + b\hat{\eta} + c \right) w \delta \boldsymbol{\theta} \cdot \boldsymbol{n} d\Gamma, \qquad (6.5.11)
\end{aligned}$$

where n_y is the $y-$coordinate of the unit normal vector $\boldsymbol{n}$. Since $\hat{\eta}$ is the y-component of $\hat{\theta}$, we can evaluate $\partial_{\boldsymbol{n}} \hat{\eta} = \partial_{\boldsymbol{n}} y = \begin{pmatrix} 0 \\ 1 \end{pmatrix} \cdot \begin{pmatrix} n_x \\ n_y \end{pmatrix} = n_y$.

According to the Bernoulli condition (6.2.4), $a \left| \nabla \hat{\phi} \right|^2 + b\hat{\eta} + c \to 0$ and can be neglected, thus the approximation is

$$\left\langle \partial_{\boldsymbol{\theta}} \mathcal{R}_2 \left(\left(\hat{\boldsymbol{\theta}}, \hat{\phi} \right); v \right), \delta \boldsymbol{\theta} \right\rangle \approx \int_{\hat{\Gamma}} \left(a \partial_{\boldsymbol{n}} \left(\left| \nabla \hat{\phi} \right|^2 \right) + b n_y \right) w \delta \boldsymbol{\theta} \cdot \boldsymbol{n} d\Gamma \qquad (6.5.12)$$

Given $\hat{\boldsymbol{\theta}} = (x, \hat{\eta}(x))$, we have the unit normal vector $\boldsymbol{n} = \frac{1}{\sqrt{1+\hat{\eta}_x^2}} (-\hat{\eta}_x, 1)$ and the unit tangential vector $\boldsymbol{\tau} = \frac{1}{\sqrt{1+\hat{\eta}_x^2}} (1, \hat{\eta}_x)$. Then the Neumann boundary condition (6.2.2) on the free boundary can be written in the form of

$$-\hat{\eta}_x \hat{\phi}_x + \hat{\phi}_y = 0.$$

This implies that its tangential derivative is also zero, i.e.

$$(\boldsymbol{\tau} \cdot \nabla) \left(-\hat{\eta}_x \hat{\phi}_x + \hat{\phi}_y \right) = 0,$$

which is equivalent to

$$-\hat{\eta}_{xx} \hat{\phi}_x - \hat{\eta}_x \hat{\phi}_{xx} + \hat{\phi}_{xy} - \hat{\eta}_x^2 \hat{\phi}_{xy} + \hat{\eta}_x \hat{\phi}_{yy} = 0. \qquad (6.5.13)$$

Then we have

$$\begin{aligned}
\partial_{\boldsymbol{n}}\left(\left|\nabla\hat{\phi}\right|^2\right) &= \frac{1}{\sqrt{1+\hat{\eta}_x^2}}\left(-\hat{\eta}_x\partial_x+\partial_y\right)\left(\hat{\phi}_x^2+\hat{\phi}_y^2\right) \\
&= \frac{2}{\sqrt{1+\hat{\eta}_x^2}}\left[-\hat{\eta}_x\left(\hat{\phi}_x\hat{\phi}_{xx}+\hat{\phi}_y\hat{\phi}_{xy}\right)+\hat{\phi}_x\hat{\phi}_{xy}+\hat{\phi}_y\hat{\phi}_{yy}\right], \\
&= \frac{2}{\sqrt{1+\hat{\eta}_x^2}}\hat{\phi}_x\left(-\hat{\eta}_x\hat{\phi}_{xx}-\hat{\eta}_x^2\hat{\phi}_{xy}+\hat{\phi}_{xy}+\hat{\eta}_x\hat{\phi}_{yy}\right) \\
&= \frac{2}{\sqrt{1+\hat{\eta}_x^2}}\hat{\eta}_{xx}\left(\hat{\phi}_x\right)^2 \\
&= 2\kappa\left(1+\hat{\eta}_x^2\right)\left(\hat{\phi}_x\right)^2 \\
&= 2\kappa\left|\nabla\hat{\phi}\right|^2, \qquad (6.5.14)
\end{aligned}$$

where $\kappa=\partial_x\left(\frac{\hat{\eta}_x}{\sqrt{1+\hat{\eta}_x^2}}\right)$. The third and fifth steps are obtained by substituting the Neumann condition, and the fourth step is obtained by substitution of (6.5.13).

On substitution from (6.5.14) into (6.5.12), the approximate shape linearisation is

$$\left\langle\partial_{\boldsymbol{\theta}}\mathcal{R}_2\left(\left(\hat{\boldsymbol{\theta}},\hat{\phi}\right);v\right),\delta\boldsymbol{\theta}\right\rangle\approx\int_{\hat{\Gamma}}\left(2a\kappa\left|\nabla\hat{\phi}\right|^2+bn_y\right)w\delta\boldsymbol{\theta}\cdot\boldsymbol{n}d\Gamma. \qquad (6.5.15)$$

6.6 Newton-like Schemes

Now, we introduce $\phi=\hat{\phi}+\delta\phi$ and $\boldsymbol{\theta}=\hat{\boldsymbol{\theta}}+\delta\boldsymbol{\theta}\in\Gamma_F$ where $\delta\phi$ and $\delta\boldsymbol{\theta}$ are the corrections evaluated in the reference domain $\hat{\Omega}$. The exact Newton method for $(\delta\boldsymbol{\theta},\delta\phi)$ would be

$$\begin{aligned}
\left\langle\partial_{(\boldsymbol{\theta},\phi)}\mathcal{R}_1\left(\left(\hat{\boldsymbol{\theta}},\hat{\phi}\right);v\right),(\delta\boldsymbol{\theta},\delta\phi)\right\rangle &= -\mathcal{R}_1\left(\left(\hat{\boldsymbol{\theta}},\hat{\phi}\right);v\right) \quad \forall v\in V, \qquad (6.6.1)\\
\left\langle\partial_{(\boldsymbol{\theta},\phi)}\mathcal{R}_2\left(\left(\hat{\boldsymbol{\theta}},\hat{\phi}\right);w\right),(\delta\boldsymbol{\theta},\delta\phi)\right\rangle &= -\mathcal{R}_2\left(\left(\hat{\boldsymbol{\theta}},\hat{\phi}\right);v\right) \quad \forall w\in W. \qquad (6.6.2)
\end{aligned}$$

The Newton-like scheme for $\mathcal{R}_1$ is obtained by combining (6.5.1) and the ap-

proximation (6.5.4) of $\partial_{\boldsymbol{\theta}}\mathcal{R}_1\left(\left(\hat{\boldsymbol{\theta}},\hat{\phi}\right);v\right)$, i.e.

$$\int_{\hat{\Omega}}\nabla\delta\phi\cdot\nabla v d\Omega-\int_{\hat{\Gamma}}\mathrm{div}_{\Gamma}\left(\delta\boldsymbol{\theta}\cdot\boldsymbol{n}\nabla\hat{\phi}\right)vd\Gamma-\int_{\hat{\Gamma}}fv\delta\boldsymbol{\theta}\cdot\boldsymbol{n}d\Gamma=-\mathcal{R}_1\left(\left(\hat{\boldsymbol{\theta}},\hat{\phi}\right);v\right),\quad\forall v\in V. \tag{6.6.3}$$

Similarly, for the Dirichlet boundary condition, the Newton-like scheme is derived based on (6.5.6) and approximation (6.5.8) as

$$\int_{\hat{\Gamma}}\delta\phi w d\Gamma-\int_{\hat{\Gamma}}\left(\partial_{\boldsymbol{n}}h\right)w\delta\boldsymbol{\theta}\cdot\boldsymbol{n}d\Gamma=-\mathcal{R}_2\left(\left(\hat{\boldsymbol{\theta}},\hat{\phi}\right);w\right),\quad\forall w\in W. \tag{6.6.4}$$

For the Bernoulli condition, introducing (6.5.10) and (6.5.15), the Newton-like scheme would be

$$\int_{\hat{\Gamma}}2a\nabla\hat{\phi}\cdot\nabla\delta\phi w d\Gamma+\int_{\hat{\Gamma}}\left(2a\kappa\left|\nabla\hat{\phi}\right|^2+bn_y\right)w\delta\boldsymbol{\theta}\cdot\boldsymbol{n}d\Gamma=-\mathcal{R}_2\left(\left(\hat{\boldsymbol{\theta}},\hat{\phi}\right);w\right),\quad\forall w\in W. \tag{6.6.5}$$

When $\hat{\phi}$ and $\hat{\boldsymbol{\theta}}$ are the exact solutions, the approximations are the same as the exact Newton scheme.

6.6.1 Coupled scheme

We can extract the boundary-value problem for $(\delta\boldsymbol{\theta},\delta\phi)$ based on the Newton-like scheme (6.6.3)-(6.6.5)

$$\nabla^2\delta\phi=-\nabla^2\hat{\phi}-f\quad\text{in }\Omega, \tag{6.6.6}$$

$$\partial_n\delta\phi+\mathrm{div}_{\Gamma}\left(\delta\theta\cdot\mathbf{n}\nabla\hat{\phi}\right)-f\delta\boldsymbol{\theta}\cdot\boldsymbol{n}=0,\quad\text{on }\hat{\Gamma}, \tag{6.6.7}$$

$$\partial_{\boldsymbol{n}}\delta\phi+\omega\delta\phi=g+\omega h-\left(\partial_{\boldsymbol{n}}\hat{\phi}+\omega\hat{\phi}\right)\quad\text{on }\Gamma_R, \tag{6.6.8}$$

1. Initialize with $\left(\boldsymbol{\theta}^0, \phi^0\right)$; set $k = 0$.

2. Given $\left(\boldsymbol{\theta}^k, \phi^k\right)$, solve the free boundary problem (6.6.6)-(6.6.8) with (6.6.9) (or(6.6.10)) for $(\delta\boldsymbol{\theta} \cdot \boldsymbol{n}, \delta\phi)$.

3. Update the free boundary displacement as

$$\boldsymbol{\theta}^{k+1} = \boldsymbol{\theta}^k + (\delta\boldsymbol{\theta} \cdot \boldsymbol{n})\, \boldsymbol{m}^k,$$

and ϕ^k as

$$\phi^{k+1} = \phi^k + \delta\phi,$$

with $\boldsymbol{m}^k \cdot \boldsymbol{n} = 1$ on $\hat{\Gamma}$. Then repeat from step 2. until convergence.

Table 6.1: The coupled shape-Newton scheme solving for $(\delta\boldsymbol{\theta}, \delta\phi)$.

with the boundary condition on the free boundary as either the Dirichlet condition

$$\delta\phi - \partial_{\boldsymbol{n}} h \delta\boldsymbol{\theta} \cdot \boldsymbol{n} = h - \phi, \quad \text{on } \hat{\Gamma} \tag{6.6.9}$$

or the Bernoulli condition

$$2a\nabla\hat{\phi} \cdot \nabla\delta\phi + \left(2a\kappa \left|\nabla\hat{\phi}\right|^2 + bn_y\right) \delta\boldsymbol{\theta} \cdot \boldsymbol{n} = -\left(a\left|\nabla\hat{\phi}\right|^2 + b\hat{\eta} + c\right), \quad \text{on } \hat{\Gamma}. \tag{6.6.10}$$

The algorithm is given in Table 6.1. The free boundary is updated along the direction of $\boldsymbol{m}^k$ with $\boldsymbol{m}^k \cdot \boldsymbol{n} = 1$ such that the free surface can be piecewise smooth. Choosing $\boldsymbol{m}^k = \left(0, \frac{1}{n_y}\right)$, the free boundary would be updated in the y direction.

Alternatively, we have $d\Gamma = ds = \sqrt{1 + \hat{\eta}_x^2} dx$ such that

$$\int_{\hat{\Gamma}} (\cdot)\, \delta\boldsymbol{\theta} \cdot \boldsymbol{n} d\Gamma = \int_{\hat{\Gamma}} (\cdot)\, \delta\eta dx, \tag{6.6.11}$$

where s is the arc length and $\delta\eta = \sqrt{1 + \hat{\eta}_x^2}\, (\delta\boldsymbol{\theta} \cdot \boldsymbol{n}) = \delta\boldsymbol{\theta} \cdot (-\hat{\eta}_x, 1)$. The boundary integrals can be evaluated in a referenced domain along the x direction, and this problem can be solved in terms of the pair $(\delta\eta, \delta\phi)$. The algorithm is now displayed as Table 6.2, and the geometry is updated vertically with $\delta\eta$.

1. Initialize with (η^0, ϕ^0); set $k = 0$.

2. Given $\left(\eta^k, \phi^k\right)$, solve the free boundary problem (6.6.6)-(6.6.8) with (6.6.10) for $(\delta\eta, \delta\phi)$.

3. Update the free boundary displacement as
$$\eta^{k+1} = \eta^k + \delta\eta,$$
and ϕ^k as
$$\phi^{k+1} = \phi^k + \delta\phi.$$
Repeat from step 2. until convergence.

Table 6.2: The coupled shape-Newton scheme for $(\delta\eta, \delta\phi)$.

6.6.2 Implementation

Now we will describe how to implement the finite element method and the shape-Newton scheme to solve the coupled problem (6.6.6)-(6.6.8) with either Dirichlet boundary condition (6.6.9) or Bernoulli condition (6.6.10) on the free boundary. The values of residual $\mathcal{R}_1$ are denoted as $\boldsymbol{R}_1$, and the residuals $\mathcal{R}_2$ are denoted as $\boldsymbol{R}_2$. The corrections $\delta\phi$ and $\delta\boldsymbol{\theta} \cdot \boldsymbol{n}$ can be stored in a vector form $\boldsymbol{\delta\phi}$ and $\boldsymbol{\delta\eta}$. The linear system is constructed based on the approximations (6.6.3) and (6.6.4) for Dirichlet condition or (6.6.5) for Bernoulli condition as

$$\begin{bmatrix} A & B \\ C & D \end{bmatrix} \begin{bmatrix} \boldsymbol{\delta\phi} \\ \boldsymbol{\delta\eta} \end{bmatrix} = \begin{bmatrix} -\boldsymbol{R}_1 \\ -\boldsymbol{R}_2 \end{bmatrix}, \tag{6.6.12}$$

where A and C are the derivative of the residual $\boldsymbol{R}_1$ and $\boldsymbol{R}_2$ with respect to $\boldsymbol{\delta\phi}$, while B and D are the derivative of the residual $\boldsymbol{R}_1$ and $\boldsymbol{R}_2$ with respect to $\boldsymbol{\delta\eta}$.

As in [56], the triangulation in the domain Ω is denoted as $\mathcal{K} = \{K_i : K_i \in \Omega, \quad \cup_{i=\{1,2,\ldots,n\}} K_i = \Omega\}$ where K_i is a triangle with three nodes $N^j = (x^j, y^j)$ for $j = 1, 2, 3$. The free boundary Γ_F can partitioned into N line segments $L_i := \{(x, y) : (x^{i-1}, y^{i-1}) \leq (x, y) \leq (x^{i+1}, y^{i+1})\}$ for $i = 1, 2, ..., N+1$ with two end points $N^l = (x^l, y^l)$ for $l = 1, 2$. The function spaces V and W are considered to have a

piecewise linear function basis. The basis function can be defined on the triangle K_i and the line segment L_i respectively as:

$$\psi_j(x,y) = a_j x + b_j y + c_j \quad \text{for } (x,y) \in K_j, \tag{6.6.13}$$

$$\xi_i\left(s(x,y)\right) = \alpha_i s(x,y) + \beta_i \quad \text{for , for } (x,y) \in L_i \tag{6.6.14}$$

such that

$$\psi_j(N_k) = \begin{cases} 1, & j = k, \\ 0, & j \neq k, \end{cases}, \qquad \text{and} \qquad \xi_i(N_k) = \begin{cases} 1, & i = k, \\ 0, & i \neq k, \end{cases}, \tag{6.6.15}$$

where s is the arclength. The coefficients are calculated by

$$a_j = \frac{x^k y^l - x^l y^k}{2\left|K_j\right|}, b_j = \frac{y^k - y^l}{2\left|K_j\right|}, \quad c_j = \frac{x^l - x^k}{2\left|K_j\right|}, \quad \text{for } k,l = 1,2,3,$$

$$\alpha_i = \begin{cases} \frac{1}{|L_i|}, & \text{for } (x,y) \in L_i, \\ -\frac{1}{|L_{i+1}|}, & \text{for } (x,y) \in L_{i+1}, \end{cases},$$

$$\beta_i = \begin{cases} -\frac{s(x^{i-1},y^{i-1})}{|L_i|}, & \text{for } (x,y) \in L_i, \\ \frac{s(x^{i+1},y^{i+1})}{|L_{i+1}|}, & \text{for } (x,y) \in L_{i+1}, \end{cases}$$

where $|K_j|$ is the area of the triangle K_j, $|L_i|$ is the length of the line segment L_i. Note that the coefficients a_j, b_j, and c_j are different from the coefficient a given in the Laplace equation, and the coefficients b, c in the Bernoulli-type equation.

The entries of the matrices A and B are given by

$$A_{ij} = \int_{K_i} \nabla\psi_i \cdot \nabla\psi_j d\Omega, \tag{6.6.16}$$

$$B_{ij} = \int_{L_i} \nabla_\Gamma \hat{\phi} \cdot \nabla_\Gamma \psi_j \xi_i ds - \int_{L_i} f \psi_j \xi_i ds. \tag{6.6.17}$$

The tangential derivative $\nabla_\Gamma = \frac{d}{ds}$ can be approximated by the finite difference method.

The residual $\boldsymbol{R}_{1,i}$ is estimated based on (6.3.2) as

$$\boldsymbol{R}_{1,i} = \int_\Omega \nabla\hat{\phi}\cdot\nabla\psi_i d\Omega - \int_{\partial\Omega\setminus\Gamma_F} g\psi_i ds - \int_\Omega f\psi_i d\Omega. \tag{6.6.18}$$

For the Dirichlet boundary condition, the entries of C and D are given by (6.5.6) and (6.5.8) respectively, which are

$$C_{ij} = \int_{L_i} \psi_j\xi_i ds, \tag{6.6.19}$$

$$D_{ij} = -\int_{L_i} \partial_{\boldsymbol{n}} h\xi_i\xi_j ds. \tag{6.6.20}$$

Since the function h is given, we can use the exact analytical expression for $\partial_{\boldsymbol{n}} h$. According to (6.5.5), the residual $\boldsymbol{R}_{2,i}$ is given by

$$\boldsymbol{R}_{2,i} = \int_{\Gamma_F} \left(h - \hat{\phi}\right)\xi_i ds. \tag{6.6.21}$$

The finite difference method can find the derivative $\hat{\eta}_x$.

For Bernoulli boundary condition, the entries of C and D are approximated by (6.5.10) and (6.5.15) as

$$C_{ij} = \int_{L_i} 2a\nabla\hat{\phi}\cdot\nabla\psi_j\xi_i ds, \tag{6.6.22}$$

$$D_{ij} = \int_{L_i} \left(2a\kappa\left|\nabla\hat{\phi}\right|^2 + bn_y\right)\xi_i\xi_j ds. \tag{6.6.23}$$

The curvature term $\kappa = \partial_x\left(\frac{\hat{\eta}_x}{\sqrt{1+\hat{\eta}_x{}^2}}\right)$ needs the second derivative of $\hat{\eta}$, but the free boundary is piecewise linear. If we use integration by parts, the first derivative term $\int_{L_i}(\cdot)\,\xi_i'\xi_j dx$ will cause the linear system to be singular such that the last N rows are linearly dependent. Thus we first fit a higher-order continuous curve to the shape of the free boundary, and then use the finite difference method to find the curvature

κ instead. In addition, the term $\left|\nabla\hat{\phi}\right|^2 = \left|\nabla_\Gamma\hat{\phi}\right|^2 = \left(\frac{d\hat{\phi}}{ds}\right)^2$ can be estimated as a constant using finite difference method on L_i.

According to (6.5.9), the residual $\boldsymbol{R}_{2,i}$ is given by

$$\boldsymbol{R}_{2,i} = \int_{\Gamma_F} \left(a\left|\nabla\hat{\phi}\right|^2 + b\hat{\eta} + c\right)\xi_i ds. \tag{6.6.24}$$

6.7 Numerical experiments

We start with a straightforward test case for the Dirichlet boundary condition problem and then focus on the submerged triangle problem. The first test case is also a Bernoulli free-boundary problem simplified from the submerged triangle problem, with a Dirichlet condition on both the fixed and free boundary. The submerged triangle problem is the problem in which we are mainly interested in applying this shape-Newton scheme. We will use the algorithm in Table 6.2 such that the displacement of the free boundary is updated vertically.

6.7.1 Dirichlet boundary condition

The test case for the free-boundary problem with Dirichlet boundary condition is a Bernoulli free-boundary problem derived from a manufactured solution,

$$\phi = x + y, \quad \eta = x + 1, \tag{6.7.1}$$

such that the data can be obtained as

$$f = 0, \quad g = 0, \quad h = \begin{cases} 2y - 1, & \text{on } \Gamma_F, \\ x + y, & \text{on } \partial\Omega \setminus \Gamma_F. \end{cases}$$

With an initial domain $\Omega_0 = \{(x, y) : x \in [0, 1], y \in [0, x^2 + 1]\}$, how the domain and the triangulation changes in the first three iterations is shown in Figure 6.2.

Starting with a parabola, the free boundary is almost a straight line after the third iteration.

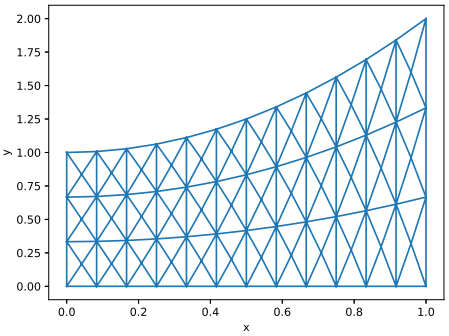

(a) *The initial domain and the triangulation.*

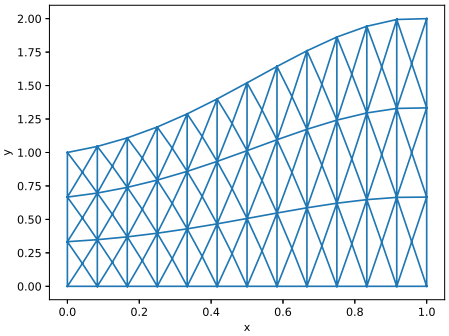

(b) *The domain and the triangulation after the first iteration.*

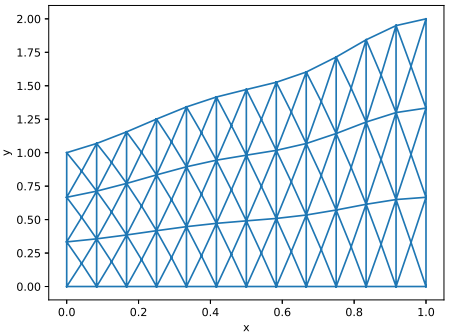

(c) *The domain and the triangulation after the second iteration.*

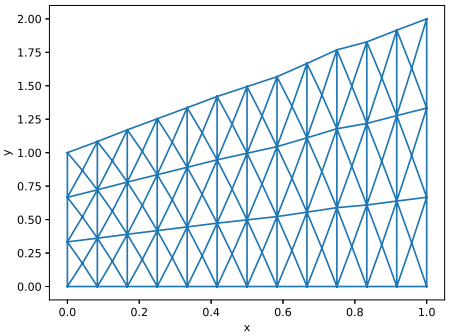

(d) *The domain and the triangulation after the third iteration.*

Figure 6.2: *The initial domain and the change of the domain in three following Newton-like iterations. The free surface is updated vertically.*

Figure 6.3 shows the error between numerical results of ϕ and η compared with the exact solution (6.7.1) on the free boundary Γ_F with a different number of finite element meshes. The value of $N+1$ represents the number of nodes along the x-axis, and the number of nodes along the y-axis is $\frac{N}{4}$. We use more nodes along the x-axis because we are more interested in how the free boundary behaves. Although the error is slightly larger with more nodes, the shape-Newton scheme converges superlinearly as shown in Figure 6.3. Moreover, there appears to be a plateau at higher iterations. One possible reason for the plateau and the rising error values is that we use a finite difference method to find the derivatives and the normal

vector. However, even though the error rises with more elements, it is still around 10^{-12} when we choose $N = 640$ such that there are 409600 elements in total in the domain.

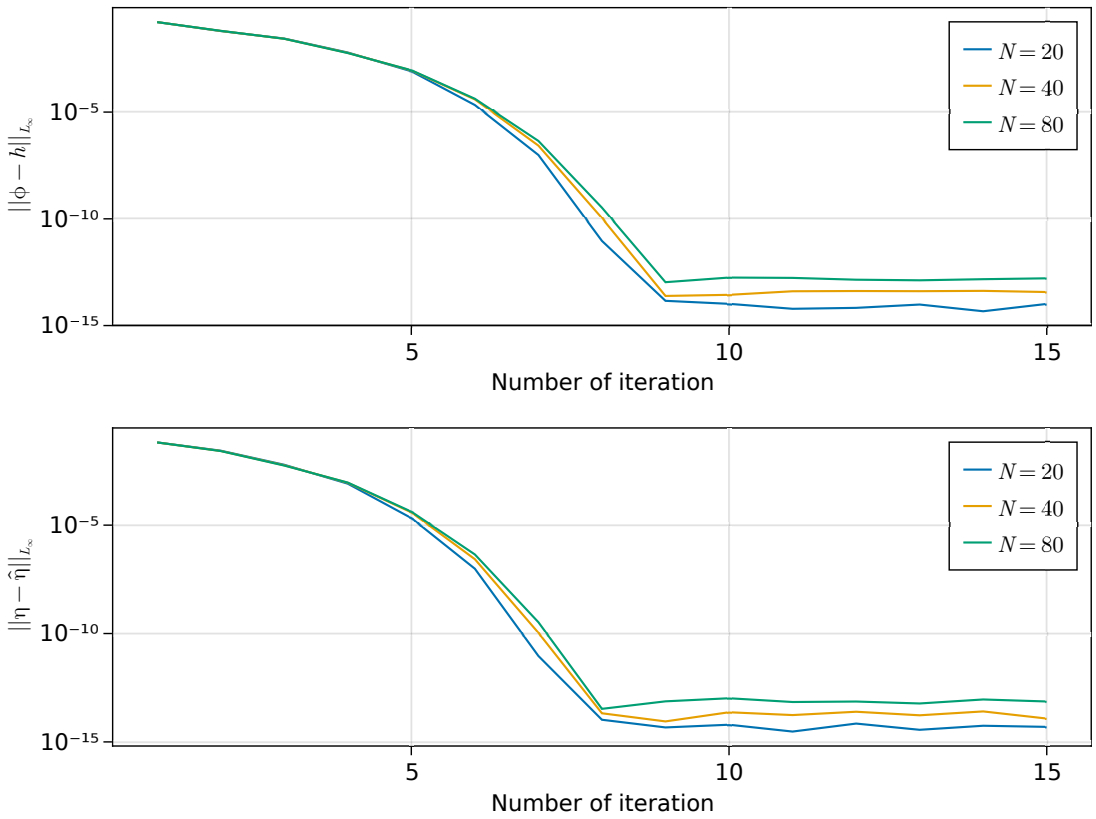

Figure 6.3: *The Dirichlet error $||\phi - h||_{L_\infty}$ and surface error $||\eta - \hat{\eta}||_{L_\infty}$ on Γ_F measured in L_∞-form against the number of iterations. The upper plot shows the Dirichlet error, and the lower shows the surface error. The values of $N + 1$ are the number of the nodes along the x-axis.*

6.7.2 The submerged triangle problem

The second test case is the submerged triangle problem investigated by Dias and Vanden-Broeck [22]. A detailed derivation of the governing equations can be found in Appendix D. Open channel flow problems can also be formulated by shallow-water theory (see e.g. [40, 58], however, since there are sharp corners on the bottom boundary in this problem, the classical analytical shallow-water solutions are not valid (see e.g. [20]). In this section, we compare our numerical solutions with the

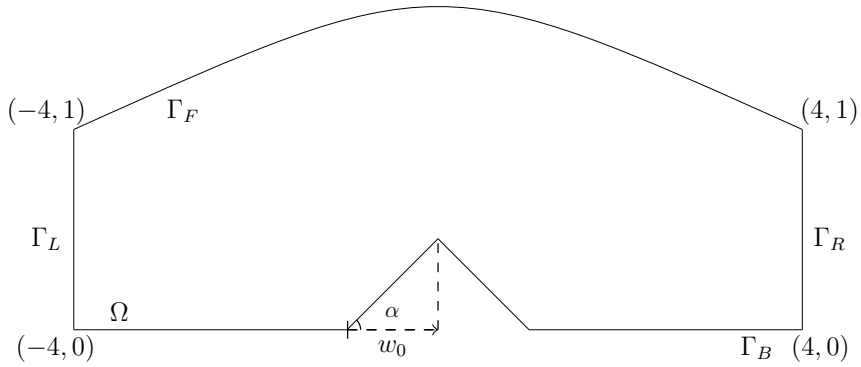

Figure 6.4: *The sketch of the domain we used for the second test case. α is denoted as the angle and w_0 as the half width of the triangle.*

numerical results obtained through series truncation in [22].

In this problem, we have a Neumann boundary condition on $\partial\Omega \setminus \Gamma_R$ and a Dirichlet boundary condition on Γ_R, i.e. $\omega = 0$ on $\partial\Omega \setminus \Gamma_R$ and $\omega \to \infty$ on Γ_R. The data defining this problem is given as follows:

$$
\begin{aligned}
f &= 0, \\
g &= \begin{cases} 0, & \text{on } \partial\Omega \setminus \Gamma_L, \\ -1, & \text{on } \Gamma_L, \end{cases} \\
h &= 0 \quad \text{on } \Gamma_R.
\end{aligned}
$$

The Bernoulli condition is obtained by giving $a = \frac{1}{2}F^2$, $b = 1$ and $c = \frac{1}{2}F^2 + 1$ where F is the Froude number. The domain is a rectangle truncated at $|x| = 4$ containing an isosceles triangle symmetric about $x = 0$ having an angle α and width $2w_0$ at the bottom, as shown in Figure 6.4. The space is discretised as shown in Figure 6.5, where it was uniformly spaced along the $x-$axis and the vertical direction for fixed values of x. Then the algorithm in Table 6.2 can be applied to solve for the pair $(\delta\eta, \delta\phi)$, and the free boundary can be updated vertically with $\delta\eta$. We evaluate accuracy by comparing the results across various mesh sizes, as displayed in the Table 6.3 by calculating $\|\eta_n - \eta_{n=1280}\|_{L_2}$, where n is the number of nodes on the free boundary Γ_F.

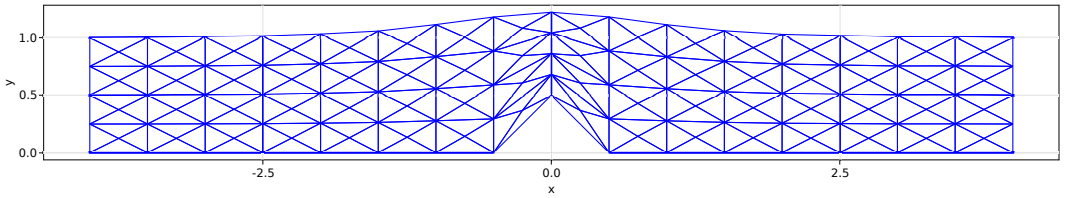

Figure 6.5: *An example of the domain and the triangulation with* $\alpha = \frac{\pi}{4}$, $F = 2$ *and the half width of the triangle* $w_0 = 0.5$.

Number of nodes on the free boundary	$\|\eta_n - \eta_{n=1280}\|_{L_2}$
$n = 80$	0.00010980320381847985
$n = 160$	$3.2666237189266785e{-5}$
$n = 320$	$9.720801400568423e{-6}$
$n = 640$	$2.318797100287373e{-6}$

Table 6.3: The convergence in space, where $\alpha = \frac{\pi}{16}$, $w_0 = 0.1$, and $F = 3$.

Dias and Vanden-Broeck [22] found that the solutions to the submerged problem have two types: One is supercritical flow both upstream and downstream, and the other is supercritical (or subcritical) upstream and subcritical (or supercritical) downstream flow. Our numerical solutions are the first type, and we can compare them with the results in [22].

Some converged grids of the whole region are shown in Figure 6.6. We noticed that $\eta(x)$ has a maximum value y_0 at $x = 0$ on the free boundary, and the value of y_0 can change with the values of α, w_0 and F. Figure 6.7 shows the value of y_0 against the Froude number F for various values of α, which shows the same qualitative results as in Figure D.2. We can observe from Figure 6.7 that y_0 will decrease when the Froude number F becomes larger for the fixed width of the triangle. In addition, for fixed values of F and angle α, y_0 will also decrease with the width of the triangle. This agrees with the results presented by Dias and Vanden-Broeck in [22], who solved this problem for fixed $\alpha = \frac{\pi}{4}$. However, as shown in Figure 6.7c and Figure 6.7d, it is hard for us to solve this problem with a larger triangle. This also explains why the critical values obtained from our algorithm are different from the results in [22]. The details about Dias and Vanden-Broeck's results will be illustrated in Appendix

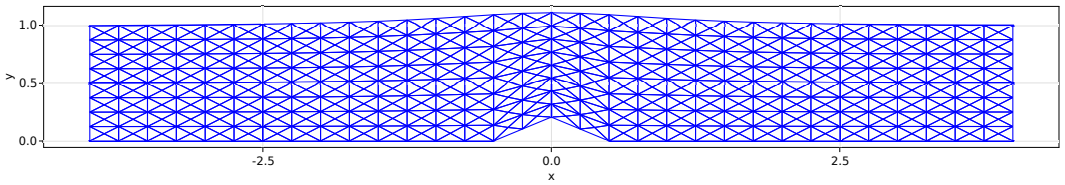

(a) *The final domain for* $\alpha = \frac{\pi}{8}$, $w_0 = 0.5$, *and* $F = 1.4$.

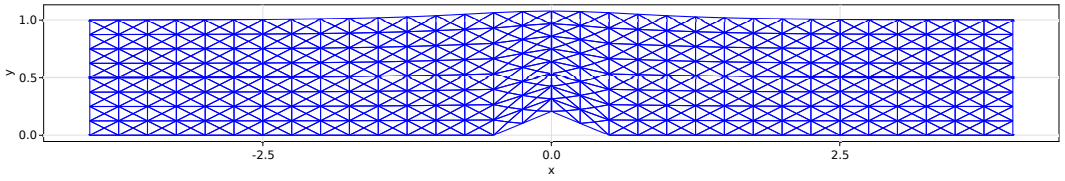

(b) *The final domain for* $\alpha = \frac{\pi}{8}$, $w_0 = 0.5$, *and* $F = 2$.

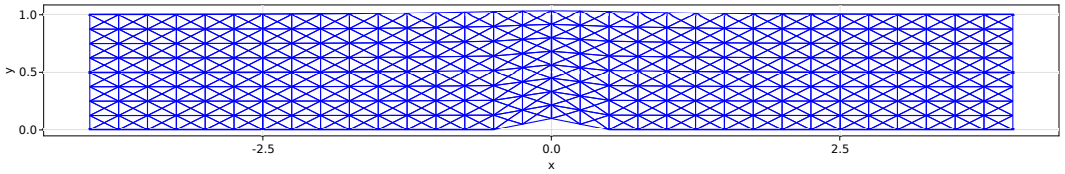

(c) *The final domain for* $\alpha = \frac{\pi}{16}$, $w_0 = 0.5$, *and* $F = 2$.

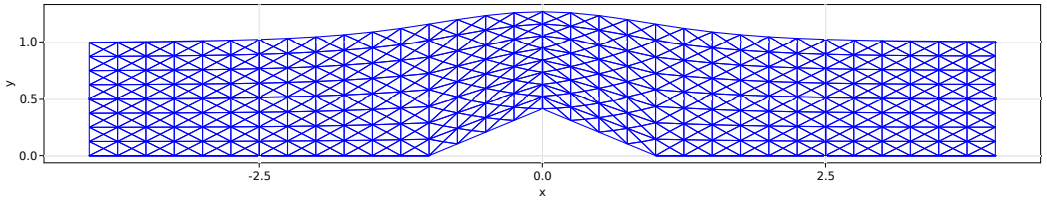

(d) *The final domain for* $\alpha = \frac{\pi}{8}$, $w_0 = 1$, *and* $F = 2$.

Figure 6.6: *The final domains for various* α, w_0 *and* F, *where their free boundarys are the numerical solutions.*

D.

We also found that the solutions are challenging for larger angle α for fixed width. The possible reason is that with a higher triangle height, the flow can approach its limiting configuration as a thin layer over the edge of the triangle with a stagnation point.

The rate of convergence is shown in Figure 6.8, where we show the error $||\delta\phi||_{L_2}$

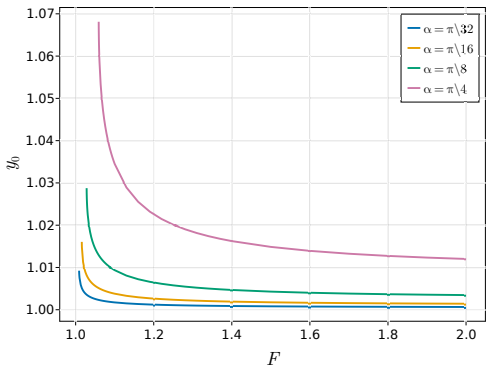

(a) *The maximum value y on the free boundary at $x = 0$ against F with $w_0 = 0.1$ for different values of α.*

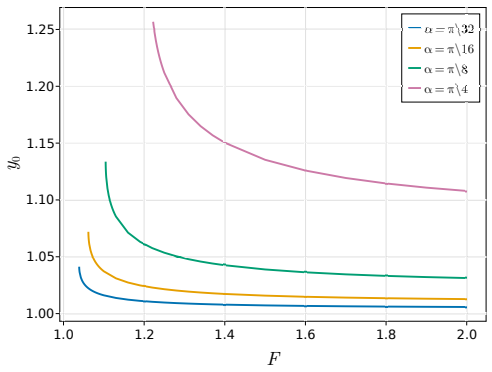

(b) *The maximum value y on the free boundary at $x = 0$ against F with $w_0 = 0.3$ for different values of α.*

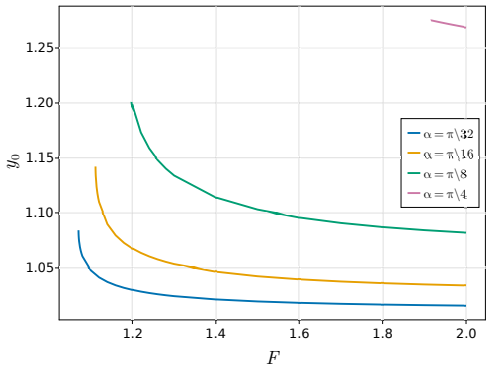

(c) *The maximum value y on the free boundary at $x = 0$ against F with $w_0 = 0.5$ for different values of α.*

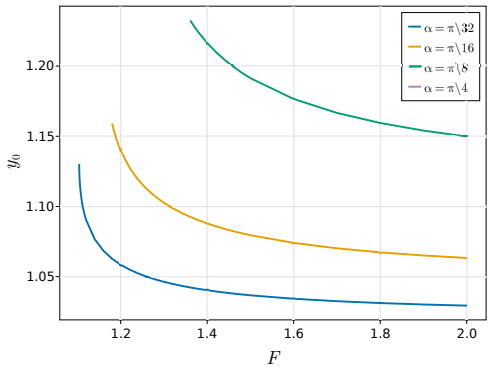

(d) *The maximum value y on the free boundary at $x = 0$ against F with $w_0 = 0.7$ for different values of α.*

Figure 6.7: *The maximum value y_0 on the free boundary at $x = 0$ against F for different values of α and w_0.*

and the surface error $||\delta\eta||_{L_2}$ against the number of iterations for $\alpha = \frac{\pi}{8}$, $w_0 = 0.3$ and $F = 3$. The Dirichlet error $\delta\phi$ in Ω and the surface error $\delta\eta$ on Γ_F show superlinear convergence. This figure also shows the comparison of the errors for different mesh densities. The Dirichlet error is slightly larger with higher mesh densities but converges faster. The convergence of surface error does not have much difference at the beginning but then has lower values for higher mesh densities. The interesting behaviour is that both the Dirichlet and the surface errors oscillate around some values between order 10^{-10} and 10^{-13}. The order of those values is higher for higher mesh densities, which the discretization error can explain. The convergence is slower as the error becomes very close to the discretization error.

In addition, the convergence of surface error slows first, which further affects the Dirichlet error as a consequence of solving as a pair.

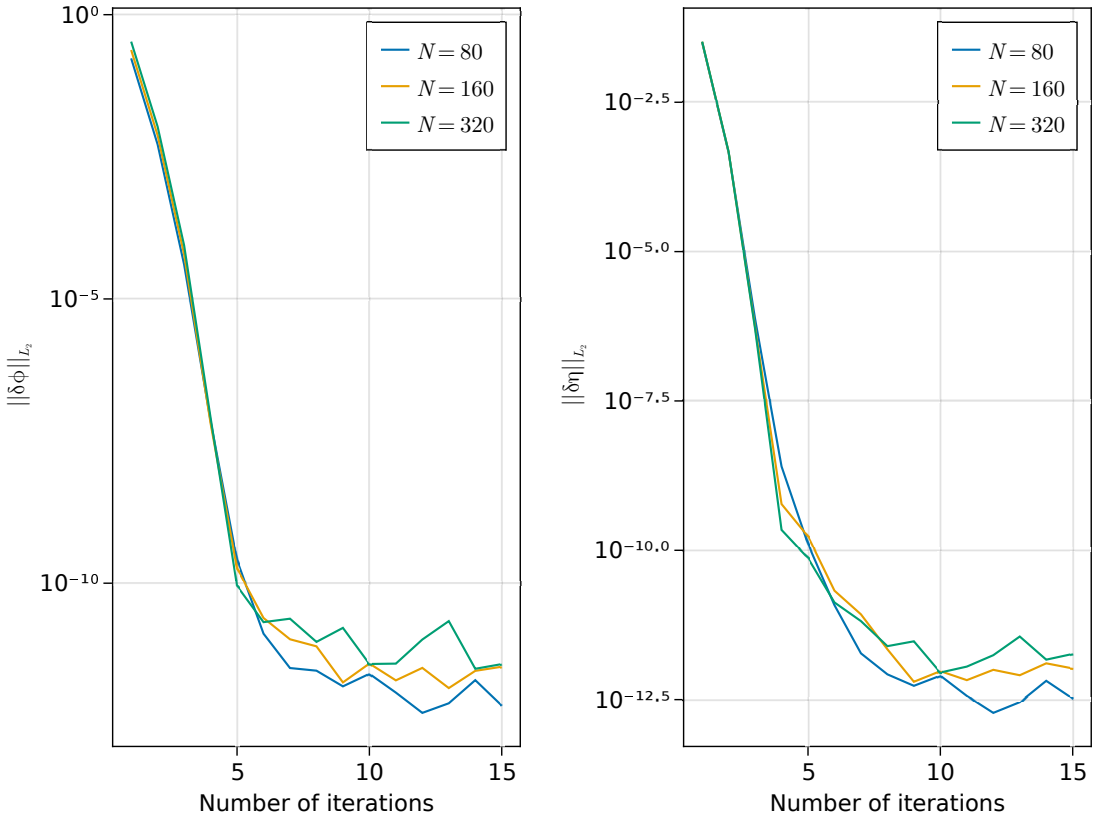

Figure 6.8: *The error $||\delta\phi||_{L_2}$ and surface error $||\delta\eta||_{L_2}$ on Γ_F measured in L_∞-form against the number of iterations with $\alpha = \frac{\pi}{8}$, $w_0 = 0.3$ and $F = 3$. The upper plot shows the Dirichlet error, and the lower shows the surface error. The values of $N + 1$ are the number of the nodes along the x-axis.*

6.8 Conclusion

In this chapter, we derive a shape-Newton method to solve generic free-boundary problems. First, as the problem is nonlinear, the linearised problems are obtained by applying the Hadamard formula for shape derivatives to the two sets of weak forms of the free boundary problem. Then, after the linearisation and neglecting the small-valued terms, the linearised problem can be solved by a Newton-like scheme with an approximated Jacobian matrix.

Although our main interest is to solve the free-boundary problem with a Bernoulli boundary condition on the free surface, the nonlinearity of this boundary condition makes the problem more complicated. So we start from a more straightforward case by considering the Dirichlet boundary condition. To be more general, we use the Robin boundary condition on the fixed boundaries.

The linearisation for the problem with the Dirichlet boundary condition is relatively standard, and we use a straightforward numerical experiment with a manufactured solution to test the numerical schemes. The results agree well with the exact solutions and converge quadratically.

The linearisation for the problem with a Bernoulli-type condition is interesting. The curvature terms of the shape derivative of the boundary integral can be neglected due to the Neumann boundary condition (6.2.2), and only the normal derivative terms remain. However, after some calculations, we find that the normal derivative term satisfies $\partial_{\boldsymbol{n}} |\phi|^2 = 2\kappa |\nabla\phi|^2$. The test problem considers the flow over the submerged triangle problem, whose detail is shown in Appendix D. This chapter only assumes that the inflow and outflow have the same depth and speed. The results in [22] show that for the fixed shape of the triangle, the Froude number F first decreases and then increases when the maximum deviation of the free boundary increases. This indicates that for some values of F, two solutions exist. However, our method can only find the solution with the lower maximum deviation due to the limitation of solving the problem with a larger triangle. Despite this, both numerical tests show that the shape-Newton method converges superlinearly.

Chapter 7

Conclusion

We presented asymptotic solutions and numerical methods for some free-boundary problems in fluid mechanics. We studied three main topics: the small-time asymptotic solutions for a two-fluid dam-break problem and a solid/two-fluid interaction problem in chapters 3 and 4 correspondingly, a finite element method to solve the small-time inner-region problem of the solid/single interaction problem in chapter 5, and a shape-Newton method for generic free-boundary problems in chapter 6.

The two-fluid dam-break problem in chapter 3 and the solid/two-fluid interaction problem in chapter 4 has the same local problem when time t is small. In both problems, there is a singularity at the contact point between the interface of two fluids and the solid plate. To resolve the singularity, the problem is rescaled into an inner region around the contact points. In order to numerically solve the inner problem using finite element methods, we start with the solid/single fluid interaction problem with an inclined accelerating plate in [64] in chapter 5, which is a limiting case ($\bar{\rho} \to +\infty$) of the problem in chapter 4 and can be numerically solved in one domain by ignoring the effect of the fluid on the top. However, the numerical method used in chapter 5 is slow and converges linearly, which motivates us to develop a shape-Newton method in chapter 6 for a generic steady free-boundary problem.

In chapter 3, we investigated a two-fluid dam-break problem in a channel at

initial stage, where a plate separates two immiscible, inviscid and incompressible fluids. The interface between the fluids initially has an angle α with the horizontal, and the fluids remain at rest. The two-dimensional irrotational flows start to move when the plate is suddenly removed and are confined by an upper and a solid bottom wall. By applying the asymptotic and numerical methods, there is a singularity in the shape of the interface at the top contact point between the interface and the solid boundary at small time.

We formulate the outer-region problem using a small-time expansion, which can be solved by eigenfunction expansions and the Plemelj formula. Introducing the velocity potential in the leading order of the form

$$\bar{\phi}_1 \sim A_1 r^{\beta_0} \cos \beta_0 (\pi - \theta), \quad \bar{\phi}_2 \sim A_2 r^{\beta_0} \cos \beta_0 \theta, \tag{7.0.1}$$

as $r \to 0$, where $(x, y) = (r \cos\theta, r \sin\theta)$, and A_1,A_2 are real constants, the eigenvalue problem for β_0 at the bottom contact point

$$\frac{\tan \beta_0 \alpha}{1 + \bar{\rho}} = -\tan \beta_0 (\pi - \alpha), \tag{7.0.2}$$

while the problem for the upper intersection point is

$$\frac{\tan \beta_0 (\pi - \alpha)}{1 + \bar{\rho}} = -\tan \beta_0 \alpha. \tag{7.0.3}$$

The value of β_0 is always larger than 1 at the lower contact point with the bottom solid boundary but smaller than 1 at the upper intersection point. The vertical displacement of the interface denoted as $\bar{Y}$ in the leading order satisfies

$$\bar{Y} \sim O\left(r^{\beta_0 - 1}\right),$$

where a singularity appears as $r = 0$ at the upper contact point. In addition, we solve

the limiting case when the density difference ratio $\bar{\rho}$ of the two fluids is extremely small to test our numerical results.

The numerical results of velocity potential are obtained by evaluating the Plemelj formula (3.4.16) with the Trapezium rule. To apply the Plemelj formula effectively and simplify the calculation, it is essential to reflect the interface with $y = 0$ and extend the surface periodically. This extension ensures the inclusion of all singularities along the contour. The numerical results show great agreement with the asymptotic solutions and the values of β_0 as shown in Figure 3.6 for the upper contact point. However, for the values of β_0 close to the lower intersection point, the difference between the numerical results and the eigenvalues of β_0 is obvious. This is because the leading term in the asymptotic solution is linear, and terms with an order of magnitude β_0 are considered higher-order terms.

To resolve the singularity at the upper contact point where the interface meets the solid upper boundary, we rescale the problem into an inner region. The inner problem has the same formulation as the solid/single fluid interaction problem with an inclined accelerating plate in the inner region in [64]. Following the similar analysis in that paper, we can find its local solutions for the velocity potential and the displacement of the interface, which implies that the interface is always perpendicular to the solid upper boundary and there are small oscillations near the intersection point at small time. However, because this problem is nonlinear and involves two different fluids, the inner-region problem is hard to solve numerically using finite element method.

In chapter 4, we studied the initial stage of the solid/two-fluid interaction problem with an inclined accelerating plate by asymptotic and numerical methods. This extends the problem addressed in [64], where only a single fluid was considered in prior research. We consider the situation where two layers of immiscible, inviscid and incompressible fluid initially stay at rest above a horizontal bed, and an inclined plate having an angle $\alpha \in \left(\frac{\pi}{2}, \pi\right)$ with the horizontal moves horizontally with a con-

stant acceleration towards the fluids. The local problem near the intersection point has the same formulation as the two-fluid dam-break problem in chapter 3 around the top intersection point. Hence, we can derive the same form of the asymptotic solutions as (7.0.1) satisfying the same condition (7.0.3) for β_0. Since β_0 is always smaller than 1, the interface is singular at the intersection point of the interface and the moving plate. Considering the limiting case where the depth of the bottom layer fluid d is almost equal to the depth of the total depth of two fluids ($d \to 1$), the constant coefficient A_1 in (7.0.1) satisfies

$$A_1 \sim (1-d)^{\frac{\pi}{2\alpha}-\beta_0} A, \tag{7.0.4}$$

where A is some constant. Another limiting case where $d \to 0$ satisfies

$$A_1 \sim A_0 d^{\gamma}, \tag{7.0.5}$$

where γ can be determined numerically.

To solve this asymptotic problem numerically, we reflect the domain with $x = 0$ and use the Schwarz-Christoffel transformation such that we can apply the Plemelj formula along a smooth contour. Truncated with the arc of a circle with radius R, the Plemelj formula can be evaluated along a closed contour by Gaussian quadrature. Compared with the values of β_0, the numerical results are consistent with the asymptotic solutions where $\beta_0 < 1$. This indicates that there is a singularity in the interface at the intersection point with the moving plate. In addition, the numerical results and the asymptotic solutions show that the coefficient A_1 in (7.0.1) satisfies (7.0.4) for the limiting cases $d \to 1$ while for $d \to 0$, A_1 satisfies (7.0.5). Similar to the two-fluid dam-break problem in chapter 3, we formulate an inner-region problem and find the local solution having the same form, which also needs to be solved numerically.

In chapter 5, to develop a proper numerical method to solve the inner-region

problem of the two-fluid dam-break problem and solid/two-fluid interaction problem using the finite element method, we started with solving the single fluid/solid interaction problem in the inner region [64]. We first used finite element and trial methods to solve the linearised problem as $\alpha \to \frac{\pi}{2}$ such that the Bernoulli equation on the free boundary is linearised and the free surface is fixed. However, the numerical results converge to a different solution such that they agree well with the far-field condition but are inconsistent with the local solutions. Hence, we used Newton's method to solve the whole nonlinear problem, where the Jacobian matrix is approximated by the finite difference method. The numerical results agree well with those obtained by the boundary integral method in [64], but the small oscillations near the intersection point are not captured. The possible reason is that the finite element method suffers from additional numerical dissipation owing to the discretization of the Laplace operator in the interior, which causes fewer oscillations to be resolved on the grid than expected. The critical value of the angle α is $\alpha_c \approx 1.8886$ such that there is no numerical solution for $\alpha > \alpha_c$, which is slightly larger than that in [64]. In addition, although the rate of convergence is quadratic, it is expensive to approximate the Jacobian matrix using standard solvers.

In chapter 6, we developed the Shape-Newton method as a fast numerical solver with superlinear convergence rate for free-boundary problems. We considered the generalised steady free-boundary problem where the boundary conditions on the fixed boundary are Robin boundary conditions, and one of the free-boundary conditions is the Neumann boundary condition. Two different free-boundary conditions are considered: the Dirichlet boundary condition or the Bernoulli boundary condition. In order to apply a Newton-type method to numerically solve the problems, the linearization is required. For both conditions, we use shape calculus to linearise the problem with respect to the geometry of the current approximated free boundary. The shape linearisation of the nonlinear Bernoulli equation is novel. In its derivation, many terms can be neglected due to the homogeneous Neumann boundary condition.

After some calculations, we find that the result involves the normal derivative of the velocity squared, i.e. $\partial_{\boldsymbol{n}} |\nabla\phi|^2$. We tested the problem with the Dirichlet boundary condition using a numerical experiment with manufactured solutions, where the numerical results agree well with the exact solutions and converge quadratically. The test case for the problem with the Bernoulli equation is the flow over the submerged triangle problem [22]. This problem is similarly formulated as the solid/single fluid interaction problem, but the free-boundary conditions are simpler. In addition, setting the top right node on the free boundary to be free to move for the update of the solution in each iteration, the numerical results converge to the solution where the outflow has the same depth and speed as the inflow. This is consistent with the results in [22], and the Shape-Newton method converges superlinearly.

The application of the shape-Newton method can be extended to find the solutions of the flow over a submerged triangle in the situation where the depths of the upstream and downstream are different. This requires to carefully choose the different boundary conditions for the upstream and downstream flow.

It can also be extended to numerically solve the similar problems of one layer [30] and two layers [23, 73, 75] of flow over a submerged semi-circular obstacle. In addition, these problems of two layers fluids have a similar formulation as the two-fluid dam-break problem and the solid/two-fluid interaction problem, but the free-boundary conditions are less complicated because the effect of the moving plate is not included. In these problems, the application of the shape derivative to obtain the linearisation can be extended into two domains occupied by different fluids, such that a Newton-type method can be used to numerically solve the nonlinear problems.

The Shape-Newton method has a superlinear convergence rate in numerically solving free-boundary problems with the Bernoulli condition on the free surface. It can be further applied to finding the numerical solutions to the inner problem of the two-fluid dam-break scenario discussed in Chapter 3 and the solid/two-fluid interaction problem explored in Chapter 4.

Moreover, another possible future research is the incorporation of surface tension effects into the two-fluid dam-break problem and the solid/two-fluid interaction problem with an accelerating plate. It is essential to acknowledge that our current work assumed the absence of surface tension. However, the surface tension is important and can resolve the singularity in the shape of the free surface, as referenced in [5, 84, 98]. Including the surface tension in the two-fluid dam-break problem and the solid/two-fluid interaction problem could provide valuable insights and a deeper understanding of the behaviour of the flows.

Bibliography

[1] M. J. Ablowitz and A. S. Fokas. *Complex Variables: Introduction and Applications*, volume 35. Cambridge University Press, 2003.

[2] G. R. Baker. Generalized vortex methods for free-surface flows. In Richard E. Meyer, editor, *Waves on Fluid Interfaces*, pages 53 – 81. Academic Press, 1983.

[3] D. Begis and R. Glowinski. Application de la méthode des éléments finis à l'approximation d'un problème de domaine optimal. méthodes de résolution des problèmes approchés. *Applied Mathematics and Optimization*, 2:130–169, 1975.

[4] J. Billingham. A dam break driven by a moving source: a simple model for a powder snow avalanche. *Journal of Fluid Mechanics*, 870:353–388, 2019.

[5] J. Billingham, D. J. Needham, E. Korsukova, and R. J. Munro. The initial development of a jet caused by fluid, body and free surface interaction. part 5. parasitic capillary waves on an initially horizontal surface. *Journal of Fluid Mechanics*, 836:850–872, 2018.

[6] O. Bokhove, A. Kalogirou, and W. Zweers. From bore–soliton–splash to a new wave-to-wire wave-energy model. *Water Waves*, 1(2):217–258, 2019.

[7] F. Bouchon, S. Clain, and R. Touzani. Numerical solution of the free boundary bernoulli problem using a level set formulation. *Computer methods in applied mechanics and engineering*, 194(36-38):3934–3948, 2005.

[8] P. Brufau and P. Garcia-Navarro. Two-dimensional dam break flow simulation. *International Journal for numerical methods in fluids*, 33(1):35–57, 2000.

[9] G. F. Carrier. *Functions of a complex variable : theory and technique / George F.Carrier, Max Krook, Carl E. Pearson.* McGraw-Hill, New York ; London, 1966.

[10] R. K. C. Chan. *SUMMAC-A numerical model for water waves.* Stanford University, 1970.

[11] H. Chanson. *The hydraulics of open channel flow: an introduction. physical modelling of hydraulics.* Butterworth-Heinemann, 1999.

[12] H. Chanson. *The hydraulics of open channel flow : an introduction : basic principles, sediment motion, hydraulic modelling, design of hydraulic struc-*

tures / Hubert Chanson. Elsevier Butterworth-Heinemann, Oxford, 2nd ed. edition, 2004.

[13] C. J. Chen and H. C. Chen. Finite analytic numerical method for unsteady two-dimensional navier-stokes equations. *Journal of Computational Physics*, 53(2):209–226, 1984.

[14] A. T. Chwang. Hydrodynamic pressures on sloping dams during earthquakes. part 2. exact theory. *Journal of Fluid Mechanics*, 87(2):343–348, 1978.

[15] A. T. Chwang. Nonlinear hydrodynamic pressure on an accelerating plate. *The Physics of Fluids*, 26(2):383–387, 1983.

[16] J. B. Conway. *Functions of One Complex Variable I.* Functions of One Complex Variable. Springer, 1978.

[17] M. J. Cooker, D. H. Peregrine, C. Vidal, and J. W. Dold. The interaction between a solitary wave and a submerged semicircular cylinder. *Journal of Fluid Mechanics*, 215:1–22, 1990.

[18] J. Crank. *Free and Moving Boundary Problems.* Oxford science publications. Clarendon Press, 1987.

[19] A. J. Crespo, M. Gómez-Gesteira, and R. A. Dalrymple. Modeling dam break behavior over a wet bed by a SPH technique. *Journal of waterway, port, coastal, and ocean engineering*, 134(6):313–320, 2008.

[20] O. Delestre, C. Lucas, P. A. Ksinant, F. Darboux, C. Laguerre, T. N. T. Vo, F. James, and S. Cordier. Swashes: a compilation of shallow water analytic solutions for hydraulic and environmental studies. *International Journal for Numerical Methods in Fluids*, 72(3):269–300, 2013.

[21] M. C. Delfour and J. P. Zolésio. *Shapes and Geometries: Analysis, Differential Calculus, and Optimization.* Advances in Design and Control. Society for Industrial and Applied Mathematics, 2001.

[22] F. Dias and J. M. Vanden-Broeck. Open channel flows with submerged obstructions. *Journal of Fluid Mechanics*, 206:155–170, 1989.

[23] F. Dias and J. M. Vanden-Broeck. Steady two–layer flows over an obstacle. *Philosophical Transactions of the Royal Society of London. Series A: Mathematical, Physical and Engineering Sciences*, 360(1799):2137–2154, 2002.

[24] Z. N. Dobrovol'Skaya. On some problems of similarity flow of fluid with a free surface. *Journal of Fluid Mechanics*, 36(4):805–829, 1969.

[25] J. W. Dold and D. H. Peregrine. An efficient boundary-integral method for steep unsteady water waves. *Numerical methods for fluid dynamics II*, 671:679, 1986.

[26] R. F. Dressler. *Hydraulic resistance effect upon the dam-break functions*, volume 49. National Bureau of Standards Washington, DC, 1952.

[27] K. Eppler and H. Harbrecht. Efficient treatment of stationary free boundary problems. *Applied numerical mathematics*, 56(10-11):1326–1339, 2006.

[28] Y. Fan, J. Billingham, and K. G. van der Zee. A shape-newton method for free-boundary problems subject to the bernoulli boundary condition, 2023.

[29] J. Faure and N. Nahas. Etude numérique et expérimentale d'intumescences a forte courbure du front. *La houille blanche*, (5):576–587, 1961.

[30] L. K. Forbes and L. W. Schwartz. Free-surface flow over a semicircular obstruction. *Journal of Fluid Mechanics*, 114:299–314, 1982.

[31] L. Fraccarollo and E. F. Toro. Experimental and numerical assessment of the shallow water model for two-dimensional dam-break type problems. *Journal of hydraulic research*, 33(6):843–864, 1995.

[32] P. R. Garabedian. Oblique water entry of a wedge. *Communications on Pure and Applied Mathematics*, 6(2):157–165, 1953.

[33] M. Gertler and G. R. Hagen. Standard equations of motion for submarine simulation. Technical report, Naval Ship Research and Development Center Bethesda MD, 1967.

[34] P. Glaister. Approximate Riemann solutions of the shallow water equations. *Journal of Hydraulic Research*, 26(3):293–306, 1988.

[35] M. Greenhow. A complex variable method for the floating-body boundary-value problem. *Journal of computational and applied mathematics*, 46(1-2):115–128, 1993.

[36] M. Greenhow and W. M. Lin. Nonlinear-free surface effects: experiments and theory. Technical report, Massachusetts Inst Of Tech Cambridge Dept Of Ocean Engineering, 1983.

[37] J. Haslinger, K. H. Hoffmann, and R. A. E. Mäkinen. *Optimal control, dual approach for the numerical solution of a dam problem.* Inst. für Angewandte Mathematik und Statistik, Techn. Univ. München, 1992.

[38] J. T. Haslinger, K. Kunisch, and G. Peichl. Shape optimization and fictitious domain approach for solving free boundary problems of Bernoulli type. *Computational Optimization and Applications*, 26(3):231–251, 2003.

[39] M. Hintermüller and W. Ring. A second order shape optimization approach for image segmentation. *SIAM Journal on Applied Mathematics*, 64(2):442–467, 2004.

[40] D. D. Houghton and A. Kasahara. Nonlinear shallow fluid flow over an isolated ridge. *Communications on Pure and Applied Mathematics*, 21(1):1–23, 1968.

[41] S. D. Howison, J. R. Ockendon, and S. K. Wilson. Incompressible water-entry problems at small deadrise angles. *Journal of Fluid Mechanics*, 222:215–230, 1991.

[42] O. F. Hughes. Solution of the wedge entry problem by numerical conformal mapping. *Journal of Fluid Mechanics*, 56(1):173–192, 1972.

[43] B. Hunt. Asymptotic solution for dam-break problem. *Journal of the Hydraulics Division*, 108(1):115–126, 1982.

[44] B. Hunt. Asymptotic solution for dam break on sloping channel. *Journal of hydraulic engineering*, 109(12):1698–1706, 1983.

[45] A. Iafrati and A. A. Korobkin. Initial stage of flat plate impact onto liquid free surface. *Physics of fluids*, 16(7):2214–2227, 2004.

[46] A. Iafrati and A. A. Korobkin. Starting flow generated by the impulsive start of a floating wedge. *Journal of engineering mathematics*, 51(2):99–126, 2005.

[47] A. K. Jha, J. Akiyama, and M. Ura. First-and second-order flux difference splitting schemes for dam-break problem. *Journal of Hydraulic Engineering*, 121(12):877–884, 1995.

[48] S. W. Joo, W. W. Schultz, and A. F. Messiter. An analysis of the initial-value wavemaker problem. *Journal of Fluid Mechanics*, 214:161–183, 1990.

[49] K. T. Kärkkäinen and T. Tiihonen. Free surfaces: shape sensitivity analysis and numerical methods. *International Journal for Numerical Methods in Engineering*, 44(8):1079–1098, 1999.

[50] K. T. Kärkkäinen and T. Tiihonen. Shape calculus and free boundary problems. In *Proceedings of the European Congress on Computational Methods in Applied Sciences and Engineering, ECCOMAS*, 2004.

[51] A. C. King and D. J. Needham. The initial development of a jet caused by fluid, body and free-surface interaction. part 1. a uniformly accelerating plate. *Journal of Fluid Mechanics*, 268:89–101, 1994.

[52] A. Korobkin and O. Yilmaz. The initial stage of dam-break flow. *Journal of Engineering Mathematics*, 63(2-4):293–308, 2009.

[53] A. Korobkin and O. Yilmaz. Initial stages of gravity driven flow of two fluids of equal depth. *Physics of Fluids*, 2023.

[54] E. Korsukova. *An experimental study of the initial evolution of a fluid's free surface when displaced by an accelerating plate.* PhD thesis, University of Nottingham, 2015.

[55] C. M. Kuster, P. A. Gremaud, and R. Touzani. Fast numerical methods for Bernoulli free boundary problems. *SIAM journal on scientific computing*, 29(2):622–634, 2007.

[56] M. G. Larson and F. Bengzon. *The finite element method: theory, implementation, and applications*, volume 10. Springer Science & Business Media, 2013.

[57] G. Lauber. *Experimente zur Talsperrenbruch-Welle im glatten geneigten Rechteckkanal.* PhD thesis, ETH Zurich, 1997.

[58] I. MacDonald. *Analysis and computation of steady open channel flow.* PhD thesis, PhD thesis, University of Reading — Department of Mathematics, 1996.

[59] A. G. Mackie. The water entry problem. *The Quarterly Journal of Mechanics and Applied Mathematics*, 22(1):1–17, 1969.

[60] G. Mejak. Numerical solution of bernoulli-type free boundary value problems by variable domain method. *International journal for numerical methods in engineering*, 37(24):4219–4245, 1994.

[61] G. Mejak. Finite element solution of a model free surface problem by the optimal shape design approach. *International journal for numerical methods in engineering*, 40(8):1525–1550, 1997.

[62] M. Montardini, F. Remonato, and G. Sangalli. Isogeometric methods for free boundary problems. In *Isogeometric Analysis and Applications 2018 3*, pages 131–155. Springer, 2021.

[63] D. J. Needham, J. Billingham, and A. C. King. The initial development of a jet caused by fluid, body and free-surface interaction. Part 2. An impulsively moved plate. *Journal of Fluid Mechanics*, 578:67–84, 2007.

[64] D. J. Needham, P. G. Chamberlain, and J. Billingham. The initial development of a jet caused by fluid, body and free surface interaction. Part 3. an inclined accelerating plate. *The Quarterly Journal of Mechanics and Applied Mathematics*, 61(4):581–614, 08 2008.

[65] B. D. Nichols and C. W. Hirt. Methods for calculating multidimensional, transient free surface flows past bodies. In *Proceedings of the First International Conference on Numerical Ship Hydrodynamics*, volume 20. Naval Ship Research and Development Center Bethesda, MD, USA, 1975.

[66] D. H. Peregrine. Flow due to a vertical plate moving in a channel. *Unpublished note*, 1972.

[67] F. V. Pohle. *The Lagrangian equations of hydrodynamics: solutions which are analytic functions of the time.* New York University, 1951.

[68] F. V. Pohle. Motion of water due to breaking of a dam, and related problems. In *Proceedings of NBS Semicentennial Symposium on Gravity Waves Held at the NBS on June 18-20, 1951*, volume 521, page 47. NBS, 1952.

[69] A. Ritter. Die Fortpflanzung der Wasserwellen. *Zeitschrift des Vereines Deutscher Ingenieure*, 36(33):947–954, 1892.

[70] A. J. Roberts. Transient free-surface flows generated by a moving vertical plate. *The Quarterly Journal of Mechanics and Applied Mathematics*, 40(1):129–158, 1987.

[71] M. Rumpf and M. Flucher. Bernoulli's free-boundary problem, qualitative theory and numerical approximation. *Journal für die reine und angewandte Mathematik*, 1997(486):165–204, 1997.

[72] J. G. Sakkas and T. Strelkoff. Dam-break flood in a prismatic dry channel. *Journal of the Hydraulics Division*, 99(12):2195–2216, 1973.

[73] H. Sha and J. M. Vanden-Broeck. Two-layer flows past a semicircular obstruction. *Physics of Fluids A: Fluid Dynamics*, 5(11):2661–2668, 1993.

[74] D. H. Sharp. An overview of Rayleigh-Taylor instability. *Physica D: Nonlinear Phenomena*, 12(1-3):3–18, 1984.

[75] S. S. P. Shen. Forced solitary waves and hydraulic falls in two-layer flows. *J. Fluid Mech*, 234:583–612, 1992.

[76] M. Shiffman and D. C. Spencer. The force of impact on a cone striking a water surface (vertical entry). *Communications on pure and applied mathematics*, 4(4):379–417, 1951.

[77] J. Sokolowski and J. P. Zolésio. *Introduction to shape optimization: shape sensitivity analysis.* Springer Series in Computational Mathematics. Springer, Berlin, Heidelberg, 1992.

[78] J. Spurk and N. Aksel. *Fluid mechanics.* Springer Science & Business Media, 2007.

[79] P. K. Stansby, A. Chegini, and T. C. D Barnes. The initial stages of dam-break flow. *Journal of Fluid Mechanics*, 374:407–424, 1998.

[80] J. J. Stoker. *Water waves: The mathematical theory with applications*, volume 36. John Wiley & Sons, 1992.

[81] G. Symonds, K. P. Black, and I. R. Young. Wave-driven flow over shallow reefs. *Journal of Geophysical Research: Oceans*, 100(C2):2639–2648, 1995.

[82] T. Tiihonen. Shape optimization and trial methods for free boundary problems. *ESAIM: Mathematical Modelling and Numerical Analysis*, 31(7):805–825, 1997.

[83] J. I. Toivanen, J. Haslinger, and R. A. E. Mäkinen. Shape optimization of systems governed by bernoulli free boundary problems. *Computer Methods in Applied Mechanics and Engineering*, 197(45-48):3803–3815, 2008.

[84] J. Uddin and D. J. Needham. The effects of surface tension on the initial development of a free surface adjacent to an accelerated plate. *Journal of Fluid Mechanics*, 776:37–73, 2015.

[85] A. Valiani, V. Caleffi, and A. Zanni. Case study: Malpasset dam-break simulation using a two-dimensional finite volume method. *Journal of Hydraulic Engineering*, 128(5):460–472, 2002.

[86] E. H. Van Brummelen and A. Segal. Numerical solution of steady free-surface

flows by the adjoint optimal shape design method. *International Journal for Numerical Methods in Fluids*, 41(1):3–27, 2003.

[87] K. G. van der Zee, E. H. van Brummelen, I. Akkerman, and R. de Borst. Goal-oriented error estimation and adaptivity for fluid–structure interaction using exact linearized adjoints. *Computer Methods in Applied Mechanics and Engineering*, 200(37):2738–2757, 2011. Special Issue on Modeling Error Estimation and Adaptive Modeling.

[88] K. G. van der Zee, E. H. Van Brummelen, and R. de Borst. Goal-oriented error estimation and adaptivity for free-boundary problems: The domain-map linearization approach. *SIAM Journal on Scientific Computing*, 32(2):1064–1092, 2010.

[89] K. G. van der Zee, E. H. Van Brummelen, and R. de Borst. Goal-oriented error estimation and adaptivity for free-boundary problems: The shape-linearization approach. *SIAM Journal on Scientific Computing*, 32(2):1093–1118, 2010.

[90] K. G. van der Zee, G. J. van Zwieten, C. V. Verhoosel, and E. H. van Brummelen. Shape-newton method for isogeometric discretizations of free-boundary problems. In *MARINE 2011, IV International Conference on Computational Methods in Marine Engineering*, pages 85–102. Springer, 2013.

[91] M. Van Dyke. Perturbation methods in fluid mechanics/annotated edition. *NASA STI/Recon Technical Report A*, 75:46926, 1975.

[92] J. A. Viecelli. A computing method for incompressible flows bounded by moving walls. *Journal of Computational Physics*, 8(1):119–143, 1971.

[93] T. Von Karman. The impact on seaplane floats during landing. 1929.

[94] H. Wagner. Landing of seaplanes. Technical report, 1931.

[95] D. G. Watson. *Practical ship design*, volume 1. Elsevier, 2002.

[96] J. E. Welch, F. H. Harlow, J. P. Shannon, and B. J. Daly. The MAC method-a computing technique for solving viscous, incompressible, transient fluid-flow problems involving free surfaces. Technical report, Los Alamos National Lab.(LANL), Los Alamos, NM (United States), 1965.

[97] G. B. Whitham. The effects of hydraulic resistance in the dam-break problem. *Proceedings of the Royal Society of London. Series A. Mathematical and Physical Sciences*, 227(1170):399–407, 1955.

[98] S. A. Yang and A. T. Chwang. *Nonlinear viscous waves produced by an impulsively moving plate*. The University of Iowa, 1989.

[99] S. A. Yang and A. T. Chwang. An experimental study of nonlinear waves produced by an accelerating plate. *Physics of Fluids A: Fluid Dynamics*, 4(11):2456–2465, 1992.

[100] R. W. Yeung. Numerical methods in free-surface flows. *Annual review of fluid mechanics*, 14(1):395–442, 1982.

[101] O. Yilmaz, A. Korobkin, and A. Iafrati. The initial stage of dam-break flow of two immiscible fluids. linear analysis of global flow. *Applied Ocean Research*, 42:60 – 69, 2013.

[102] R. Zhao and O. Faltinsen. Water entry of two-dimensional bodies. *Journal of fluid mechanics*, 246:593–612, 1993.

[103] O. C. Zienkiewicz and A. H. C. Chan. Coupled problems and their numerical solution. In *Advances in Computational Nonlinear Mechanics*, pages 139–176. Springer, 1989.

[104] C. Zoppou and S. Roberts. Numerical solution of the two-dimensional unsteady dam break. *Applied Mathematical Modelling*, 24(7):457–475, 2000.

[105] C. Zoppou and S. Roberts. Explicit schemes for dam-break simulations. *Journal of Hydraulic Engineering*, 129(1):11–34, 2003.

Appendix A

Two-fluid Dam-Break Problem Around The Upper Contact Point

To investigate the two-fluid dam-break problem around the upper contact point, we shift the coordinate system by introducing

$$x^* = x + \cot\alpha, \quad y^* = y - 1$$

such that the interface is at $Y^*(s,t) = Y(s,t) - 1$ and drop the asterisk sign for simplicity. Now the governing equations (3.2.2)-(3.2.5) are

$$\nabla^2\phi_i = 0, (x,y) \in \mathcal{D}_i, \quad t > 0, \quad \text{for } i = 1,2, \tag{A.0.1}$$

$$(1+\bar{\rho})\left(\frac{\partial\phi_1}{\partial t} + \frac{1}{2}|\nabla\phi_1|^2\right) - \left(\frac{\partial\phi_2}{\partial t} + \frac{1}{2}|\nabla\phi_2|^2\right) = -\bar{\rho}\,(1+y)\,, \quad y = Y(x,t), \tag{A.0.2}$$

$$\boldsymbol{n}\cdot\frac{\partial\boldsymbol{X}}{\partial t} = \boldsymbol{n}\cdot\nabla\phi_1 = \boldsymbol{n}\cdot\nabla\phi_2, \quad \boldsymbol{x} = \boldsymbol{X}(x,t), \tag{A.0.3}$$

$$\frac{\partial\phi_1}{\partial y} = \frac{\partial\phi_2}{\partial y} = 0, \quad y = 0, \tag{A.0.4}$$

where $\boldsymbol{X}(x,t) = (x, Y(x,t))$ denotes the position of the interface between two fluids. The initial conditions for ϕ_i and Y are now

$$\phi_i(x,y,0) = 0, \quad (x,y) \in \mathcal{D}_i, \quad \text{for } i = 1,2, \tag{A.0.5}$$

$$Y(x,0) = -x\tan\alpha, \quad 0 < x < \cot\alpha, \quad 0 < \alpha < \frac{\pi}{2}. \tag{A.0.6}$$

We use the same scaled variables as (3.3.1) with $Y_0(x) = -x\tan\alpha$. The leading order problem as $t \to 0^+$ is obtained by substituting the scaled variables into (A.0.1)-

(A.0.4), which is

$$\nabla^2 \bar{\phi}_i = 0 \quad \text{in } \mathcal{D}_i(0), \quad i = 1, 2, \tag{A.0.7}$$

$$\frac{\partial \bar{\phi}_i}{\partial y} = 0 \quad \text{at } y = 0, \tag{A.0.8}$$

$$(1 + \bar{\rho})\, \bar{\phi}_1 - \bar{\phi}_2 = -\bar{\rho}\,(1 + y) \quad \text{at } y = Y_0(x), \tag{A.0.9}$$

$$2\bar{Y} = \frac{\partial \bar{\phi}_i}{\partial x} \tan\alpha + \frac{\partial \bar{\phi}_i}{\partial y} \quad \text{at } y = Y_0(x). \tag{A.0.10}$$

Similar to (3.3.6), we seek a solution of the form

$$\bar{\phi} \sim A_1 r^{\beta_0} \cos\beta_0(\pi + \theta) - 1, \quad \bar{\phi}_2 \sim A_2 r^{\beta_0} \cos\beta_0\theta - 1, \tag{A.0.11}$$

as $r \to 0$, where $(x, y) = (r\cos\theta, r\sin\theta)$, and A_1, A_2 are real constants. The condition (A.0.2) at $O(r^{\beta_0})$ is

$$(1 + \bar{\rho})\bar{\phi}_1 - \bar{\phi}_2 = 0. \tag{A.0.12}$$

On substitution from (A.0.11) into (A.0.10) and (A.0.12) with $\theta = -\alpha$ on the interface, we find that

$$\begin{aligned} (1 + \bar{\rho})A_1 \cos\left(\beta_0\left(\pi - \alpha\right)\right) &= A_2 \cos\left(\beta_0\alpha\right), \\ A_1 \sin\left(\beta_0\left(\pi - \alpha\right)\right) &= -A_2 \sin\left(\beta_0\alpha\right), \end{aligned}$$

which indicates the equation (3.3.9) for β_0.

Considering the case $\bar{\rho} \to 0$, we introduce the scaled variables

$$\bar{\phi}_i(x, y) = \bar{\rho}\hat{\phi}_i(x, y) - 1, \hat{\phi}_i(x, y) = O(1), \tag{A.0.13}$$

and the asymptotic expansion

$$\hat{\phi}_i(x, y) = \hat{\phi}_{i0}(x, y) + \bar{\rho}\hat{\phi}_{i1}(x, y) + O(\bar{\rho}^2), \tag{A.0.14}$$

such that the leading order problem (A.0.7)-(A.0.10) becomes

$$\nabla^2 \hat{\phi}_{i0} = 0 \quad \text{in } \mathcal{D}_i(0), \quad i = 1, 2, \tag{A.0.15}$$

$$\frac{\partial \hat{\phi}_{10}}{\partial \theta} = 0 \quad \text{at } \theta = -\pi, \tag{A.0.16}$$

$$\frac{\partial \hat{\phi}_{20}}{\partial \theta} = 0 \quad \text{at } \theta = 0, \tag{A.0.17}$$

$$\hat{\phi}_{10} - \hat{\phi}_{20} = -r\sin\theta \quad \text{at } \theta = -\alpha, \tag{A.0.18}$$

$$\frac{\partial \hat{\phi}_{10}}{\partial \theta} = \frac{\partial \hat{\phi}_{20}}{\partial \theta} \quad \text{at } \theta = -\alpha. \tag{A.0.19}$$

Similar to (3.3.17) and (3.3.18), we look for a local solution of the form

$$\hat{\phi}_{10}(r,\theta) \sim A(r\log r\cos\theta - r(\pi+\theta)\sin\theta) + B_1 r\cos\theta, \tag{A.0.20}$$
$$\hat{\phi}_{20}(r,\theta) \sim A(r\log r\cos\theta - r\theta\sin\theta) + B_2 r\cos\theta. \tag{A.0.21}$$

where

$$A = -\frac{\sin^2\alpha}{\pi}, B_2 - B_1 = -\sin\alpha\cos\alpha. \tag{A.0.22}$$

As $r \to 0$, we have $\phi_{i0} = O(r\log r)$, so the Bernoulli condition at order $O(\bar{\rho})$ for $\hat{\phi}_{i1}$ satisfies

$$\hat{\phi}_{11} - \hat{\phi}_{21} = -\hat{\phi}_{10} = O(r\log r) \quad \text{at } \theta = -\alpha \text{ as } r \to 0. \tag{A.0.23}$$

Since the non-uniformity will appear in $\hat{\rho}_i$ as $r \to 0$, the new variable $\tilde{s}$ is introduced as (3.3.21) and we have

$$r = e^{\frac{\tilde{s}}{\bar{\rho}}}, \quad \hat{\phi}_i = O(\bar{\rho}^{-1}e^{\frac{\tilde{s}}{\bar{\rho}}}) \quad \text{when } \tilde{s} = O(1). \tag{A.0.24}$$

which is the same as (3.3.22). Hence, Laplace's equation can now be written in terms of $(\tilde{s},\theta)$ as (3.3.23).

Let

$$\hat{\phi}_i = r\tilde{\phi}_i = \bar{\rho}^{-1}e^{\frac{s}{\bar{\rho}}}\tilde{\phi}_i, \quad \tilde{\phi}_i = O(1), \quad \text{as } r \to 0,\ \bar{\rho} \to 0, \tag{A.0.25}$$

the new form of Laplace's equation is given by substituting (3.3.24) into (3.3.23) as

$$\frac{\partial^2\tilde{\phi}_i}{\partial\theta^2} + \tilde{\phi}_i + 2\bar{\rho}\frac{\partial\tilde{\phi}_i}{\partial\tilde{s}} + \bar{\rho}^2\frac{\partial^2\tilde{\phi}_i}{\partial\tilde{s}^2} = 0, \tag{A.0.26}$$

and it should satisfy the boundary conditions

$$\frac{\partial\tilde{\phi}_1}{\partial\theta} = 0 \quad \text{at } \theta = -\pi, \tag{A.0.27}$$
$$\frac{\partial\tilde{\phi}_2}{\partial\theta} = 0 \quad \text{at } \theta = 0, \tag{A.0.28}$$
$$(1+\bar{\rho})\tilde{\phi}_1 - \tilde{\phi}_2 = -\bar{\rho}\sin\alpha \quad \text{at } \theta = -\alpha, \tag{A.0.29}$$
$$\frac{\partial\tilde{\phi}_1}{\partial\theta} = \frac{\partial\tilde{\phi}_2}{\partial\theta} \quad \text{at } \theta = -\alpha. \tag{A.0.30}$$

Based on (A.0.25) and the matching condition

$$\hat{\phi}_i \sim -\frac{\sin^2\alpha}{\pi}r\log r\cos\theta, \quad \text{as } r \to 0, \tag{A.0.31}$$

$\tilde{\phi}_i$ must satisfy

$$\tilde{\phi}_i \sim -\frac{\sin^2\alpha}{\pi}\tilde{s}\cos\theta \quad \text{as } \tilde{s} \to 0. \tag{A.0.32}$$

Now we introduce the asymptotic expansion

$$\tilde{\phi}_i(\tilde{s}) = \tilde{\phi}_{i0}(\tilde{s}) + \bar{\rho}\tilde{\phi}_{i1}(\tilde{s}) + O(\bar{\rho}^2),$$

and find the leading order term

$$\tilde{\phi}_{i0} = c(\tilde{s})\cos\theta, \quad c(\tilde{s}) \sim -\frac{\sin^2\alpha}{\pi}\tilde{s} \quad \text{as } \tilde{s} \to 0. \tag{A.0.33}$$

The Laplace's equation (A.0.26) at $O(\bar{\rho})$ is given by

$$\frac{\partial^2\tilde{\phi}_{i1}}{\partial\theta^2} + \tilde{\phi}_{i1} = -2\frac{\partial\tilde{\phi}_{i0}}{\partial s} = -2c'(\tilde{s})\cos\theta. \tag{A.0.34}$$

Thus, considering the boundary conditions (A.0.27) and (A.0.28), the local solution is

$$\tilde{\phi}_{11}(\tilde{s},\theta) = -c'(\tilde{s})(\pi+\theta)\sin\theta + b_1\cos\theta, \tag{A.0.35}$$
$$\tilde{\phi}_{21}(\tilde{s},\theta) = -c'(\tilde{s})\theta\sin\theta + b_2\cos\theta. \tag{A.0.36}$$

The boundary conditions (A.0.27)-(A.0.30) are applied to these local solutions and give

$$c(\tilde{s}) = -\tan\alpha + ke^{-\frac{\cos\alpha\sin\alpha}{\pi}\tilde{s}}$$

where k is a constant. According to the matching condition (A.0.33), we find that

$$c(\tilde{s}) = \tan\alpha(-1 + e^{-\frac{\cos\alpha\sin\alpha}{\pi}\tilde{s}}), \tag{A.0.37}$$

which gives

$$\tilde{\phi}_{i0} = \tan\alpha(-1 + e^{-\frac{\cos\alpha\sin\alpha}{\pi}s})\cos\theta. \tag{A.0.38}$$

By using this result, we find that

$$\bar{\phi}_i = \bar{\rho}\hat{\phi}_i = r\tilde{\phi}_i \sim \tan\alpha(-r\cos\theta + r^{1-\frac{\sin\alpha\cos\alpha}{\pi}\bar{\rho}}\cos\theta), \quad \text{as } r \to 0,\ \bar{\rho} \to 0. \tag{A.0.39}$$

This also indicates the solution (3.3.8) to the eigenvalue problem in Section 3.3.1 is

$$\beta_0 \sim 1 - \frac{\sin\alpha\cos\alpha}{\pi}\bar{\rho} \quad \text{as } \bar{\rho} \to 0, \tag{A.0.40}$$

such that $\beta_0 < 1$ is always true for $\alpha \in \left(0, \frac{\pi}{2}\right)$. Consequently, the local solution must have the form

$$\bar{\phi}_i \sim \tan\alpha(-r\cos\theta + r^{1-\frac{\sin\alpha\cos\alpha}{\pi}\bar{\rho}}\cos[(1-\frac{\sin\alpha\cos\alpha}{\pi})\theta]) \quad \text{as } r \to 0,\ \bar{\rho} \to 0. \tag{A.0.41}$$

However, this does not satisfy the boundary condition (A.0.27) for $\bar{\phi}_1$ at $\theta = -\pi$. Thus, in order to satisfy all the boundary conditions (A.0.27)-(A.0.30), the local

solution is

$$\bar{\phi}_1(r,\theta) \sim \tan\alpha\{-r\cos\theta + r^{1-\frac{\sin\alpha\cos\alpha}{\pi}\bar{\rho}}\cos[(1-\frac{\sin\alpha\cos\alpha}{\pi}\bar{\rho})(\pi+\theta)]\}, \tag{A.0.42}$$

$$\bar{\phi}_2(r,\theta) \sim \tan\alpha\{-r\cos\theta + r^{1-\frac{\sin\alpha\cos\alpha}{\pi}\bar{\rho}}\cos[(1-\frac{\sin\alpha\cos\alpha}{\pi}\bar{\rho})\theta]\}, \tag{A.0.43}$$

as $r \to 0$.

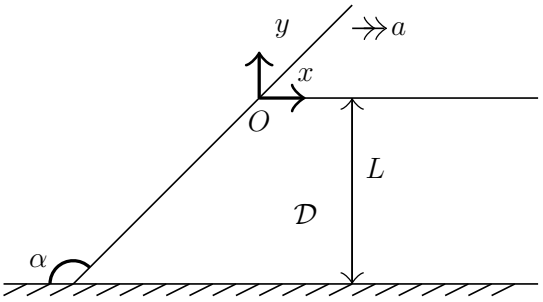

Figure B.1: *The sketch of a fluid with an inclined plate at* $y = -\tan\alpha x$.

Appendix B

Single Fluid Problem with an Inclined Accelerating Plate in the Inner Region

The solid/single fluid interaction problem in this appendix is to investigate the incompressible and irrotational flow caused by an inclined plate moving towards an ideal fluid with a constant acceleration a as shown in Fig.B.1. The problem and the method demonstrated in this appendix follow the paper [64]. The fluid initially lies at rest above a horizontal plane at $y = -L$ with a horizontal free surface at $y = 0$. The plate having an angle α with the flat bed moves towards the fluid in direction x^+ with an acceleration σ. The dimensionless variables are introduced by taking a/g as unit acceleration, L as unit length and $L\sqrt{gL}$ as unit velocity potential, where g is the gravity. The dimensionless distance moved by the plate is calculated as $s(t) = \frac{1}{2}\sigma t^2$ with $\sigma = \frac{a}{g}$. To keep the interaction point at the origin, the coordinate system $(\bar{x}, y)$ is introduced with $\bar{x} = x - s(t)$. Now, the boundary value problem for

the velocity potential ϕ and the displacement of the free boundary $\eta(\bar{x},t)$ is

$$\begin{aligned}
\nabla^2\phi &= 0, \quad (\bar{x},y)\in\mathcal{D}, t>0, && \text{(B.0.1)}\\
\nabla\phi\cdot\boldsymbol{n} &= s'(t)\sin\alpha, \quad y=-\bar{x}\tan\alpha, && \text{(B.0.2)}\\
\min(\bar{x}_b,\bar{x}_p(t)) < &\ \bar{x} < \max(\bar{x}_b,\bar{x}_p(t)), \quad t>0, && \text{(B.0.3)}\\
\phi_y &= 0, \quad y=-1, \bar{x}<\bar{x}_b, t>0, && \text{(B.0.4)}\\
\eta_t+[\phi_{\bar{x}}-s'(t)]\eta_{\bar{x}}-\phi_y &= 0, \quad y=\eta(\bar{x},t), \bar{x}>\bar{x}_p(t), \quad t>0, && \text{(B.0.5)}\\
\phi_t-s'(t)\phi_{\bar{x}}+\frac{1}{2}\left|\nabla\phi\right|^2+\eta &= 0, \quad y=\eta(\bar{x},t), \quad \bar{x}>\bar{x}_p(t), t>0, && \text{(B.0.6)}\\
|\nabla\phi|\to 0, \quad \text{as } \bar{x}\to\infty &\ , \quad \text{uniformly for } -1\le y\le\eta\left(\bar{x},t\right), \quad t>0, && \text{(B.0.7)}\\
\eta &\to 0, \quad \text{as } \bar{x}\to\infty, \quad t>0. && \text{(B.0.8)}
\end{aligned}$$

The outer region problem as $t\to 0^+$ is derived by introducing

$$\phi\left(\bar{x},y,t\right)=t\sigma\sin\alpha\bar{\phi}\left(\bar{x},y\right)+O\left(t^2\right), \quad \eta\left(\bar{x},t\right)=t^2\bar{\eta}\left(\bar{x}\right)+O\left(t^3\right). \tag{B.0.9}$$

On substitution from (B.0.9) into (B.0.1)-(B.0.8), the BVP (boundary value problem) for the leading order $\bar{\phi}\left(\bar{x},y\right)$ and $\bar{\eta}\left(\bar{x}\right)$ is

$$\begin{aligned}
\nabla^2\bar{\phi} &= 0, \quad (\bar{x},y)\in\mathcal{D};\\
\nabla\bar{\phi}\cdot\boldsymbol{n} &= 0, \quad y=-\tan\bar{x}, \quad \min\left(0,\cot\alpha\right)<\bar{x}<\max\left(0,\cot\alpha\right);\\
\bar{\phi}_y &= 0, \quad y=-1, \quad \bar{x}>\cot\alpha; && \text{(B.0.10)}\\
\bar{\phi} &= 0, \quad y=0, \quad \bar{x}>0;\\
\left|\nabla\bar{\phi}\right|\to 0, \quad \text{as } \bar{x} &\to 0, \quad \text{uniformly for } -1\le y\le 0;\\
\bar{\eta} &= \frac{1}{2}\sigma\sin\alpha\bar{\phi}_y\left(\bar{x},0\right), \quad \bar{x}\ge 0.
\end{aligned}$$

The analytical solution for this BVP can be directly established in polar coordinates (r,θ) as

$$\bar{\phi}\left(r,\theta\right) = \frac{r\sin\theta}{\cos\alpha}+\sum_{n=0}^{\infty}A_n r^{\left(n+\frac{1}{2}\right)\frac{\pi}{\alpha}}\sin\left(\left(n+\frac{1}{2}\right)\frac{\pi\theta}{\alpha}\right), \tag{B.0.11}$$

$$\bar{\eta}\left(\bar{x}\right) = \frac{1}{a}\sigma\tan\alpha+\frac{1}{2}\sigma\sin\alpha\sum_{n=0}^{\infty}\left(n+\frac{1}{2}\right)\frac{\pi A_n}{\alpha}\bar{x}^{\left(n+\frac{1}{2}\right)\frac{\pi}{\alpha}-1}, \tag{B.0.12}$$

for $r\to 0$, where $r^2=\bar{x}^2+y^2$, $\tan\theta=\frac{y}{\bar{x}}$, and A_n are real constants. The leading order coefficient A_0 can be determined by Schwarz-Christoffel conformal mapping, which transforms the domain from z-plane with $z\equiv\bar{x}+iy$ to w-plane with $w\equiv u+iv$ by

$$z=\frac{\sqrt{\pi}e^{\mathrm{i}\left(\frac{\pi}{2}-\alpha\right)}}{\sin\alpha\Gamma\left(1-\frac{\alpha}{\pi}\right)\Gamma\left(\frac{1}{2}+\frac{\alpha}{\pi}\right)}\int_0^w s^{\frac{2\alpha}{\pi}-1}\left(1-s^2\right)^{-\frac{\alpha}{\pi}}ds. \tag{B.0.13}$$

For $\alpha\in\left(0,\frac{\pi}{2}\right)$, a weak singularity can be observed in $\bar{\eta}'(x)$ as $\bar{x}\to 0^+$, while

for $\alpha \in \left(\frac{\pi}{2}, \pi\right)$, a strong singularity can be found in both $\left|\nabla\bar{\phi}\left(r,\theta\right)\right|$ as $r \to 0$, $-\alpha \leq \theta \leq 0$ and $\bar{\eta}\left(\bar{x}\right)$ as $\bar{x} \to 0$. This requires inner region for $\alpha \in \left(0, \frac{\pi}{2}\right)$ and $\alpha \in \left(\frac{\pi}{2}, \pi\right)$ separately such that $\left(\bar{x}, y\right) = o\left(1\right)$ for $t \to 0^{+}$.

For $\alpha \in \left(0, \frac{\pi}{2}\right)$, the inner coordinates $\left(X, Y\right)$ are defined by introducing

$$\bar{x} = t^{2}X, \quad y = t^{2}Y, \tag{B.0.14}$$

and the asymptotic expansions in the inner region are introduced as

$$\begin{aligned} \phi\left(X,Y,t\right) &= t^{3}\phi_{0} + t^{1+\frac{\pi}{\alpha}}A_{0}\sigma\sin\alpha\phi_{1}\left(X,Y\right) + o\left(t^{1+\frac{\pi}{\alpha}}\right), \\ \eta\left(X,t\right) &= t^{2}\eta_{0}\left(X\right) + t^{\frac{\pi}{\alpha}-2}A_{0}\sigma\sin\alpha\eta_{1}\left(X\right) + o\left(t^{\frac{\pi}{\alpha}-2}\right) \end{aligned} \tag{B.0.15}$$

as $t \to 0^{+}$. The leading order solution for $\phi_{0}\left(X,Y\right)$ and $\eta_{0}\left(X\right)$ can be found by substituting the inner-region asymptotic expansions back into the IVBP (B.0.1)-(B.0.9). To further solve for $\phi_{1}\left(X,Y\right)$ and $\eta_{1}\left(X\right)$, new coordinates $\left(\bar{X},\bar{Y}\right)$ are introduced by simply shift the origin as

$$X = -\frac{1}{2}\sigma + \bar{X}, \quad Y = \frac{1}{2}\sigma\tan\alpha + \bar{Y}. \tag{B.0.16}$$

The BVP for $\phi_{1}\left(\bar{X},\bar{Y}\right)$ can be solved analytically and numerically by finite difference method in terms of polar coordinates. The solutions show that the moving plate produces a vertical pressure which further drives a jet close to the intersection point between the free surface and the plate. Furthermore, there is an inflection point on the free surface for $\alpha \in \left(0, \frac{\pi}{4}\right)$ while no inflection point for $\alpha \in \left[\frac{\pi}{4}, \frac{\pi}{2}\right)$.

For $\alpha \in \left(\frac{\pi}{2}.\pi\right)$, the scaled inner coordinates are different with those for $\alpha \in \left(0, \frac{\pi}{2}\right)$ because the leading order in (B.0.12) now becomes $\bar{x}^{\frac{\pi}{2\alpha}-1}$. In this case, the inner region coordinates $\left(\tilde{X},\tilde{Y}\right)$ are introduced as

$$\bar{x} = t^{\gamma}\left(A_{0}\sigma\sin\alpha\right)^{\frac{\gamma}{2}}\tilde{X}, \quad y = t^{\gamma}\left(A_{0}\sigma\sin\alpha\right)^{\frac{\gamma}{2}}\tilde{Y} \tag{B.0.17}$$

with $\gamma = \frac{1}{1-\frac{\pi}{\alpha}}$ and $\left(A_{0}\sigma\sin\alpha\right)^{\frac{\gamma}{2}}$ to scale out the coefficients A_{0} and σ. The asymptotic solutions for $\phi\left(\tilde{X},\tilde{Y},t\right)$ and $\eta\left(\tilde{X},t\right)$ in the inner region are in the form

$$\begin{aligned} \phi\left(\tilde{X},\tilde{Y},t\right) &= t^{2\gamma-1}\left(A_{0}\sigma\sin\alpha\right)^{\gamma}\phi_{0}\left(\tilde{X},\tilde{Y}\right) + o\left(t^{2\gamma-1}\right), \\ \eta\left(\tilde{X},t\right) &= t^{\gamma}\left(A_{0}\sigma\sin\alpha\right)^{\frac{\gamma}{2}}\eta_{0}\left(\tilde{X}\right) + o\left(t^{\gamma}\right) \end{aligned} \tag{B.0.18}$$

as $t \to 0^+$. Then the BVP in the inner region for $\phi_0\left(\tilde{X}, \tilde{Y}\right)$ and $\eta_0\left(\tilde{X}\right)$ becomes

$$\tilde{\nabla}^2\phi_0 = 0, \quad -\infty < \tilde{X} < \infty, \tilde{Y} < \begin{cases} -\tilde{X}\tan\alpha, \tilde{X} < \tilde{X}_0 \\ \eta_0\left(\tilde{X}\right), \tilde{X} \geq \tilde{X}_0 \end{cases} ; \tag{B.0.19}$$

$$\tilde{\nabla}\phi_0 \cdot \tilde{\boldsymbol{n}} = 0, \quad \tilde{X} < \tilde{X}_0, \tilde{Y} = -\tilde{X}\tan\alpha; \tag{B.0.20}$$

$$\gamma\tilde{\eta}_0 + \left(\phi_{0\tilde{X}} - \gamma\tilde{X}\right)\eta_{0\tilde{X}} - \phi_{0,\tilde{Y}} = 0, \quad \tilde{X} > \tilde{X}_0, \tilde{Y} = \eta_0\left(\tilde{X}\right); \tag{B.0.21}$$

$$(2\gamma - 1)\,\phi_0 - \gamma\eta_0\phi_{0\tilde{Y}} - \gamma\tilde{X}\phi_{0\tilde{X}} + \frac{1}{2}\left|\tilde{\nabla}\phi_0\right|^2 = 0, \quad \tilde{X} > \tilde{X}_0, \tilde{Y} = \eta_0\left(\tilde{X}\right), \tag{B.0.22}$$

with the far-field conditions

$$\begin{aligned} \phi_0\left(\tilde{R}, \theta\right) &\sim \tilde{R}^{\frac{\pi}{2\alpha}}\sin\frac{\pi\theta}{2\alpha} + \frac{\pi^2}{12\alpha^2\cos 2\alpha}\tilde{R}^{\frac{\pi}{\alpha}-2}\cos\left[\left(\frac{\pi}{\alpha} - 2\right)(\theta + \alpha)\right] \\ &\quad \text{as } \tilde{R} \to +\infty, -\alpha < \theta < 0; \end{aligned} \tag{B.0.23}$$

$$\eta_0\left(\tilde{X}\right) \sim -\frac{\pi}{4\alpha}\tilde{X}^{\frac{\pi}{2\alpha}-1}, \quad \text{as } \tilde{X} \to +\infty, \tag{B.0.24}$$

where $\tilde{\nabla} = (\partial_{\tilde{X}}, \partial_{\tilde{Y}})$, $\left(\tilde{R}, \theta\right)$ is the polar coordinates in the inner region, and $\tilde{X}_0$ is the $\tilde{X}$-coordinate of the contact point between free surface and the moving plate. The system (B.0.19)-(B.0.24) is the same system (5.2.1)-(5.2.6) used in chapter 5. This problem is solved by the asymptotic method and boundary integral method. The solutions show small but rapid oscillations in $\eta_0\left(\tilde{X}\right)$ close to the intersection point and the free surface is always vertical to the moving plate when $\tilde{X} \to 0^+$. A corner point can be observed in the free surface when $\alpha \to 1.791$. The angle of this interior corner is $\frac{2}{3}\pi$ such that the slope of the free surface becomes discontinuous, thus for a larger angle α this inner-region problem does not have classical solutions.

Appendix C

Simplified Free boundary problem with Dirichlet Condition or Tangential Condition

This appendix shows two simplified free-boundary problems of single fluid/solid interaction problem in the inner region [64] numerically solved by Picard iteration and Newton's method, which are the most straightforward methods to solve nonlinear problems. The Bernoulli equation on the free boundary is simplified in two different approaches: replaced by Dirichlet boundary condition or tangential condition. The comparison between the numerical results solved by Picard iteration and Newton's method for both problems confirms that Newton's method shows more precise solutions and converges faster. Hence, we choose to use Newton's method and finite element method to solve the single fluid/solid interaction problem in the inner region as shown in Chapter 5.

Note that in this appendix, we use the same finite element mesh as shown in Figure 5.2.

C.1 Simplified problem for Dirichlet boundary condition

Here, a simplified problem of the inner region problem in Appendix B is investigated by replacing the Bernoulli equation on the free boundary with a Dirichlet condition. Let Ω be a domain in (x, y)-space with the free boundary

$$\Gamma_F = \{(x, y) : 0 \leq x \leq L, y = \eta(x)\},$$

and the fixed boundary Γ_D, which consists of the Γ_L and Γ_N defined as

$$\begin{aligned} \Gamma_L &= \{(x, y) : 0 \leq y \leq L, x = 0\}, \\ \Gamma_N &= \left\{(x, y) : \begin{cases} 0 \leq y \leq L, x = L, \\ 0 \leq x \leq L, y = -L. \end{cases} \right\}. \end{aligned} \tag{C.1.1}$$

The function $\eta(x)$ represents the vertical displacement of the free surface. A simpler problem is then abstracted from (B.0.19)-(B.0.24),

$$
\begin{aligned}
-\nabla^2\phi &= f, \quad \text{in } \Omega, && \text{(C.1.2)}\\
\partial_n\phi &= \gamma\boldsymbol{x}\cdot\boldsymbol{n}, \quad \text{on } \Gamma_F, && \text{(C.1.3)}\\
\phi &= g, \quad \text{on } \Gamma_F, && \text{(C.1.4)}\\
\frac{\partial\phi}{\partial n} &= 0, \quad \text{on } \Gamma_L, && \text{(C.1.5)}\\
\phi &= g, \quad \text{on } \Gamma_N, && \text{(C.1.6)}\\
\eta(x) &= \eta_\infty(x), \quad \text{at } x = L, && \text{(C.1.7)}
\end{aligned}
$$

where γ is some constant, and f, g are some smooth functions, and the function $\eta_\infty(x)$ represents the Dirichlet condition for η at $x = L$. The vector $\boldsymbol{x}$ is the point at (x, y) and $\boldsymbol{n} = \frac{1}{\sqrt{1+(\eta'(x))^2}}(-\eta'(x), 1)$ represents the unit normal vector to Γ_F. Hence, the free-boundary condition (C.1.3) is the vector form of the condition (B.0.21) in the inner region problem.

Given Γ_0 as the initial free boundary at $y = 0$, and Γ_η as the free boundary satisfying $y = \eta(x)$, we define the map

$$
T_\eta : \quad \Gamma_0 \to \Gamma_\eta, \quad T_\eta(\boldsymbol{x}_0) = \boldsymbol{x}_0 + \begin{pmatrix} 0 \\ \eta(x_0) \end{pmatrix}, \tag{C.1.8}
$$

where $\boldsymbol{x}_0 = \begin{pmatrix} x_0 \\ 0 \end{pmatrix}$.

The Neumann boundary condition (C.1.3) can be written as

$$
\frac{\partial\phi}{\partial n} \circ T_\eta \begin{pmatrix} x \\ y_0 \end{pmatrix} = \gamma \frac{-x\eta'(x) + \eta(x)}{\sqrt{1 + (\eta'(x))^2}} \tag{C.1.9}
$$

C.1.1 Picard iteration

Introducing $\hat{v} \in \hat{V} := \{\hat{v} \in \mathcal{C}^1(\Gamma_F) \,|\, \hat{v} = 0 \text{ at } x = L\}$, multiplying (C.1.3) with the test function $\hat{v}$, the integration can be evaluated as

$$
\begin{aligned}
\int_{\Gamma_0} \left(\frac{\partial\phi}{\partial n} \circ T_\eta\right) \hat{v}\sqrt{1 + (\eta'(x))^2} d\Gamma_0 &= \gamma \int_{\Gamma_0} (-x\eta'(x) + \eta(x))\, \hat{v} d\Gamma_0 \\
&= \int_{\Gamma_F} \frac{\partial\phi}{\partial n} (\hat{v} \circ T_\eta)^{-1} d\Gamma_\eta. \qquad \text{(C.1.10)}
\end{aligned}
$$

Let $v \in V := \{v \in \mathcal{C}^1(\Omega) \,|v = 0 \text{ on } \Gamma_F\}$, the weak forms for (C.1.2)-(C.1.7) are:

$$\int_\Omega \nabla\phi \cdot \nabla v d\Omega + \int_{\Gamma_N} \kappa\phi v d\Gamma = \int_\Omega f v d\Omega + \int_{\Gamma_N} \kappa g v d\Gamma, \tag{C.1.11}$$

$$\int_\Omega \nabla\phi \cdot \nabla\tilde{v} d\Omega - \gamma \int_{\Gamma_0} \left[-(x\hat{v})'\eta + \eta\hat{v}\right] d\Gamma_0 = \int_\Omega f\tilde{v} d\Omega - \gamma\eta_\infty(1)\hat{v}(1), \tag{C.1.12}$$

where $\tilde{v}$ is the natural lifting of $\hat{v}$ into $\mathcal{C}^1(\Omega)$. The second weak form is obtained by integrating (C.1.10) by parts

$$\int_{\Gamma_0} -x\eta'(x)\hat{v} d\Gamma_0 = (x\eta(x)\hat{v}(x))\big|_{x=L} - \int_{\Gamma_0} (x\hat{v})'\eta d\Gamma_0.$$

Let span$\{\zeta_i\}$, span$\{\hat{\zeta}_i\}$, span$\{\tilde{\zeta}_i\}$ and span$\{\xi_i\}$ be the basis for V, $\hat{V}$, $\tilde{V}$ and $\mathcal{C}^0(\Gamma_F)$ correspondingly. The finite element approximation (η_h, ϕ_h) for (η, ϕ) is defined as

$$\eta_h(x) = \sum_i \eta_{h,i}\xi_i(x); \tag{C.1.13}$$

$$\phi_h(x,y) = \begin{cases} \sum_i \phi_{h,i}\zeta_i(x,y) & \text{in } \Omega \setminus \Gamma_F, \\ \sum_i \phi_{h,i}\tilde{\zeta}_i(x,y) & \text{on } \Gamma_F. \end{cases} \tag{C.1.14}$$

The Galerkin approximations of (C.1.11) and (C.1.12) are

$$\int_\Omega \nabla\phi_h \cdot \nabla\zeta_i d\Omega + \int_{\Gamma_N} \kappa\phi_h\zeta_i d\Gamma = \int_\Omega f\zeta_i d\Omega + \int_{\Gamma_N} \kappa g\zeta_i d\Gamma, \tag{C.1.15}$$

$$\int_\Omega \nabla\phi_h \cdot \nabla\tilde{\zeta}_i d\Omega - \gamma \int_{\Gamma_0} \left[-\left(x\hat{\zeta}_i\right)'\eta_h + \eta_h\hat{\zeta}_i\right] d\Gamma_0 = \int_\Omega f\hat{\zeta}_i d\Omega - \gamma\eta_\infty(L)\hat{\zeta}_i(L). \tag{C.1.16}$$

The value of ϕ at $x = L$ is enforced by the strong form,

$$\lambda\phi_h = \lambda g. \tag{C.1.17}$$

The scheme of Picard iteration is shown in Table C.1. Since η_h is piecewise constant, the free boundary is updated as (C.1.19) in Table C.1 such that the left node on the free boundary is free to move and the right node is fixed by far-field condition (C.1.7).

Denoting $\mathbf{\Phi}_h = (\phi_1, \phi_2, ...)$ and $\boldsymbol{\eta}_h = (\eta_1, \eta_2, ...)$ as the vectors of degree-of-freedom, the system (C.1.15)-(C.1.17) can be written in the matrix form as

$$\boldsymbol{M} \cdot \mathbf{\Phi}_h = \boldsymbol{b}_1, \quad \boldsymbol{A} \cdot \boldsymbol{\eta}_h = \boldsymbol{b}_2, \tag{C.1.18}$$

0. Initialize with η^0 and let $k = 0$.
1. Given η^k, solve the system (C.1.15) and (C.1.17) for ϕ^{k+1}.
2. Given ϕ^{k+1}, solve (C.1.16) for η^{k+1}.
3. Update the free boundary

$$y_j = \begin{cases} \eta_j^{k+1}, & 0 < j < n, \\ \eta_\infty(L), \end{cases} \tag{C.1.19}$$

where n is the number of nodes on Γ_F.
4. Set $k \leftarrow k+1$, and repeat step 1-4 until convergence for η.

Table C.1: The Picard iteration scheme.

where

$$\begin{aligned}
\boldsymbol{M}_{ij} &= \begin{cases} \int_\Omega \nabla\zeta_j \cdot \nabla\zeta_i d\Omega + \int_{\Gamma_N} \kappa\zeta_j\zeta_i d\Gamma, & \text{on } \Omega \setminus \Gamma_F, \quad \text{on } \Omega \setminus \Gamma_F, \\ \lambda, \quad \text{on } \Gamma_F. \end{cases} \\
\boldsymbol{b}_{1i} &= \begin{cases} \int_\Omega f\hat{\zeta}_i d\Omega + \int_{\Gamma_N} \kappa g\hat{\zeta}_i d\Gamma, & \mathbf{x}_j \text{ is not on } \Gamma_F, \\ \lambda g, \quad \text{is on } \Gamma_F, \end{cases} \\
\boldsymbol{A}_{ij} &= -\gamma \int_{\Gamma_0} \left[-(x\hat{\zeta}_i)' + \hat{\zeta}_i \right] \xi_j d\Gamma_0, \quad \text{on } \Gamma_F \\
\boldsymbol{b}_{2i} &= \int_\Omega f\tilde{\zeta}_i d\Omega - \gamma\eta_\infty(L)\hat{\zeta}_i(L) - \int_\Omega \nabla\phi^k \cdot \nabla\tilde{\xi}_i d\Omega, \quad \text{on } \Gamma_F.
\end{aligned}$$

C.1.2 Newton's method

Newton's method is the other technique to solve a nonlinear finite element problem, which is more complicated but faster than Picard iteration. Instead of using piecewise constant approximation for η, piecewise linear approximation ensures the more accurate results of the free surface. Now we construct the coupled problem of (C.1.2)-(C.1.7) as

$$\partial_n\phi = \gamma\left(\vec{X} - \vec{x_0}\right) \cdot \vec{n}, \quad \text{on } \Gamma_F, \tag{C.1.20}$$

$$\Phi = g, \quad \text{on } \Gamma_F, \tag{C.1.21}$$

$$\Phi\big|_{\Gamma_R} = g\big|_{\Gamma_R}, \tag{C.1.22}$$

$$\eta\big|_{\Gamma_R} = \eta_\infty\big|_{\Gamma_R}, \tag{C.1.23}$$

where

$$
\begin{aligned}
-\nabla^2\phi &= f, \quad \text{in } \Omega, && \text{(C.1.24)}\\
\phi &= \Phi, \quad \text{on } \Gamma_F, && \text{(C.1.25)}\\
\frac{\partial\phi}{\partial\boldsymbol{n}} &= 0, \quad \text{on } \Gamma_L, && \text{(C.1.26)}\\
\phi &= g, \quad \text{on } \Gamma_N. && \text{(C.1.27)}
\end{aligned}
$$

Here, the function f, g and η_∞ are smooth, and Φ is the function defined on the free boundary Γ_F, which can be extended into the region Ω by ϕ.

Let $v \in V := \{v \in \mathcal{C}^1(\Omega)\}$, the weak form of the boundary value problem (C.1.24)-(C.1.27) is

$$
\int_\Omega \nabla\phi\cdot\nabla v d\Omega + \int_{\Gamma_F} \kappa\phi v d\Gamma + \int_{\Gamma_N} \kappa\phi v d\Gamma = \int_\Omega f v d\Omega + \int_{\Gamma_F} \kappa\Phi v d\Gamma + \int_{\Gamma_N} \kappa g v d\Gamma. \tag{C.1.28}
$$

Then multiplying (C.1.20) with a test function $w \in W := \{w \in \mathcal{C}^0(\Gamma_F)\,|w = 0 \text{ at } x = L\}$ and using Green's formula, the weak form of the problem (C.1.20)-(C.1.23) is

$$
\int_\Omega \nabla\phi\cdot\nabla\tilde{w} d\Omega - \int_{\Gamma_F} f w d\Gamma = \gamma\int_{\Gamma_F} \left[-(xw)'\eta + \eta w\right] d\Gamma, \tag{C.1.29}
$$

where $\tilde{w} \in V$ is the natural lifting of w into Ω. The boundary condition for η on Γ_R can be represented in a strong form

$$
\lambda\eta|_{\Gamma_R} = \lambda\eta_\infty|_{\Gamma_R}, \tag{C.1.30}
$$

where λ is a real constant.

To linearise this problem, the residuals for the problem (C.1.20)-(C.1.23) are introduced as

$$
\begin{aligned}
\mathcal{R}_1\left((\Phi,\eta);w\right) &= \begin{cases} \int_\Omega \nabla\phi\cdot\nabla\tilde{w} d\Omega - \int_\Omega f\tilde{w} d\Omega - \gamma\int_{\Gamma_F}\left(-x\eta' + \eta\right) w d\Gamma, & \text{on } \Gamma_F\setminus\Gamma_R,\\ \lambda\left(\eta\big|_{\Gamma_R} - \eta_\infty\big|_{\Gamma_R}\right), & \text{on } \Gamma_R, \end{cases}\\
\mathcal{R}_2\left((\Phi,\eta);w\right) &= \lambda\left(\Phi(x,y) - g(x,y)\right), \quad \text{for } (x,y) \text{ on } \Gamma_F,
\end{aligned}
$$

for $i = 1, ..., n$, where $\Gamma_R = \{\boldsymbol{x} \text{ on } \Gamma_F : x = L\}$.

In order to apply Newton's method, the residuals $\mathcal{R}_1\left((\Phi,\eta);w\right)$ and $\mathcal{R}_2\left((\Phi,\eta);w\right)$ can be linearised at an arbitrary approximation pair $\left(\hat{\Phi}, \hat{\eta}(x)\right)$ by finding the partial

derivatives concerning $\hat{\Phi}$ and $\hat{\eta}$ as

$$\partial_{\delta\Phi}\mathcal{R}_j\left(\left(\hat{\Phi},\hat{\eta}\right);w\right) = \lim_{t\to 0}\frac{\mathcal{R}_j\left(\left(\hat{\Phi}+t\delta\Phi,\hat{\eta}\right);w\right)-\mathcal{R}_j\left(\left(\hat{\Phi},\hat{\eta}\right);w\right)}{t}, \tag{C.1.31}$$

$$\partial_{\delta\eta}\mathcal{R}_j\left(\left(\hat{\Phi},\hat{\eta}\right);w\right) = \lim_{t\to 0}\frac{\mathcal{R}_j\left(\left(\hat{\Phi},\hat{\eta}+t\delta\eta\right);w\right)-\mathcal{R}_j\left(\left(\hat{\Phi},\hat{\eta}\right);w\right)}{t}, \tag{C.1.32}$$

for $j = 1, 2$.

Since the function Φ is only defined on the free boundary Γ_F, the boundary condition (C.1.26) at $x = 0$ may not be satisfied for Φ, which can cause instability in ϕ. Thus, we reflect the domain Ω and the free boundary Γ_F with respect to the axis $x = 0$. Since ϕ has the natural boundary condition on Γ_L, Φ and ϕ can be extended to the reflected free boundary such that the residual $\mathcal{R}_1\left(\left(\hat{\Phi},\hat{\eta}\right);w\right)$ can be approximated by including the elements in the reflected domain for the node at $x = 0$ on Γ_F.

Introducing the approximations

$$\Phi = \hat{\Phi} + \delta\Phi, \quad \eta = \hat{\eta} + \delta\eta,$$

the Newton's method for correction pair $(\delta\Phi, \delta\eta)$ is

$$\left\langle \partial_{(\delta\Phi,\delta\eta)}\mathcal{R}_1\left(\left(\hat{\Phi},\hat{\eta}\right);w\right),(\delta\Phi,\delta\eta)\right\rangle = -\mathcal{R}_1\left(\left(\hat{\Phi},\hat{\eta}\right);w\right) \quad \forall w\in W, \tag{C.1.33}$$

$$\left\langle \partial_{(\delta\Phi,\delta\eta)}\mathcal{R}_2\left(\left(\hat{\Phi},\hat{\eta}\right);w\right),(\delta\Phi,\delta\eta)\right\rangle = -\mathcal{R}_2\left(\left(\hat{\Phi},\hat{\eta}\right);w\right) \quad \forall w\in W. \tag{C.1.34}$$

Following from (C.1.33)-(C.1.34), we obtain the following scheme

$$\begin{aligned}-\mathcal{R}_1\left(\left(\hat{\Phi},\hat{\eta}\right);w\right) &= \lim_{t\to 0}\frac{\mathcal{R}_1\left((\hat{\Phi}+t\delta\Phi,\hat{\eta});w\right)-\mathcal{R}_1\left((\hat{\Phi}_F,\hat{\eta});w\right)}{t}\\ &+ \lim_{t\to 0}\frac{\mathcal{R}_1\left((\hat{\Phi},\hat{\eta}+t\delta\eta);w\right)-\mathcal{R}_1\left((\hat{\Phi},\hat{\eta});w\right)}{t}; \end{aligned} \tag{C.1.35}$$

$$\begin{aligned}-\mathcal{R}_2\left(\left(\hat{\Phi}_F,\hat{\eta}\right);w\right) &= \lim_{t\to 0}\frac{\mathcal{R}_2\left((\tilde{\Phi}+t\delta\Phi,\tilde{\eta});w\right)-\mathcal{R}_2\left((\hat{\Phi}_F,\hat{\eta});w\right)}{t}\\ &+ \lim_{t\to 0}\frac{\mathcal{R}_2\left((\hat{\Phi},\hat{\eta}+t\delta\eta);w\right)-\mathcal{R}_2\left((\hat{\Phi},\hat{\eta});w\right)}{t}; \end{aligned} \tag{C.1.36}$$

for $\forall w \in W$.

Note that the finite element mesh has to be reconstructed and the corresponding values of $\hat{\Phi}$ needs to be obtained by solving the boundary-value problem (C.1.24)-

0. Initialize with $\left(\hat{\Phi}^0, \hat{\eta}^0\right)$; set $k = 0$.
1. Given $\left(\hat{\Phi}^k, \hat{\eta}^k\right)$, solve the problem (C.1.24)-(C.1.27) for ϕ^k.
2. Given $\left(\hat{\Phi}^k, \hat{\eta}^k\right)$ and ϕ^k, solved the system (C.1.20)-(C.1.23) for $(\delta\Phi, \delta\eta)$.
3. Update the free boundary $$y^{k+1} = \hat{\eta}^{k+1}.$$ where $\hat{\eta}^{k+1} = \hat{\eta}^k + \delta\eta$, and update Φ^k as $$\hat{\Phi}^{k+1} = \hat{\Phi}^k + \delta\Phi,$$ repeat from step 1. until convergence.

Table C.2: The Newton scheme.

(C.1.27) when evaluating the residual $\mathcal{R}_j\left(\left(\hat{\Phi}, \hat{\eta} + t\delta\eta\right); w\right)$. The Newton's algorithm is now shown in Table C.2.

Let $\phi \in V$, $\Phi \in \hat{V} := \{\hat{v} \in \mathcal{C}^1(\Gamma_F)\}$, and $\eta \in \hat{V}$, we have

$$\delta\Phi \in \hat{V}, \quad \hat{\Phi}_F \in \hat{V}, \quad \delta\eta \in \hat{V}, \quad \hat{\eta} \in \hat{V}.$$

Introducing $\{\zeta_i\}_{i=1}^n$, $\{\hat{\zeta}_i\}_{i=1}^n$, $\{\tilde{\xi}_i\}_{i=1}^n$ and $\{\xi_i\}_{i=1}^n$ be the basis for V, $\hat{V}$, $\tilde{W}$ and W correspondingly associated with n nodes on Γ_F. The finite element approximation pair $(\delta\Phi_h, \delta\eta_h)$ for $(\delta\Phi, \delta\eta)$ is defined as

$$\delta\Phi_h(x, y) = \sum_i \delta\Phi_{h,i}\hat{\zeta}_i(x, y); \tag{C.1.37}$$

$$\delta\eta_h(x) = \sum_i \delta\eta_{h,i}\hat{\zeta}_i(x, \hat{\eta}(x)). \tag{C.1.38}$$

Similarly, we have the finite element approximation pair (Φ_h, η_h) for $(\hat{\Phi}, \hat{\eta})$ defined as

$$\Phi_h(x, y) = \sum_i \Phi_{h,i}\hat{\zeta}_i(x, y); \tag{C.1.39}$$

$$\eta_h(x) = \sum_i \eta_{h,i}\hat{\zeta}_i(x, \hat{\eta}(x)). \tag{C.1.40}$$

and the finite element approximation ϕ_h for ϕ is

$$\phi_h(x, y) = \sum_i \phi_{h,i}\zeta_i(x, y). \tag{C.1.41}$$

Similar to section 5.5.1, we collect the independent variables in the vectors

$$\delta\boldsymbol{\Phi} = \begin{pmatrix} \delta\Phi_{h,1} \\ \delta\Phi_{h,2} \\ \vdots \end{pmatrix} \quad \delta\boldsymbol{\eta} = \begin{pmatrix} \delta\eta_{h,1} \\ \delta\eta_{h,2} \\ \vdots \end{pmatrix}. \quad \boldsymbol{\Phi}_h = \begin{pmatrix} \Phi_{h,1} \\ \Phi_{h,2} \\ \vdots \end{pmatrix} \quad \boldsymbol{\eta}_h = \begin{pmatrix} \eta_{h,1} \\ \eta_{h,2} \\ \vdots \end{pmatrix}.$$

Now the Newton's scheme (C.1.35) and (C.1.36) can be written as a linear system

$$\boldsymbol{J} \cdot \begin{pmatrix} \delta\boldsymbol{\Phi} \\ \delta\boldsymbol{\eta} \end{pmatrix} = \boldsymbol{r}. \tag{C.1.42}$$

The Jacobian matrix $\boldsymbol{J}$ and the residual vector $\boldsymbol{r}$ are denoted as

$$\boldsymbol{J} = \begin{pmatrix} \boldsymbol{A} & \boldsymbol{B} \\ \boldsymbol{C} & \boldsymbol{D} \end{pmatrix}, \qquad \boldsymbol{r} = \begin{pmatrix} \boldsymbol{r}^1 \\ \boldsymbol{r}^2 \end{pmatrix}. \tag{C.1.43}$$

where

$$\begin{aligned}
\boldsymbol{A}_{ij} &= \partial_{\delta\Phi}\mathcal{R}_1\left(\left(\Phi_{h,j}\hat{\zeta}_j, \eta_h\right); \xi_i\right) = \lim_{t\to 0} \frac{\mathcal{R}_1\left(\left((\Phi_{h,j}+t)\hat{\zeta}_j, \eta_h\right); \xi_i\right) - \mathcal{R}_1\left(\left(\Phi_{h,j}\hat{\zeta}_j, \eta_h\right); \xi_i\right)}{t}, \\
\boldsymbol{B}_{ij} &= \partial_{\delta\eta}\mathcal{R}_1\left(\left(\Phi_h, \eta_{h,j}\hat{\zeta}_j\right); \xi_i\right) = \lim_{t\to 0} \frac{\mathcal{R}_1\left(\left(\Phi_h, (\eta_{h,j}+t)\hat{\zeta}_j\right); \xi_i\right) - \mathcal{R}_1\left(\left(\Phi_h, \eta_{h,j}\hat{\zeta}_j\right); \xi_i\right)}{t}, \\
\boldsymbol{C}_{ij} &= \partial_{\delta\Phi}\mathcal{R}_2\left(\left((\Phi_{h,j}\hat{\zeta}_j, \eta_h\right); \xi_i\right) = \lim_{t\to 0} \frac{\mathcal{R}_2\left(\left(\Phi_{h,j}+t)\hat{\zeta}_j, \eta_h\right); \xi_i\right) - \mathcal{R}_2\left(\left(\Phi_{h,j}\hat{\zeta}_j, \eta_h\right); \xi_i\right)}{t}, \\
\boldsymbol{D}_{ij} &= \partial_{\delta\eta}\mathcal{R}_2\left(\left(\Phi_h, \eta_{h,j}\hat{\zeta}_j\right); \xi_i\right) = \lim_{t\to 0} \frac{\mathcal{R}_2\left(\left(\Phi_h, (\eta_h+t)\hat{\zeta}_j\right); \xi_i\right) - \mathcal{R}_2\left(\left(\Phi_h, \eta_{h,j}\hat{\zeta}_j\right); \xi_i\right)}{t}, \\
\boldsymbol{r}_i^1 &= \begin{cases} \mathcal{R}_1\left((\Phi_h, \eta_h); \xi_i\right) = \int_{\Gamma_F} \nabla\phi_h \cdot \nabla\tilde{\xi}_i d\Gamma - \int_{\Gamma_0} \gamma\left(-x\eta_h' + \eta_h\right)\xi_i dx, & \text{on } \Gamma_F \setminus \gamma_R \\ \lambda\left(\eta_h|_{\Gamma_R} - \eta_\infty|_\Gamma R\right), & \text{on } \Gamma_R, \end{cases} \\
\boldsymbol{r}_i^2 &= \mathcal{R}_2\left((\Phi_h, \eta_h); \xi_i\right) = \lambda\left(\hat{\Phi}_{h,i} - g\right).
\end{aligned} \tag{C.1.44}$$

The finite element approximation of the weak form (C.1.28) for ϕ_h is obtained as:

$$\int_\Omega f v d\Omega = \int_\Omega \hat{\nabla}\phi_h \cdot \hat{\nabla} v d\Omega + \int_{\Gamma_D} \kappa\left(\phi_h - \hat{\Phi}_\infty\right) v d\Gamma + \int_{\Gamma_F} \kappa\left(\phi_h - \Phi_h\right) v d\Gamma. \tag{C.1.45}$$

Collecting the degrees of freedom in the vector

$$\boldsymbol{\phi} = \begin{pmatrix} \phi_{h,1} \\ \phi_{h,2} \\ \vdots \end{pmatrix},$$

and inserting (C.1.41) into (C.1.45), we have the linear system

$$\boldsymbol{M} \cdot \boldsymbol{\phi} = \boldsymbol{b} \tag{C.1.46}$$

where

$$\begin{aligned} \boldsymbol{M}_{ij} &= \int_{\Omega} \nabla\zeta_i \cdot \nabla\zeta_j d\Omega + \int_{\Gamma_D} \kappa\zeta_i\zeta_j f\Gamma + \int_{\Gamma_F} \kappa\zeta_i\zeta_j d\Gamma, \\ \boldsymbol{b}_i &= \int_{\Gamma_D} \kappa g\zeta_i d\Gamma + \int_{\Gamma_F} \kappa\Phi_h\zeta_i d\Gamma. \end{aligned}$$

C.1.3 Numerical experiment

The test case is derived from a manufactured solution satisfying Laplace's equation in $\Omega = \{(x, y) : (0, 1) \times (-1, 0)\}$, which is

$$\phi(x, y) = \frac{x^2 - y^2}{6}, \tag{C.1.47}$$

$$\eta(x) = x^2, \tag{C.1.48}$$

such that

$$\begin{aligned} f &= 0, \\ g &= \frac{x^2 - y^2}{6}. \end{aligned}$$

The initial free boundary is at $y = 0$, and the initial guess of Φ on the free boundary is $\hat{\Phi}^0 = \frac{x^2}{6}$. Figure C.1 shows the comparison between the numerical results and exact solutions (C.1.47)-(C.1.48). Figure C.1a and C.1c are the numerical results obtained by Picard iteration, while Figure C.1b and C.1d are obtained by Newton's method. The numerical solutions for η obtained by both methods are consistent with the exact solution (C.1.48), but the value of Φ evaluated by Newton's method is more accurate. This indicates that the numerical results of η solved by Newton's method are closer to the exact solution because of the Dirichlet boundary condition (C.1.25) used in the boundary value problem for ϕ in the whole domain Ω. Furthermore, Newton's method converges much faster than Picard iteration as shown in Figure C.1e and C.1f. The increasing error of Φ for Newton's method at the second iteration is because of the significant changing of the free boundary at the first iteration, which causes the rising error of η at the next iteration. Both the rate of convergence and the accuracy imply that Newton's method has better performance.

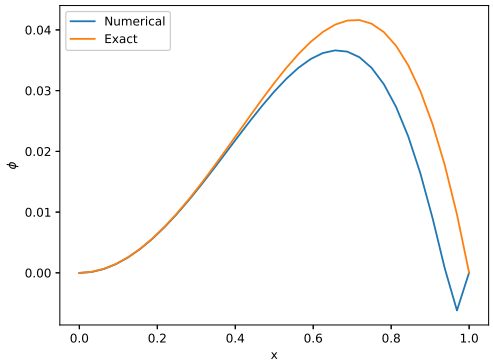

(a) *The numerical results and exact solution for Φ solved by Picard iteration.*

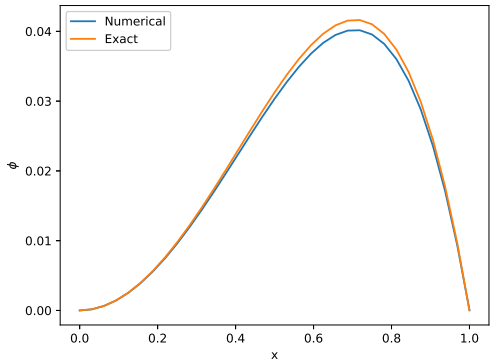

(b) *The numerical results and exact solution for Φ solved by Newton's method.*

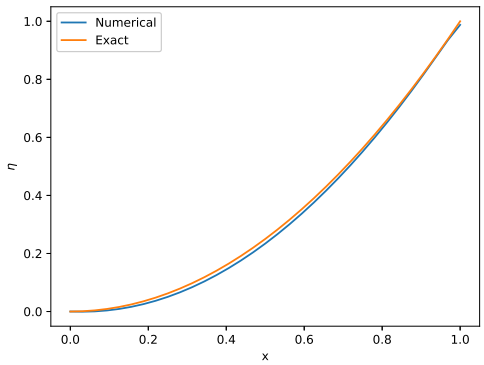

(c) *The numerical results and exact solution for η solved by Picard iteration.*

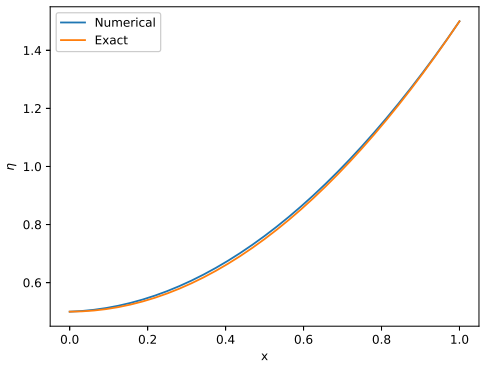

(d) *The numerical results and exact solution for η solved by Newton's method.*

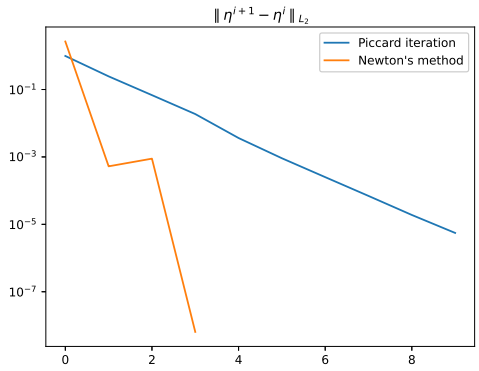

(e) *The error of η for Picard ieration and Newton's method.*

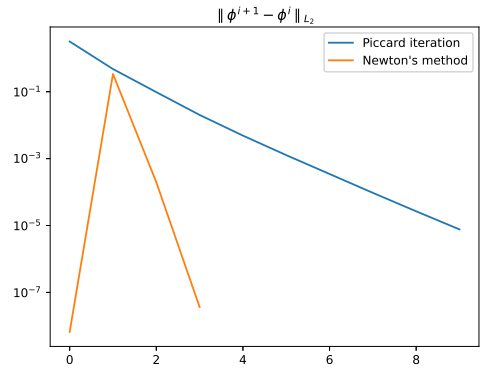

(f) *The error of ϕ for Picard ieration and Newton's method.*

Figure C.1: *Comparison between Picard iteration and Newton's method for the second simplified problem. (a) and (c) are the results solved by Picard iteration, while (b) and (d) are for Newton's method. (e) and (f) compares the rate of convergence of Picard iteration and Newton's method.*

C.2 Simplified problem for tangential boundary condition

Now we consider the simplified problem by replacing the Dirichlet boundary condition with the tangential boundary condition on the free boundary:

$$
\begin{aligned}
-\nabla^2\phi &= f, \quad \text{in } \Omega, && \text{(C.2.1)}\\
\partial_n\phi &= \gamma_1\left(\vec{x}-\vec{x_0}\right)\cdot\vec{n}, \quad \text{on } \Gamma_F, && \text{(C.2.2)}\\
\frac{\partial\phi}{\partial\tau} &= \gamma_2\left(\vec{x}-\vec{x_0}\right)\cdot\vec{\tau}+m, \quad \text{on } \Gamma_F, && \text{(C.2.3)}\\
\phi &= g, \quad \text{on } \Gamma_N, && \text{(C.2.4)}\\
\eta(x) &= \eta_\infty(x), \quad \text{at } x=L, && \text{(C.2.5)}
\end{aligned}
$$

where m and g are some smooth functions, with real constants γ_1 and γ_2. Here we generalise this problem by introducing the point $\vec{x_0}=(x_0,y_0)$ which represents the contact point of the free surface and the fixed boundary on the left. The function $\eta_\infty(x)$ represents the Dirichlet condition for η at $x=L$. We denote $\vec{n}=\frac{1}{\sqrt{1+(\eta'(x))^2}}\left(-\eta'(x),1\right)$ as the unit normal vector to Γ_F, and $\vec{\tau}=\frac{1}{\sqrt{1+(\eta'(x))^2}}\left(1,\eta'(x)\right)$ as the unit tangential vector of Γ_F. The tangential free-boundary condition is a simplified boundary condition from the Bernoulli equation.

Introducing the test function $w\in W:=\{w\in\mathcal{C}^0\left(\Gamma_F\right)|w=0 \text{ at } x=L\}$ and the map (C.1.8), we multiply (C.2.3) with a test function w such that

$$
\int_{\Gamma_F}\frac{\partial\phi}{\partial\tau}\left(w\circ T_\eta\right)^{-1}d\Gamma_\eta=\gamma_2\int_{\Gamma_0}\left[(x-x_0)+(\eta(x)-y_0)\,\eta'(x)\right]wd\Gamma_0+\int_{\Gamma_0}m\sqrt{1+(\eta')^2}wd\Gamma_0, \tag{C.2.6}
$$

where $\frac{\partial\phi}{\partial\tau}=\nabla\phi\cdot\vec{\tau}=\gamma_2\frac{1}{\sqrt{1+(\eta'(x))^2}}\left(\phi_x+\eta'(x)\phi_y\right)$.

C.2.1 Picard iteration

Let $v\in V:=\{v\in\mathcal{C}^1\left(\Omega\right)|v=0 \text{ on } \Gamma_F\}$, $\hat{v}\in\hat{V}:=\mathcal{C}^1\left(\Gamma_F\right)$, and $w\in\mathcal{C}^0(\Gamma_F)$, the weak forms for (C.2.1)-(C.2.5) are:

$$
\int_\Omega\nabla\phi\cdot\nabla vd\mathbf{x}+\int_{\Gamma_N}\kappa\phi_\infty vds=\int_\Omega fvd\mathbf{x}+\int_{\Gamma_N}\kappa gvds, \tag{C.2.7}
$$

$$
\int_\Omega\nabla\phi\cdot\nabla\tilde{v}d\mathbf{x}-\gamma_1\int_{\Gamma_0}\left[((x-x_0)\eta)'+(\eta-y_0)\right)\hat{v}dx=\int_\Omega f\tilde{v}d\mathbf{x}-\gamma_1\eta_\infty(L)\hat{v}(L), \tag{C.2.8}
$$

$$
\begin{aligned}
\int_{\Gamma_F}\frac{\partial\phi}{\partial\tau}\left(w\circ T_\eta\right)^{-1}d\Gamma_\eta &= \gamma_2\int_{\Gamma_0}\left[(x-x_0)+(\eta(x)-y_0)\eta'(x)\right]wd\Gamma_0\\
&\quad+\int_{\Gamma_0}m\sqrt{1+(\eta')^2}wdx, && \text{(C.2.9)}\\
\lambda\phi\big|_{\Gamma_R} &= \lambda g\big|_{\Gamma_R}, && \text{(C.2.10)}
\end{aligned}
$$

where $\tilde{v}$ is the natural lifting of v into $\tilde{V}:=\{\tilde{v}\in\mathcal{C}^1(\Omega)|\tilde{v}(L)=0 \text{ on } \Gamma_F\}$. The second weak form is obtained by integration by parts using the Neumann free-

boundary condition (C.2.2). As the test function $\tilde{v}$ is zero at the top right node denoted as Γ_R on the free boundary, the strong form is used to impose the Dirichlet boundary condition (C.2.4).

Similar to section section C.1.1, we introduce span$\{\zeta_i\}$, span$\{\hat{\zeta}_i\}$, span$\{\tilde{\zeta}_i\}$ and span$\{\xi_i\}$ be the basis for V, $\hat{V}$, $\tilde{V}$ and W correspondingly. The finite element approximation η_h and ϕ_h is defined as (C.1.13) and (C.1.14). We denote $\mathbf{\Phi}_h = (\phi_1, \phi_2, ...)$ and $\eta_h = (\eta_1, \eta_2, ...)$ as the vectors of degree-of-freedom. The Galerkin approximations are

$$\int_\Omega \nabla\phi_h \cdot \nabla\zeta_i d\mathbf{x} + \int_{\Gamma_N} \kappa\phi_h\zeta_i ds = \int_\Omega f\zeta_i d\mathbf{x} + \int_{\Gamma_N} \kappa g\zeta_i ds, \tag{C.2.11}$$

$$\int_\Omega \nabla\phi_h \cdot \nabla\tilde{\zeta}_i d\mathbf{x} - \gamma_1 \int_{\Gamma_0} \left[((x-x_0)\eta_h)' + (\eta_h - y_0)\right] \hat{\zeta}_i dx = \int_\Omega f\tilde{\zeta}_i d\mathbf{x} - \gamma_1\eta_\infty(L)\zeta_i(L), \tag{C.2.12}$$

$$\lambda\phi_h\big|_{\Gamma_R} = \lambda g\big|_{\Gamma_R}, \tag{C.2.13}$$

$$\int_{\Gamma_F} \frac{\partial\phi_h}{\partial\tau} (\xi_i \circ T_\eta)^{-1} d\Gamma_\eta = \gamma_2 \int_{\Gamma_0} \left[(x-x_0) + (\eta_h(x) - y_0)\eta_h'(x)\right] \xi_i d\Gamma_0 + \int_{\Gamma_0} m\sqrt{1+(\eta_h')^2}\xi_i dx, \tag{C.2.14}$$

Using the same finite element mesh on Ω and Γ_F shown in Figure 5.2 where each element E_i on Γ_F is a line element, then

$$\int_{E_i} \frac{\partial\phi_h}{\partial\tau} (w_h \circ T_\eta)^{-1} d\Gamma_\eta = \phi_h\big|_{E_i} = \phi_h(\mathbf{x}_{i+1}) - \phi_h(\mathbf{x}_i), \tag{C.2.15}$$

where $\mathbf{x}_{i+1}$ is the right point on E_i and $\mathbf{x}_i$ is the left point.

Following the same structure of the Picard iteration scheme in Table C.1, the problem of finding ϕ^{k+1} in step 2 is the system

$$\boldsymbol{M} \cdot \mathbf{\Phi}_h = \boldsymbol{b}_1 \tag{C.2.16}$$

where

$$\begin{aligned}
\mathbf{A}_{ij} &= \begin{cases} \int_\Omega \nabla\zeta_j \cdot \nabla\zeta_i d\mathbf{x} + \int_{\Gamma_N} \kappa\, g\zeta_i ds, & \text{in } \Omega \setminus \Gamma_F, \\ \int_\Omega \nabla\zeta_j \cdot \nabla\tilde{\zeta}_i d\mathbf{x}, & \text{on } \Gamma_F \setminus \Gamma_R, \\ \lambda, \quad \mathbf{x}_j \text{ on } \Gamma_R, \end{cases} \\
\mathbf{b}_{1,i} &= \begin{cases} \int_\Omega f\hat{\zeta}_i d\mathbf{x} + \int_{\Gamma_N} \kappa g\hat{\zeta}_i ds, & \mathbf{x}_j \text{ is not on } \Gamma_F, \\ \int_\Omega f\tilde{\zeta}_i d\mathbf{x} - \gamma\eta_\infty(1)\zeta_i + \gamma \int_{\Gamma_0} \left[\left((x-x_0)\eta^k\right)' + (\eta^k - y_0)\right] \hat{\xi}_i dx, & \text{on } \Gamma_F \setminus \Gamma_R, \\ \lambda g, \quad \text{on } \Gamma_R, \end{cases}
\end{aligned} \tag{C.2.17}$$

and the equation to find η^{k+1} in step 3 is

$$\boldsymbol{A} \cdot \boldsymbol{\eta}_h = \boldsymbol{b}_2, \tag{C.2.18}$$

where

$$\begin{aligned}\mathbf{A}_{ij} &= -\gamma_2 \int_{\Gamma_0} (\eta^k)' \xi_j \xi_i dx, \\ \mathbf{b}_{2,i} &= \int_{\Gamma_0} \left[\gamma_2 (x - x_0) + m\sqrt{1 + (\eta_0')^2}\right] \xi_i dx - (\phi_{i+1}^k - \phi_i^k). \end{aligned} \tag{C.2.19}$$

C.2.2 Newton's method

We denote Φ as the velocity potential on the free boundary, such that

$$\partial_n \phi = \gamma_1 (\vec{x} - \vec{x_0}) \cdot \vec{n}, \quad \text{on } \Gamma_F, \tag{C.2.20}$$

$$\frac{\partial \Phi}{\partial \tau} = \gamma_2 (\vec{x} - \vec{x_0}) \cdot \vec{\tau} + m(\vec{x}), \quad \text{on } \Gamma_F, \tag{C.2.21}$$

$$\Phi = g, \quad \text{on } \Gamma_R \tag{C.2.22}$$

$$\eta = \eta_\infty \quad \text{on } \Gamma_R, \tag{C.2.23}$$

where

$$-\nabla^2 \phi_{\Phi,\eta} = f, \quad \text{in } \Omega, \tag{C.2.24}$$

$$\phi_{\Phi,\eta} = \Phi, \quad \text{on } \Gamma_F, \tag{C.2.25}$$

$$\frac{\partial \phi}{\partial \boldsymbol{n}} = 0, \quad \text{on } \Gamma_L, \tag{C.2.26}$$

$$\phi_{\Phi,\eta} = g, \quad \text{on } \Gamma_N. \tag{C.2.27}$$

Similar to section C.1.2, we introduce the test functions $v \in \mathcal{C}^1(\Omega)$ and $w \in W := \{w \in \mathcal{C}^0(\Gamma_F) \,|w = 0 \quad \text{at } x = L\}$. Multiplying (C.2.24) with the test function v, the weak form for the boundary value problem (C.2.24)-(C.2.27) is the same as (C.1.28). The residuals for problem (C.2.20)-(C.2.23) are obtained by using the test function w such that

$$\mathcal{R}_1((\phi,\eta);w) = \begin{cases} \int_\Omega \nabla\phi \cdot \nabla\tilde{w} d\Omega - \int_\Omega f w d\Omega - \gamma_1 \int_{\Gamma_F} [(x - x_0)\eta' + (\eta - y_0)] \, w d\Gamma, \\ \qquad\qquad\qquad\qquad\qquad\qquad \text{on } \Gamma_f \setminus \Gamma_R, \\ \lambda\Phi|_{\Gamma_R} - \lambda g, \quad \text{on } \Gamma_R, \end{cases} \tag{C.2.28}$$

$$\begin{aligned}\mathcal{R}_2((\phi,\eta);w) &= \int_{\Gamma_F} \frac{\partial \phi}{\partial \tau} (w \circ T_\eta)^{-1} d\Gamma_\eta \\ &\quad -\gamma_2 \int_{\Gamma_0} \left[(x - x_0) + (\eta - y_0)\eta'\right] w d\Gamma - \int_{\Gamma_0} m\sqrt{1 + (\eta')^2} w d\Gamma_0, \end{aligned} \tag{C.2.29}$$

where λ is a real constant. Residual $\mathcal{R}_1$ is derived using integration by parts for the points on $\Gamma_F \setminus \Gamma_R$ and a strong form on Γ_R, while residual $\mathcal{R}_2$ is developed from (C.2.6).

Using the same definition of the finite element approximation Φ_h, η_h, ϕ_h and the functions basis in section C.1.2 and the equation (C.2.15), we introduce the linear

system

$$\boldsymbol{J} \cdot \begin{pmatrix} \delta\boldsymbol{\Phi} \\ \delta\boldsymbol{\eta} \end{pmatrix} = \boldsymbol{r}. \tag{C.2.30}$$

The Jacobian matrix $\boldsymbol{J}$ and the residual vector $\boldsymbol{r}$ are denoted as

$$\boldsymbol{J} = \begin{pmatrix} \boldsymbol{A} & \boldsymbol{B} \\ \boldsymbol{C} & \boldsymbol{D} \end{pmatrix}, \qquad \boldsymbol{r} = \begin{pmatrix} \boldsymbol{r}^1 \\ \boldsymbol{r}^2 \end{pmatrix}. \tag{C.2.31}$$

where

$$\begin{aligned}
\boldsymbol{A}_{ij} &= \partial_{\delta\Phi}\mathcal{R}_1\left(\left(\Phi_{h,j}\hat{\zeta}_j, \eta_h\right); \xi_i\right) = \lim_{t\to 0} \frac{\mathcal{R}_1\left(\left((\Phi_{h,j}+t)\hat{\zeta}_j, \eta_h\right); \xi_i\right) - \mathcal{R}_1\left(\left(\Phi_{h,j}\hat{\zeta}_j, \eta_h\right); \xi_i\right)}{t}, \\
\boldsymbol{B}_{ij} &= \partial_{\delta\eta}\mathcal{R}_1\left(\left(\Phi_h, \eta_{h,j}\hat{\zeta}_j\right); \xi_i\right) = \lim_{t\to 0} \frac{\mathcal{R}_1\left(\left(\Phi_h, (\eta_{h,j}+t)\hat{\zeta}_j\right); \xi_i\right) - \mathcal{R}_1\left(\left(\Phi_h, \eta_{h,j}\hat{\zeta}_j\right); \xi_i\right)}{t}, \\
\boldsymbol{C}_{ij} &= \partial_{\delta\Phi}\mathcal{R}_2\left(\left((\Phi_{h,j}\hat{\zeta}_j, \eta_h\right); \xi_i\right) = \lim_{t\to 0} \frac{\mathcal{R}_2\left(\left(\Phi_{h,j}+t)\hat{\zeta}_j, \eta_h\right); \xi_i\right) - \mathcal{R}_2\left(\left(\Phi_{h,j}\hat{\zeta}_j, \eta_h\right); \xi_i\right)}{t}, \\
\boldsymbol{D}_{ij} &= \partial_{\delta\eta}\mathcal{R}_2\left(\left(\Phi_h, \eta_{h,j}\hat{\zeta}_j\right); \xi_i\right) = \lim_{t\to 0} \frac{\mathcal{R}_2\left(\left(\Phi_h, (\eta_h+t)\hat{\zeta}_j\right); \xi_i\right) - \mathcal{R}_2\left(\left(\Phi_h, \eta_{h,j}\hat{\zeta}_j\right); \xi_i\right)}{t}, \\
\boldsymbol{r}_i^1 &= \mathcal{R}_1\left((\Phi_h, \eta_h); \xi_i\right), \\
\boldsymbol{r}_i^2 &= \mathcal{R}_2\left((\Phi_h, \eta_h); \xi_i\right).
\end{aligned} \tag{C.2.32}$$

The linear system for the boundary value problem (C.2.1)-(C.2.4) is the same as (C.1.46).

C.2.3 Numerical experiment

We use the test case

$$\begin{aligned}
f &= 0, \\
m &= -\frac{2}{3}\eta\eta' + \frac{2}{3}\eta', \\
g &= \frac{X^2 - Y^2}{6} + \frac{2}{3}Y, \\
\eta_\infty &= x^2 + \frac{1}{2},
\end{aligned}$$

in the domain $\Omega := \{(x, y) = (0, 1) \times (-1, 0)\}$ such that the left node of Γ_F is not at the origin. The initial free boundary is at $\eta^0(x) = 0$ and the initial guess for Newton's iteration is $\Phi = \frac{X^2}{6}$. Figure C.2 shows the comparison between the Picard iteration and Newton's method. Figure C.2a and C.2c are the numerical results obtained by Picard iteration, while Figure C.2b and C.2d are obtained by Newton's method. The results of Picard iteration have some obvious differences with the exact solution when $x \to 1$, while the results of Newton's method agree well with the exact solution. Furthermore, Newton's method converges a lot faster than Picard iteration

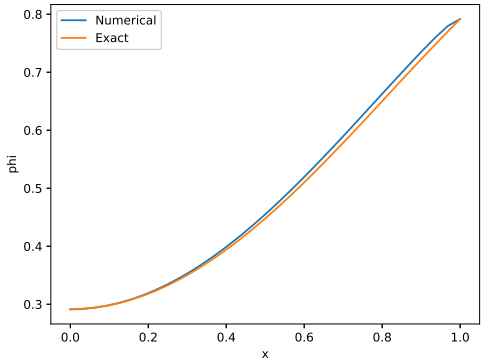

(a) *The numerical results and exact solution for Φ solved by Picard iteration.*

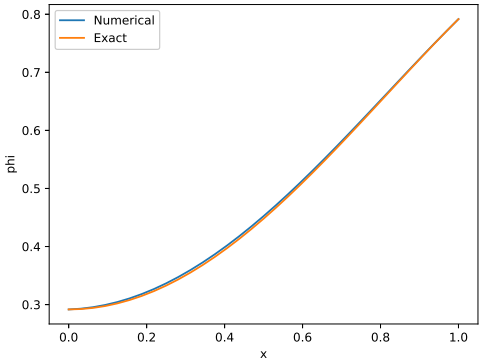

(b) *The numerical results and exact solution for Φ solved by Newton's method.*

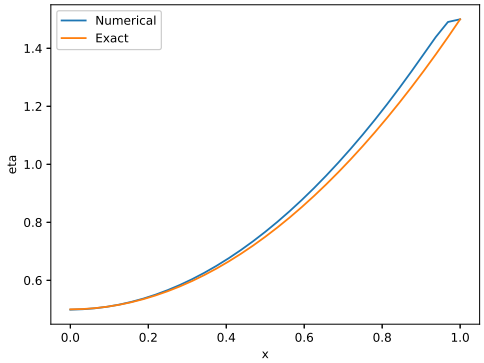

(c) *The numerical results and exact solution for η solved by Picard iteration.*

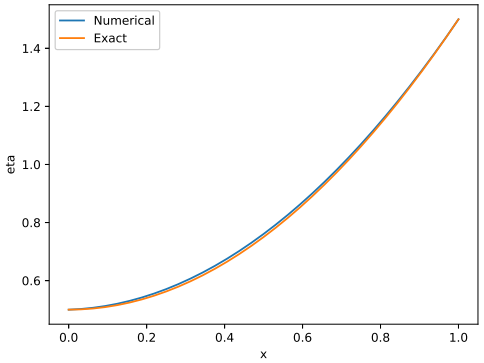

(d) *The numerical results and exact solution for η solved by Newton's method.*

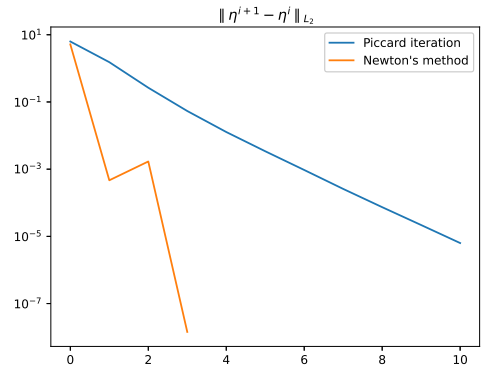

(e) *The error of η for Picard ieration and Newton's method.*

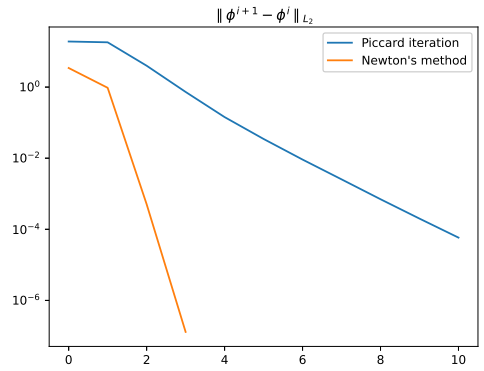

(f) *The error of Φ for Picard ieration and Newton's method.*

Figure C.2: *Comparison between Picard iteration and Newton's method for the third simplified problem. (a) and (c) are the results solved by Picard iteration, while (b) and (d) are for Newton's method. (e) and (f) compares the rate of convergence of Picard iteration and Newton's method.*

as shown in Figure C.2e and C.2f. Thus, we apply Newton's method to solve the solid/single fluid interaction problem in the inner region in chapter 5.

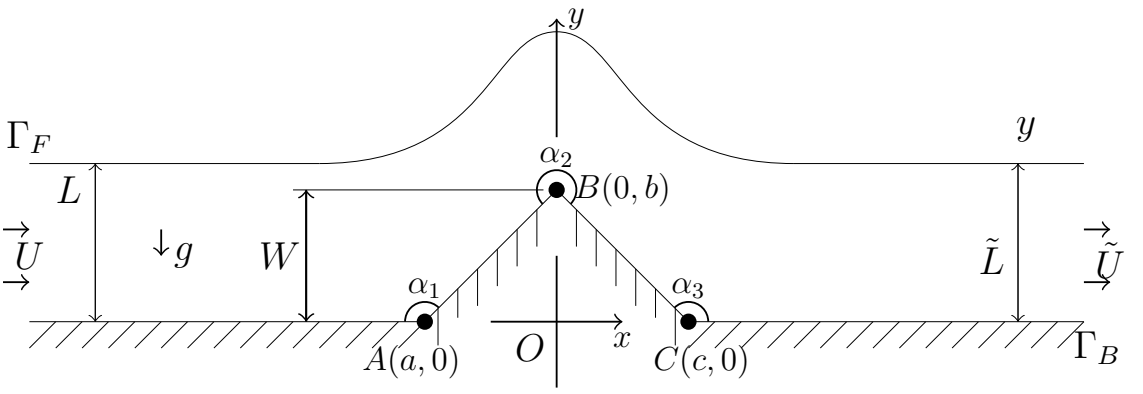

(a) *Sketch of the flow.*

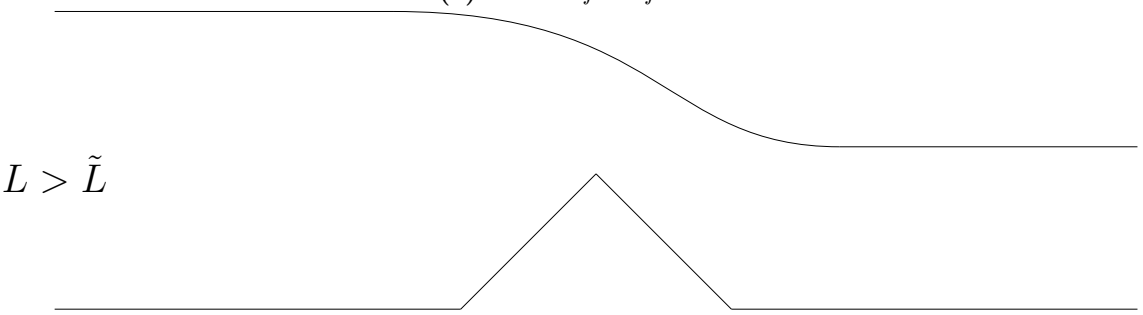

(b) *An example of subcritical flow upstream and supercritical flow downstream.*

Figure D.1: *This shows two different types of solutions and the sketch of the flow. D.1a is a sketch of the flow for $U = \tilde{U}$ $L = \tilde{L}$ and $F \geq 1$. D.1b is an example of subcritical flow upstream and supercritical flow downstream.*

Appendix D

Submerged Triangle Problem

The submerged triangle problem is from [22], and we will give the details about how Dias and Vanden-Broeck formulate this problem. The model considers a steady irrotational flow of an incompressible, inviscid fluid over a triangular obstruction as shown in Fig.D.1a. A system of Cartesian coordinates is introduced, where the x-axis is along the parallel bottom plate and the y-axis goes through the apex (point B) of the triangle. The acceleration of gravity g acts in the negative y-direction. The flow approaches a uniform stream when $|x| \to \infty$, where the upstream flow has velocity U and depth L, and the downstream flow has velocity $\tilde{U}$ and depth $\tilde{L}$. The

height of the triangle is denoted as W. We introduce the velocity potential of this flow as $\phi(x, y)$ and the location of the free surface $y(x)$. The Froude number F is defined as

$$F = \frac{U}{(gL)^{\frac{1}{2}}}. \tag{D.0.1}$$

Now we introduce dimensionless variables

$$x' = \frac{x}{L}, \quad y' = \frac{y}{L}, \quad \phi' = \frac{\phi}{UL}, \quad y' = \frac{y}{L}, \quad \tilde{L}' = \frac{\tilde{L}}{L}, \quad \tilde{U}' = \frac{\tilde{U}}{U}. \tag{D.0.2}$$

We drop primes for convenience of notations. When $\tilde{L} \leq 1$, the flow is defined as subcritical upstream and supercritical downstream (as shown in Fig.D.1b). Moreover, the flow is supercritical upstream and downstream when $\tilde{L} = 1$ and $F \geq 1$.

We denote the whole region of the flow as Ω, the bottom plate as Γ_B, and the free surface as Γ_F. The Bernoulli condition on Γ_F is

$$\frac{1}{2}F^2|\nabla\phi|^2 + y = \text{constant}, \quad \text{on } \Gamma_F. \tag{D.0.3}$$

The constant value on the right-hand side of the Bernoulli equation can be evaluated by considering the conditions upstream. Then the Bernoulli equation on the free surface is

$$\frac{1}{2}F^2|\nabla\phi|^2 + y = \frac{1}{2}F^2 + 1. \tag{D.0.4}$$

Now the governing equation and boundary conditions are

$$\begin{aligned}
\nabla^2\phi &= 0, \quad \text{in } \Omega, && \text{(D.0.5)}\\
\frac{1}{2}F^2|\nabla\phi|^2 + y &= \frac{1}{2}F^2 + 1, \quad \text{on } \Gamma_F, && \text{(D.0.6)}\\
\frac{\partial\phi}{\partial\mathbf{n}} &= 0, \quad \text{on } \Gamma_F, && \text{(D.0.7)}\\
\frac{\partial\phi}{\partial\mathbf{n}} &= 0, \quad \text{on } \Gamma_B, && \text{(D.0.8)}\\
\phi_x &= 1, \quad x \to -\infty, && \text{(D.0.9)}\\
\phi &= 0, \quad x \to +\infty, && \text{(D.0.10)}\\
y &= 1, \quad x \to -\infty, && \text{(D.0.11)}
\end{aligned}$$

where $\mathbf{n}$ is the unit normal to the boundary pointing out the flow.

According to [22], two different types of solutions are derived by considering the Bernoulli condition at $|x| \to \infty$ as

$$\frac{1}{2}F^2 + 1 = \frac{1}{2}F^2\tilde{U}^2 + \tilde{L}. \tag{D.0.12}$$

The discharge Q is defined as

$$Q = UL = \tilde{U}\tilde{L}. \tag{D.0.13}$$

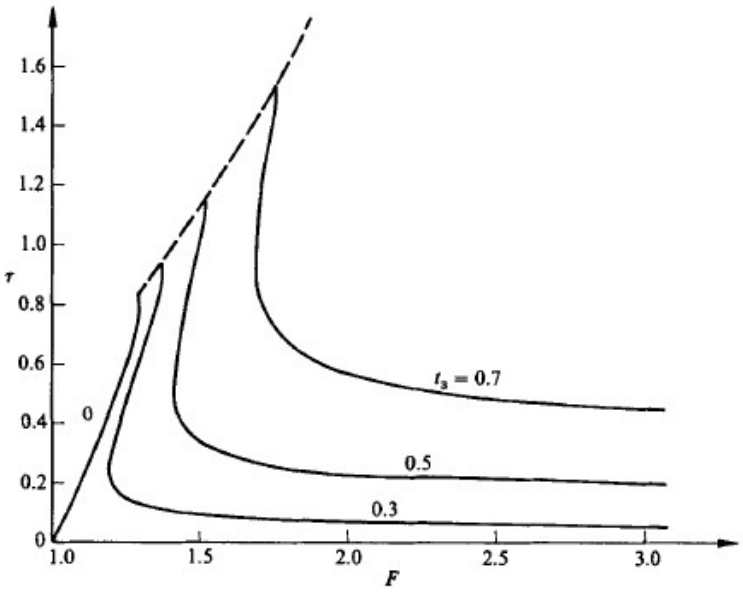

Figure D.2: *τ is the maximum value of the deviation of the free surface. t_3 defines the geometry of the triangle by using conformal mapping and then mapping to a half-unit circle called $t-$plane. The dashed line shows the analytical values of the maximum of τ with respect to F. The curve noted 0 is the solitary wave when $t_4 = 0$. This graph is from [22].*

Then we can eliminate $\tilde{U}$ in (D.0.12) by substituting (D.0.13) such that

$$\left(\tilde{L} - 1\right)\left[\frac{1}{2}F^2\left(\frac{1}{\tilde{L}} + 1\right) - \tilde{L}\right] = 0. \tag{D.0.14}$$

It is obvious that this equation has two solutions :

$$\tilde{L} = 1, \tag{D.0.15}$$

and

$$F^2 = \frac{2\tilde{L}^2}{1 + \tilde{L}}. \tag{D.0.16}$$

The first solution (D.0.15) indicates that $\tilde{L} = L$ and $\tilde{U} = U$. For the solution (D.0.16), it can be shown that $F \geq 1$ when $\tilde{L} \geq 1$, and $F \leq 1$ when $\tilde{L} \leq 1$. In [22], when considering the second type of the solutions, Dias and Vanden-Broeck assume that $\tilde{L} \leq 1$, thus the flow is subcritical upstream and supercritical downstream. An example of this flow is shown in Fig.D.1b.

The results we compare in this thesis are for the first solution for $F \geq 1$ as shown in Figure D.2 [22]. τ is the maximum value of the deviation of the free surface, which is equivalent to y_0 in our notation. t_3 defines the geometry of the triangle by using conformal mapping and then mapping to a half-unit circle called t-plane. Dias and Vanden-Broeck found that F first decrease then increase as τ becomes larger, which indicates for some values of F there exist two solutions. By considering the solitary wave, i.e. $t_3 = 0$, they found that the maximum of τ satisfies $\tau_{max} = \frac{1}{2}F^2$.